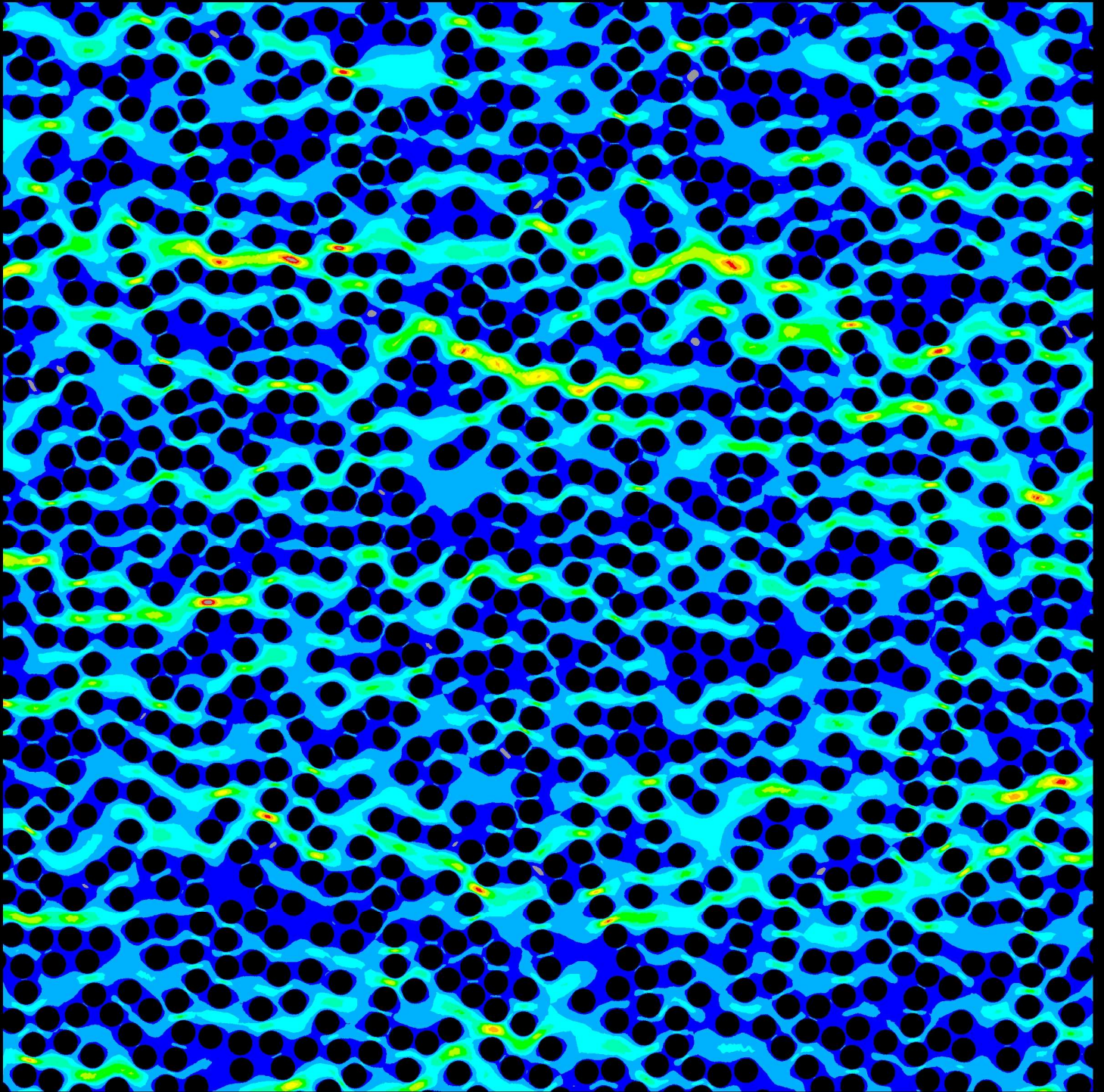


# MICRO-MACRO RELATIONS FOR FLOW THROUGH FIBROUS MEDIA



KAZEM YAZDCHI

# MICRO-MACRO RELATIONS FOR FLOW THROUGH FIBROUS MEDIA

Kazem Yazdchi

**Samenstelling promotiecommissie:**

Prof. dr. F. Eising (voorzitter)	University of Twente
Prof. dr. S. Luding (promotor)	University of Twente
Prof. dr. D. Lohse	University of Twente
Prof. dr. A. de Boer	University of Twente
Prof. dr. H. Steeb	Ruhr-University Bochum, Germany
Dr. C. O'Sullivan	Imperial College London, UK
Dr. N. P. Kruyt	University of Twente
Dr. M.A. van der Hoef	University of Twente
Dr. H. Wachtel	Boehringer Ingelheim, Germany



This research was carried out at the Multi Scale Mechanics (MSM) group, MESA+ Institute for Nanotechnology, Faculty of Engineering Technology of the University of Twente. It has been supported by the STW through the STW-MuST program, Project Number 10120.

Nederlandse titel:

*Micro-macro relaties voor stroming door vezelachtige media*

Published by ..... , Enschede, The Netherlands

ISBN: 978-90-365-3414-7

Cover Illustration: (Front cover) Horizontal velocity field of fluid flow through random, fibrous media; (Back cover) Coarse-grained horizontal velocity field based on Delaunay triangulation. Copyright © 2012 by Kazem Yazdchi.

Copyright © 2012 by Kazem Yazdchi

No part of the materials protected by this copyright notice may be reproduced or utilized in any form or by any means, electronic or mechanical, including photocopying, recording or by any information storage and retrieval system, without written permission of the author.

# MICRO-MACRO RELATIONS FOR FLOW THROUGH FIBROUS MEDIA

PROEFSCHRIFT

ter verkrijging van  
de graad van doctor aan de Universiteit Twente,  
op gezag van de rector magnificus,  
Prof. dr. H. Brinksma,  
volgens besluit van het College voor Promoties  
in het openbaar te verdedigen  
op woensdag 28 november 2012 om 12:45 uur

door

Kazem Yazdchi  
geboren op 21 september 1984  
te Esfahan, Iran

Dit proefschrift is goedgekeurd door de promotor:

Prof. dr. rer. nat. Stefan Luding

# Abstract

Flow and transport in porous media are essential in many processes in mechanical, chemical, and petrochemical industries. Despite the wide variety of applications and intensive research efforts, the complex hydrodynamics of these systems is still not fully understood, which renders their design and scale-up difficult. Most porous media have a particulate origin but some are composed of long particles/fibres and, therefore, are considered as fibrous media. They are encountered in a variety of modern technological applications, predominantly in the manufacturing of fibre-reinforced composites, with extensive use in the aerospace and automobile industries.

The aim of this thesis is to further develop our understanding of the drag closures, i.e. the connection between microstructure (particle shape, orientation and arrangement) and macroscopic permeability/drag. To address this problem, we employ fully resolved finite element (FE) simulations of flow in static, regular and random arrays of cylinders (and other shapes) at low and moderate Reynolds numbers. Asymptotic analytical solutions at both dense and dilute limits are used to construct drag relations that are universal, i.e. valid for all porosities. Those relations are needed for coupling of the fluid and solid phases (particles) in multi-phase flow codes.

The numerical experiments suggest a unique, scaling power law relationship between the permeability and the mean value of the shortest Delaunay triangulation edges, constructed using the centers of the fibres (which is identical to the averaged second nearest neighbor fibre distances). It is complemented by a closure relation that relates the effective microscopic channel lengths to the macroscopic porosity. This percolating network of narrow channels controls the macro flow properties.

From our fully resolved FE results, for both ordered and random fibre arrays, we find that (i) the weak inertia correction to the linear Darcy relation is third power in superficial velocity,  $U$ , up to small Reynolds number,  $Re \sim 1-5$ . When attempting to fit our data with a particularly simple relation, (ii) a non-integer power law in  $U$  performs astonishingly well up to the moderate  $Re \sim 30$ . However, for randomly distributed arrays, (iii) a quadratic correction performs quite well as used in the Forchheimer (or Ergun) equation, from small to moderate  $Re$ .

Finally, the universal fluid-particle drag relations have been incorporated into a coarse FE two-phase framework, based on coupling an unstructured FE mesh and a soft-sphere discrete element method (DEM) for moving particles. The mesh is a dynamic Delaunay triangulation based on the particle positions. This provides a framework for FE method discretization of the equations of fluid dynamics as well as a simple tool for detecting contacts between moving particles.

# Samenvatting

Stroming en transport in poreuze media zijn essentiële mechanismes in vele processen in mechanische, chemische en petrochemische industrie. Ondanks de grote verscheidenheid van toepassingen en intensief onderzoek, is de complexe hydrodynamica van deze mechanismes nog steeds niet volledig begrepen, wat het ontwerp van processen en schaalvergroting van laboratorium modellen moeilijk maakt. De meeste poreuze media hebben een deeltjes structuur, maar sommige bestaan uit lange deeltjes/vezels en worden daarom beschouwd als vezelachtige media. Dit soort materialen worden gebruikt voor een verscheidenheid van moderne technologische toepassingen, voornamelijk in de productie van vezelversterkte composieten, die veelvuldig worden gebruikt in de luchtvaart- en automobiël industrie.

Het doel van dit proefschrift is de verdere ontwikkeling van ons begrip van de weerstand sluiting, dat wil zeggen de verbinding tussen de microstructuur (deeltjes vorm, oriëntatie en plaatsing) en de macroscopische permeabiliteit/weerstand. Om hierin meer inzicht te verkrijgen, gebruiken we hoge resolutie eindige elementen simulaties van de stroming in statische, regelmatige en willekeurige configuraties van cilinders (en andere vormen) bij lage en gematigde Reynolds getallen. Asymptotisch analytische oplossingen voor limiet gevallen van veel en weinig deeltjes zijn gebruikt om universele relaties te construeren. Deze relaties zijn nodig voor de koppeling van de vloeistof en de vaste fase (deeltjes) in meerfasenstroming. De numerieke experimenten suggereren een unieke schaal machtswet tussen de permeabiliteit en de gemiddelde waarde van de kortste Delaunay triangulatie randen geconstrueerd met de centra van de vezels. Het percolatie netwerk van smalle kanalen controleert de macroscopische vloeieigenschappen.

Van onze volledig eindige elementen opgelost resultaten, zowel voor geordende en willekeurige vezel pakking, vinden we dat (i) de zwakke traagheid correctie op de lineaire Darcy relatie is de derde macht in superficiële snelheid,  $U$ , tot klein getal van Reynolds,  $Re \sim 1-5$ . Bij een poging onze gegevens te beschrijven met een bijzonder eenvoudige relatie (ii) een niet-integer machtswet in  $U$  geeft verbazingwekkend goede resultaten tot gemiddelde  $Re$  getallen (tot  $Re \sim 30$ ). Echter, bijvoorbeeld voor willekeurig arrays (iii) presteert een kwadratische correctie zoals gebruikt in de Forchheimer of Ergun vergelijking goed voor kleine tot gemiddelde  $Re$  getallen.

Tenslotte zijn de universele vloeistof-deeltjes weerstands relaties opgenomen in een grof eindige elementen, twee fasen kader gebaseerd op de koppeling van een ongestructureerde eindige elementen rooster en een zacht-bol discrete elementen methode (DEM) voor het verplaatsen van deeltjes. Het rooster is een dynamische Delaunay-triangulatie op de posities van de deeltjes. Dit biedt een kader voor de eindige elementen discretisatie van de vergelijkingen van de stromingsleer en een eenvoudige tool voor het opsporen van contacten tussen bewegende deeltjes.



# Contents

<b>Abstract</b>	<b>(i)</b>
<b>Samenvatting</b>	<b>(ii)</b>
<b>1. Introduction</b>	<b>1</b>
1.1 General introduction .....	2
1.2 Motivation and background .....	2
1.3 Multi-level (hierarchy) modeling approach .....	3
1.4 Fluid permeability (drag force) and interfacial closures .....	5
1.5 Scope and objectives .....	7
1.6 Organization of the dissertation .....	8
References .....	9
<b>2. Microstructural effects on the permeability of periodic fibrous porous media</b>	<b>14</b>
2.1 Introduction .....	16
2.2 Results from FE simulations .....	18
2.2.1 Introduction and terminology .....	18
2.2.2 Mathematical formulation and boundary conditions .....	19
2.2.3 Permeability of the square and hexagonal arrays .....	21
2.2.4 Effect of shape on the permeability of regular arrays .....	24
2.2.5 Effect of aspect ratio on the permeability of regular arrays of ellipses .....	25
2.2.6 Effect of orientation on the permeability of regular arrays .....	26
2.2.7 Effects of staggered cell angle .....	29
2.3 Theoretical prediction of the permeability for all porosities .....	32
2.3.1 From special cases to a more general CK equation .....	32
2.3.2 Measurement of the tortuosity .....	35
2.3.3 Measurement of the shape/fitting factor .....	36
2.3.4 Corrections to the limit theories .....	38
2.4 Summary and conclusions .....	40
References .....	42
<b>3. Micro-macro relations for flow through random arrays of cylinders</b>	<b>45</b>
3.1 Introduction .....	47
3.2 Mathematical formulation and methodology .....	48
3.3 Generation of the fibrous microstructure .....	51



3.3.1 Method of generation .....	51
3.3.2 Statistical analysis of the microstructure .....	53
3.3.3 Isotropy and homogeneity of the packing .....	55
3.3.4 Effect of minimum inter-fibre distance .....	55
3.3.5 Summary .....	60
3.4 Theoretical prediction of the permeability .....	60
3.4.1 Statistical characterization of effective channels .....	61
3.4.2 Permeability prediction in terms of effective channels .....	67
3.5 Summary and conclusions .....	71
Appendix 3.A Mesh sensitivity analysis .....	72
Appendix 3.B Study of the system size (edge) effects .....	73
Appendix 3.C Towards the dense regime .....	78
Appendix 3.D Purely empirical, macroscopic permeability-porosity relation based on asymptotic solutions .....	78
References .....	80
<b>4. Upscaling the transport equations: Microstructural analysis</b> .....	<b>83</b>
4.1 Introduction .....	85
4.2 Mathematical formulation and methodology .....	86
4.3 Microstructure characterization .....	88
4.3.1 Voronoi diagram (VD) .....	88
4.3.2 Bond orientational order parameter .....	94
4.4 Macroscopic properties .....	95
4.4.1 Effective channels based on Delaunay triangulations .....	95
4.4.2 Permeability calculation .....	97
4.5 Darcy's law – upscaling the transport equations .....	98
4.5.1 Uniform cells .....	99
4.5.2 Unstructured cells .....	103
4.6 Summary and conclusions .....	105
References .....	106
<b>5. Towards unified drag laws for inertial flow through fibrous materials</b> .....	<b>111</b>
5.1 Introduction .....	113
5.2 Theoretical background .....	115
5.3 Numerical results .....	122
5.3.1 Ordered structure .....	122
5.3.2 Structural disorder .....	129
5.4 Summary and conclusions .....	138

Appendix 5.A Comparison of the fit quality for ordered/disordered configurations	140
Appendix 5.B Mesh sensitivity analysis for random arrangements	142
Appendix 5.C An alternative cubic correction fit for the friction factor	144
Appendix 5.D Towards unifying friction factor using different definitions of Re numbers	145
References	147
<b>6. Mesoscale coupling of FEM/DEM for fluid-particle interactions</b>	<b>153</b>
6.1 Introduction	155
6.2 Mathematical model	157
6.2.1 Drag force model	158
6.2.2 Contact force model	160
6.3 Finite element formulation	160
6.3.1 The mesh and drag force computation	162
6.3.2 Local porosity calculation	164
6.3.3 Time integration	165
6.4 Numerical results	166
6.4.1 Static particles	166
6.4.2 Moving particles	170
6.5 Summary and conclusions	172
References	173
<b>7. Summary and recommendations</b>	<b>177</b>
7.1 Summary and general conclusions	178
7.2 Outlook and recommendations	180
<b>Acknowledgements</b>	<b>182</b>
<b>Curriculum vitae</b>	<b>183</b>

# 1

## Introduction

*"Real knowledge is to know the extent of one's ignorance"*

*~ Confucius ~*

## 1.1 General introduction

In this chapter I present some background materials for subsequent chapters, aiming at developing an intuitive (physical) understanding of the essential underlying concepts and methodologies, before presenting a new multiscale framework for modeling two-phase flows.

## 1.2 Motivation and background

The modeling of realistic systems is already a challenge when several fields are involved only on a single scale. Usually fields or phases, e.g. discrete particles, solid walls and fluids/gases, are coupled and affect each other continuously at different length scales. Examples are, but not limited to, fluidized bed reactors in chemical engineering, mechanical engineering unit-processes like silos, mixers, ball-mills, or transport belts, modern engineering materials like composites, geotechnical and geophysical systems, micro-fluidic reactors, and electrostatic field-structure-particle interactions [1]. Fig. 1.1 shows some examples of multiphase phenomena occurring at various length scales.

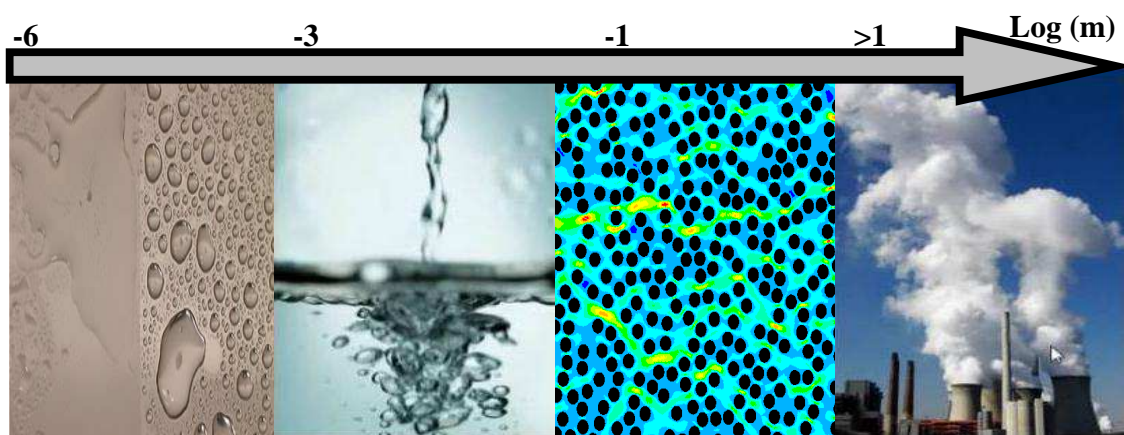


**Figure 1.1:** Some examples of multiphase phenomena occurring at various length scales. From left to right: Nanoparticles for self-cleaning surfaces, gases (like bubbles) in a liquid, flow in porous media and industrial chemical reactors.

The particle (solid) phase is usually described by means of the so-called discrete element method (DEM), where all information on particle position, velocity and forces is available in detail [2, 3]. The DEM is essentially a numerical technique to model the motion of an assembly of particles interacting with each other through collisions. It is quite efficient for investigating phenomena occurring at the length scale of a particle

diameter. The computational cost relies on several factors, including the geometric representation and contact detection algorithm used [4]. On the other hand, continuum methods are used for chemical engineering applications like granular and gas-particle flows [5, 6] silos and unusual flow-zones and geometries [7, 8], fluid flow, aerodynamics, and many others, on much larger scales. Attempts to couple particle- and continuum methods have been successful in rather simple model systems and special cases [9, 10] and are still subject of ongoing research.

The discrete particle model (DPM) is considered to be the most suitable model to describe the hydrodynamics of dispersed multiphase flows [11-13]. The DPM is based on Lagrangian tracking of individual particles, i.e. DEM, combined with computational fluid dynamics (CFD), i.e. the volume-averaged Navier-Stokes equations, for the continuous phase. Two-way coupling is achieved via the momentum sink/source term which includes the fluid-particle drag force. This type of model falls in between the two-fluid model (TFM) used for simulations of large scale processes, and the direct numerical simulations (DNS) that are applicable only for small scale systems (see next section where different modeling schemes at various length scales are compared). A common deficiency of this model is the incompatibility between the resolutions for the two phases. Typically, a fluid cell must contain many particles so as to be consistent with the volume averaging concept used in the fluid/gas phase. Since the fluid/gas-phase mesh size is much larger than the individual particle, it is not possible to resolve the drag numerically. Moreover, the DPM traditionally calculates the drag on a particle with a local slip velocity interpolated at the particle position from values on neighboring grid nodes, which deviates further from the original meaning of the empirical drag closures. This has motivated the development of more accurate relationships between macroscopic parameters, like permeability/drag, and microstructural parameters, like fibre/particle arrangements, shape and orientation or tortuosity (flow path), see chapters 2 and 3.

### 1.3 Multi-level (hierarchy) modeling approach

The general approach in modeling industrial multiphase flow processes is at the continuum scale. Semi-empirical expressions, such as Darcy's law, are substituted for velocity in the continuity equation, which is then coupled with a momentum, mass, and energy balance. While a continuum approach is acceptable in some cases, additional modeling (small scale simulations) is required for certain multiphase flows, where the detailed information is desired. The basic idea is that the smaller scale models, which take into account the various interactions (fluid-particle, particle-particle/wall) in detail, are used to develop closure laws which can represent the effective coarse-grained interactions in the larger scale models [14].

Fig. 1.2 shows a schematic representation of various models, including the information that is abstracted from the simulations, which is incorporated in higher scale models via closure relations. At the most detailed level of description, the fluid/gas flow field is modeled at scales smaller than the particle size using one of the finite element (FE),

lattice Boltzmann (LB), immersed boundary (IB), finite difference (FD) or finite volume (FV) approaches. The momentum exchange (drag closures) between the particles and the fluid/gas phase is determined, which can be used in the higher (larger) scale models.

At the intermediate level, i.e. DPM, the flow field is treated as a continuum and usually solved on a computational grid with a grid size of a few particle diameters. The motion of individual particles is tracked using Newton's laws, accounting for collisions with other particles, with walls and the fluid-particle interaction forces. This Euler-Lagrangian model has been widely used over the last decade to study the complicated flow behaviors in gas-solid fluidized beds. The advantage of DPM is that the particle-particle/wall interactions are taken into account for sufficiently large systems to allow for a direct comparison with laboratory-scale experiments (~0.1 meter). However, this approach requires accurate closure (drag) relations for the unresolved solid-fluid interactions, see next section.

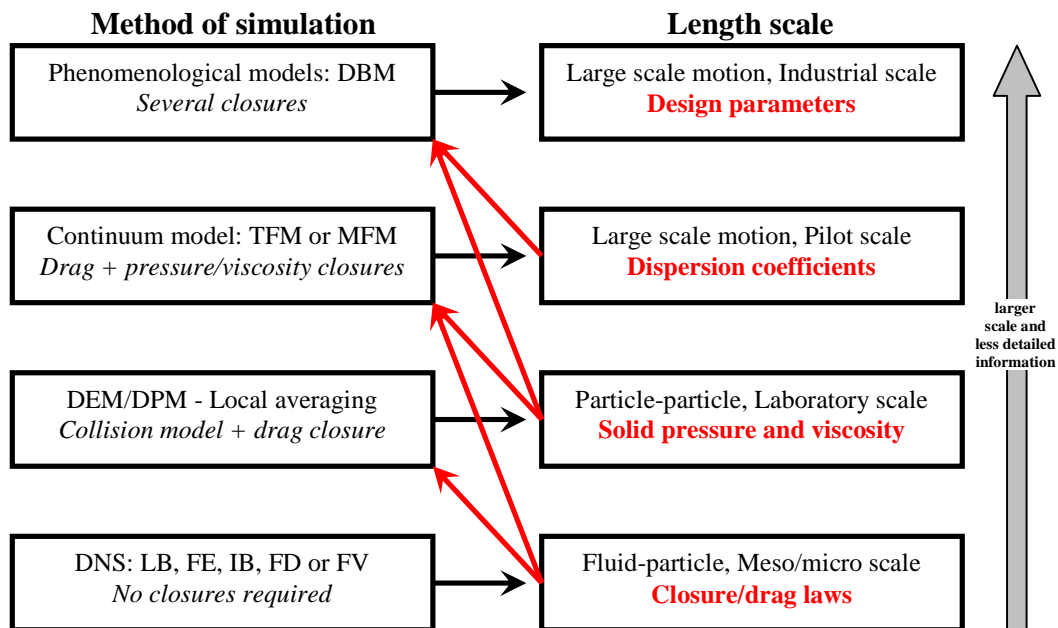


**Figure 1.2:** Schematic representation of the multi-level modeling scheme. The italic and red, bold text show the closures one need and the information one obtain from that level of simulation, respectively.

The third model is the continuum model, i.e. the Two Fluid Model (TFM) or the Multi Fluid Model (MFM), where two or multiple phases are considered as interpenetrating continua that are described by the averaged Navier-Stokes equations [15, 16]. The TFM equations relate the spatial distributions of averaged physical quantities of continuous or dispersed phases to the interaction force at the interface. This Euler-Euler model relies

heavily on closure relations for the effective solid pressure and viscosity, and gas-solid drag, which are obtained from DNS. With this approach a bed behavior of gas-solid flows can be predicted using at intermediate pilot-industrial scale (~1 meter).

At the highest level (~10 meter), industrial scale fluidized bed reactors are simulated with the phenomenological Discrete Bubble Model (DBM), where the voids or bubbles are tracked by evaluating the net force acting on each bubble (similar to the particles in DEM) and the emulsion phase treated as the continuum phase [17]. It has been extensively used to investigate the hydrodynamics, coalescence, and breakup occurring in large scale bubble columns [18].

#### 1.4 Fluid permeability (drag force) and interfacial closures

The prime difficulty of modeling two-phase gas/fluid-solid flows (in both Euler-Euler and Euler-Lagrangian approaches) is the interphase coupling, which deals with the effects of gas/fluid flow on the solids motion and vice versa. Among all the coupling terms emerging from averaging (e.g. fluid-particle drag, added-mass, lift, history, Magnus forces, and particle and fluid phase stresses), the fluid-particle drag is particularly important: it is usually the primary force to suspend and transport the particles; it has a significant influence on the bed expansion and stability of the suspension. The drag force depends (among many parameters such as particle size/spatial distribution, particle shape, and orientation, etc.) on the local relative velocity between phases and the average porosity. It was shown in several case studies that the drag law has a significant influence on the qualitative and quantitative nature of the flow [19-21], which may result in differences in the heat and mass transfer and hence the overall chemical conversion in the bed. Therefore, establishing accurate drag force relations is crucial for obtaining good performance and has challenged both the physics and the engineering community for many years.

The most widely used drag laws, i.e. Ergun equation [22] at low and Wen & Yu correlation [23] at high porosities, are generally based on experimental measurements and are empirical in nature. While experiments are time consuming, costly and easily influenced by disturbances, analytical predictions are limited to idealized situations, for instance spherical particles at very dense or dilute regimes in the limit of low Reynolds numbers,  $Re$ . A relatively new, accurate and efficient way is to use DNS, which is neither restricted to any idealized situation nor suffers from experimental difficulties. The typical simulation strategy is to specify a constant pressure gradient in a given direction and then obtain the averaged flow velocity through static spherical/cylindrical particles/fibers. At the creeping flow regime, the macroscopic permeability/drag of the porous medium can then be obtained using Darcy's law, which states that the superficial velocity in the medium is directly proportional to the applied pressure gradient.

Detailed LB simulations of the flow through uniform and random spherical particles were carried out at low  $Re$  and wide range of porosity by Hill et al. [24] and at low and



moderate  $Re$  by van der Hoef et al. [25]. In both studies a model was derived by fitting the numerical simulations into an empirical relation which shows some discrepancy compared to commonly established and well verified correlations. Benyahia et al. [26] developed a drag law, applicable to the full range of porosity and  $Re$ , by blending the previous drag correlations such that the blended function is continuous with respect to  $Re$  and porosity. Kandhai et al. [19] compared the LB simulation results to both the Ergun and the Wen & Yu correlations for  $Re$  up to 60. The Wen & Yu correlation was found to present a good match with the simulation results for porosity larger than 0.7, while the Ergun correlation shows good agreement for porosity less than 0.5. Beetstra et al. [27] reported that the Ergun correlation over-predicts drag force in monodisperse systems with Reynolds numbers greater than  $\sim 400$  and porosity larger than 0.4 and always over predicts for systems with higher Reynolds numbers, regardless of the porosity. Note that the experimental measurements made by Ergun were done for crushed (irregular) materials and with some degree of polydispersity in the particles whereas the LB simulations were done for monodisperse, perfectly spherical particles. This may account for some of the observed discrepancies.

In almost all previous studies, the drag closures were obtained by smoothing out the small-scale effects and fitting the numerical/experimental data of nearly homogeneous systems into complicated, empirical equations without any physical or microstructural insights/effects. However, in many applications, the local, micro-scale phenomena and physics are relevant for the macroscopic behavior on much larger scale. The (possibly evolving) size, shape, physical properties and spatial distribution of the microstructural constituents largely determine the macroscopic, overall behavior of multi-phase materials. Agrawal et al. [28] established that coarse-grid simulation of gas-particle flows must include sub-grid models, to account for the effects of the unresolved mesoscale structures. Similarly, Boemer et al. [29] pointed out the need to correct the drag coefficient to account for the consequences of clustering, and proposed a correction for the very dilute limit. Due to both the inhomogeneity in porosity distribution and the additional wetted surface introduced by the containing wall, the pressure drop can differ from that of the homogeneous bed. Consequently, it is important to accurately predict the effect of the containing wall. Despite the controversy over the wall effect [30, 31], recent studies [32-34] have concluded that the pressure drop can be increased by wall friction or decreased by an increase in porosity near the wall, and the predominance of one effect over the other depends on the flow regime. In a recent study, Kriebitzsch et al. [35] showed that the drag on individual particles in a homogeneous random array depends strongly on all its surrounding neighbors within a distance of at least two particle diameters. They showed that this drag can differ up to 40% with the drag that would be used in DPM simulations. Finally, the drag force for polydisperse systems was recently described by extending the monodisperse drag laws in an *ad hoc* manner [36-39]. Beside all these attempts, a systematic approach that combines the influence of the unresolved (micro) structures on the macroscopic drag/permeability coefficient has not yet emerged.

This research aims at proposing a reformulated drag force model for monodisperse fiber arrays as function of microstructural parameters that improve the consistency, accuracy and computational efficiency compared to those appeared until now. To this end, extensive calculations of the permeability for (dis)ordered fiber arrays in a wide range of

porosity and  $Re$  are carried out using a steady, incompressible FE scheme. The permeability values, computed from pressure drop and flow rate through Darcy's law, were calculated and given as function of porosity and Reynolds number.

## 1.5 Scope and objectives

On one hand, it is nearly impossible to resolve all heterogeneous (small-scale) flow structures in large-scale industrial gas/fluid-particle flows using a computational grid size of the order of a few particle diameters. On the other hand, for the design and optimization of industrial processes, it is important to faithfully model the physics due to interactions at the microstructural scales. The goals of this research are twofold: (i) the derivation of accurate correlations for the drag force, taking into account the effect of microstructure, to improve the higher scale models and (ii) incorporating such closures into a "compatible" multi-phase/scale model that uses a (particle-based) Delaunay triangulation (DT) of space as basis – in future, possibly involving also multiple fields. Due to a special property of DT, a unique decomposition of space can be obtained which provides a discretization framework for the continuum fluid solver as well as a simple tool for detecting contacts between moving particles. The remaining scientific challenge is to understand systems composed of different phases, which interact continuously at various length scales. This involves multi-physics, micro-systems, (moving) interfaces and multi-field problems in general.

The focus of this work is on high-resolution FE modeling, a rigorous approach that represents detailed geometry and first-principle physics at the small scales. The systems studied here are composed of unidirectional, monosize, (dis)ordered arrays of cylinders/fibers oriented perpendicular to the flow direction. Such systems have wide variety of applications including textile reinforcements [40, 41], design of a mould for the production of composite parts [42] and in resin transfer molding (RTM), i.e. an efficient and frequently used process for producing fibre reinforced polymer composites [42].

A microstructural model for predicting the macroscopic drag/permeability is obtained from the pore-level modeling of transport in such fibrous media at both creeping (i.e. small fluid velocity) and inertial flows. The comparison is made with asymptotic analytical solutions for the dense and dilute limit cases. The results are given in the form of closures, i.e. as function of macroscopic porosity and Reynolds number, which can readily be incorporated into existing (non)commercial multi-phase flow codes. In the next step, a coarse-grained FE framework based on coupling an unstructured FE mesh and a soft-sphere DEM for moving particles has been proposed. The fluid-particle interactions have been incorporated using the previously obtained accurate drag closures. This approach provides computing dynamics of particles using a deforming mesh while reasonably resolving the fluid/gas flow around the particles.

## 1.6 Organization of the dissertation

The rest of this dissertation is organized as follows:

- **Chapter 2:** is a study of the effect of microstructural parameters like particle shape, orientation and unit cell stagger angle on the macroscopic permeability. Detailed FE simulations for viscous, incompressible flow through a *regular* array of cylinders/fibers are employed for predicting the permeability/drag associated with this type of media [43, 44].
- **Chapter 3:** presents a prediction for the transverse permeability of creeping flow through unidirectional *random* arrays of fibres. Different microstructures (due to four random generator algorithms) are compared as well as the effect of boundary conditions, finite size, homogeneity and isotropy of the structure on the macroscopic permeability of the fibrous medium. I find a unique, scaling power law relationship between the permeability obtained from fluid flow simulations and the mean value of the second nearest neighbor fibre distances. Finally, the results are compared against a purely phenomenological model which connects the analytical solution of the dense and dilute limits [45, 46].
- **Chapter 4:** introduces several order parameters, based on Voronoi and Delaunay tessellations, to characterize the microstructure of randomly distributed non-overlapping fibre arrays. In particular, by analyzing the mean and distribution of topological and metrical properties of Voronoi polygons, I observe a smooth transition from disorder to order, controlled by the effective packing fraction. I summarize the theoretical links between the macroscopic phenomenological Darcy's law and the pore-scale fundamental Stokes equations, and recognized that the application of the pore-scale analysis requires characterization of the pore-scale geometry (size) of the porous material. The Voronoi tessellation and their statistics have been employed to obtain this essential geometrical (length scale) information [47, 48].
- **Chapter 5:** gives a comprehensive survey of published experimental, numerical and theoretical work on the drag law correlations for fluidized beds and flow through porous media, together with an attempt at systematization. Ranges of validity as well as limitations of commonly used relations (i.e. the Ergun and Forchheimer relations for laminar and inertial flows) are studied for a wide range of porosities. From my fully resolved finite element (FE) results, for both ordered and random fibre arrays, (i) the weak inertia correction to the linear Darcy relation is third power in  $U$ , up to small  $Re \sim 1-5$ . When attempting to fit the data with a particularly simple relation, (ii) a non-integer power law performs astonishingly well up to the moderate  $Re \sim 30$ . However, for randomly distributed arrays, (iii) a quadratic correction performs quite well as used in the Forchheimer (or Ergun)

equation, from small to moderate  $Re$  [49-51]. The FE results show an accurate quantitative agreement with the lattice Boltzmann (LB) results<sup>1</sup>.

- **Chapter 6:** presents a method for two-way fluid-particle coupling on an unstructured mesh<sup>2</sup>. The mesh is a deforming Delaunay triangulation based on the particle positions. The particulate phase is modeled using the DEM and the fluid phase via a stabilized higher order FE scheme [52, 53]. A two-way momentum exchange is implemented through the previously obtained drag laws.
- **Chapter 7:** summarizes the contributions of the thesis and makes recommendations for future work to better understand the connection between small-scale fluid-particle interactions and the macroscopic phenomena occurring at industrial multiphase flow units.

It is important to note that the core chapters of this dissertation, i.e. Chapters 2–6, are self-contained since they have been or are in the process of being published as individual journal articles. As a result, there will be some repetition of fundamental concepts and references.

## References

- [1] H.P. Zhu, Z.Y. Zhou, R.Y. Yang, A.B. Yu, Discrete particle simulation of particulate systems: A review of major applications and findings, *Chemical Engineering Science*, 63 (2008) 5728–70.
- [2] P.A. Cundall, O.D.L. Strack, A discrete numerical model for granular assemblies, *Geotechnique*, 29 (1979) 47–65.
- [3] S. Luding, Cohesive frictional powders: Contact models for tension, *Granular Matter*, 10 (2008) 235-246.
- [4] V. Ogarko, and S. Luding, A fast multilevel algorithm for contact detection of arbitrarily polydisperse objects, *Comp. Phys. Communications*, 183 (2012) 931-36.
- [5] A. W. Vreman, M. Al-Tarazi, J. A. M. Kuipers, M. V. Annaland, and O. Bokhove, Supercritical shallow granular flow through a contraction: experiment, theory and simulation, *J. Fluid. Mech*, 578 (2007) 233–269.
- [6] N. G. Deen, M. A. van der Hoef, M. V. Annaland, and J. A. M. Kuipers, Numerical simulation of dense gas-particle flows using the Euler-Lagrange approach, *Progress in Computational Fluid Dynamics*, 7 (2007) 152–162.

---

<sup>1</sup> The LB data were provided by A. Narvaez & J. Harting, our collaborators at TU Eindhoven.

<sup>2</sup> This chapter was done mostly together with S. Srivastava, a former postdoc in our group.

- [7] J. M. Rotter, J. M. F. G. Holst, J. Y. Ooi, and A. M. Sanad, Silo pressure predictions using discrete element and finite element analyses, *Phil. Trans. R. Soc. Lond. A*, 356 (1998) 2685–2712.
- [8] J. Tejchman, Patterns of shear zones in granular bodies within a polar hypoplastic continuum, *Acta Mechanica*, 155 (2002) 71–94.
- [9] A. Munjiza, D. R. J. Owen, and N. Bicanic, A combined finite-discrete element method in transient dynamics of fracturing solids, *Eng. Comput.*, 12 (1995) 145–74.
- [10] P. A. Vermeer, S. Diebels, W. Ehlers, H. J. Herrmann, S. Luding, and E. Ramm, editors. *Continuous and Discontinuous Modelling of Cohesive Frictional Materials*, Berlin, 2001. Springer. Lecture Notes in Physics 568.
- [11] Y. Tsuji, T. Kawaguchi, T. Tanaka, Discrete particles simulation of two dimensional fluidized bed, *Powder Technology*, 77 (1993) 79–87.
- [12] B.P.B. Hoomans, J.A.M. Kuipers, W.J. Briels, W.P.M. Van Swaaij, Discrete particle simulation of bubble and slug formation in a two-dimensional gas-fluidized bed: a hard-sphere approach, *Chemical Engineering Science*, 51 (1996) 99–118.
- [13] Z.Y. Zhou, S.B. Kuang, K.W. Chu and A.B. Yu, Discrete particle simulation of particle–fluid flow: model formulations and their applicability, *JFM*, 661 (2010) 482–510.
- [14] M.A. van der Hoef, M. Ye, M. van Sint Annaland, A.T. Andrews, S. Sundaresan, J.A.M. Kuipers, *Multiscale Modeling of Gas-Fluidized Beds*, *Advances in Chemical Engineering*, 31 (2006) 65–149.
- [15] K. Ueyama, A study of two-fluid model equations, *JFM*, 690 (2012) 474–498.
- [16] Y. Igci, A.T. Andrews IV, and S. Sundaresan, Filtered two-fluid models for fluidized gas-particle suspensions, *AIChE J.*, 54 (2008) 1431–48.
- [17] E. Delnoij, F.A. Lammers, J.A.M. Kuipers, W.P.M. van Swaaij, Dynamic simulation of dispersed gas-liquid two-phase flow using a discrete bubble model, *Chemical Engineering Science*, 52 (1997) 1429–58.
- [18] E. I. V. van den Hengel, N. G. Deen, and J. A. M. Kuipers, Application of Coalescence and Breakup Models in a Discrete Bubble Model for Bubble Columns, *Ind. Eng. Chem. Res.*, 44 (2005) 5233–5245.
- [19] D. Kandhai, J.J. Derksen, H.E.A. Van den Akker, Interphase drag coefficients in gas–solid flows, *AIChE J.*, 49 (2003) 1060–1065.
- [20] W. Du, X. Bao, J. Xu, W. Wei, Computational fluid dynamics (CFD) modeling of spouted bed: Assessment of drag coefficient correlations, *Chemical Engineering Science*, 61 (2006) 1401–20.

- [21] J. Gan, H. Zhao, A. S. Berrouk, C. Yang, H. Shan, Impact of the drag law formulation on the predicted binary-particle segregation patterns in a gas–solid fluidized bed, *Powder Technology*, 218 (2012) 69–75.
- [22] S. Ergun, Fluid Flow through Packed Columns, *Chem. Eng. Prog.*, 48 (1952) 89-94.
- [23] C.Y. Wen, and Y.H. Yu, Mechanics of fluidization, *AIChE J.*, 62 (1966) 100-11.
- [24] R.J. Hill, D.L. Koch and A.J.C. Ladd, Moderate-Reynolds-number flows in ordered and random arrays of spheres, *J. Fluid Mech.*, 448 (2001) 243–78.
- [25] M.A. van der Hoef, R. Beetstra, J.A.M. Kuipers, Lattice-Boltzmann simulations of low-Reynolds-number flow past mono- and bidisperse arrays of spheres: results for the permeability and drag force, *JFM*, 528 (2005) 233-254.
- [26] S. Benyahia, M. Syamlal, T.J. O'Brien, Extension of Hill–Koch–Ladd drag correlation over all ranges of Reynolds number and solids volume fraction, *Powder Technology*, 162 (2006) 166–174.
- [27] R. Beetstra, M.A. Van Der Hoef, J.A.M. Kuipers, Drag force of intermediate reynolds number flow past mono- And bidisperse arrays of spheres, *AIChE J.*, 53 (2007) 489-501.
- [28] K. Agrawal, P.N. Loezos, M. Syamlal, S. Sundaresan, The role of meso-scale structures in rapid gas–solid flows, *JFM*, 445 (2001) 151–181.
- [29] A. Boemer, H. Qi, J. Hannes, and U. Renz, Eulerian simulation of bubble formation at a jet in a two-dimensional fluidized bed, *International Journal of Multiphase Flow*, 23 (1997) 927–44.
- [30] C.F. Chu, K.M Ng, Flow in packed tubes with a small tube to particle diameter ratio, *AIChE J.*, 35 (1989) 148–158.
- [31] E. Tsotsas, E.-U. Schlünder, The influence of tube to particle diameter ratio on pressure drop in packed tubes: Remarks on a recent paper by Chu and Ng, *AIChE J.*, 36 (1990), 151-154.
- [32] B. Eisfeld, K. Schnitzlein, The influence of confining walls on the pressure drop in packed beds, *Chem. Eng. Sci.*, 56 (2001) 4321–29.
- [33] R. Di Felice, L.G. Gibilaro, Wall effects for the pressure drop in fixed beds, *Chem. Eng. Sci.*, 59 (2004) 3037–3040.
- [34] Y. Seok Choi, S. Jin Kim, D. Kim, A Semi-empirical Correlation for Pressure Drop in Packed Beds of Spherical Particles, *Transp Porous Med*, 75 (2008) 133–149.

- [35] S. H. L. Kriebitzsch, M. A. van der Hoef, J. A. M. Kuipers, Drag force in discrete particle models—Continuum scale or single particle scale?, *AICHE J.*, (2012), in press, DOI: 10.1002/aic.13804.
- [36] S. Sarkar, M.A. van der Hoef, J.A.M. Kuipers, Fluid–particle interaction from lattice Boltzmann simulations for flow through polydisperse random arrays of spheres, *Chemical Engineering Science*, 64 (2009) 2683–91.
- [37] R. Beetstra, M.A. van der Hoef, J.A.M. Kuipers, Numerical study of segregation using a new drag force correlation for polydisperse systems derived from lattice-Boltzmann simulations, *Chemical Engineering Science*, 62 (2007) 246–255.
- [38] X. Yin, S. Sundaresan, Fluid-particle drag in low-Reynolds-number polydisperse gas-solid suspensions, *AICHE J.*, 55 (2009) 1352–68.
- [39] F. Cello, A. Di Renzo, F.P. Di Maio, A semi-empirical model for the drag force and fluid–particle interaction in polydisperse suspensions, *Chemical Engineering Science*, 65 (2010) 3128–39.
- [40] E.B. Belov, S.V. Lomov, I. Verpoest, T. Peters, D. Roose, R.S. Parnas, K. Hoes, H. Sol, Modelling of permeability of textile reinforcements: lattice Boltzmann method, *Composites Science and Technology*, 64 (2004) 1069–1080.
- [41] B. Verleye, M. Klitz, R. Croce, D. Roose, S.V. Lomov, and I. Verpoest, Computation of the permeability of textiles with experimental validation for monofilament and non crimp fabrics, *Studies in Computational Intelligence*, 55 (2007) 93–109.
- [42] B. Verleye, S.V. Lomov, A. Long, I. Verpoest, D. Roose, Permeability prediction for the meso–macro coupling in the simulation of the impregnation stage of Resin Transfer Moulding, *Composites: Part A*, 41 (2010) 29–35.
- [43] K. Yazdchi, S. Srivastava, S. Luding, Microstructural effects on the permeability of periodic fibrous porous media, *Int. J. Multiphase Flow*, 37 (2011) 956–66.
- [44] K. Yazdchi, S. Srivastava and S. Luding, Multi-Scale permeability of particulate and porous media, *World Congress Particle Technology 6* (2010), Nuremberg, Germany.
- [45] K. Yazdchi, S. Srivastava and S. Luding, Micro-macro relations for flow through random arrays of cylinders, *Composites Part A*, 43 (2012) 2007–2020.
- [46] K. Yazdchi, S. Srivastava and S. Luding, On the validity of the Carman-Kozeny equation in random fibrous media, *Particle-Based Methods II - Fundamentals and Applications* (2011), 264–273, Barcelona, Spain.
- [47] K. Yazdchi and S. Luding, *Fibrous materials: Microstructure and macroscopic properties*, (2012) in preparation.



- [48] K. Yazdchi and S. Luding, Upscaling the transport equations in fibrous media, ECCOMAS (2012), 2 pages, Vienna, Austria.
- [49] K. Yazdchi, S. Luding, Towards unified drag laws for inertial flow through fibrous materials, CEJ, 207 (2012) 35-48.
- [50] K. Yazdchi, S. Srivastava and S. Luding, On the transition from creeping to inertial flow in arrays of cylinders, Proceedings of IMECE (2010), Vancouver, Canada.
- [51] A. Narvaez, K. Yazdchi, S. Luding and J. Harting, From creeping to inertial flow in porous media: a lattice Boltzmann - Finite Element comparison, JSTAT, (2012) submitted.
- [52] S. Srivastava, K. Yazdchi, S. Luding, Meso-scale coupling of FEM/DEM for fluid-particle interactions, (2012) in preparation.
- [53] S. Srivastava, K. Yazdchi and S. Luding, Two way coupled fluid-particle interaction on a deforming unstructured mesh, ECCOMAS (2012), 2 pages, Vienna, Austria.

# 2

## Microstructural effects on the permeability of periodic fibrous porous media

*"It is vain to do with more what can be done with less"*  
~William Occam~

## Abstract

An analytical-numerical approach is presented for computing the macroscopic permeability of fibrous porous media taking into account their micro-structure. A finite element (FE) based model for viscous, incompressible flow through a regular array of cylinders/fibers is employed for predicting the permeability associated with this type of media. High resolution data, obtained from my simulations, are utilized for validating the commonly used semi-analytical models of drag relations from which the permeability is often derived. The effect of porosity, or volume fraction, on the macroscopic permeability is studied. Also micro-structure parameters including particle shape, orientation and unit cell stagger angle are varied. The results are compared with the Carman-Kozeny (CK) equation and the Kozeny factor (often assumed to be constant) dependence on the micro-structural parameters is reported and used as an attempt to predict a closed form relation for the permeability in a variety of structures, shapes and wide range of porosities.<sup>1</sup>

## Highlights

- A unified understanding of the effect of microstructure on the macroscopic permeability of fibrous media is presented.
- Based on hydraulic diameter concept, the permeability is expressed in the general form of the Carman–Kozeny (CK) equation.
- The finite element (FE) results show that the CK factor depends on the porosity and pore structure.
- These results can be utilized for validation of advanced, coarse-grained models for particle–fluid interactions.

---

<sup>1</sup> K. Yazdchi, S. Srivastava and S. Luding, Microstructural effects on the permeability of periodic fibrous porous media, *International Journal of Multiphase Flow*, 37 (2011) 956-966.

K. Yazdchi, S. Srivastava and S. Luding, Multi-Scale permeability of particulate and porous media, *World Congress Particle Technology 6* (2010), Nuremberg, Germany.

## 2.1 Introduction

The problem of creeping flow (i.e. very small fluid velocity) through solid bodies arranged in a regular array is fundamental in the prediction of seepage through porous media and has many applications, including: composite materials [10, 22], rheology [24, 23], geophysics [3], polymer flow through rocks [30], statistical physics [14, 7], colloid science [29], soil mechanics [26, 8] and biotechnology [36]. A compelling motivation for such studies concerns the understanding, and eventually the prediction, of single and multiphase transport properties of the pore structure.

A specific category of porous media is formed by 2D long cylinders or fiber-like particles (such as composite materials). Restricted flow through fibrous porous materials has applications in several engineering/industrial areas including: filtration and separation of particles, composite fabrication, heat exchangers, thermal insulations, etc. Prediction of the hydraulic permeability of such materials has been vastly studied in the past decades. It is known that, for fiber reinforced composites, the microstructure of the reinforcement strongly influences the permeability. This study presents an interesting step towards a unified understanding of the effect of microstructure (e.g. particle/fiber shape and orientation) on the macroscopic permeability by combining numerical simulations with analytical prediction in a wide range of porosity.

Usually, when treating the medium as a continuum, satisfactory predictions can be obtained by Darcy's law, which lumps all complex interactions between the fluid and fibers/particles into  $K$ , the permeability (tensor). Accurate permeability data, therefore, are a critical requirement for macroscopic simulations based on Darcy's law – to be successfully used for design and optimization of industrial processes.

The Ergun equation is a semi-empirical drag relation from which the permeability of porous media can be deduced. It is obtained by the direct superposition of two asymptotic solutions, one for very low Reynolds number, the Carman-Kozeny (CK) equation [4], and the other for very high Reynolds numbers, the Forchheimer correction [4]. However, these approximations do not take into account the micro-structural effects, namely the shapes and orientations of the particles, such that not only local field properties but also some global properties (such as anisotropy) cannot be addressed.

In this respect, two distinct approaches seem to have emerged. The first approach is based on lubrication theory and considers the pores of a porous medium as a bunch of capillary tubes which are tortuous or interconnected in a network [4]. Even though this model has been used successfully for isotropic porous media, it does not work well for either axial or transverse permeability of aligned fibrous media [5].

The second approach (cell method) considers the solid matrix as a cluster of immobile solid obstacles, which collectively contribute Stokes resistance to the flow. For a review of these theories, see Dullien [10] and Bird et al. [4]. When the solids are dilute, i.e. at high porosities, the particles do not interact with each other, so that the cell approach is appropriate. Bruschke and Advani [5] used lubrication theory in the high fiber volume

fraction range but adopted an analytical cell model for lower fiber volume fractions. A closed form solution, over the full fiber volume fraction range, is obtained by matching both solutions asymptotically.

Prediction of the permeability of fibrous media dates back to experimental work of Sullivan [31] and theoretical works of Kuwabara [20], Hasimoto [13], and Happel [12]. The parallel flow solutions are idealized solutions for the flow through cigarette filters, plant stems and around pipes in heat exchange tanks. The transverse solutions are applicable to transverse fibrous filters used for cleaning liquids and gases and regulating their flow. Both types of solutions can also be applicable to the settling of suspensions of long thin particles. A comprehensive review of experimental works of permeability calculation of these systems is available in Jackson et al. [17] and Astrom et al. [2]. Sangani and Acrivos [28], performed analytical and numerical studies of the permeability of square and stagger arrays of cylinders. Their analytical models were accurate in the limits of low and high porosity. For high densities they obtained the lubrication type approximations for narrow gaps. Drummond and Tahir [9] modeled the flow around a fiber using a unit cell approach (by assuming that all fibers in a fibrous medium experience the same flow field) and obtained equations that are applicable at lower volume fractions. Gebart [11] presented an expression for the longitudinal flow, valid at high volume fractions, that has the same form as the well-known CK equation. For transverse flow, he also used the lubrication approximation, assuming that the narrow gaps between adjacent cylinders dominate the flow resistance. Using the eigen-function expansions and point match methods, Wang [35] studied the creeping flow past a hexagonal array of parallel cylinders.

This literature survey indicates that the majority of the existing correlations for permeability of ordered periodic fibrous materials are based on curve-fitting of experimental or numerical data. Additionally, most of the analytical models found in the literature are not general and fail to predict permeability over the wide range of porosity, since they contain some serious assumptions that limit their range of applicability.

In this chapter, periodic arrays of parallel cylinders (with circular, ellipse and square cross-section) perpendicular to the flow direction are considered and studied with a FE based model in Section 2.2. The effects of shape and orientation as well as porosity and structure on the macroscopic permeability of the porous media are discussed in detail. In order to relate my results to available work, the data are compared with previous theoretical and numerical data for square and hexagonal packing configurations and a closed form relation is proposed in Section 2.3 in the attempt to combine my various simulations. The chapter is concluded in Section 2.4 with a summary and outlook for future work.

## 2.2 Results from FE simulations

This section is dedicated to the FE based model simulations and the results that consider permeability as function of porosity, structure, shape and anisotropy.

### 2.2.1 Introduction and terminology

The horizontal *superficial* (discharge) velocity,  $U$ , of the fluid within the porous media in a unit cell is defined as

$$U = \frac{1}{V} \int_{V_f} u dv = \varepsilon \langle u \rangle , \quad (2.1)$$

where  $u$ ,  $\langle u \rangle$ ,  $V$ ,  $V_f$  and  $\varepsilon$  are the local microscopic velocity of the fluid, corresponding *intrinsic* averaged velocity, total volume, volume of the fluid and porosity, respectively. For the case where the fluid velocity is sufficiently small (creeping flow), the well-known Darcy's law relates the superficial fluid velocity,  $U$  through the pores with the pressure gradient,  $\nabla p$ , measured across the system length,  $L$ , so that

$$U = -\frac{K}{\mu} \nabla p , \quad (2.2)$$

where  $\mu$  and  $K$  are the viscosity of the fluid and the permeability of the sample, respectively. At low Reynolds numbers, which are relevant for most of the composite manufacturing methods, the permeability depends only on the geometry of the pore structure. By increasing the pressure gradient, one observed the typical departure from Darcy's law (creeping flow) at sufficiently high Reynolds number,  $Re > 0.1$  (data not shown here). In order to correctly capture the influence of the inertial term, Yazdchi et al. [37] showed that the original Darcy's Law can be extended with a power law correction with powers between 2 and 3 for square or hexagonal configurations, see chapter 5 for detail. Hill et al. [15, 16] examined the effect of fluid inertia in cubic, face-centered cubic and random arrays of spheres by means of lattice-Boltzmann simulations. They found good agreement between the simulations and Ergun correlation at solid volume fractions approaching the closely-packed limit at moderate Reynolds number ( $Re < 100$ ). Similarly, Koch and Ladd [18] simulated moderate Reynolds number flows through periodic and random arrays of aligned cylinders. The study showed that the quadratic inertial effect became smaller at higher volume fractions, see chapter 5 for detail.

Recently, models based on Lagrangian tracking of particles combined with computational fluid dynamics for the continuous phase, i.e. discrete particle methods (DPM), have become the state-of-the-art for simulating gas-solid flows, especially in fluidization processes [19]. In this method, two-way coupling is achieved via the momentum sink/source term,  $S_p$  which models the fluid-particle drag force

$$S_p = \beta (\langle u \rangle - v_p), \quad (2.3)$$

where the interphase momentum-transfer coefficient,  $\beta$ , describes the drag of the gas/fluid phase acting on the particles and  $v_p$  is the velocity of particles (additional effects like the added mass contributions are disregarded here for the sake of simplicity). In steady state, without acceleration, wall friction, or body forces such as gravity, the fluid momentum balance equation reduces to

$$-\varepsilon \nabla p - \beta (\langle u \rangle - v_p) = 0. \quad (2.4)$$

By comparing Eqs. (2.2) and (2.4), using the definition of Eq. (2.1), and assuming immobile particles, i.e.  $v_p = 0$ , the relation between  $\beta$  and permeability  $K$  is

$$\beta = \frac{\mu \varepsilon^2}{K}. \quad (2.5)$$

Accurate permeability data, therefore, is a critical requirement in simulations based on DPM to be successfully used in the design and optimization of industrial processes.

In the following, results on the permeability of two-dimensional (2D) regular periodic arrays of cylinders with different cross section are obtained by incorporating detailed FE simulations. This is part of a multiscale modeling approach and will be very useful to generate closure or coupling models required in more coarse-grained, large-scale models.

### 2.2.2 Mathematical formulation and boundary conditions

Both hexagonal and square arrays of parallel cylinders perpendicular to the flow direction are considered, as shown in Fig. 2.1. The basis of such model systems lies on the assumption that the porous media can be divided into representative volume elements (RVE) or unit cells. The permeability is then determined by modeling the flow through one of these, more or less, idealized cells. The FEM software (ANSYS) was used to calculate the superficial velocity and, using Eq. (2.2), the permeability of the fibrous material. A segregated, sequential solution algorithm was used to solve the steady state Navier-Stokes (NS) equations and the continuity equation. In this approach, the momentum equations (i.e. NS equations) are used to generate an expression for the velocity in terms of the pressure gradient. This is used in the continuity equation after it has been integrated by parts. This nonlinear solution procedure belongs to a general class of the Semi-Implicit Methods for Pressure Linked Equations (SIMPLE). The matrices developed from assembly of linear triangular elements are solved based on a Gaussian elimination algorithm. It is robust and can be used for symmetric as well as non-symmetric equation systems but requires extensive computational memory already in 2D. At the left and right pressure- and at the top and bottom periodic-boundary conditions are applied. The no-slip boundary condition is applied on the surface of the particles/fibers. A typical unstructured, fine triangular FE mesh is shown in Fig. 2.1(c). The mesh size



effect was examined by comparing the simulation results for different resolutions (data are not shown here). The range of number of elements varied from  $10^3$  to  $10^4$  depending on the porosity regime. It should be noted that in Darcy's linear regime (creeping flow) – although we have applied pressure boundary conditions at left and right – identical velocity profile at inlet and outlet are observed, due to the symmetry of this geometry and linearity. However, by increasing the pressure gradient (data not shown), the flow regime changes to non-linear and becomes non-symmetric. Furthermore, because of the symmetry in the geometry and boundary conditions, the periodic boundary condition and symmetry boundary condition, i.e. zero velocity in vertical direction at top and bottom of the unit cells, will lead to identical results (as confirmed by simulations – data not shown).

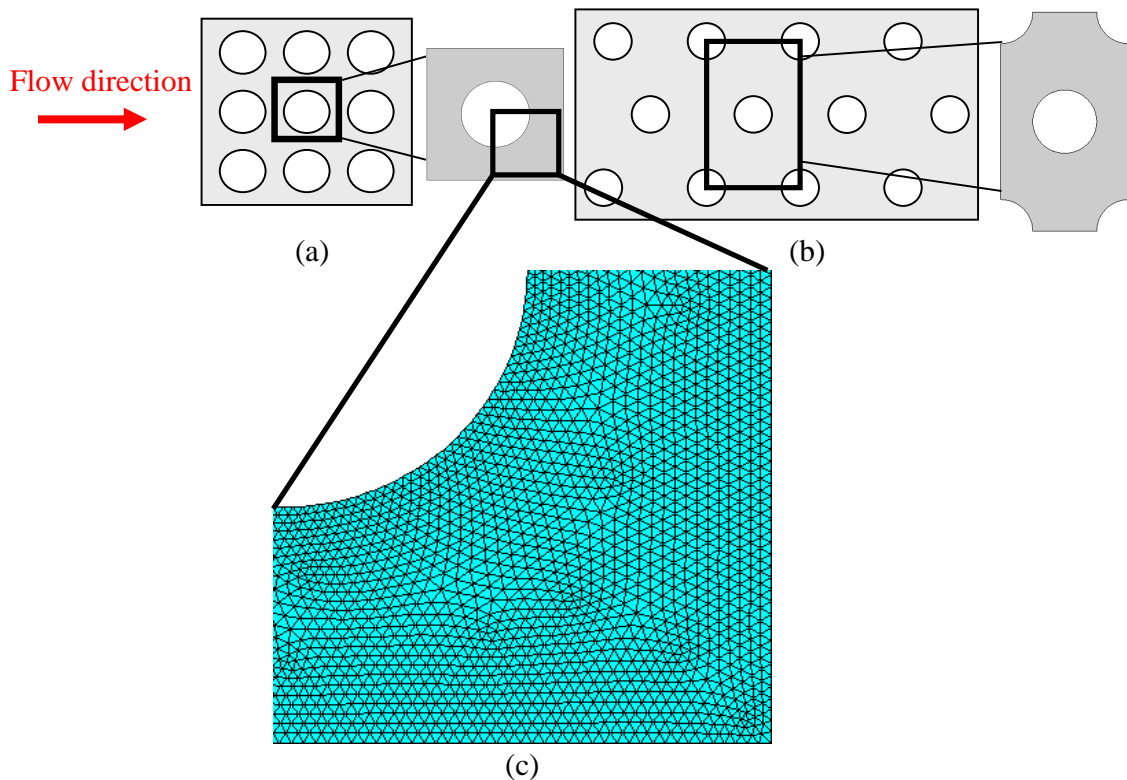


**Figure 2.1:** The geometry of the unit cells used for (a) square and (b) hexagonal configurations, with angles  $45^\circ$  and  $60^\circ$  between the diagonal of the unit-cell and the horizontal flow direction (red arrow), respectively. (c) shows a typical quarter of an unstructured, fine and triangular FE mesh.

### 2.2.3 Permeability of the square and hexagonal arrays

Under laminar, steady state condition, the flow through porous media is approximated by Darcy's law. By calculating the superficial velocity,  $U$ , from my FE simulations and knowing the pressure gradient,  $\nabla p$ , over the length of the unit cell,  $L$ , one can calculate the dimensionless permeability (normalized by the cylinder diameter,  $d$ ),  $K/d^2$ . In Table 2.1, various correlations from the literature are listed. The first relation by Gebart [11] has an analytical form and is valid in the limit of high density, i.e. low porosity – close to the close packing limit  $\varepsilon_c$  (the same as Bruschke et al. [5] in the low porosity limit, with maximum discrepancy less than 1%). Note that the relations by Happel [12], Drummond et al. [9], Kuwabara [20], Hasimoto [13], and Sangani et al. [28] have identical first terms and this term is not dependent on the structure, in the limit of small solid volume fraction  $\phi$ , i.e. large porosity. In contrast, their second term is weakly dependent on the structure (square or hexagonal). Bruschke et al. [5] proposed relations that are already different in their first term. The last two relations in the table are only valid in intermediate porosity regimes and do not agree with any of the above relations in either of the limit cases.

In Fig. 2.2, the variation of the (normalized) permeability,  $K/d^2$ , with porosity, for square and hexagonal packings is shown. The lubrication theory presented by Gebart [11] agrees well with my numerical results at low porosities ( $\varepsilon \ll 0.6$ ), whereas, at high porosities ( $\varepsilon \gg 0.6$ ), the prediction by Drummond et al. [9] better fits my data. Drummond et al. [9] have found the solution for the Stokes equations of motion for a viscous fluid flowing in parallel or perpendicular to the array of cylinders by matching a solution outside one cylinder to a sum of solutions with equal singularities inside every cylinder of an infinite array. This was in good agreement with other available approximate solutions, like the results of Kuwabara [20] and Sangani et al. [28] at high porosities, as also confirmed by my numerical results (data not shown). Note that my proposed merging function in Section 2.3.4, fits to our FE results within 2% error for the whole range of porosity.

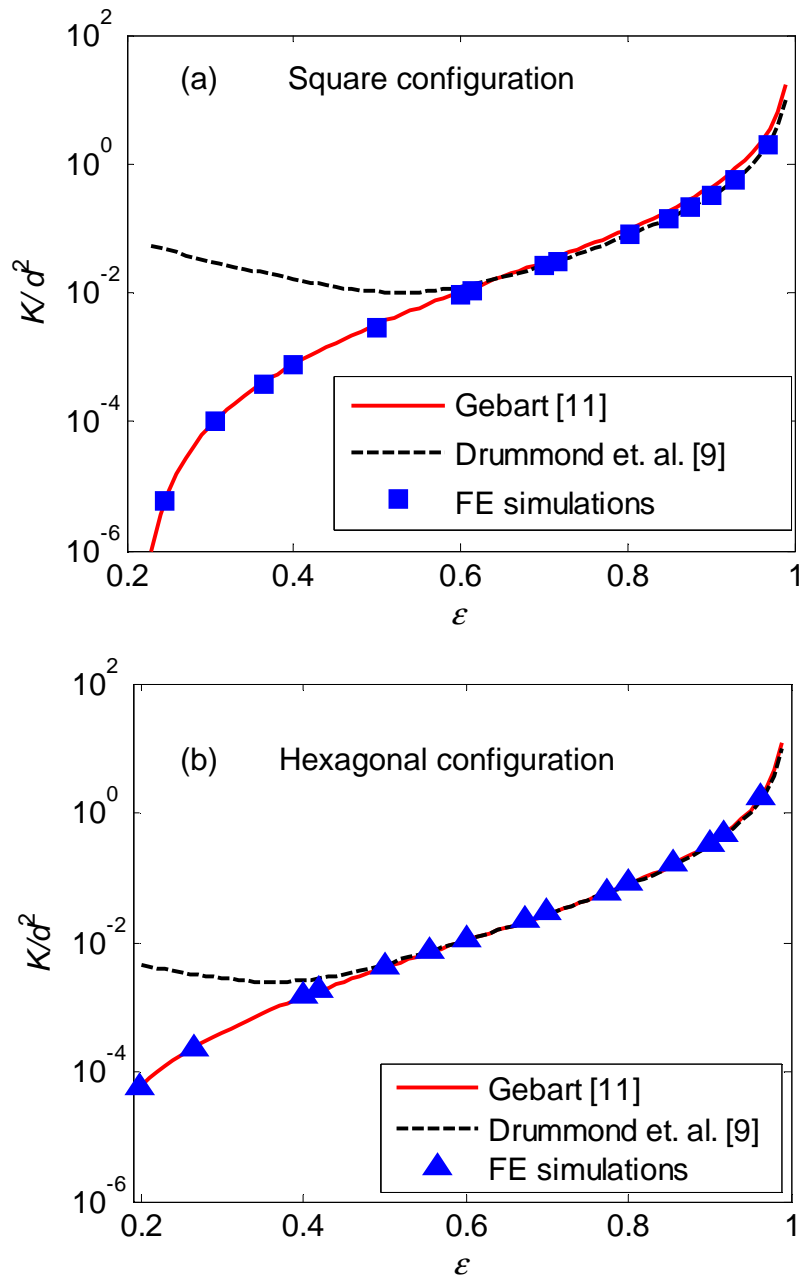


**Figure 2.2:** Normalized permeability plotted against porosity for (a) square and (b) hexagonal packing for circular shaped particles/cylinders with diameter  $d$ , for perpendicular flow. The lines give the theoretical predictions, see inset. For high porosities, the difference between Gebart [11] and Drummond et al. [9], in the hexagonal configuration, is less than 5%, while for the square configuration it is less than 30%.

**Table 2.1:** Summary of correlations between normalized permeability,  $K/d^2$  and porosity, with  $\phi = 1 - \varepsilon$ , the solid volume fraction at creeping flow regime.

Author	$K/d^2$	Comments
Gebart [11]	$C \left( \sqrt{\frac{1-\varepsilon_c}{1-\varepsilon}} - 1 \right)^{5/2} \left\{ \begin{array}{l} C = \frac{4}{9\pi\sqrt{2}}, \varepsilon_c = 1 - \pi/4 \\ C = \frac{4}{9\pi\sqrt{6}}, \varepsilon_c = 1 - \pi/(2\sqrt{3}) \end{array} \right\}$	Square configuration: $K_G^s/d^2$ Hexagonal config.: $K_G^h/d^2$
Bruschke and Advani [5]	$\frac{(1-l^2)^2}{12l^3} \left( 3l \frac{\tan^{-1}\left(\sqrt{\frac{1+l}{1-l}}\right)}{\sqrt{1-l^2}} + \frac{l^2}{2} + 1 \right)^{-1}$	Lubrication theory, square config.: $l^2 = \frac{4}{\pi}(1-\varepsilon)$
Drummond et al. [9]	$\frac{1}{32\phi} \left( \ln\left(\frac{1}{\phi}\right) - 1.476 + \frac{2\phi - 0.796\phi^2}{1 + 0.489\phi - 1.605\phi^2} \right)$ $\frac{1}{32\phi} \left( \ln\left(\frac{1}{\phi}\right) - 1.497 + 2\phi - \frac{\phi^2}{2} - 0.739\phi^4 + \frac{2.534\phi^5}{1 + 1.2758\phi} \right)$	Square configuration: $K_D^s/d^2$ Hexagonal config.: $K_D^h/d^2$
Bruschke and Advani [5]	$\frac{1}{32\phi} \left( \ln\left(\frac{1}{\phi}\right) - \frac{3}{2} + 2\phi - \frac{\phi^2}{2} \right)$	Cell method, square config.
Kuwabara [20]	$\frac{1}{32\phi} \left( \ln\left(\frac{1}{\phi}\right) - 1.5 + 2\phi - \frac{\phi^2}{2} \right)$	Based on Stokes approximation
Hasimoto [13]	Using elliptic functions: $\frac{1}{32\phi} \left( \ln\left(\frac{1}{\phi}\right) - 1.476 + 2\phi + O(\phi^2) \right)$	Square configuration
Sangani et al. [28]	$\frac{1}{32\phi} \left( \ln\left(\frac{1}{\phi}\right) - 1.476 + 2\phi - 1.774\phi^2 + 4.076\phi^3 \right)$	-----
Happel [12]	$\frac{1}{32\phi} \left( \ln\left(\frac{1}{\phi}\right) - \frac{1-\phi^2}{1+\phi^2} \right)$	-----
Lee and Yang [21]	$\frac{\varepsilon^3(\varepsilon - 0.2146)}{31(1-\varepsilon)^{1.3}}$	Valid for $0.435 < \varepsilon < 0.937$
Sahraoui et al. [27]	$\frac{0.0152\pi\varepsilon^{5.1}}{1-\varepsilon}$	Valid for $0.4 < \varepsilon < 0.8$

### 2.2.4 Effect of shape on the permeability of regular arrays

In this subsection, I investigate the anisotropic behavior of permeability due to particle shape using the square configuration. Using elementary algebraic functions, Zhao et al. [38] derived the analytical solutions for pore-fluid flow around an inhomogeneous elliptical fault in an elliptical coordinate system. Obdam and Veling [25] employed the complex variable function approach to derive the analytical solutions for the pore-fluid flow within an elliptical inhomogeneity in a two-dimensional full plane. Zimmerman [40] extended their solutions to a more complicated situation, where a randomly oriented distribution of such inhomogeneous ellipses was taken into account. Wallstrom et al. [34] later applied the two-dimensional potential solution from an electrostatic problem to solve a steady-state pore-fluid flow problem around an inhomogeneous ellipse using a special elliptical coordinate system. More recently, Zhao et al. [39] used inverse mapping to transform those solutions into a conventional Cartesian coordinate system.

Here, in order to be able to compare different shapes and orientations, the permeability is normalized with respect to the obstacle length,  $L_p$ , which is defined as

$$L_p = 4 \text{ area} / \text{circumference}$$

$$L_p = 2r = d \text{ (for circle)}, \quad L_p = c \text{ (for square)}, \quad L_p = 4\pi ab / A_L \text{ (for ellipse)} \quad (2.6)$$

where  $r$ ,  $c$ ,  $a$  and  $b$  are the radius of the circle, the side-length of the square, the major (horizontal) and minor (vertical) length of the ellipse, respectively.  $A_L$  is the circumference of the ellipse.

By applying the same procedure as was used in the previous section, the normalized permeability (with respect to obstacle length,  $L_p$ ) is calculated for different shapes on a square configuration. In Fig. 2.3 the normalized permeability is shown as function of porosity for different shapes. At high porosities the shape of particles does not affect much the normalized permeability, but at low porosities the effect is more pronounced. Circles have the lowest and horizontal ellipses the highest normalized permeability.

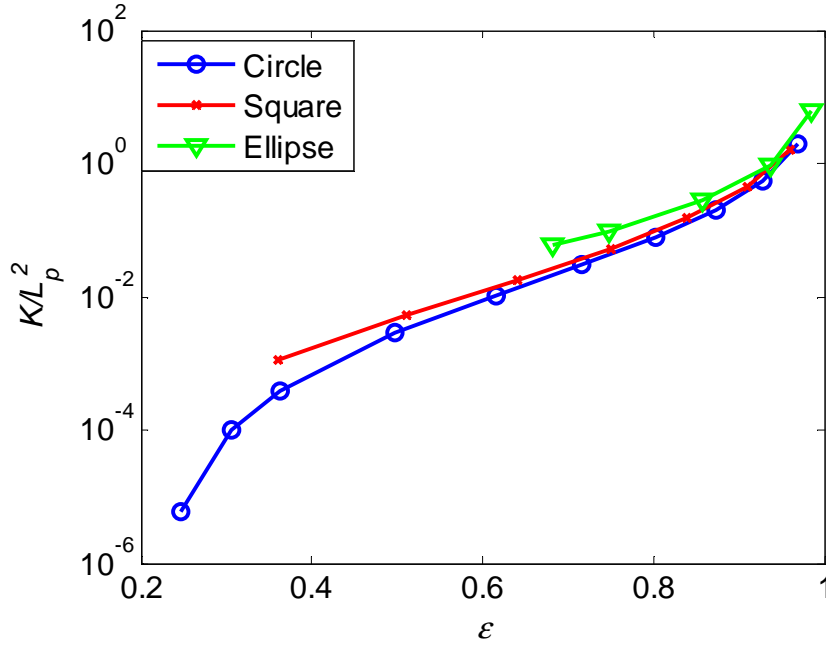


**Figure 2.3:** Effect of shape on the normalized permeability from a square packing configuration of circles, squares and ellipses ( $a/b=2$ , major axis in flow direction). The lines are only connecting the data-points as a guide to the eye.

### 2.2.5 Effect of aspect ratio on the permeability of regular arrays of ellipses

In this subsection the effect of aspect ratio,  $a/b$  on the normalized permeability of square-arrays of ellipses is investigated. In fact, the case of high aspect ratio at high porosity represents the flow between parallel plates (slab flow). The relation between average velocity,  $\langle u \rangle$ , and pressure drop for slab flow (i.e. flow between parallel plates) is

$$\langle u \rangle = -\frac{h_s^2}{12\mu} \frac{\Delta p}{L} \quad (2.7)$$

where  $h_s$  is the distance between parallel plates (in my square configuration, in the limit  $a/b \gg 1$ , one has  $h_s=L$ ). Note that, since there are no particles,  $\epsilon=1$ , the average and superficial velocities are identical, i.e.  $\langle u \rangle=U$ . By comparing Eqs. (2.7) and (2.2) the permeability, i.e.  $K/h_s^2=1/12$  is obtained, which indeed shows the resistance due to no slip boundaries at the walls. The variation of permeability for a wide range of aspect ratios at different porosities is shown in Fig. 2.4. It is observed (especially at high porosities) that by increasing the aspect ratio the permeability increases until it reaches the limit case of slab flow for which the permeability is  $K/h_s^2=1/12=0.0833$ . The aspect ratio  $b/a < 1$  means that the ellipse stands vertically and therefore the permeability reduces drastically.

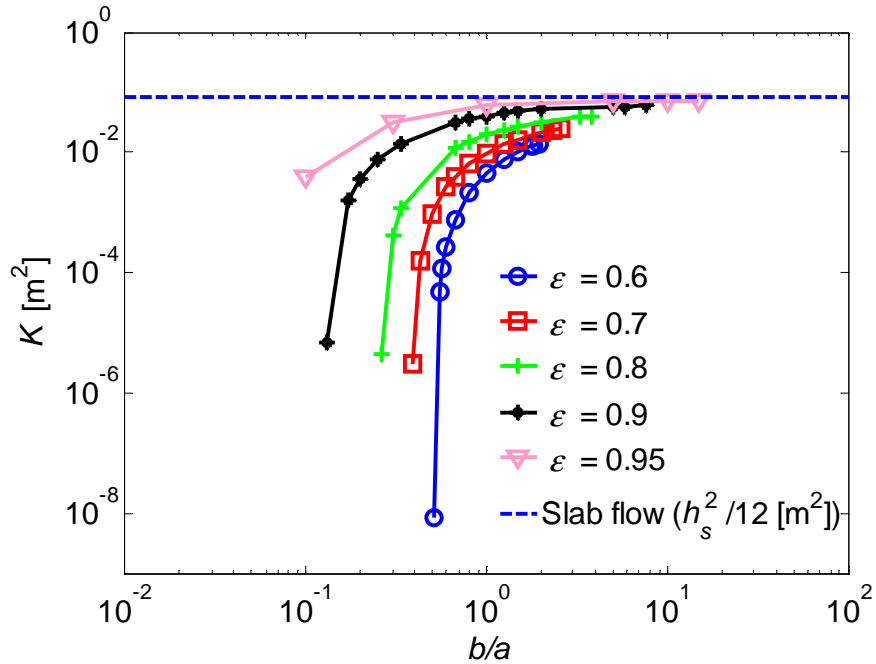


**Figure 2.4:** Effect of aspect ratio on the permeability of square configurations of ellipses with different porosities as given in the inset. The lines are only connecting the data-points as a guide to the eye.

### 2.2.6 Effect of orientation on the permeability of regular arrays

By changing the orientation ( $\theta$ ), i.e. the angle between the major axis of the obstacle and the horizontal axis, not only will the values of the permeability tensor change, but also its anisotropy will become apparent (so that the pressure gradient and the flow velocity are not parallel anymore). Therefore, the geometry of the pore structure has great effect on the permeability in irregular fibrous media. This effect for squares and ellipses ( $a/b = 2$ ) is shown in Fig. 2.5.

For square shapes, at high porosities, the orientation does not much affect the permeability, whereas at low porosities the permeability depends a lot on the orientation. At  $\theta = 45^\circ$  we observe a drop in permeability, because we are close to the blocking situation, i.e. zero permeability, at a critical porosity (at which the permeability drops to

$$\text{zero) of } \varepsilon_c = 1 - \frac{1}{2 \sin^2(45^\circ + \theta)} = 0.5.$$

For ellipses, at high porosity, the orientation does not affect the permeability, whereas at low porosities the effect is strong. By increasing the orientation angle, i.e. by turning the major axis from being horizontal to vertical, the permeability is reduced. The critical porosity  $\varepsilon_c \approx 0.6073$  is purely determined by the major axis of the ellipse for  $\theta = 90^\circ$ .



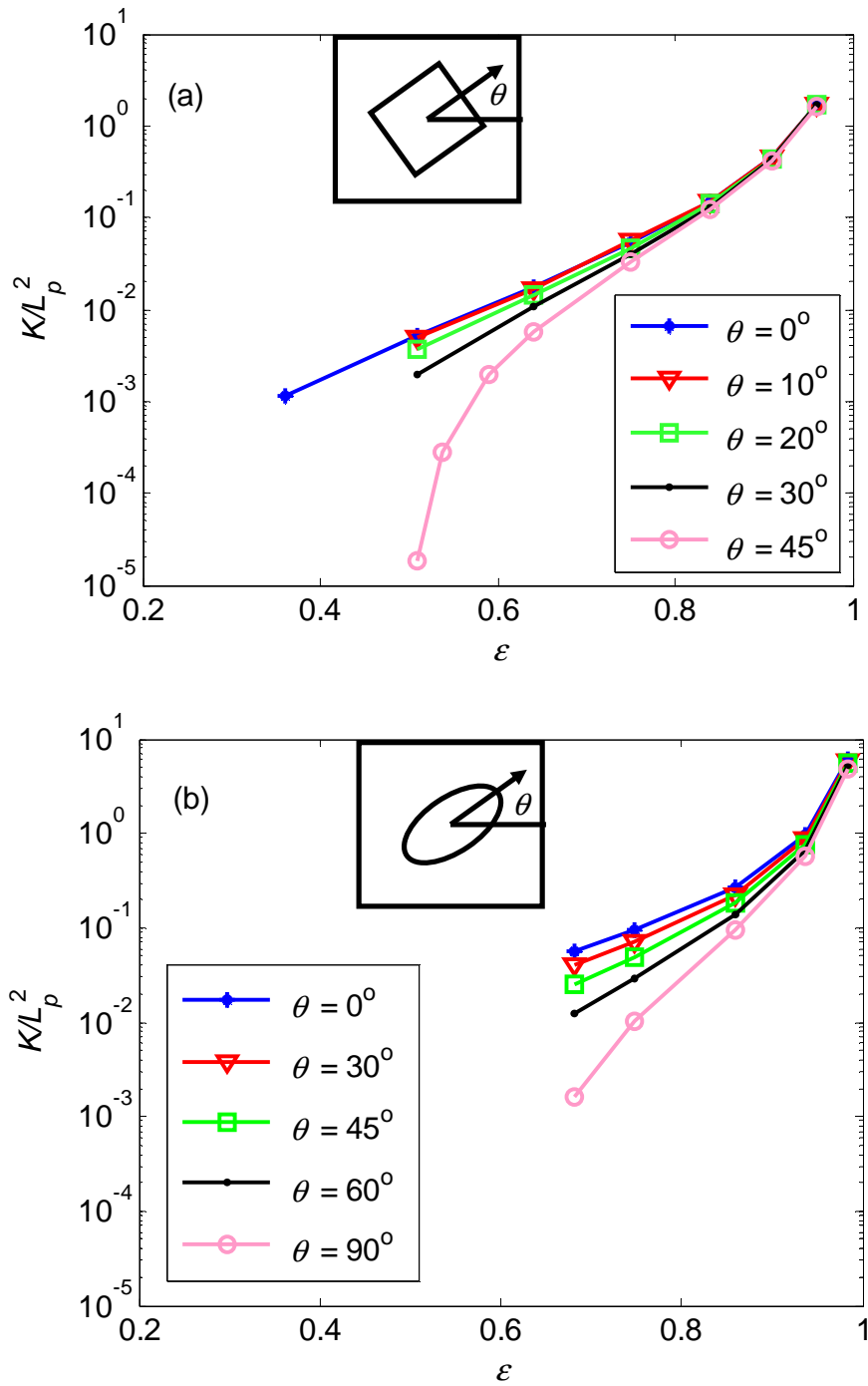


**Figure 2.5:** Effect of orientation ( $\theta$ ) on the normalized permeability for (a) square and (b) ellipse ( $a/b=2$ ) in square packing configurations at different porosity. The lines are only connecting the data-points as a guide to the eye.

The general form of Darcy's law for anisotropic media in 2D in matrix form can be written as

$$\begin{Bmatrix} U_x \\ U_y \end{Bmatrix} = -\frac{1}{\mu} \begin{bmatrix} K_{11} & K_{12} \\ K_{21} & K_{22} \end{bmatrix} \begin{Bmatrix} \frac{\partial p}{\partial x} \\ \frac{\partial p}{\partial y} \end{Bmatrix}, \quad (2.8)$$

where  $U_x$  and  $U_y$  are superficial velocities in  $x$  (i.e.  $U_x \equiv U$  as described in defined in previous section) and  $y$  direction, respectively. Then the permeability tensor for any value of  $\theta$  can be calculated as

$$K_\theta = \begin{bmatrix} K_{11} & K_{12} \\ K_{21} & K_{22} \end{bmatrix} = R^T \begin{bmatrix} K_0 & 0 \\ 0 & K_{90} \end{bmatrix} R, \quad (2.9)$$

where  $K_0$  and  $K_{90}$  are the principal values of permeability that are determined from the values of  $\theta = 0^\circ$  and  $\theta = 90^\circ$ , respectively. In Eq. (2.9),  $R^T$  is the transpose of the rotation matrix  $R$ , defined as (counterclockwise rotation by  $\theta$ )

$$R = \begin{bmatrix} \cos(\theta) & -\sin(\theta) \\ \sin(\theta) & \cos(\theta) \end{bmatrix}. \quad (2.10)$$

Eq. (2.9) shows that for  $\theta \neq 0^\circ, 90^\circ$ , one has  $K_{12} \neq 0$ , which means that by applying a pressure gradient in  $x$  direction, one gets a superficial velocity in  $y$  direction (i.e. anisotropic behavior because of oriented shape). The numerical results are in good agreement with theoretical predictions (Eq. (2.9)) especially at high porosities (see the solid lines in Fig. 2.6). We have more deviation at low porosities (maximum discrepancy  $\approx 5\%$ ) because of channel blockage and changes in flow behavior (the comparison is not shown here).

In Fig. 2.6, the variation of normalized permeability is shown as a function of the orientation angle  $\theta$ . The normalized permeability is symmetric to  $90^\circ$  and decreases by increasing the orientation angle from  $0^\circ$ . The eigenvalues of the permeability tensor are the extrema of the curves and the other data are well fitted by  $K/L_p^2 = (K_0 + K_{90})/2 + (K_0 - K_{90})\cos(2\theta)/2$ . By decreasing the aspect ratio  $a/b$ , we approach the value for the circular (cylinder) obstacle, i.e.  $a/b = 1$ . The normalized permeability is symmetric to  $45^\circ$  for square shapes.

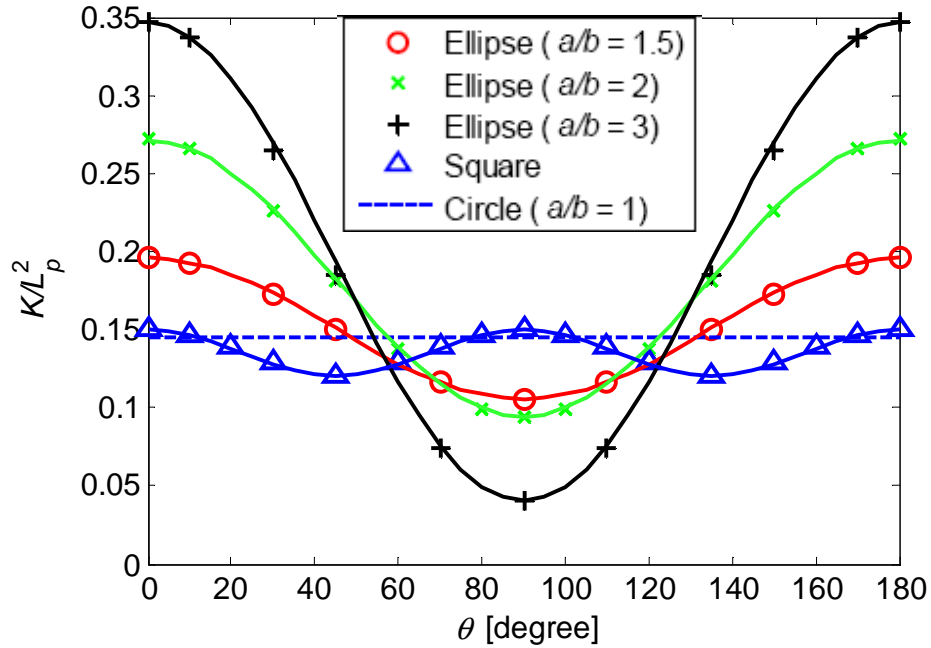


**Figure 2.6:** Normalized permeability plotted against orientation angle for different shapes at porosity  $\varepsilon = 0.85$ , for different obstacle shapes in square configurations. The dashed line represents circles. The solid lines show the theoretical predictions according to Eq. (2.9), where the eigenvalues are taken from the  $0^\circ$ ,  $90^\circ$  and  $0^\circ$ ,  $45^\circ$  degrees for ellipses and squares simulations, respectively.

### 2.2.7 Effects of stagger cell angle

In this subsection, the effect of another micro-structural parameter, the stagger cell angle,  $\alpha$ , on the normalized permeability for circles ( $L_p=d$ ) is discussed. The stagger angle is defined between the diagonal of the unit-cell and flow-direction (horizontal), see Fig. 2.7. In addition to the special cases  $\alpha = 45^\circ$  and  $\alpha = 60^\circ$ , i.e. square and hexagonal packings, respectively, several other angles are studied. The contours of the horizontal velocity field component, for different values of  $\alpha$ , at a constant porosity  $\varepsilon = 0.7$ , are shown in Fig. 2.7. By changing  $\alpha$ , the flow path and also the channel length will change. At  $\alpha = 70^\circ$  and higher, the flow mainly follows a straight line, indicated by arrows in Fig. 2.7(a), with large superficial velocity and consequently large values of permeability. However, by decreasing  $\alpha$  down to  $35^\circ$ , the flow pattern completely changes and the superficial velocity reduces, which should lead to lower and lower permeability. In brief, with increasing angle, both the superficial velocity and the permeability increase, with a plateau at around  $\alpha = 45^\circ$ .

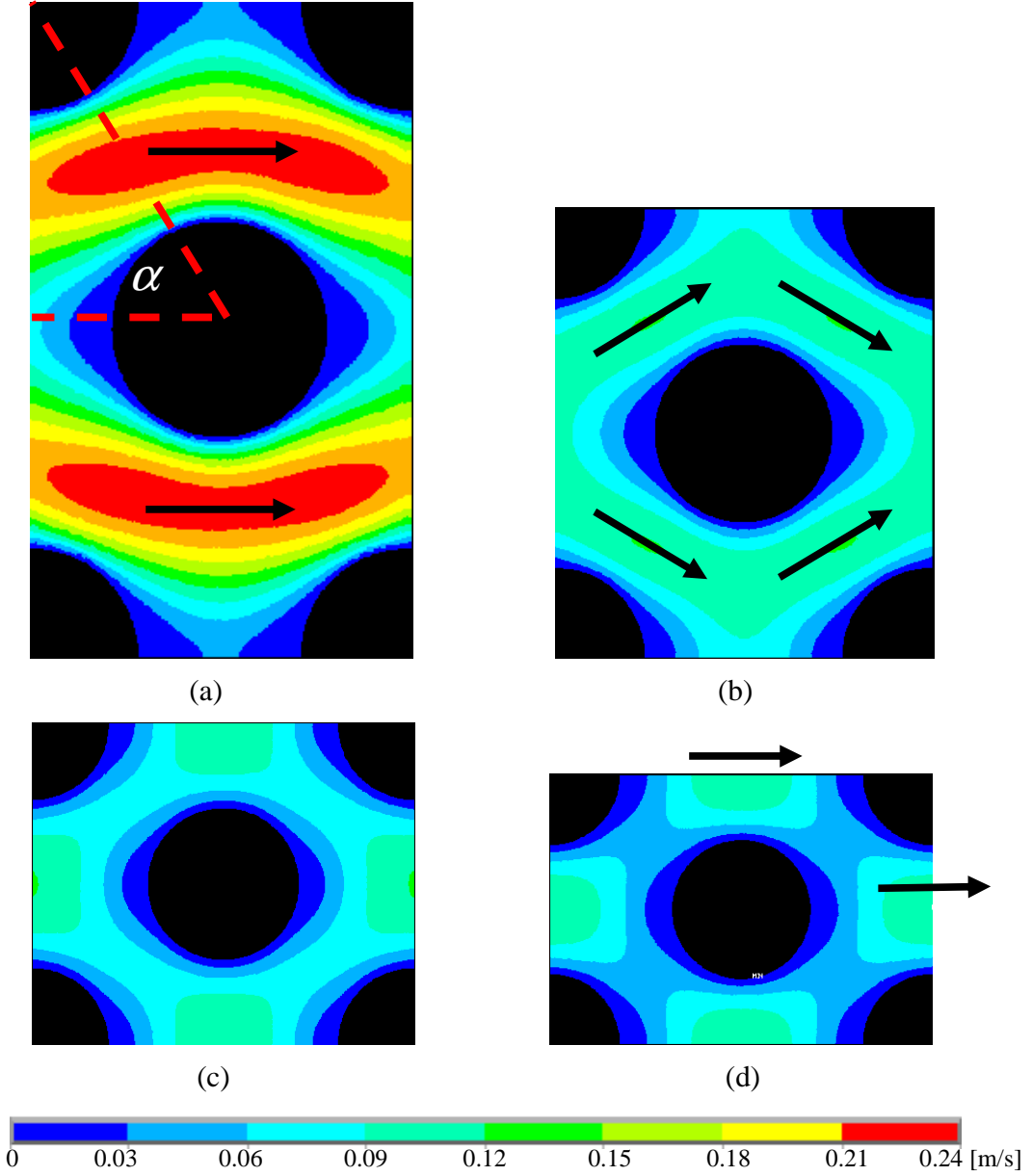


**Figure 2.7:** Horizontal velocity field components for (a)  $\alpha = 60^\circ$ , (b)  $\alpha = 50^\circ$ , (c)  $\alpha = 40^\circ$  and (d)  $\alpha = 35^\circ$  at fixed porosity  $\varepsilon = 0.7$ . The arrows indicate the main flow channel in (a) and (b). The stagger angle is defined between the diagonal of the unit-cell and flow-direction (horizontal). The minimal angle  $\alpha_{\min} = \tan^{-1}(2(1-\varepsilon)/\pi) = 10.81^\circ$  is realized when the vertical opening is closed, while the maximal angle  $\alpha_{\max} = \tan^{-1}(\pi/(2(1-\varepsilon))) = 79.18^\circ$  corresponds to the closed horizontal pore.

In Fig. 2.8 the normalized permeability is shown as function of the stagger angle,  $\alpha$ , at different porosities. As it is seen the arrangement of particles relative to the flow direction is important in determining the permeability. By increasing  $\alpha$ , the normalized permeability increases (the vertical distance between particles increases and therefore the resistance to the flow decreases) until it reaches a local maximum at  $\alpha \cong 35^\circ$  – consistently for different porosities. At larger angles, it slightly decreases and attains a local minimum at  $\alpha \cong 55^\circ$ , beyond which it increases rapidly again. This behavior can be explained by the variation of the area-fraction distribution with  $\alpha$  on the planes perpendicular to the flow direction, as discussed by Alcocer et al. [1].

The normalized permeability as a function of  $\alpha$  can be expressed as a cubic polynomial

$$\frac{K}{d^2} = A \left( \frac{\alpha - 45^\circ}{45^\circ} \right)^3 + B \left( \frac{\alpha - 45^\circ}{45^\circ} \right)^2 + C \left( \frac{\alpha - 45^\circ}{45^\circ} \right) + D \quad (2.11)$$

where A, B, C and D are dimensionless constants, listed in Table 2.2 for different porosities.

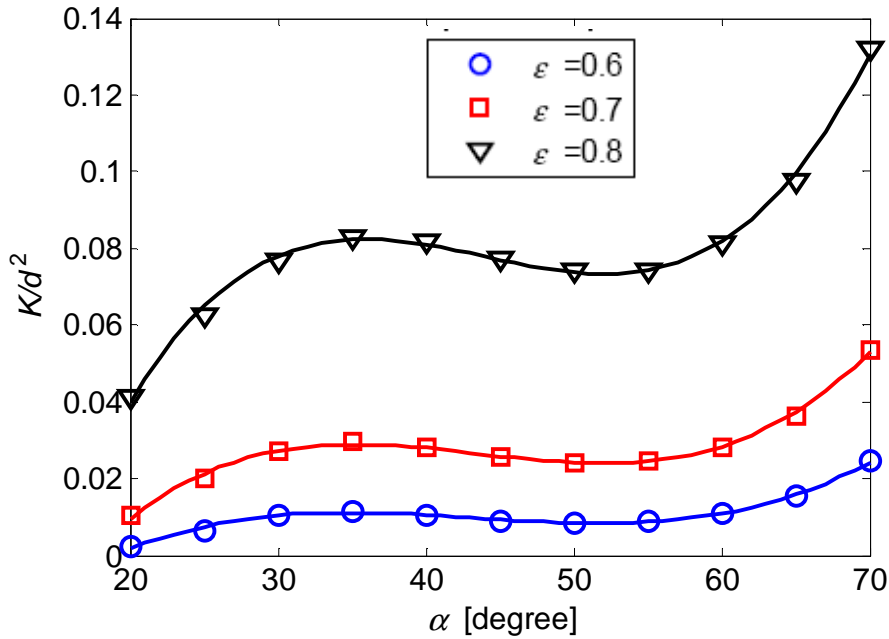


**Figure 2.8:** The variation of normalized permeability plotted against stagger unit cell angle  $\alpha$  at different porosities, as given in the inset. The solid lines show the fit (Eq. (2.11))

**Table 2.2:** Fitted parameters for the permeability-stagger angle relation

	$\varepsilon = 0.8$	$\varepsilon = 0.7$	$\varepsilon = 0.6$
A	0.38401	0.18813	0.09913
B	0.02682	0.01738	0.01171
C	-0.03693	-0.01914	-0.01027
D	0.07698	0.02584	0.009319

The leading term with A is dominating, the term with B is a rather small correction, the term with C sets the (negative) slope in the center, and the term with D determines the offset. All fit-parameters depend on porosity and it should be noted that the range of available angles is limited and also depends on porosity. Additional scaling- and fit-attempts (data not shown) did not lead to much better results, thus I only present this empirical fit here.

The decreasing region, i.e.  $35^\circ \leq \alpha \leq 55^\circ$  corresponds to the case in which the flow goes in a preferred channel orthogonal/perpendicular to the line (diagonal) connecting two particles, see Figs. 2.7(b) and (c). While in cases with larger  $\alpha$ , the flow goes at straight lines/channels, see Fig. 2.7(a), the configuration for smaller  $\alpha$  is dominated by the narrow vertical opening between two obstacles. In essence, in the plateau region, the permeability is not much affected by the stagger angle  $\alpha$ . This observation might be useful during design and manufacturing of fibrous composites.

In summary, the results of this section show that the macroscopic permeability not only depends on the porosity but also on the microstructure, namely shape, aspect ratio and orientation of particles. The main interest of such a microstructural description for predicting permeability is to provide a detailed insight into microscale flow, transport phenomena and basic fluid-solid interaction mechanisms in fibrous media.

### 2.3 Theoretical prediction of the permeability for all porosities

In this section, based on the observations in the previous section, and using the velocity profiles from FE unit cell simulations, a generalized form of the Carman Kozeny (CK) equation for the permeability of fibrous porous media (2D regular arrays of fibres) is proposed.

#### 2.3.1 From special cases to a more general CK equation

The earliest and most widely applied approach in the porous media literature, for predicting the permeability, involves capillary models [6] such as the one that leads to the

CK equation. The approach to obtain this equation is based on Poiseuille flow through pipes. Assuming pipe flow through a cylindrical channel of diameter  $h_p$ , the average velocity through the channel is

$$\langle u_p \rangle = -\frac{h_p^2}{32\mu} \frac{\Delta p}{L}, \quad (2.12)$$

and for slab flow through an infinite channel of width  $h_s$

$$\langle u_s \rangle = -\frac{h_s^2}{12\mu} \frac{\Delta p}{L}, \quad (2.13)$$

given the pressure drop  $\Delta p$  per length  $L$ , and a fluid with viscosity  $\mu$ .

Defining the hydraulic diameter to be

$$D_h = 4 \frac{\text{volume available for flow}}{\text{total wetted surface}}, \quad (2.14)$$

allows to unify the relations above, by combining Eq. (2.14) with either Eq. (2.12), with  $D_h = h_p$ , or Eq. (2.13), with  $D_h = 2h_s$ , and with Darcy's law, Eq. (2.2), so that the permeability is described by the CK relation (Carman 1937)

$$K = \frac{\varepsilon \mu \langle u \rangle}{\nabla p} = \frac{\varepsilon D_h^2}{\psi_{CK}} \quad (2.15)$$

Where,  $\psi_{CK} = 32$  (or 48) is the dimensionless Kozeny factor, characteristic of the pipe (or slab) pore structure. When one has obstacles like fibers (or particles) instead of straight pores, the hydraulic diameter can be re-written as

$$D_h = \frac{4\varepsilon V}{S_v} = \frac{4\varepsilon}{(1-\varepsilon)a_v} = \frac{\varepsilon d}{(1-\varepsilon)}, \quad \text{with } a_v = \frac{\text{particle surface}}{\text{particle volume}} = \frac{S_v}{(1-\varepsilon)V} = \frac{4}{d}, \quad (2.16)$$

with the total volume of the unit cell,  $V$ , the total wetted surface,  $S_v$ , the specific surface area,  $a_v$ , and the porosity,  $\varepsilon$ , for a fibrous medium of fiber diameter  $d$ . Note that the hydraulic diameter, in this way, is expressed as a function of the measurable quantities porosity and specific surface area. The above value of  $a_v$  is for circles (cylinders) – for spheres one has  $a_v = 6/d$ . In this formulation, one just considers the resistance due to presence of particles (no slip boundaries at the surface of the particles) and neglects the outer walls.

Inserting Eq. (2.16) into Eq. (2.15), yields the normalized permeability for fibers

$$\frac{K}{d^2} = \frac{1}{\psi_{CK}} \frac{\varepsilon^3}{(1-\varepsilon)^2}, \quad (2.17)$$

which depends non-linearly on the porosity and on a shape/structure factor,  $\psi_{CK}$ .

One of the main drawbacks of the CK equation is that the Kozeny factor  $\psi_{CK}$  is a-priori unknown in realistic systems and has to be determined experimentally. An ample amount of literature exists on the experimental and theoretical determination of the Kozeny factor, but we are not aware of a theory that relates  $\psi_{CK}$  with the microstructure, i.e. the porosity, the random configuration, tortuosity, and other microscopic quantities. An overview of experimental and theoretical approaches can be found in Astroem et al. [2], which mainly deals with fibrous media, and Torquato [32], which is based on variational principles. One of the most widely accepted approaches to generalize the CK relation was proposed by Carman [6], who noticed that the streamlines in a porous medium are far from being completely straight and parallel to each other. This effect can be described by a dimensionless parameter,  $L_e/L$  (tortuosity), with the length of the streamlines,  $L_e$ , relative to the length of the sample,  $L$ . Hence the Kozeny factor can be split into

$$\psi_{CK} = \Phi \left( \frac{L_e}{L} \right)^2 \quad (2.18)$$

where  $\Phi$  is the effect of particle shape, which can be seen as a fitting parameter. In fact, the tortuosity and the shape factor reflect the effects of microstructure on the macroscopic properties (like permeability) of the porous media.

In the original form of the CK equation for random 3D sphere structures, it is assumed that the tortuosity is a constant for all ranges of porosities and is equal to  $\sqrt{2}$  and the fitting parameter,  $\Phi$ , then becomes 90 for the case of pipe flow and 60 for slab flow.

Knowing the values of the normalized permeability from my FE simulations, one can compare the values of the Kozeny factor based on my numerical results and available theoretical data and with the original  $\psi_{CK}=120$  for slab flow, see Eqs. (2.17) and (2.18). The comparison is shown in Fig. 2.9. At a certain range of porosities,  $0.5 < \varepsilon < 0.7$ , the CK factor  $\psi_{CK}$  is indeed not varying much. However, at higher or lower porosities, it strongly depends on porosity and structure. At high and low porosities, my numerical results are in good agreement with the predictions of Drummond et al. [9] and Gebart [11], respectively (see Table 2.1). These results indicate that the Carman-Kozeny factor,  $\psi_{CK}$ , is indeed not constant and depends on the microstructure.

In the following subsections, I will study the dependency of  $\psi_{CK}$  on the micro-structural parameters.



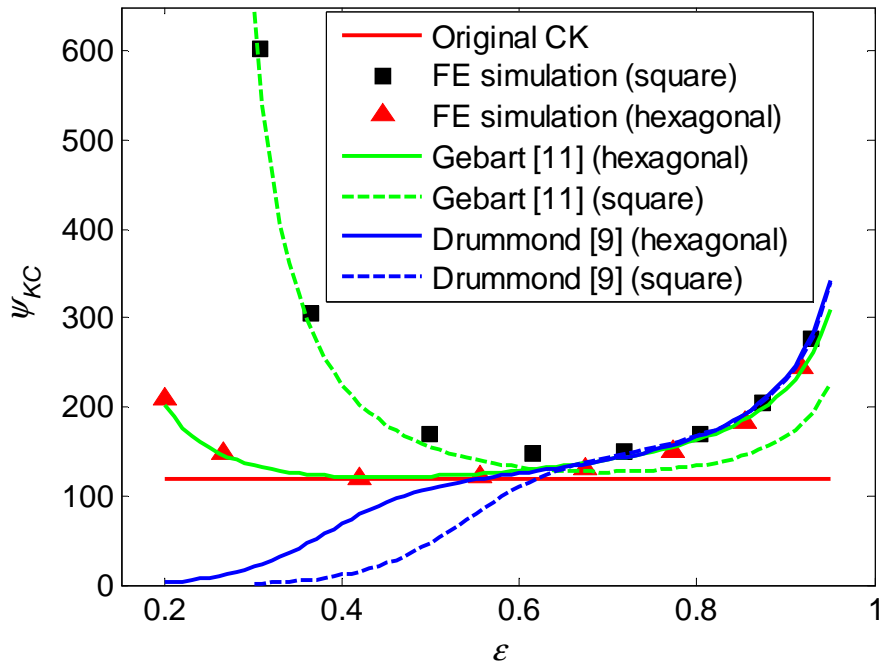


**Figure 2.9:** Kozeny factor plotted as a function of porosity for different models (lines) and data sets (symbols) as given in the inset.

### 2.3.2 Measurement of the tortuosity ( $L_e/L$ )

As discussed before, the tortuosity is the average effective streamline length scaled by system length,  $L_e/L$ , and one possible key parameters in the Kozeny factor in the CK equation [6]. From my numerical simulations, I extract the average length of several streamlines (using 8 streamlines that divide the total mass in-flux into 9 zones, thus avoiding the center and the edges). By taking the average length of these lines, the tortuosity can be obtained, while by taking the standard deviation of the set of streamlines, the homogeneity of the flow can be judged. The tortuosity is plotted in Fig. 2.10 as function of porosity for different shapes and orientations and as function of the stagger angle  $\alpha$  for different porosities.

Unlike the traditional form of the CK equation, which assumes that  $L_e/L = \sqrt{2}$  (for random 3D structures) is constant [6], my numerical results show that the tortuosity (i) is smaller and (ii) depends on the porosity and the pore structure. In Fig. 2.10(a), as intuition suggests, the vertical and horizontal ellipses have the highest and lowest average tortuosity, respectively. This goes ahead with very large and very small standard deviation, i.e. the vertical ellipse configuration involves the widest spread of streamline lengths. In the case of a circular shape obstacle, the (average) tortuosity is between the horizontal and vertical ellipse cases and, for intermediate porosity, becomes almost

independent of porosity, with constant standard deviation that is wider than the average tortuosity deviation from unity. The square shape obstacles are intermediate in tortuosity, i.e. the  $0^\circ$ -square ( $45^\circ$ -square) shapes take tortuosity values between the horizontal (vertical) ellipse and the circular obstacles.

In Fig. 2.10(b), the tortuosity is plotted against the stagger unit cell angle  $\alpha$ . By increasing  $\alpha$  the value of tortuosity increases until about  $\alpha \cong 45^\circ$ , where it reaches its maximum. Note that the standard deviation remains small for all angles smaller than  $\alpha \cong 45^\circ$ . At higher angles, tortuosity decreases, while its standard deviation considerably increases. At large values of  $\alpha$ , most of the fluid flow goes along a straight line, however, near the boundary, we have a few longer streamlines that cause the large standard deviation. At the limit case of  $\alpha \approx \alpha_{\max}$ , when the upper particles touch, see Fig. 2.7, the tortuosity approaches unity (data not shown) and the flow goes mostly along a straight channels.

### 2.3.3 Measurement of the shape/fitting factor ( $\Phi$ )

Knowing the values of tortuosity,  $L_e/L$ , and normalized permeability,  $K/d^2$ , from my FE simulations, one can obtain the values of  $\Phi$  for different shapes and orientations as

$\Phi = \psi_{CK} / \left( \frac{L_e}{L} \right)^2$ . In Fig. 2.11 the variation of  $\Phi$  as a function of porosity for different shapes and orientations is shown. Unlike the traditional CK factor, the shape/fitting factor is not only a function of porosity but also depends on the orientation of particles/cylinders. This dependency is more pronounced at high (low) porosities and close to the blocking conditions, i.e. ellipses with  $90^\circ$  and squares with  $45^\circ$ .

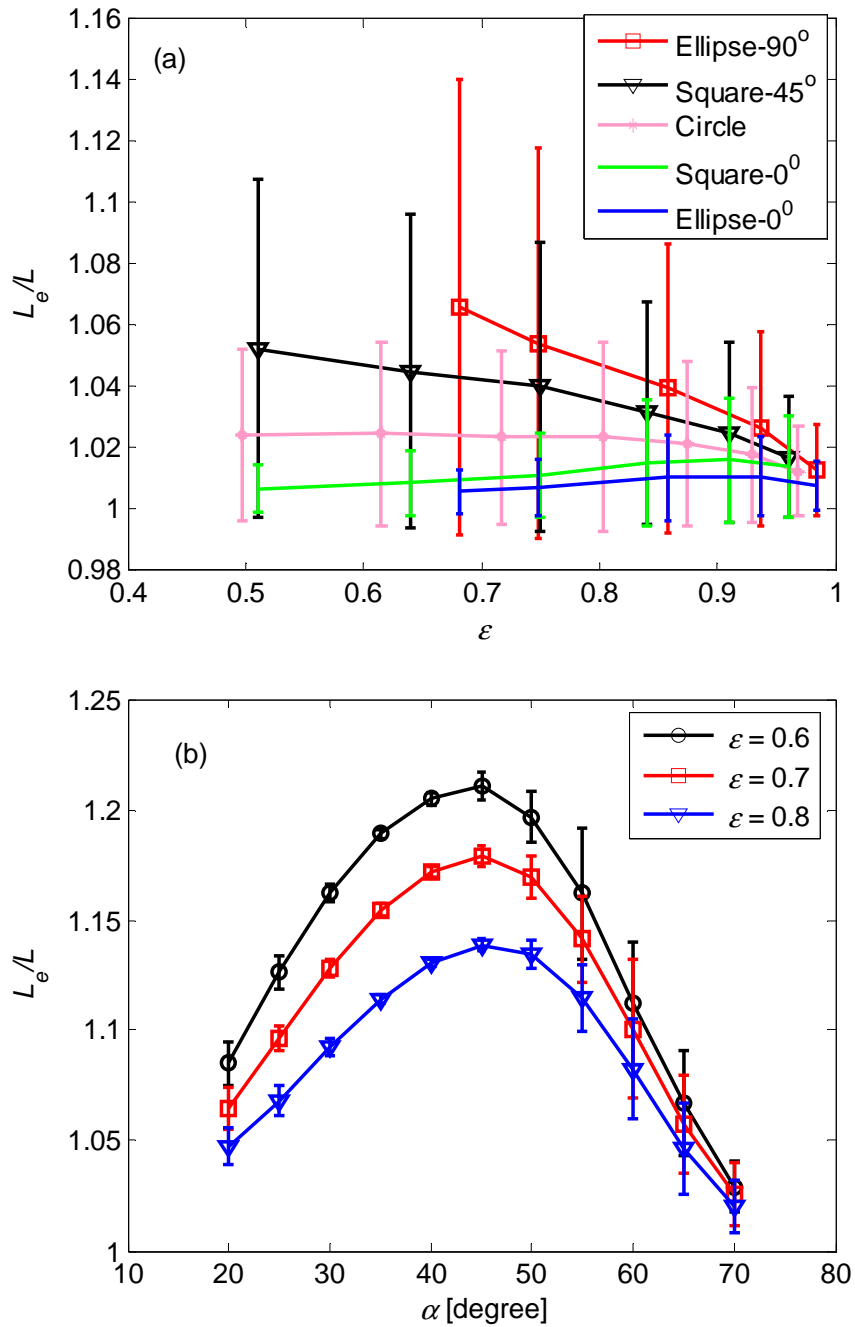


**Figure 2.10:** Tortuosity ( $L_e/L$ ) (a) plotted as a function of porosity for different obstacle shapes and orientations on square configurations,  $\alpha = 45^\circ$ , (b) plotted as a function of the stagger cell angle,  $\alpha$ , as given in the inset, for circles at different porosities on hexagonal configurations. Error bars give the standard deviation of the 8 streamline lengths, where bottom-values below unity indicate a highly non-symmetric distribution around the average.

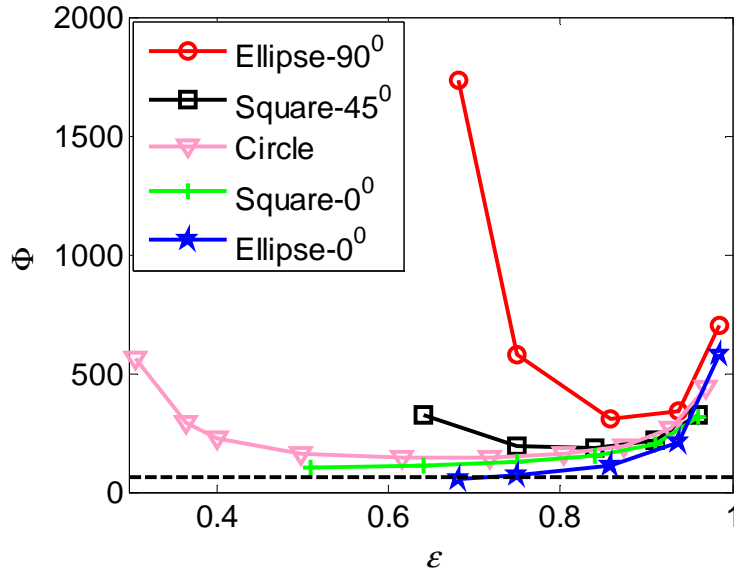


**Figure 2.11:** Shape/fitting factor,  $\Phi$ , plotted as a function of porosity for different obstacle shapes and orientations on square configurations,  $\alpha = 45^\circ$ . The straight dashed line shows the value of  $\Phi = 60$  as in the original CK factor.

### 2.3.4 Corrections to the limit theories

As it was not possible to explain the variation of permeability with tortuosity and a constant shape factor, now I attempt to optimize/correct the limit theories by Gebart [11] and Drummond et al. [9], see Table 2.1, in order to propose an analytical relation for the permeability that is valid for all porosities and for square and hexagonal arrays of cylinders.

#### 2.3.4.1 Square configuration

Assuming one particle at the center, a pressure boundary at the left and right and periodic boundaries at top and bottom, I correct the original Gebart relation from Table 2.1,  $K_G^s$ ,

by a linear correction term  $K_{G2}^s = K_G^s \frac{1}{1 + g_2(\epsilon - \epsilon_c)}$ , with  $g_2 = 0.336$ . After observation of

a linear correction term in the denominator (see the circles in Fig. 2.12), the linear least square method is used to get the coefficient  $g_2$ . In contrast to  $K_G^s$ , which asymptotically approaches the limit case,  $\epsilon \rightarrow \epsilon_c$ , but for  $\epsilon \approx 0.6$  deviates already by about 10%, the correction,  $K_{G2}$ , has a maximum discrepancy in the range  $\epsilon_c < \epsilon < 0.85$  of less than 10%, and for  $\epsilon_c < \epsilon < 0.7$  of less than 2%, see the squares in Fig. 2.12.

Since the Drummond relation from Table 2.1,  $K_D^s$ , is valid at high porosities with maximum discrepancy at  $0.7 < \varepsilon < 1$  of less than 10% and for  $0.8 < \varepsilon < 1$  of less than 2%, I propose the following merged function

$$K^s = K_{G2}^s + (K_D^s - K_{G2}^s)m(\varepsilon), \text{ with } m(\varepsilon) = \frac{1 + \tanh((\varepsilon - \varepsilon_h)/\varepsilon_t)}{2}, \quad \varepsilon_h = 0.75, \quad \varepsilon_t = 0.037,$$

that is valid for the whole range of porosity, with deviations of less than 2% that also includes the analytical relations for the limit cases. While the choice of  $m(\varepsilon)$  is arbitrary, the non-linear least square fitting procedure is used to obtain the empirical coefficients  $\varepsilon_h$  and  $\varepsilon_t$ . The error of these coefficients is defined by their standard deviation.

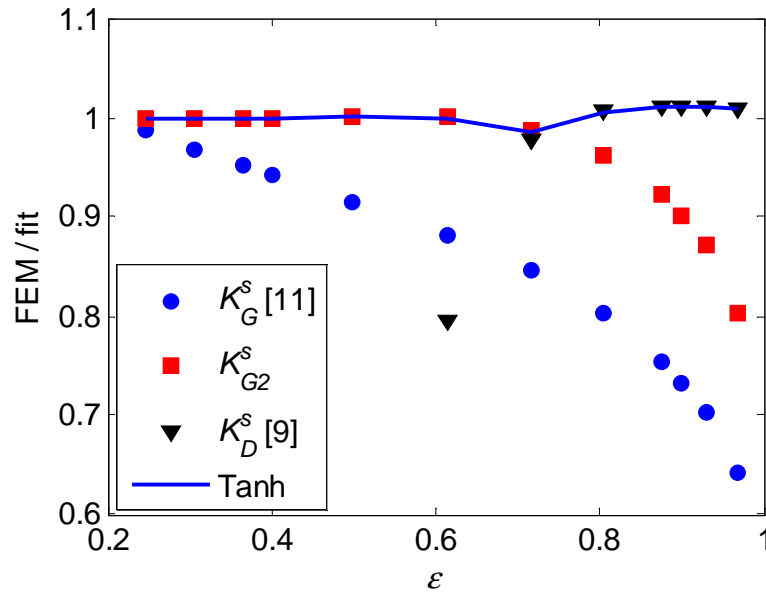


**Figure 2.12:** Relative error between FEM results and proposed corrections for square configuration with the critical porosity  $\varepsilon_c = 1 - \pi/4$ . The “Tanh” representing the proposed merging tangent hyperbolic function.

### 2.3.4.2 Stagger hexagonal configuration ( $\alpha = 60^\circ$ )

In this situation, the correction to the Drummond relation from Table 2.1 is  $K_{D2}^h = d_1 K_D^h (1 + d_2 \varepsilon)$ ,  $K^h = K_G^h + (K_{D2}^h - K_G^h)m(\varepsilon)$ , with  $d_1=0.942$ ,  $d_2=0.153$ ,  $\varepsilon_h = 0.55$ ,  $\varepsilon_t = 0.037$ , leads to a corrected permeability for all porosities, with a maximum error of less than 2%, see Fig. 2.13.

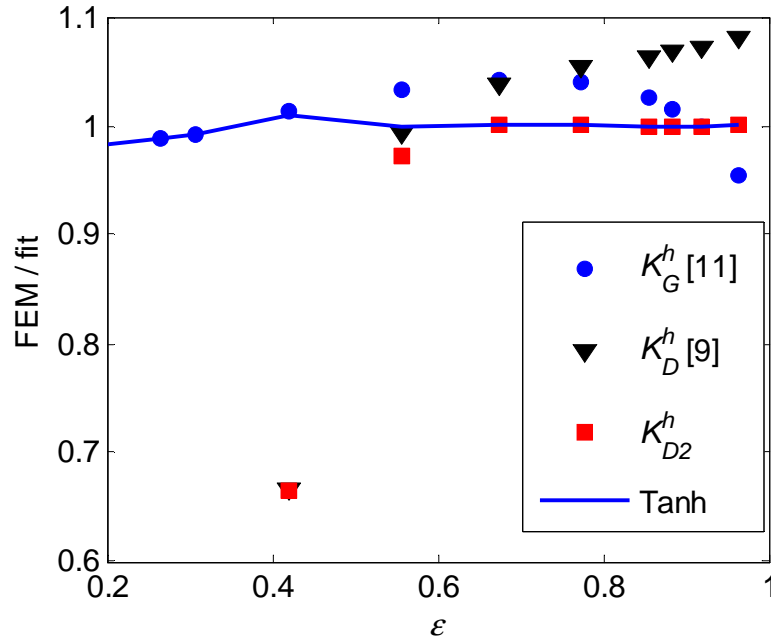


**Figure 2.13:** Relative error between FEM results and proposed fits for hexagonal configuration with the critical porosity  $\varepsilon_c = 1 - \pi / (2\sqrt{3})$ . The “Tanh” representing the proposed merging tangent hyperbolic function.

## 2.4 Summary and conclusions

The permeability of porous structures is an important property that characterizes the transport properties of porous media; however, its determination from first principals is challenging due to its complex dependence on the microstructure of the media. Using an appropriate representative volume element, transverse flow in aligned, periodic fibrous porous media has been investigated based on high resolution (fine grid) FE simulations. This is complementary to previous studies by Hill et al. [15, 16] and Van der Hoef et al. [33] who obtained the drag/permeability relation for random arrays of mono- and bi-disperse spheres at low and moderate Reynolds numbers. In all of my simulations, the total pressure drop has been chosen small, such that we are always in Darcy’s regime (creeping flow). In particular, the effects of different parameters including fiber (particle) shape, aspect ratio, orientation, and stagger unit cell angle on the normalized permeability are measured and discussed in detail for the full range of porosities. The conclusions are:

- The current results for the permeability are validated by comparing with available theoretical and numerical data for square and hexagonal arrays over a wide range of porosities. Especially in the limits of high and low porosity, agreement with previous theoretical results is established.

- By increasing the stagger unit cell angle,  $\alpha$  (where 60 degrees corresponds to the hexagonal array), from the blocked configuration with minimal angle  $\alpha_{\min}$ , the normalized permeability increases until it reaches its local maximum at  $\alpha \cong 35^\circ$ . Then it decreases a bit (almost plateau) until it reaches its local minimum at  $\alpha \cong 55^\circ$ . From there it increases again until a maximum porosity is reached at  $\alpha_{\max}$ . The best-fit (3<sup>rd</sup> order) polynomials at different porosities are presented as reference for later use.
- By increasing the orientation angle of the ellipses (here the longer axis of ellipses was used to define the orientation relative to the flow direction), the permeability decreases and its anisotropy becomes apparent. The permeability values for the extreme cases, i.e. eigenvalues at  $0^\circ$  and  $90^\circ$ , can be used to predict the permeability for arbitrary orientation angles, see Eq. (2.9).
- By increasing the aspect ratio of horizontal ellipses, the permeability increases and approaches the permeability of slab flow, i.e.  $K/h_s^2 = 1/12 = 0.0833$ , at high porosities.
- Using the hydraulic diameter concept the permeability can be expressed in the general form of the (Carman-Kozeny) CK equation. The numerical results show that the CK factor not only depends on the porosity but also on the pore structure, namely particle shape, orientation and stagger angle  $\alpha$ .
- The numerical results show that immobile circles and ellipses have the lowest and highest permeability, respectively. The relevance of this observation for flows of gas/fluid-solid with moving non-spherical particles is an open question.

Since analytical forms with the power as a free fit-parameter are neither consistent with the highest porosity asymptote, nor with the lowest porosity limit case, those fits are only an attempt to describe the intermediate regime of practical importance with a closed functional form. In order to improve the analytical relation for the permeability, to be applied, e.g., for DEM-FEM coupling, I proposed a combined/merging function that includes both limit cases of low and high porosity and is smooth in between with maximal deviation from my numerical results of less than 2%.

Future work will investigate the creep and inertial flow regime through periodic and disordered arrays, the relation between microstructure and (macro) permeability, and the effect of the size of the system, especially for random/disordered structures. Since already the packing generation algorithm affects the permeability in random arrays of parallel cylinders, different procedures have to be compared and evaluated with respect to the microstructure, see next chapter. These results can then be utilized for validation of advanced, more coarse-grained models for particle-fluid interaction and their coupling-terms between the discrete element method (DEM) for the particles and the FEM or CFD solver for the fluid, in a multi-scale coarse grained approach.

### Acknowledgements:

The authors thank N. P. Kruyt, A. Thornton and T. Weinhart for helpful discussion and acknowledge the financial support of STW through the STW-MuST program, Project Number 10120.

### References

- [1] F.J. Alcocer, V. Kumar, and P. Singh, Permeability of periodic porous media, *Physical Review E*, 59 (1999) 711-14.
- [2] B. Astroem, R. Pipes, S. Advani, On flow through aligned fiber beds and its application to composite processing, *J. Compos. Mater.*, 26 (1992) 1351–73.
- [3] J.G. Berryman, H.F. Wang, Elastic wave propagation and attenuation in a double-porosity dual-permeability medium, *International Journal of Rock Mechanics and Mining Sciences*, 37 (2000) 63-78.
- [4] R.B. Bird, W.E. Stewart, and E.N. Lightfoot, *Transport Phenomena*, 2nd edn., John Wiley & Sons, 2001.
- [5] M.V. Brusckhe, and S.G. Advani, Flow of generalized Newtonian fluids across a periodic array of cylinders, *Journal of Rheology*, 37 (1993) 479-98.
- [6] P.C. Carman, Fluid flow through granular beds, *Transactions of the Institute of Chemical Engineering*, 15 (1937) 150–166.
- [7] X. Chen, T.D. Papathanasiou, The transverse permeability of disordered fiber arrays: A statistical correlation in terms of the mean nearest inter fiber spacing, *Transport in Porous Media*, 71 (2008) 233-251.
- [8] J.W. Crawford, N. Matsui, I.M. Young, The relation between the moisture-release curve and the structure of soil, *Euro J. Soil Sci.*, 46 (1995) 369-75.
- [9] J.E. Drummond, and M.I. Tahir, Laminar viscous flow through regular arrays of parallel solid cylinders, *Int. J. Multiphase Flow*, 10 (1984) 515-40.
- [10] F.A.L. Dullien, *Porous Media: Fluid Transport and Pore Structure*, 2nd edn. Academic Press, New York, 1992.
- [11] B.R. Gebart, Permeability of Unidirectional Reinforcements for RTM, *Journal of Composite Materials*, 26 (1992) 1100–33.
- [12] J. Happel, Viscous flow relative to arrays of cylinders, *AIChE*, 5 (1959) 174–7.
- [13] H. Hasimoto, On the periodic fundamental solutions of the Stokes equations and their application to viscous flow past a cubic array of spheres, *JFM*, 5 (1959) 317-28.



- [14] R. Hilfer, Local porosity theory and stochastic reconstruction for porous media, in: K. Mecke and D. Stoyan (eds.), *Statistical Physics and Spatial Statistics*, Lecture Notes in Physics, Springer, Berlin, 2000.
- [15] R.J. Hill, D.L. Koch, and A.J.C. Ladd, Moderate-Reynolds-number flows in ordered and random arrays of spheres, *JFIM*, 448 (2001) 243-278.
- [16] R.J. Hill, D.L. Koch, and A.J.C. Ladd, The first effects of fluid inertia on flows in ordered and random arrays of spheres, *JFM*, 448 (2001) 213-241.
- [17] G.W. Jackson, D.F. James, The permeability of fibrous porous media, *Can. J. Chem. Eng.*, 64 (1986) 364-374.
- [18] D.L. Koch, A.J.C. Ladd, Moderate Reynolds number flows through periodic and random arrays of aligned cylinders, *JFIM*, 349 (1997) 31-66.
- [19] J.A.M. Kuipers, K.J. Van Duin, F.P.H. Van Beckum, W.P.M. Van Swaaij, Computer simulation of the hydrodynamics of a two-dimensional gas-fluidized bed, *Computers Chem. Eng.*, 17 (1993) 839-858.
- [20] S. Kuwabara, The forces experienced by randomly distributed parallel circular cylinders or spheres in a viscous flow at small Reynolds numbers, *Journal of the Physical Society of Japan*, 14 (1959) 527-532.
- [21] S.L. Lee, J.H. Yang, Modeling of Darcy-Forchheimer drag for fluid flow across a bank of circular cylinders, *Int. J. Heat Mass Transfer*, 40 (1997) 3149-55.
- [22] K. Laakkonen, Method to model dryer fabrics in paper machine scale using small scale simulations and porous media model, *Int. J. Heat Fluid Fl.*, 24 (2003) 114-21.
- [23] G.R. Moss, J.P. Rothstein, Flow of wormlike micelle solutions through a periodic array of cylinders, *Journal of Non-Newtonian Fluid Mechanics*, 165 (2010) 1-13.
- [24] A.J. Muller, and A.E. Saez, *The Rheology of Polymer Solutions in Porous Media, Flexible Polymer Chains in Elongational Flow, Theories and Experiments*, Springer-Verlag, Heidelberg, 1999.
- [25] A.N.M. Obdam, E.J.M. Veling, Elliptical inhomogeneities in groundwater flow-An analytical description, *Journal of Hydrology*, 95 (1987) 87-96.
- [26] K. Roth, Scaling of water flow through porous media and soils, *Euro. J. Soil Sci.*, 59 (2008) 125-130.
- [27] M. Sahraoui, M. Kaviany, Slip and no-slip boundary conditions at interface of porous, plain media, *Int. J. Heat Mass Transfer*, 35 (1992) 927-43.
- [28] A.S. Sangani, A. Acrivos, Slow flow past periodic arrays of cylinders with application to heat transfer, *Int. J. Multiphase Flow*, 8 (1982) 193-206.

- [29] C. Shani, N. Weisbrod, A. Yakirevich, Colloid transport through saturated sand columns: Influence of physical and chemical surface properties on deposition, *Colloids and Surfaces A: Physicochemical and Eng. Aspects*, 316 (2008) 142-50.
- [30] K.S. Sorbie, A. Parker, P.J. Clifford, Experimental and theoretical study of polymer flow in porous media, *SPE Reservoir Eng.*, 2 (1987) 281-304.
- [31] R.R. Sullivan, Specific surface measurements on compact bundles of parallel fibers, *J. Appl. Phys.*, 13 (1942) 725–730.
- [32] S. Torquato, Random heterogeneous media: Microstructure and improved bounds on effective properties, *Appl. Mech. Rev.*, 44 (1991) 37-77.
- [33] M.A. Van der Hoef, R. Beetstra, J.A.M. Kuipers, Lattice-Boltzmann simulations of low-Reynolds-number flow past mono- and bidisperse arrays of spheres: Results for the permeability and drag force, *JFM*, 528 (2005) 233-254.
- [34] T.C. Wallstrom, M.A. Christie, L.J. Durlofsky D.H. Sharp, Effective flux boundary conditions for upscaling porous media equations, *Trans. Porous Med*, 46 (2002) 139-53.
- [35] C.Y. Wang, Slow Viscous Flow between Hexagonal Cylinders, *Transport in Porous Media*, 47 (2002) 67–80.
- [36] O. Wanner, A.B. Cunningham, R. Lundman, Modeling biofilm accumulation and mass transport in a porous medium under high substrate loading, *Biotechnology and bioengineering*, 47 (1995) 703-712.
- [37] K. Yazdchi, S. Srivastava, and S. Luding, On the transition from creeping to inertial flow in arrays of cylinders, *Proceedings of IMECE*, (2010), Vancouver, Canada, 6 pages, ISBN-978-0-7918-3891-4.
- [38] C. Zhao, B.E. Hobbs, A. Ord, S. Peng, L. Liu, H.B. Mühlhaus, Analytical solutions for pore-fluid flow focusing within inclined elliptic inclusions in pore-fluid-saturated porous rocks: Solutions derived in an elliptical coordinate system. *Mathematical Geology*, 38 (2006) 987–1010.
- [39] C. Zhao, B.E. Hobbs, A. Ord, S. Peng, L. Liu, Inversely-Mapped Analytical Solutions for Flow Patterns around and within Inclined Elliptic Inclusions in Fluid-Saturated Rocks, *Mathematical Geosciences*, 40 (2008) 179–197.
- [40] R.W. Zimmerman, Effective conductivity of a two-dimensional medium containing elliptical inhomogeneities, *Proceedings of the Royal Society A: Mathematical, Physical and Engineering Sciences*, 452 (1996) 1713–27.

# 3

## Micro-macro relations for flow through random arrays of cylinders

*"The person with a new idea is a crank, until the idea succeeds"*  
~Mark Twain~

## Abstract

The transverse permeability for creeping flow through unidirectional random arrays of fibres with various structures is revisited theoretically and numerically using the finite element method (FEM). The microstructure at various porosities has a strong effect on the transport properties, like permeability, of fibrous materials. We compare different microstructures (due to four random generator algorithms) as well as the effect of boundary conditions, finite size, homogeneity and isotropy of the structure on the macroscopic permeability of the fibrous medium. Permeability data for different minimal distances collapse when their minimal value is subtracted, which yields an empirical macroscopic permeability master function of porosity. Furthermore, as main result, a microstructural model is developed based on the lubrication effect in the narrow channels between neighboring fibres. The numerical experiments suggest a unique, scaling power law relationship between the permeability obtained from fluid flow simulations and the mean value of the shortest Delaunay triangulation edges (constructed using the centers of the fibres), which is identical to the averaged second nearest neighbor fibre distances. This universal lubrication relation, as valid in a wide range of porosities, accounts for the microstructure, e.g. hexagonally ordered or disordered fibrous media. It is complemented by a closure relation that relates the effective microscopic length to the packing fraction<sup>1</sup>.

## Highlights

- I numerically investigate the effect of several microstructural parameters on the macroscopic permeability of random arrays of fibres.
- Numerical FE results suggest a unique, scaling power law relationship between the permeability and the averaged second nearest neighbor fibre distances.
- A closure relation is presented that relates the effective microscopic channel length to the macroscopic porosity.

---

<sup>1</sup> K. Yazdchi, S. Srivastava and S. Luding, Micro-macro relations for flow through random arrays of cylinders, *Composites Part A*, 43 (2012) 2007-2020.

K. Yazdchi, S. Srivastava and S. Luding, On the validity of the Carman-Kozeny equation in random fibrous media, *Particle-Based Methods II - Fundamentals and Applications* (2011), 264-273, Barcelona, Spain.

### 3.1 Introduction

Understanding and predicting transport properties of porous media is essential in chemical, mechanical and petroleum industries [1]. This has motivated the development of relationships between macroscopic parameters, like permeability, and microstructural parameters, like fibre arrangements, shape and orientation or tortuosity (flow path) [2]. Most porous media are particulate, but some are composed of long particles/cylinders and, therefore, may be considered as fibrous media. Common examples of fibrous media include composite materials, industrial filters, biological tissues, etc.

Resin transfer molding (RTM) is an efficient and frequently used process for producing fibre reinforced polymer composites with simple or complex shapes. The permeability is essential in such process and can be determined by various methods, e.g., experimental measurements, numerical calculations or analytical predictions. Experimental measurements often require a large number of carefully controlled experiments and are normally expensive. Analytical predictions based on theoretical assumptions (and validated by experiments and/or numerical studies) are often applicable in a certain range of fibre volume fraction only.

With the recent progress in computational and numerical tools, one can now predict the macroscopic properties of fibrous materials with rather complex microstructure. Chen and Papathanasiou [3-4] computationally investigated the flow across randomly distributed unidirectional arrays using the boundary element method (BEM) and found a direct correlation between the permeability of fibrous media and the mean nearest inter-fibre spacing. Papathanasiou [5] performed a similar study for unidirectional square arrays of fibre clusters (tows) using the BEM. He stated that the overall flow rate through a multiscale fibre reinforcement is determined mostly by the flow in the mesoscale region, which consequently implies that the saturated permeability is also determined mostly by the flow in that region. Song et al. [6] calculated the permeability tensor for a 3D circular braided preform by solving a boundary problem of a periodic unit cell. The flow field through the unit cell is then obtained by using a 3D finite volume method and Darcy's law is utilized to obtain the permeability tensor. Their numerical results show that the permeability in the machine direction of the preform was the highest among three directions. Takano et al. [7] employed an asymptotic homogenization theory to evaluate the permeability of woven fabrics with the help of finite element method (FEM). They investigated the effect of woven architecture on the permeability characteristics for plain-woven fabrics with and without shearing deformation. In my recent study [8], the effect of several microstructural parameters such as fibre shape and orientation on the macroscopic permeability of 2D regular fibrous media was investigated using a large set of FEM simulations.

The permeability of ordered (regular) fibrous media is known to be a deterministic function of their porosity in the limit of large and small volume fractions, see previous chapter. However, the parameters affecting the permeability of disordered (random) fibre arrays are not very well understood. Random fibre arrays are, in principle, well suited to analysis using effective medium approaches. By averaging the conservation equations,

Koch and Brady [9] derived a relation for the effective diffusivity coefficients in the limit of high porosity  $\varepsilon$ , however, that remains questionable in the porosity range of interest in composites manufacturing, e.g.,  $0.4 < \varepsilon < 0.9$ . Similarly, considering large  $\varepsilon$  values, Drummond and Tahir [10] modeled the flow around a fibre using a unit cell approach by assuming that all fibres in a fibrous medium experience the same flow field (i.e. no interaction between them) and, therefore, the permeability can be obtained by adding the resistance of individual particles/fibres. The dependence of permeability in this limit involves logarithmic, linear and quadratic functions of the solid concentration.

Based on the lubrication approximation and assuming that the narrow gaps between adjacent cylinders dominate the flow resistance for small  $\varepsilon$ , Gebart [11] presented an expression for the transverse permeability of square or hexagonally ordered arrays. He found that the dependence of permeability on fibre volume fraction in this limit is a power law. Using percolation theory, Katz and Thompson [12] found a power law relation between the macroscopic permeability and microstructural descriptors for sedimentary rocks, i.e. the critical pore diameter.

The earliest and most widely applied models in the composites literature, i.e. intermediate porosity regimes, for predicting permeability are capillary models such as the Carman-Kozeny (CK) equation [13] where a constant (Kozeny constant) is supposed to account for the structure at different porosities. While some studies have reported success with this relation [14], discrepancies are also reported [15]. Results from numerical modeling [3] and experimental studies [16] indicate that, at best, capillary models represent the behavior of fibrous materials over a limited porosity range. To my knowledge, relation between microstructure and macroscopic permeability of the fibrous media, such as composite materials, has not been studied systematically.

The objective of this study is to computationally investigate the effects of microstructural parameters such as fibre arrangements on the macroscopic permeability by using a FEM for fluid flow over a wide range of porosity. To this end, the macro description of fluid flow equations and the numerical tool employed to solve these equations are presented in Section 3.2. Volumes of different sizes, formed by randomly placed non-overlapping arrays of parallel cylinders perpendicular to the flow direction, are constructed in four different ways as discussed in Section 3.3. The size effect, the homogeneity and the isotropy of the fibre arrangements are analyzed using several statistical tools. In Section 3.4, I present a microstructural model based on the lubrication effect of the narrow channels as an attempt to (i) combine my various simulations in a wide range of porosity and (ii) relate the micro to the macro properties of fibrous materials. The chapter is concluded in Section 3.5 with a summary and outlook for future work.

## 3.2 Mathematical formulation and methodology

This section considers the macroscopic description of the flow equations applied in fibrous structures and my methodology, e.g., the method of discretization of the domain and boundary conditions applied to my FEM based simulations.

The velocity and pressure profiles through the fibrous media can be obtained from the solution of the conservation laws, namely, the continuity equation (conservation of mass) and the Navier–Stokes (NS) equations (conservation of momentum). In the absence of body forces and for Newtonian fluid, incompressible, steady state flow, the equations of conservation of mass and momentum are:

$$\begin{aligned}\nabla \cdot u &= 0, \\ \rho(u \cdot \nabla u) &= -\nabla p + \mu \nabla^2 u.\end{aligned}\tag{3.1}$$

where  $\rho$ ,  $u$ ,  $p$  and  $\mu$  are density, velocity, pressure and viscosity of the fluid, respectively. According to Darcy's law for unidirectional flow through a porous medium in the creeping flow regime, the horizontal *superficial* (discharge) fluid velocity  $U = \frac{1}{V} \int_{V_f} u dv$  ( $V$ ,  $V_f$  are the total volume and volume of the fluid) is proportional to the pressure gradient:

$$U = -\frac{K}{\mu} \nabla p.\tag{3.2}$$

The proportionality constant  $K$ , is called the permeability of the medium, which strongly depends on the microstructure (such as fibre arrangement, void connectivity and inhomogeneity of the medium) and also on porosity. By increasing the pressure gradient, one can observe a typical departure from Darcy's law (creeping flow) at sufficiently high Reynolds number,  $Re > 0.1$  [17]. However, in the following, I restrict myself to creeping flow regime, i.e.  $Re \ll 1$ .

The FEM software ANSYS<sup>®</sup> is used to calculate the fluid velocity from discretization of Eq. (3.1) into linear triangular elements. They were then solved using the segregated, sequential solution algorithm. This means that element matrices are formed, assembled and the resulting systems solved for each degree of freedom separately. Some more technical details are given in Ref. [8]. Afterwards, the superficial velocity and the permeability of the fibrous material are obtained using Eq. (3.2). Fig. 3.1 shows a 3D/2D representation of 200 randomly distributed fibres normal to the flow direction at porosity  $\varepsilon = 0.6$  with minimum inter fibre distance  $\delta_{\min} = 0.05d$  ( $d$  is the diameter of the fibres) or the minimum dimensionless distance  $\Delta_{\min} = \delta_{\min} / d = 0.05$ . Just as in the work of Chen and Papathanasiou [3, 4], a minimal distance is needed in 2D to avoid complete blockage. The microstructural parameters, namely the system size, the method of generation, the homogeneity and the isotropy of the structure will be discussed in more detail in the next section. At the left and right boundary pressure is set and at the top and bottom wall surfaces ( $z$  direction) and at the surface of the particles/fibres no-slip boundary conditions are applied. Some simulations are formed with periodic boundaries instead of walls with normal in the  $z$  direction (the differences are detailed in Appendix 3.B.3). The fibres are assumed to be very long so that a 2D solution can be applied. A typical unstructured, fine and triangular FEM mesh is also shown in Fig. 3.1. The mesh size effect is examined by comparing the simulation results for different resolutions. The number of elements is

varies from  $5 \times 10^5$  to  $10^6$  depending on the porosity regime. The lower the porosity the more elements are needed in order to resolve the flow within the neighboring fibres, see appendix 3.A for more details. To obtain good statistical accuracy, the permeability values were averaged over 10 realizations.

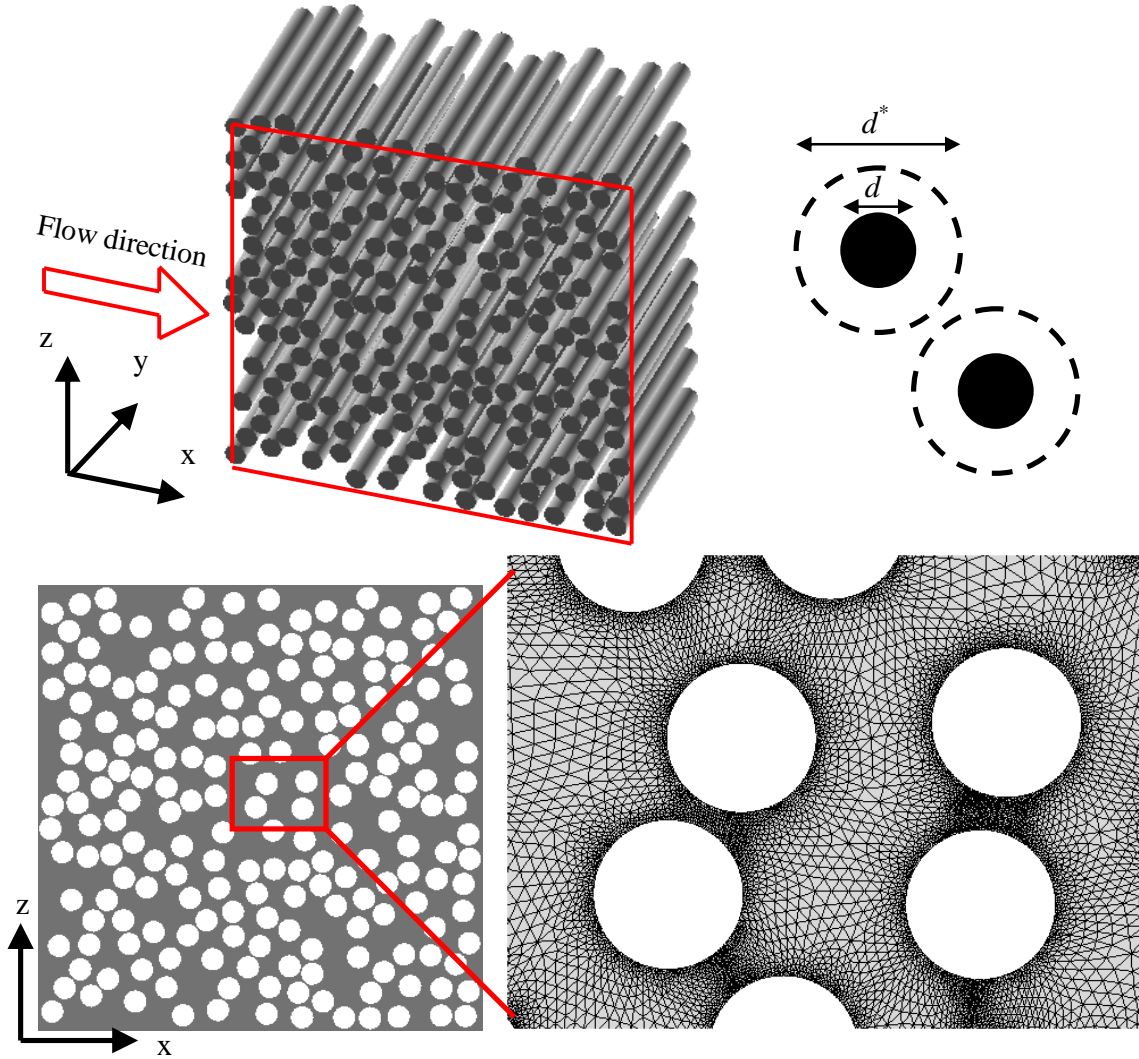


**Figure 3.1:** Fibre distributions generated by a Monte Carlo procedure (see subsection 3.3.1), with 200 unidirectional, monosize cylinders, normal ( $y$ ) to the flow direction ( $x$ ), with minimum inter fibre distance  $\Delta_{\min}=0.05$  at porosity  $\varepsilon=0.6$ . At the top the diameter,  $d$  and virtual diameter  $d^* = d(1 + \Delta_{\min})$  are shown, schematically. At the top 3D and bottom 2D representation of fibre distribution are shown. The zoom shows the fine, unstructured, triangular FEM mesh.



### 3.3 Generation of the fibrous microstructure

Developing a model for predicting the permeability as a function of porosity and structure of the fibrous materials would help to reduce the experiments in liquid composite molding (LCM) processes such as RTM or resin infusion. Furthermore, by understanding the physics of the flow through such materials, one may tailor the microstructure such that it has both the desired reinforcing capability and also the permeability to be filled efficiently. To get reliable evidence and to quantify the non-uniform spatial distribution of fibres, several microstructural characteristics of fibrous material will be discussed here in detail.

Note that to ensure a gap between particles ( $\Delta_{\min}$ ), I assign a virtual diameter  $d^* = d(1 + \Delta_{\min})$  to each fiber, leading to the virtual porosity  $\varepsilon^* = 1 - (1 - \varepsilon)(1 + \Delta_{\min})^2$ , see Fig. 3.1, which has been used for packing generation in the rest of this section.

#### 3.3.1 Method of generation

Most of representative volume elements (RVE) rely on the assumption of a periodic distribution of fibres, i.e. the structures at the boundaries are similar to those in the bulk. However, realistic media are finite and confined with walls. Some systems can be very large so that boundary effects can be neglected; on the other hand, in micro-systems, the effect of the walls might show up. Therefore, unless specified otherwise, in the rest of the chapter I consider a 2D representation of the fibrous composite in which the fibres are randomly distributed in a square domain and confined by walls with normal in  $z$  direction. In order to understand the wall-effects, I will vary the system size (see appendix 3.B for details).

To generate random, non-overlapping fibre arrays, I use different algorithms, namely, (i) random placement (RP), (ii) a Monte Carlo (MC) procedure, (iii) an energy minimization (EM) approach and (iv) molecular dynamic (MD) simulations. Note that in all methods, we have a minimal distance ( $\Delta_{\min}$ ) between fibres to avoid complete blockage.

(i) In the RP the position of fibres is randomly drawn from a uniform distribution; then this location is taken as valid if it does not overlap a previously positioned fibre. The insertion of fibres will continue until it reaches the desired number of fibres. This process leads to an asymptotic jamming limit since the space available to place successive particles decreases with the addition of each new particle. The minimum porosity for RP in 2D is estimated to be  $\sim 0.447$  [18], and has found to be  $\sim 0.453$  [19] via computer simulations.

(ii) Given an initial fibre configuration on a triangular lattice, the MC procedure perturbs fibre centre locations in randomly chosen directions and magnitudes [3-4, 20]. The perturbation is rejected if it leads to overlap with a neighboring disk. One step consists of trying to move each disk once. I use up to  $10^6$  steps for each realization at low porosities to get a good random configuration i.e. the MC process should generate a random

position field which is short range correlated. However, at the lowest porosity, the particles remain ordered and show some dependence on the number of steps/perturbations, even for the longest simulations. For high porosities, the structures show no dependence on number of MC perturbations. Moreover, the MC algorithm can generate denser systems as compared to RP.

(iii) In the EM approach, infinitesimal disks are placed at random positions in the system. Then, they are gradually expanded and moved at each step to prevent particles from overlapping. When the desired porosity is reached the algorithm terminates [21]. We assume that the particles interact via the soft potential given by:

$$V(r_{ij}) = \begin{cases} \frac{\beta}{2} \left(1 - \frac{r_{ij}}{d}\right)^2 & \text{for } r_{ij} < d, \\ 0 & \text{for } r_{ij} \geq d, \end{cases} \quad (3.3)$$

where  $\beta$  is the characteristic energy scale and  $r_{ij}$  is the separation of particles  $i$  and  $j$ . Potential of this form was motivated by simulation of granular materials, see next subsection, where the particles do not interact except for a strong repulsive force that keeps the particles from overlapping/deforming too much<sup>2</sup>. With this procedure, one can generate very dense systems down to  $\varepsilon \sim 0.158$ .

(iv) Finally, a 2D discrete element method (DEM) or soft-sphere model is used to generate a random non-overlapping disks configuration. The motion of particles is described by Newton's laws of motion. A characteristic feature of the soft-sphere models is that they are capable of handling multiple particle contacts, which are of importance when modeling dense, quasi-static systems. Particle overlaps are indicative of a collision. For all identified collisions, a contact model (here I use a simple spring/dash pot model, similar potential as Eq. (3.3)) is applied and the simulation is then advanced again in time [22]. The typical contact duration is:

$$t_c = \pi / \omega, \quad \text{with } \omega = \sqrt{2k/m - (\eta_0/m)^2}, \quad (3.4)$$

where  $k$ ,  $\omega$ ,  $\eta_0$  and  $m$  are the spring stiffness, eigen-frequency of the contact, viscous damping and mass of the particles/fibres, respectively. Note that the integration of the equations of motion is stable only if the integration time-step,  $\Delta t_{MD}$ , is much smaller than  $t_c$ . The difference to EM is that inertia (dynamical motion of particles) is taken into account in MD<sup>3</sup>.

<sup>2</sup> After each expansion step, we check if any disks overlap by checking the condition  $1 - r_{ij}/d > 10^{-5}$  for each particle pair. Below this limit, the overlap is neglected. If any particles do overlap, i.e. the total energy is  $E > 0$ , the nonlinear conjugate gradient method is used to decrease the total energy by adjusting the position of disks so they no longer overlap ( $E=0$ ). Therefore, in this method, the value of  $\beta$  will not affect the minimization procedure.

<sup>3</sup> Contact force parameters used in MD simulations:  $k=10^6$  [kg/s<sup>2</sup>],  $m=100$  kg,  $\eta_0=10^{-4}$  [kg/s],  $\Delta t_{MD}=10^{-4}$  [s] with the total time of simulation  $t_T=500$  [s].

Having an initial fibre configuration on a regular triangular lattice, we assign random velocities in random direction to each particle and run a MD simulation for sufficiently long time such that all particles are separated by the minimum gap ( $\Delta_{\min}$ ). A random structure is obtained by taking a snapshot of the final fibre positions.

In the following, I compare the statistics of the fibre arrangements generated by the four methods and investigate the influence of the packing generator algorithm on the macroscopic permeability of the medium, where [3-4] used the MC procedure only.

### 3.3.2 Statistical analysis of the microstructure

Various statistical descriptors have been proposed to characterize and classify microstructures based on the spatial arrangement of heterogeneities, see for example [23, 24]. Popular among these is the radial (pair) distribution function  $g(r)$ , which is defined as the probability of finding the centre of a fibre inside an annulus of internal radius  $r$  and thickness  $dr$  with centre at a randomly selected fibre. It is mathematically defined as:

$$g(r) = \frac{1}{2\pi r} \frac{dK(r)}{dr}, \quad \text{where } K(r) = \frac{A}{N^2} \sum_{k=1}^N I_k(r). \quad (3.5)$$

where  $K(r)$  is a second-order intensity function, also known as Ripley's function [3-4, 23] and  $I_k(r)$  is defined as the number of centers of fibres that lie within a circle of radius  $r$  about an arbitrarily chosen fibre and  $N$  is the number of fibres in the observation area  $A$ . Given a Poisson point distribution, the complete randomness of the fibre distribution will assure that  $g(r)=1$  (with some fluctuations) for all distances considered. A statistically valid fibre distribution without long-range order will have  $g(r)$  tending to 1 as the distance  $r$  increases. The comparison of  $g(r)$  for packings generated with different methods is shown in Fig. 3.2(a). In this graph  $r$  varies from  $d$  (diameter of the fibre) to approximately  $1/3$  of the sample size to avoid boundary (edge) effect on the statistics. Fig. 3.3 shows the actual area and the center area which we used to calculate  $g(r)$  for various creation methods. In all methods the specimen contains 800 fibres at constant porosity  $\varepsilon=0.6$  with minimum inter fibre distance  $\Delta_{\min}=0.05$ . Local maxima indicate the most frequent distances and local minima correspond to the least frequent distances between pairs. The first (highest) peak in the graph is caused by the physical area (excluded "volume") of the fibres with virtual diameter  $d^*$ . As  $r$  increases, we observe a number of oscillations until  $g(r)$  approaches the value of unity indicating the numerically generated microstructures are statistically random for larger  $r$ . The EM method has the largest peak at  $r/d \sim 1.05$  (minimum allowable inter fibre distance) and the most rapid decay with distance, followed by a second peak at  $r/d \sim 2.1$  (equivalent to  $r/d^* \sim 2$ ), which is an indication of fibre agglomeration (or a clustered structure). For the RP algorithm the oscillations around the complete randomness value of  $g(r)=1$  are the smallest compared to the other methods, however, the location of local maxima/minima is almost the same as for MD and MC, which lead to the most similar  $g(r)$  among the four methods. For

configurations with more fibres and different porosities (data not shown), qualitatively, the same trends are observed.

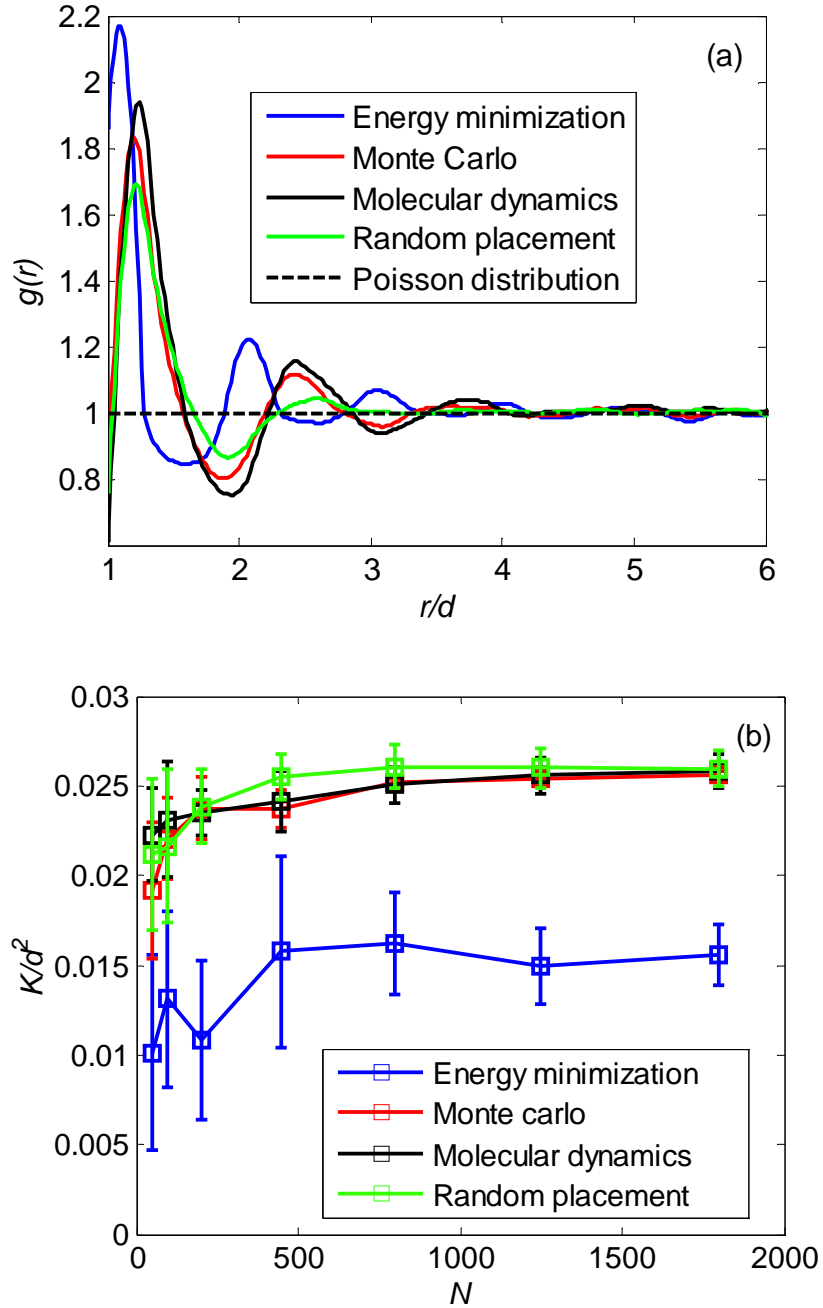


**Figure 3.2:** (a) plots of  $g(r)$  for 800 fibres generated by different methods with  $\Delta_{\min}=0.05$  at porosity  $\varepsilon=0.6$ , (b) comparison of the normalized permeability of the fibre arrangements from (a) plotted against the number of fibres. All data are averaged over 10 realizations with  $10^4$  perturbations. The error bars indicate the standard deviation. Larger numbers of perturbations do not lead to a visible difference.

The fibre arrangement has a direct influence on the effective properties of the medium. In Fig. 3.2(b) the variation of the normalized permeability,  $K/d^2$ , as a function of the number of fibres  $N$ , is shown. As expected, the packings generated with MC, MD or RP (with similar fibre distribution) have practically the same permeability, especially for larger  $N$ . However, the clustered structure (generated by EM) has a lower permeability for all numbers of fibres. This is due to the fact that many particles are arranged along lines - sometimes with local square or triangular structure - but no long range order is evident as one would have in a crystal (see Fig. 3.3 and the peak locations in Fig. 3.2(a)). This leads into more resistance to the flow (i.e. lower permeability) even at intermediate porosities (see next section). By increasing the system size the standard deviation decreases but it remains largest – for EM – indicating correlations built into the method. For most data presented in Section 3.4, I stick to the MC procedure that generates the structures similar to what is observed in real composite manufacturing processes [20] and since it is faster than the MD method. More details on the effect of system size and boundary conditions on statistical descriptors and macroscopic permeability are provided in appendix 3.B.

### 3.3.3 Isotropy and homogeneity of the packing

Since the media studied here consist of randomly distributed fibres, they are expected to be isotropic (no preferential flow direction). Therefore, the normalized permeability as a function of porosity in both horizontal and vertical directions, as shown in Fig. 3.4, is independent of flow direction. As mentioned before, the EM approach tends to generate clustered packings unlike the MC procedure (or MD simulations), which create more homogenous structures. Fig. 3.4 shows that all methods (namely MC, MD and EM) create isotropic media (with respect to horizontal and vertical flow) for all porosities. For comparison, the numerical results of Sangani and Yao [25] and Chen and Papathanasiou [3] for transverse flow are also included in Fig. 3.4. The homogeneity of the packing has negligible effect on permeability at high porosity ( $\varepsilon > 0.65$ ), however, at lower porosities the clustered structure has lower permeability as compared to the homogenous configuration. The reason is that for dilute fibrous media there is no correlation between the solid fibre bundles, however, at lower porosities in the packing generated with the EM approach, we see local fibre clusters, which tend to block the channel and cause a drop in permeability. This was confirmed by studying the velocity fields (not shown here) and is also visible in the PDF of neighbor distances.

### 3.3.4 Effect of minimum inter-fibre distance ( $\Delta_{\min}$ )

The minimum inter-fibre distance ( $\Delta_{\min}$ ) was taken as 5% of the “true” fibre diameter,  $d$  in my simulations up to now to avoid complete blockage in 2D. In the following we scale the permeability values such that they collapse on a single curve valid for all values of  $\Delta_{\min}$  ranging from 0.2 to 0.005. Note that the lower the  $\Delta_{\min}$  the more elements are needed to resolve the flow in the gaps between fibres.

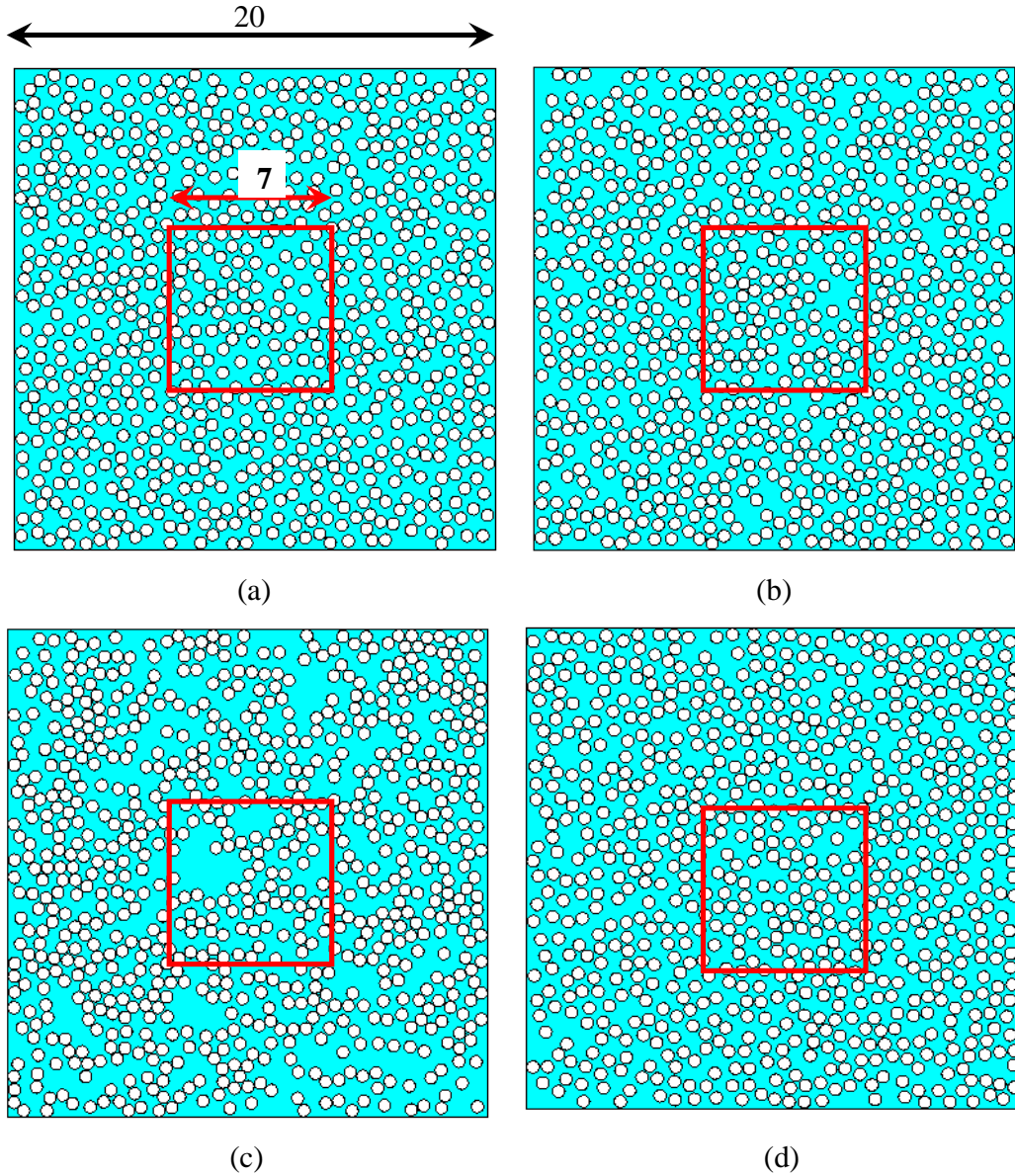
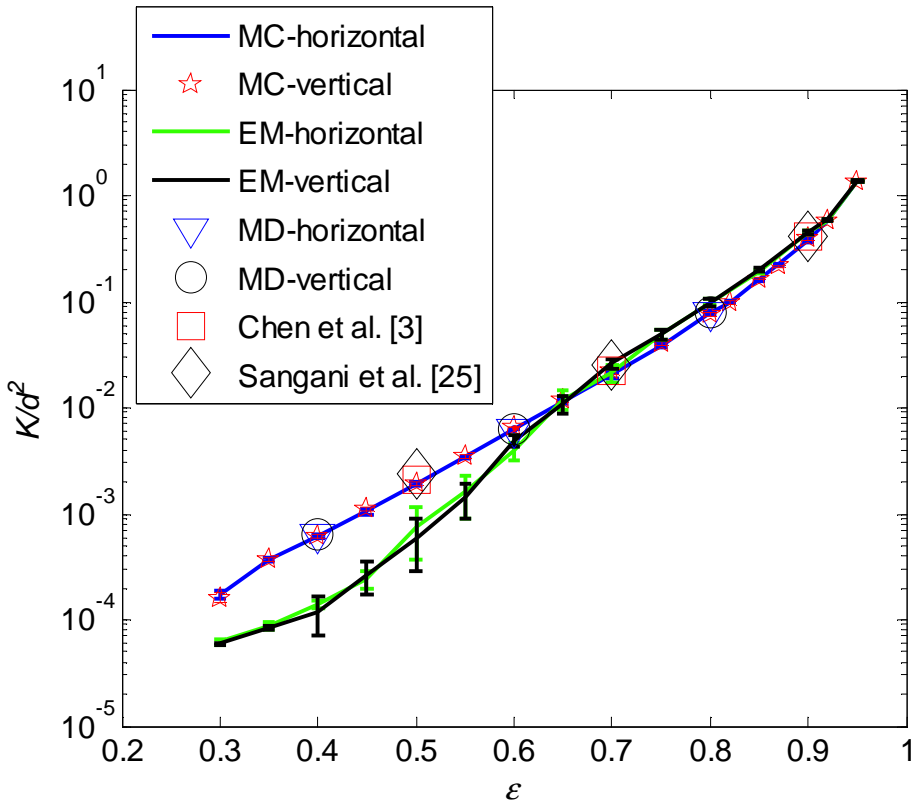


**Figure 3.3:** Each image consists of 800 fibres with minimum inter fibre distance  $\Delta_{\min} = 0.05$  and  $\varepsilon = 0.6$ . They are generated by (a) Random Placement (RP), (b) Monte Carlo (MC) procedure, (c) Energy Minimization (EM) approach and (d) Molecular Dynamics (MD) simulations. The red box shows the center area which has been used to calculate  $g(r)$ . For the chosen reference particles only those in the inner red square are used, while the distances to all others are considered.

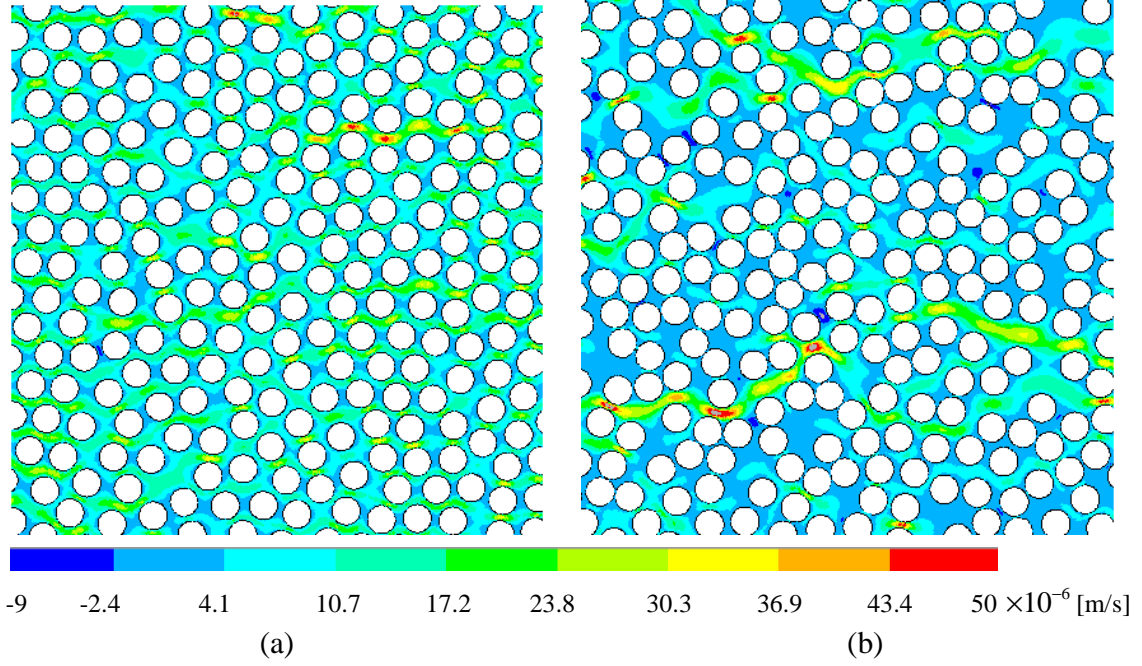
Fig. 3.5 shows the effect of  $\Delta_{\min}$  on the fibre arrangements and fluid velocity. Note that large values of  $\Delta_{\min}$  lead to local (triangular) ordering (Fig. 3.5(a)), whereas a small  $\Delta_{\min}$

results in a pattern showing local fibre aggregation (Fig. 3.5(b)). We observe stagnancy of the fluid between fibre aggregates or within rings of close-by fibres, while a few major flow paths with relatively high flow speed exist in all configurations with disorder.

The permeability,  $K/d^2$ , for small porosity (i.e. the maximum random close packing fraction  $\sim 0.84$  ( $\varepsilon_c^r = 0.16$ ) [26], see the appendix 3.C.) saturates at an a-priori finite value. Larger minimal distances  $\Delta_{\min}$  lead to over-proportionally larger permeability (plot not shown). When the data are scaled by the permeability expected for a periodic hexagonal cell as  $(K - K_{\Delta_{\min}}^{\text{hex}})/d^2$ , see Ref. [8], the data vanishes at a finite porosity, which decays with decaying  $\Delta_{\min}$ . Therefore, I conclude that the minimal permeability of my random structure is somewhat lower than the one of a hexagonal lattice (see the inset in Fig. 3.6). In other words, the systems with more uniform and weak channels (Fig. 3.5(a)) have higher permeability than the systems with fewer dominant channels (Fig. 3.5(b)).



**Figure 3.4:** Normalized permeability as a function of porosity for homogenous (generated with MC procedure or MD simulations) and clustered correlated (generated with EM approach) structure in both horizontal and vertical directions. Error bars indicate standard deviation from 10 realizations.



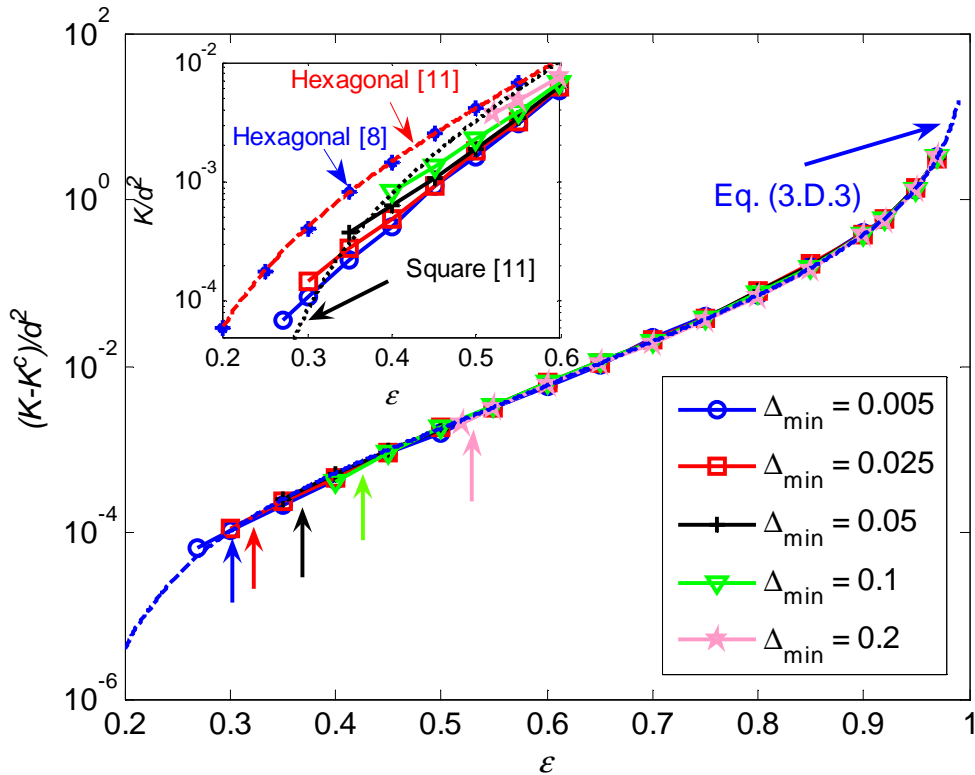
**Figure 3.5:** Typical fibre distributions generated by a Monte Carlo (MC) procedure, each with 800 fibres at  $\varepsilon=0.5$  with minimum inter fibre distance (a)  $\Delta_{\min}=0.2$  ( $\varepsilon^*=0.28$ ) and (b)  $\Delta_{\min}=0.005$  ( $\varepsilon^*=0.49$ ). The color code shows the horizontal velocity field in a pressure driven system. Only the center part of the system is shown.

Fig. 3.6 shows the effect of  $\Delta_{\min}$  on the normalized permeability – after scaling with an appropriate permeability  $K^c/d^2$  that is obtained by multiplying the  $K_{\Delta_{\min}}^{\text{hex}}/d^2$  with a prefactor such that all the data collapse onto a single curve<sup>4</sup>. The minimal permeability for disordered fibre-arrays can then be cast into a formula:  $K^c/d^2 \simeq \eta K_{\Delta_{\min}}^{\text{hex}}/d^2$ , with factor  $\eta = (1 + \Delta_0/\Delta_{\min})$  where  $\Delta_0 = 0.14$  (fitting parameter) and accounts for the minimal inter fibre distance. The numerical values of the critical porosity,  $\varepsilon_{\Delta_{\min}}^{\text{hex}}$  and permeability  $K_{\Delta_{\min}}^{\text{hex}}/d^2$  (for a perfectly hexagonal lattice) and corrected permeability,  $K^c/d^2$  at different  $\Delta_{\min}$  are given in Table 3.1. The scaling factor,  $\eta$  was obtained by fitting the  $K^c/K_{\Delta_{\min}}^{\text{hex}}$  ratios at different  $\Delta_{\min}$ , using a least square approach. With increasing  $\Delta_{\min}$  the scaling factor decreases towards unity and the corrected permeability values,  $K^c/d^2$ , approach the hexagonal cell values. Note that the last data point at each  $\Delta_{\min}$  branch is slightly below  $\varepsilon_{\text{order}}^* \cong 0.3$  (see the arrows). Because all  $\varepsilon^* > \varepsilon_{\text{order}}^*$  can be

<sup>4</sup> The value of  $K^c/d^2$  at large values of  $\Delta_{\min}$  can be approximated as  $(K^c/d^2)_{\Delta_{\min}} \sim (K/d^2)_{\Delta_{\min}} - (K/d^2)_{\Delta_{\min}=0.005}$ . By plotting the values of  $((K^c/d^2)_{\Delta_{\min}} / (K^{\text{hex}}/d^2)_{\Delta_{\min}})$  against  $\Delta_{\min}$ , we observed that the data are fitted best to  $(1 + \Delta_0/\Delta_{\min})$  with  $\Delta_0=0.14$ .



considered as random (almost), whereas  $\varepsilon^* < \varepsilon_{\text{order}}^*$  are partially ordered, we exclude the latter. The inset in Fig. 3.6 shows the zoom of permeability data before scaling at low porosities together with the perfectly hexagonal values obtained from lubrication theory [11] (red dashed line) and finite element results [8] (blue stars). The permeability of random fibre arrangements tends to be smaller than for hexagonally ordered arrays. In the next section, my attempt is to extend the lubrication theory for ordered arrays [11] into random configurations.



**Figure 3.6:** Variation of corrected normalized permeability plotted against porosity for different minimum inter fibre distances  $\Delta_{\text{min}}$ , with  $N=800$ . The five arrows show the expected onset of ordering at  $\varepsilon_{\text{order}}^* \approx 0.3$  for decreasing  $\Delta_{\text{min}}$  (from right to left). The dashed blue line shows the empirical merging function, Eq. (3.D.3), in appendix 3.D. The inset shows the low permeability data without scaling at low porosities. The dashed red line and blue stars correspond to the periodic hexagonal cell values of lubrication theory [11] and finite element results [8], respectively.

**Table 3.1:** The values of the critical porosity,  $\varepsilon_{\Delta_{\min}}^{\text{hex}} = 1 - (1 - \varepsilon_{\text{hex}}^*) / (1 + \Delta_{\min})^2$  with  $\varepsilon_{\text{hex}}^* = 1 - \pi / (2\sqrt{3}) \cong 0.0931$ , and permeability (for a perfectly hexagonal lattice,  $K_{\Delta_{\min}}^{\text{hex}} / d^2$ , and corrected permeability for random lattices  $K^c / d^2$ ) at different  $\Delta_{\min}$ .

$\Delta_{\min}$	$\varepsilon_{\Delta_{\min}}^{\text{hex}}$	$K_{\Delta_{\min}}^{\text{hex}} / d^2$	$K^c / d^2$
0.2	0.3702	$1.035 \times 10^{-3}$	$1.7 \times 10^{-3}$
0.1	0.2505	$1.801 \times 10^{-4}$	$4.3 \times 10^{-4}$
0.05	0.1774	$3.172 \times 10^{-5}$	$1.3 \times 10^{-4}$
0.025	0.1368	$5.587 \times 10^{-6}$	$3.5 \times 10^{-5}$
0.005	0.1021	$1.006 \times 10^{-7}$	$2.8 \times 10^{-6}$

### 3.3.5 Summary

In summary, the random generator algorithm used to generate the fibre packing for analysis can affect the local fibre distribution especially at low porosities. All methods used in this study generate isotropic structures with respect to vertical and horizontal direction. The EM approach used has created more heterogeneous packings compared to other methods.

Note that in general, the optimum number of particles (as small as possible but large enough to represent bigger samples) depends on the porosity. Periodic boundary conditions can reduce this number since inhomogeneity at the walls is removed (see appendix 3.B). As standard  $N=800$  was applied and, as before, the permeability is calculated on the center part of the system (see Fig. 3.3).

Putting an artificial gap between fibres ( $\Delta_{\min}$ ) changes the microstructure and accordingly the permeability of the packing, at high volume fractions (small  $\varepsilon$ ). As the main result of this section, correcting the permeability values with the empirical minimal permeability for random structures,  $K^c / d^2$ , leads to perfect scaling (standard deviation discrepancy less than 5%) of all random/disordered structures data for all permeabilities, valid for all  $\Delta_{\min}$ , as shown in Fig. 3.6. Understanding the microscopic origin of this scaling is the subject of the next section.

## 3.4 Theoretical prediction of the permeability

In this section, a microstructural model is presented for predicting the macroscopic permeability based on the lubrication effect of the narrow/effective channels.

### 3.4.1 Statistical characterization of effective channels

Several statistical and structural descriptors, i.e. Delaunay triangulation (DT), Delaunay edges (DE), hydraulic diameter ( $D_h$ ) and fibre/particle nearest neighbor distances  $\langle D_n \rangle$ , obtained from fibre distributions, are discussed here and used to characterize the narrow channels.

#### 3.4.1.1 Nearest neighbor distances

Here I define the mean value of the  $n$ -th nearest neighbor distances  $\langle D_n \rangle$  normalized with the diameter of the fibres  $\gamma_n = (\langle D_n \rangle - d) / d$ . The diameter,  $d$  can be expressed in terms of macroscopic porosity as  $d = \sqrt{4(1-\varepsilon)/(\lambda\pi)}$  where  $\lambda = (1-\varepsilon)/V_p$  is the number density (number of fibers per unit area). The value of  $\lambda$  is 2 in my simulations (800 fibres in a box of  $20 \times 20$  [m<sup>2</sup>]). Similarly, one can define the effective normalized  $n$ -th nearest neighbor distances as  $\gamma_n^* = (\langle D_n \rangle - d^*) / d^*$  with  $d^* = d(1 + \Delta_{\min})$ . The former,  $\gamma_n$ , quantifies the channel width available for flow, while the latter is a measure for the effective distance due to the minimum inter fibre distance, which is relevant for microstructure but not so much for fluid flow.

Fig. 3.7(a) and (b) show the 2<sup>nd</sup> and 1<sup>st</sup> nearest neighbor distances, respectively. Note that the network in Fig. 3.7(b) appears considerably more dilute than that in 7(a). While neither network percolates, when combined the first and second neighbor network does percolate. Flow is less likely to go through the narrowest gaps, but there are sufficient numbers of 2<sup>nd</sup> channels, that the second neighbor distances are likely to control the flow.

#### 3.4.1.2 Normalized hydraulic diameter ( $D_h/d$ )

Another measurable quantity that is frequently used in modeling of porous/fibrous structures is the hydraulic diameter  $D_h$  [1]. When one has obstacles like fibres (or particles) instead of straight pores, the hydraulic diameter can be defined as:

$$D_h = \frac{4\varepsilon V}{S_v} = \frac{4\varepsilon}{(1-\varepsilon)a_v} = \frac{\varepsilon d}{(1-\varepsilon)}, \quad \text{with } a_v = \frac{\text{particle surface}}{\text{particle volume}} = \frac{S_v}{(1-\varepsilon)V} = \frac{4}{d}, \quad (3.6)$$

with the total volume of the unit cell,  $V$ , the total wetted surface,  $S_v$ , and the specific surface area,  $a_v$ . Note that the hydraulic diameter, in this way, is expressed as a function of the measurable quantities porosity and specific surface area. The above value of  $a_v$  is for circles (cylinders) – for spheres one has  $a_v = 6/d$ . Therefore the relation between normalized hydraulic diameter  $D_h/d$  and porosity for fibres will reduce to:

$$\frac{D_h}{d} = \frac{\varepsilon}{(1-\varepsilon)} \quad (3.7)$$

Note that in the following the hydraulic diameter, even though it could be defined per particle or per Delaunay triangle, will only be used as averaged quantity.

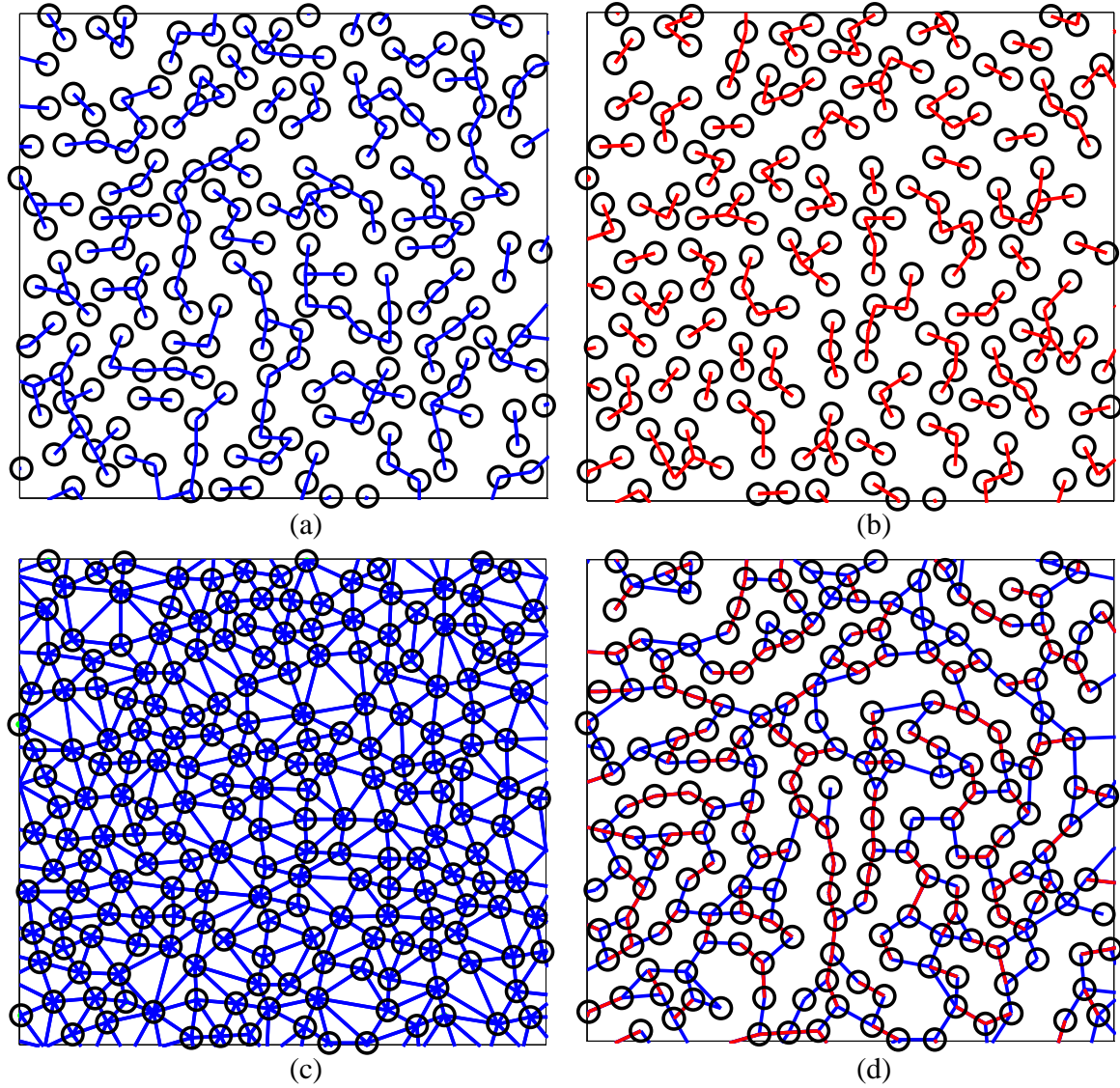


**Figure 3.7:** Various microstructural descriptors used in this study: (a) The 2<sup>nd</sup> and (b) the 1<sup>st</sup> nearest neighbor distances plotted for each fibre. (c) The blue lines delineate the Delaunay triangles. (d) The minimum Delaunay edges plotted for each DT. The red lines show the repeated edges from neighboring triangles. All graphs show the center part of 800 randomly distributed fibres generated by the MC procedure at  $\varepsilon=0.6$  with minimum inter fibre distance  $\Delta_{\min}=0.05$ .

### 3.4.1.3 Delaunay triangulation (DT)

A Delaunay triangulation (DT) is the set of lines joining a set of points such that each point is joined to its nearest neighbors [27]. It satisfies an “empty circle” property, i.e. the circumcircle of each triangle (formed by three points) does not contain any of the other points. It is the dual graph of the Voronoi diagram (VD) and has a node (fibre center) for every Voronoi cell and an edge between two nodes if the corresponding cells share an edge (see Fig. 3.7(c), the blue lines show the DT edges). This concept is suitable for the characterization of the arrangement of dispersed fibres [28]. The DT has many other applications such as finding the nearest neighbor, mesh generation and surface reconstruction, interpolation and extrapolation, strain calculation [29], etc. Here we used the statistics of the Delaunay edges as a descriptor to characterize the spatial dispersion of fibres. One average quantity is the mean value of all DT edge lengths  $\langle e_{DT}^p \rangle$  normalized with the diameter of the fibres  $d$ , i.e.  $\gamma_{DT}^p = (\langle e_{DT}^p \rangle - d) / d$ . For a perfect triangular lattice it reduces to exactly the inter fibre (surface-to-surface) distance and for the lowest porosity  $\varepsilon_{hex}^* = (1 - \pi / (2\sqrt{3}))$  one has  $\gamma_{DT}^p = \Delta_{min}$ .

Similarly, one can find the shortest Delaunay edges for each particle and then average over all particles, i.e. the first,  $\gamma_1^p = (\langle e_1^p \rangle - d) / d$ , the second,  $\gamma_2^p = (\langle e_2^p \rangle - d) / d$ , etc. The numerical results show that  $\gamma_{1,2,3}^p \cong \gamma_{1,2,3}$  (for  $\gamma_1^p \cong \gamma_1$  see Fig. 3.8).

### 3.4.1.4 Delaunay edges (DE)

For a given Delaunay triangulation the local mass conservation implies that in steady state condition the net flow through all the DT edges belonging to one triangle is zero. Therefore, the characteristic length of these edges might also be useful to describe the macroscopic flow field.

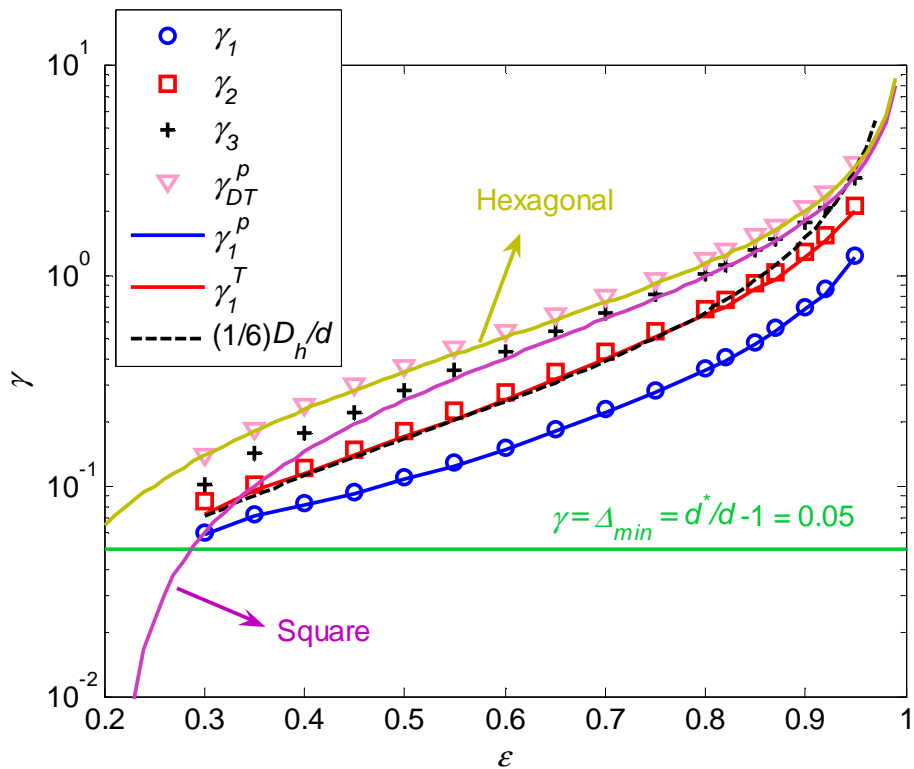
We define  $\gamma_1^T$  as the mean value of the shortest Delaunay edges  $\langle e_1^T \rangle$ , (averaged over Delaunay triangles and not fibres) normalized by the fibre diameter,  $\gamma_1^T = (\langle e_1^T \rangle - d) / d$ .

Fig. 3.7(d) shows these shortest edges. The red color shows the repeated edges of neighboring triangles. Note that the superposition of the network in Fig. 3.7(a) and (b) is very similar to (d) – not shown here. The shortest Delaunay triangle edges form a percolated edge-network, where empty “channels” indicate the regions (channels) in which the fluid is most likely flowing (fast).

Fig. 3.8 shows the variation of all these descriptors as a function of porosity. The normalized mean nearest neighbor distances approach the minimum inter fibre distance (i.e.  $\Delta_{min} \sim 0.05$ ) at low porosities (locally crystalline structure). On the other hand, at high porosities we are reaching the analytical values of random point patterns at  $\varepsilon = 1$ .

As expected, the values obtained by averaging the shortest Delaunay edges for each fibre  $\gamma_1^p$ , match the results of nearest neighbor distances  $\gamma_1$ . Astonishingly, we observe that the mean values of the 2<sup>nd</sup> nearest neighbors  $\gamma_2$  (red squares) approximately match the values of the shortest DT edges  $\gamma_1^T$  (averaged over triangles). So far I have not found a mathematical proof for this observation. For regular (i.e. square or hexagonal) arrays, the statistical descriptors are the same ( $\gamma_1 = \gamma_2 = \gamma_3 = \gamma_1^T$ ) and  $\gamma_1^T$  is thus a deterministic function of porosity, see next section. Interestingly the values of  $\gamma_{DT}^p$  for random and hexagonal arrays are almost the same, showing that the mean value of neighboring fibre distances obtained by averaging over all DE does not depend much on the structure.

Another interesting observation is that for  $\varepsilon < 0.8$  the normalized hydraulic diameter  $D_h/d$  has also the same trend as the shortest Delaunay edges and the 2<sup>nd</sup> nearest neighbor distances<sup>5</sup> and, when scaled by a factor 1/6, even agrees quantitatively well.



**Figure 3.8:** Variation of normalized mean nearest neighbor distances (1<sup>st</sup>, 2<sup>nd</sup> and 3<sup>rd</sup>), the mean length of all Delaunay edges ( $\gamma_{DT}^p$ ), the mean shortest Delaunay edge averaged over particles ( $\gamma_1^p$ ) and triangles ( $\gamma_1^T$ ) and the normalized hydraulic diameter ( $D_h/d$ ) as

<sup>5</sup> This may explain the limitation/failure of capillary models such as the Carman-Kozeny (CK) equation at high porosities which are based on the hydraulic diameter concept.

a function of porosity. Average is taken over 10 realizations with 800 randomly distributed fibres. Only the center part of the system is considered to avoid edge effects.

### 3.4.1.5 Microscopic channel width in terms of macroscopic porosity

Based on a least square fit approach, an empirical expression is obtained for the mean values of the  $n$ -th nearest neighbor distances,  $\gamma_n$  as functions of porosity:

$$\gamma_n = \langle D_n \rangle / d - 1 \quad \text{with} \quad \frac{\langle D_n \rangle}{\langle D_n^p \rangle} = 1 + \varphi_n \left( \frac{1 - \varepsilon}{1 - \varepsilon_c^r} \right)^{\xi_n}, \quad (3.8)$$

where  $\varepsilon_c^r(\Delta_{\min})$  and  $\langle D_n^p \rangle$  are the corresponding critical porosity of a random packing with  $\varepsilon_c^* \cong 0.16$  and mean nearest neighbor distance for random points calculated analytically from Eq. (3.B.1), respectively. The quantities  $\varphi_n$  and  $\xi_n$  are fitting constants for a given  $n$  and, in general, weakly depend on  $\Delta_{\min}$ . The numerical values of  $\langle D_n^p \rangle$ ,  $\varepsilon_c^r$ ,  $\varphi_n$  and  $\xi_n$  for  $n=1, 2, 3$  and various  $\Delta_{\min}$  are given in Table 3.2. Thus, one can easily estimate the  $n$ -th nearest neighbor distances of hard disc packings by only knowing its macroscopic porosity. Fig. 3.9 shows the variation of mean values of the 2<sup>nd</sup> nearest neighbors,  $\gamma_2$  as function of porosity together with the best fits, Eq. (3.8), at different  $\Delta_{\min}$ . At high porosities,  $\Delta_{\min}$  has less effect on  $\gamma_2$ , however, by decreasing porosity,  $\gamma_2$  has larger values at higher  $\Delta_{\min}$  and approaches the limit value  $\gamma_2 = \Delta_{\min}$ . The inset of Fig. 3.9 shows that by plotting the effective  $\gamma_2^* = \langle D_2 \rangle / d^* - 1$  against the effective porosity  $\varepsilon^*$ , all data collapse and one gets the universal curve in Eq. (3.8) with  $\varepsilon_c^r \cong 0.16$ ,  $\varphi_2 \cong 0.35$  and  $\xi_2 \cong 0.7$  corresponding to  $\Delta_{\min}=0$ , i.e.  $\gamma_2^* = \gamma_2$  and  $\varepsilon^* = \varepsilon$ .

One of my hypotheses is that the percolated network of the shortest (triangle) edges,  $\gamma_1^r \cong \gamma_2$ , controls the overall drag (permeability) of the fibrous material (which is confirmed a-posteriori by my numerical results below). However, the microstructure is controlled by  $\gamma_2^*$  which leads to larger excluded volume during packing generation. In the next subsection I will show that, similar to regular fibre arrays [11], these channels between triangles are correlated with the macroscopic permeability of the porous medium for a very wide range of porosities.

**Table 3.2:** The numerical values of  $\varepsilon_c^r = 1 - (1 - \varepsilon_r^*) / (1 + \Delta_{\min})^2$  with  $\varepsilon_r^* \cong 0.16$ ,  $\langle D_n^p \rangle$ ,  $\varphi_n$  and  $\xi_n$  for various  $n$  and  $\Delta_{\min}$  which are obtained analytically from Eq. (3.B.1) and by least square fitting of numerical simulation in the range of  $0.3 < \varepsilon^* < 0.95$ .

$\Delta_{\min}$	$n$	$\varepsilon_c^r$	$\langle D_n^p \rangle$	$\varphi_n$	$\xi_n$
0.2	1	0.4167	0.3535	1.0727	0.7904
	2	0.4167	0.5303	0.3372	0.6790
	3	0.4167	0.6629	0.1049	0.2502
0.1	1	0.3058	0.3535	1.0757	0.7910
	2	0.3058	0.5303	0.3509	0.7048
	3	0.3058	0.6629	0.1065	0.2454
0.05	1	0.2381	0.3535	1.0732	0.7867
	2	0.2381	0.5303	0.3495	0.7017
	3	0.2381	0.6629	0.1064	0.2412
0.025	1	0.2005	0.3535	1.0771	0.7887
	2	0.2005	0.5303	0.3557	0.7084
	3	0.2005	0.6629	0.1099	0.2567
0.005	1	0.1683	0.3535	1.0806	0.7948
	2	0.1683	0.5303	0.3611	0.7314
	3	0.1683	0.6629	0.1123	0.2969



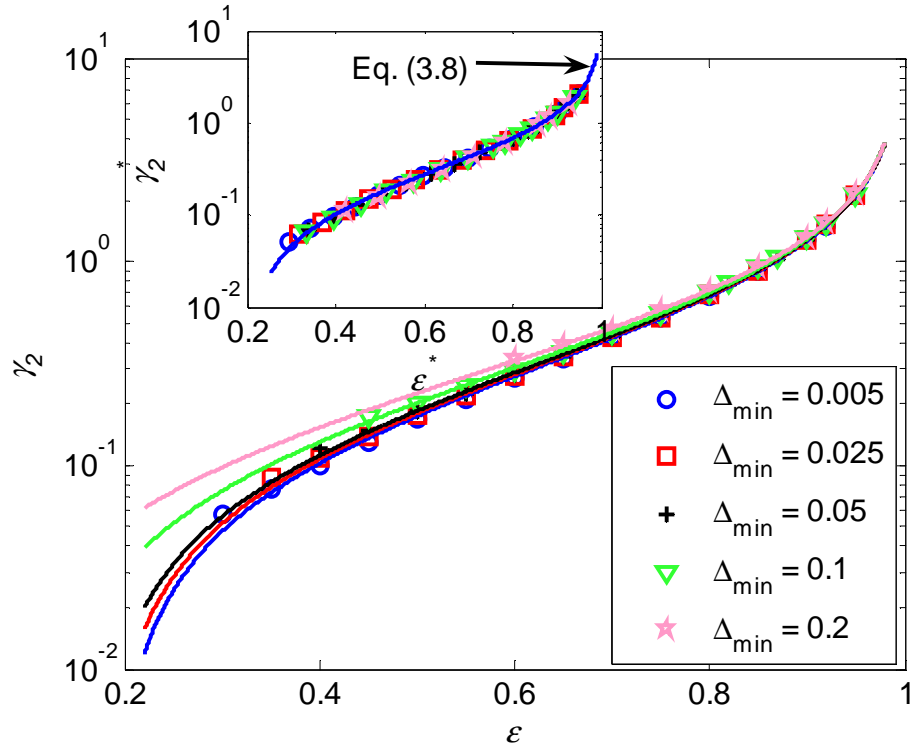


**Figure 3.9:** Variation of mean values of the 2<sup>nd</sup> nearest neighbors,  $\gamma_2$  as function of porosity together with the best fits from Eq. (3.8) (solid lines) at different  $\Delta_{\min}$ . The inset shows the scaled data by plotting  $\gamma_2^*$  as function of effective porosity  $\epsilon^*$ .

### 3.4.2 Permeability prediction in terms of effective channels

Based on the Navier-Stokes equation, Gebart [11] derived the permeability of an idealized unidirectional reinforcement consisting of regularly ordered, parallel fibres both for flow along and for flow perpendicular to the fibres. The solution for flow along fibres has the same form as the CK equation [13], while the solution for transverse flow has a different form as:

$$\frac{K}{d^2} = C \left( \sqrt{\frac{1-\epsilon_c}{1-\epsilon}} - 1 \right)^{2.5}, \quad (3.9)$$

where  $\epsilon_c$  is the critical porosity below which there is no permeating flow and  $C$  is a geometric factor ( $C = \frac{4}{9\pi\sqrt{2}} \cong 0.1$ ,  $\epsilon_c = 1 - \frac{\pi}{4} \cong 0.2146$  for a square array and  $C = \frac{4}{9\pi\sqrt{6}} \cong 0.0578$ ,  $\epsilon_c = 1 - \frac{\pi}{2\sqrt{3}} \cong 0.0931$  for a hexagonal array [8]). Gebart [11]

presents numerical results, obtained using a finite difference solution of the NS equations that show excellent agreement with Eq. (3.9) up to porosities of  $\sim 0.65$ .

In order to rewrite Eq. (3.9) in terms of  $\gamma_2$ , we express the porosity as function of the lattice distance  $a$  and fiber-diameter  $d$ :

$$\begin{cases} 1-\varepsilon = \frac{\pi}{2\sqrt{3}}\left(\frac{d}{a}\right)^2 = (1-\varepsilon_c)\left(\frac{d}{a}\right)^2, & \text{for hexagonal arrays} \\ 1-\varepsilon = \frac{\pi}{4}\left(\frac{d}{a}\right)^2 = (1-\varepsilon_c)\left(\frac{d}{a}\right)^2, & \text{for square arrays} \end{cases} \Rightarrow \sqrt{\frac{1-\varepsilon_c}{1-\varepsilon}} = \frac{a}{d}. \quad (3.10)$$

For regular arrays  $\gamma_1 = \gamma_2 = \gamma_3 = \gamma_1^T$ , whereas for random arrays  $\gamma_2 \simeq \gamma_1^T$  (see Fig. 3.8), so that  $\gamma_2 = \langle D_2 \rangle / d - 1$  can be written in terms of the lattice distance as:

$$\gamma_2 = \left(\frac{a}{d}\right) - 1. \quad (3.11)$$

Inserting Eq. (3.11) into Eq. (3.10) and combining it with Eq. (3.9), leads to:

$$\frac{K}{d^2} = C\gamma_2^{2.5}, \quad (3.12)$$

as exactly valid for regular square or hexagonal arrays at low and moderate porosities with corresponding  $C$ , see above.

In this representation, the normalized permeability scales with the (for example 2<sup>nd</sup>) narrowest channels, i.e.  $\gamma_2$ , as a power law with power 2.5. Relation (12) is remarkable, since it enables one to accurately determine the macroscopic permeability of a given packing just by measuring the 2<sup>nd</sup> narrowest channels, i.e.  $\gamma_2$ , from particle positions or the narrowest Delaunay edges, i.e.  $\gamma_1^T$ , from Delaunay triangles. Below, I numerically confirm the validity of Eq. (3.12) for both regular and also random configurations.

The shortest Delaunay edges and the 2<sup>nd</sup> neighbor distances practically coincide and form the network of channels through which the flow must go. Therefore, I expect that the parameter, which characterizes the system and correlates with the permeability, is  $\gamma_1^T$  or  $\gamma_2$ . Fig. 3.10 shows the variation of the normalized permeability as a function of the statistical descriptors discussed in Section 3.3. Each data point represents the results for 800 randomly distributed fibres, averaged over 10 realizations. The largest and smallest  $\gamma$  correspond to the porosity  $\sim 0.95$  and  $\sim 0.3$ , respectively. The macroscopic permeability almost correlates with the shortest Delaunay triangle edges as a power law, similar to Eq. (3.12) for regular arrays, in a wide range of porosity. The solid blue line is the best power law fit (with fixed power 2.5). The universal random configuration pre-factor ( $C \sim 0.2$ )

seems to be only weakly dependent on the minimum inter fibre distance, data not shown. With decreasing porosity the data deviate from the solid line showing the appearance of ordering in the structure. By correcting Eq. (3.12) as

$$\frac{K}{d^2} = C\gamma_2^{2.5}\chi(\gamma_2) \quad \text{with} \quad \chi(\gamma_2) = (1 - \chi_0 e^{-m\gamma_2}), \quad \chi_0 \cong 0.5, \quad m \cong 3, \quad (3.13)$$

we now present a universal law for predicting the macroscopic permeability in terms of  $\gamma_2$  (with Eq. (3.8) as closing relation with porosity) in a wide range of porosities ( $0.3 < \varepsilon^* < 0.95$ ) for disordered arrays. The exponential correction factor,  $\chi(\gamma_2)$  was obtained by least square fitting the ratio between numerical data and Eq. (3.12) and accounts for (partial) ordering effects. This observation is remarkable as it indicates that the Gebart lubrication theory (Eq. (3.12)), originally obtained for dense ordered arrays, is also valid for random arrays in moderate and dilute regimes by using the  $\gamma_2$  or  $\gamma_1^T$  as the effective channel width. Fig. 3.11 shows the variation of the normalized permeability as function of  $\gamma_2$  at different values of  $\Delta_{\min}$  together with the proposed closed form relations in Eqs. (3.12) and (3.13). In contrast to Fig. 3.6, here, the permeability data are not corrected by  $K_c$ , but are collapsed as the microscopic effective channel width  $\gamma_2 = \gamma_2(\gamma_2^*)$  takes care of the effect of  $\Delta_{\min}$ . For all values of  $\Delta_{\min}$ , Eq. (3.13) correctly predicts the macroscopic permeability with maximum deviation of 10% for  $\varepsilon^* > 0.3$ . The permeability values for square and hexagonal configurations have the same power/slope and just shifted as they have different pre-factors,  $C$ , see Eq. (3.9). More discussion on very dense regimes, i.e.  $\varepsilon^* < 0.3$ , where we have long range correlations due to partial up to strong ordering, is given in appendix 3.C. For comparison, the analytical prediction for ordered arrays (square and hexagonal configurations), i.e. Eq. (3.12) with the same power 2.5 but different constants  $C$ , are also shown. As an alternative to the microstructural model presented in Eq. (3.13), I propose a purely empirical merging function which combines the analytical solutions of dilute and dense limit cases in appendix 3.D.

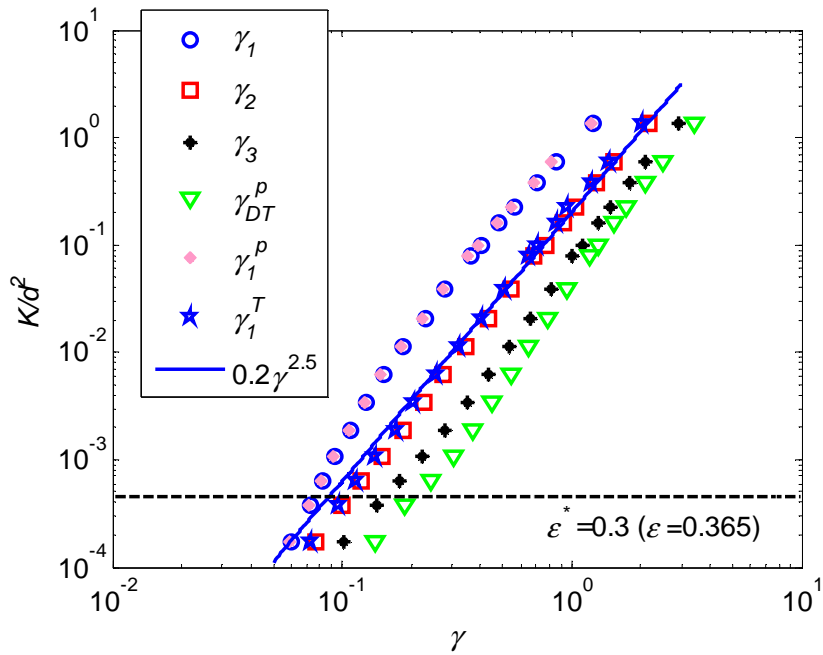


**Figure 3.10:** Variation of normalized permeability, plotted as function of various statistical descriptors. 2<sup>nd</sup> nearest neighbor distance  $\gamma_2$  (or shortest Delaunay edges,  $\gamma_1^T$ ) show the best (almost power law) correlation in a wide range of porosity at  $\Delta_{\min}=0.05$ . The solid blue line shows the power law fit.

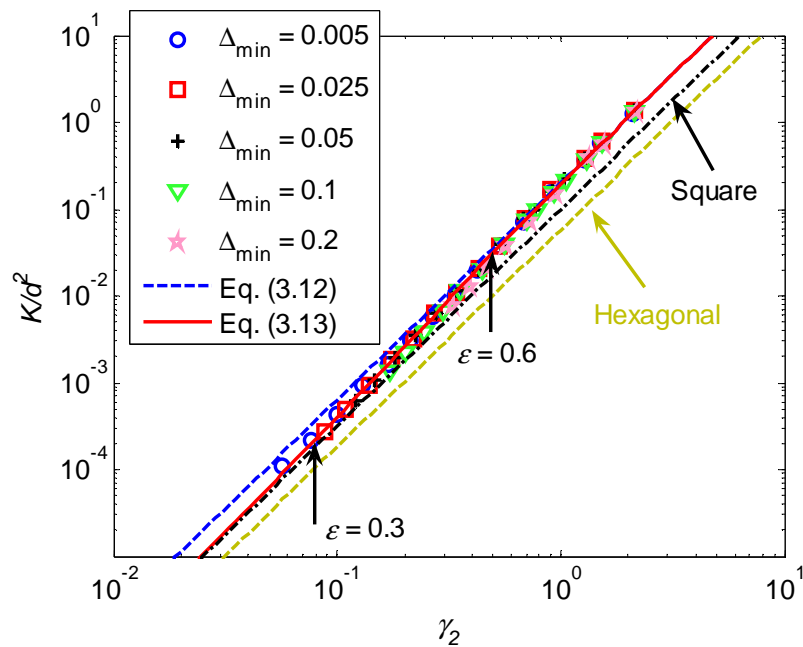


**Figure 3.11:** Variation of normalized permeability as function of mean value of 2<sup>nd</sup> nearest neighbor distance,  $\gamma_2$  at different values of  $\Delta_{\min}$ .

### 3.5 Summary and conclusions

A finite element method (FEM) based model has been employed to calculate the transverse permeability of random fibrous media composed of long unidirectional cylinders/fibres for a wide range of porosity. The microstructure of the fibrous media has been characterized using the pair distribution function and neighbor distance statistics. Providing information about short range correlations, these microstructure descriptors allow us to characterize the spatial heterogeneity of the fibre structures, construct computer generated microstructures for further simulation, or correlate the material microstructure to macroscopic properties as, e.g., permeability. The conclusions from my statistical analysis of the microstructures and the permeability are:

- For relatively large systems, the packings obtained from different random generator algorithms are isotropic and homogenous (far away from the walls). Their properties are similar and independent of the system size, except for the energy minimization (EM) approach, which generates clustered structures. Periodic boundary conditions reduce the minimum required number of fibres to reach size-independence.
- By increasing porosity, the PDF of nearest neighbor distances will change from exponential to Gaussian, as relevant for random point patterns only, not shown here.
- The packings with higher inter fibre distance,  $\Delta_{\min}$ , have more uniform and weaker flow channels and therefore higher permeability and the behavior is determined by  $\varepsilon^* = f(\varepsilon, \Delta_{\min}) = 1 - (1 - \varepsilon)(1 + \Delta_{\min})^2$ .
- All random structure permeability data (for all studied minimal inter-fibre distances) are scaled by subtracting the random packing minimal permeability  $K^c/d^2 \simeq \eta K_{\Delta_{\min}}^{\text{hex}}/d^2$  that is proportional to the equivalent minimum of a regular structure and a pre-factor that increases with decreasing minimal distance. The low porosity random regime cannot be reached, since partial ordering sets in below a certain threshold ( $\varepsilon^* \simeq 0.3$ ).

Based on the lubrication effect of the narrow channels, I found a universal power law relationship between the permeability values obtained from fluid flow simulations and the microscopic mean values of shortest Delaunay triangulation edges constructed on the fibre center positions. From the microscopic point of view, the numerical results show that the mean values of the 2<sup>nd</sup> nearest neighbors  $\gamma_2 = (\langle D_2 \rangle - d)/d$  (averaged over all fibres) match the values of shortest DT edges  $\gamma_1^T = (\langle e_1^T \rangle - d)/d$  (averaged over all triangles). Astonishingly, the proposed power law is valid for both ordered and disordered arrays at all porosities, given a correction dependent only on  $\gamma_2$ . The superposition of 1<sup>st</sup> and 2<sup>nd</sup> nearest neighbor channels forms a similar percolated network

as the shortest DT edges, with average  $\gamma_1^T$ , which dominate the flow since they represent the fluid channels through which the flow must go (with preference for the wider 2<sup>nd</sup> neighbor channels).

In summary, a closed form relation for predicting the macroscopic permeability for ordered/disordered fibre arrangements is observed in terms of the microstructural average channel width  $\gamma_2$  as  $K/d^2 = C\gamma_2^{2.5}(1 - \chi_0 e^{-m\gamma_2})$ , valid for wide range of porosities and all values of inter-fibre distance  $\Delta_{\min}$ . Note that Eq. (3.8) relates  $\gamma_2 = \gamma_2(\gamma_2^*)$  with  $\gamma_2^* = \gamma_2^*(\varepsilon^*)$  and  $\varepsilon^* = \varepsilon^*(\varepsilon)$  to macroscopic porosity and therefore closes this relation.

The results obtained in this study and the general relationships proposed for the permeability, can be utilized for composite manufacturing, e.g. resin transfer moulding processes. Furthermore, these results can be used for validation of advanced models for particle-fluid interactions in a multi-scale coarse graining approach, as carried out in my ongoing work. By analogy, the permeability in 3D random packings should depend on the smallest faces of Delaunay tetrahedrons  $\gamma_1^{T3D}$ , possibly with the chance for similar unique scaling relations as in 2D, a prediction that waits for numerical/experimental proof.

### Acknowledgements:

The authors would like to thank M. van der Hoef, A. J. C. Ladd, C. S. O'Hern, X. Chen, K.W. Desmond and A.R. Thornton for helpful discussion and acknowledge the financial support of STW through the STW-MuST program, Project Number 10120.

### Appendix 3.A Mesh sensitivity analysis

Due to the difference in scale between domain size and gap size between neighboring fibers, this typically requires local mesh refinement. For different porosities, flow through random fiber arrangements was simulated at different mesh resolutions (number of elements,  $N_e$ ). The dependence of the solution in terms of the calculated normalized permeability at dense,  $\varepsilon = 0.4$  (in blue) and dilute,  $\varepsilon = 0.8$  (in red) regimes is shown in Fig. 3.A1. At larger porosities (dilute systems) fewer numbers of elements would be sufficient to get convergent solution. The numerical results show that in all simulations one need at least  $\sim 10$  rows of elements between neighboring particles to correctly capture the fluid behavior and obtain a converging solution.

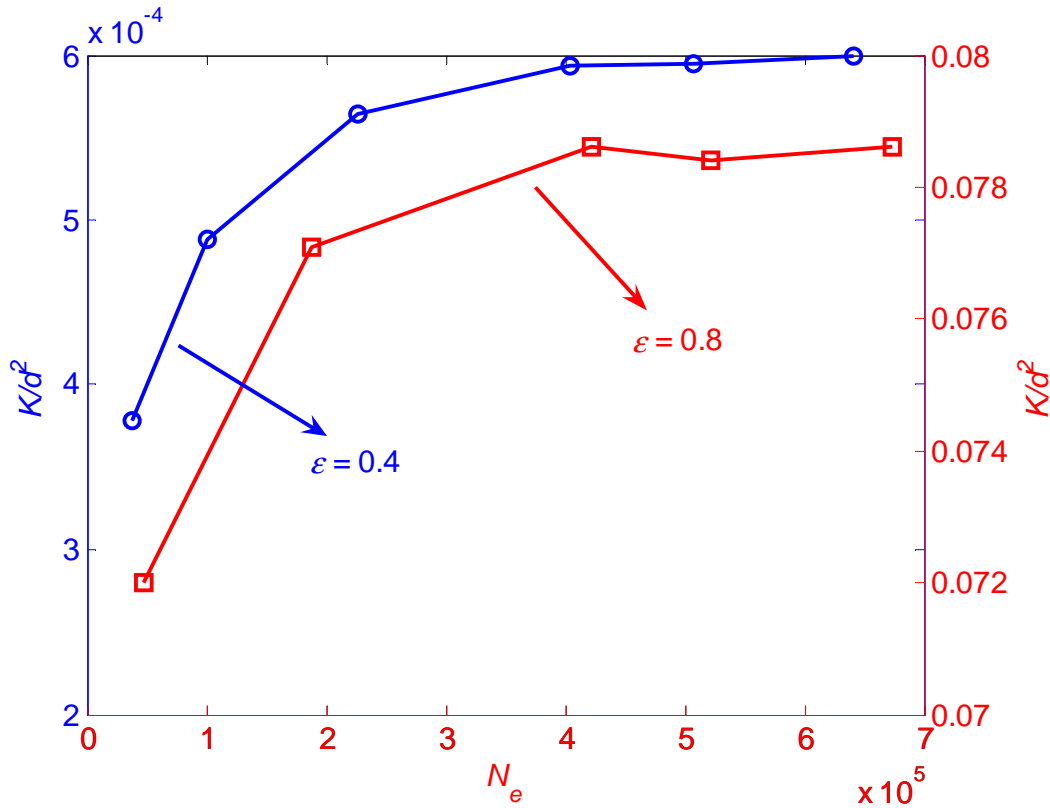


**Figure 3.A1:** Plot of normalized permeability for different resolutions (number of elements,  $N_e$ ) at porosity  $\varepsilon = 0.4$  (in blue) and  $\varepsilon = 0.8$  (in red).

### Appendix 3.B Study of the system size (edge) effects

The random fibrous structure should be large enough to capture the microscopic properties and/or the flow characteristics in the matrix. Increase in the system area implies a linear increase in the number of grid points in the computational mesh. Therefore, we need to find an optimum system size. Related to this, Grufman and Ellyin [30] determined a representative volume element size for composite laminate by applying the Kolmogorov goodness-of-fit test. Du and Ostoja-Starzewski [31] studied the finite-size scaling trend to RVE of the Darcy law for Stokesian flow in random porous media without invoking any periodic structure assumptions, but only assuming the microstructure's statistics to be spatially homogeneous and ergodic. They show that the higher the density of random disks, the smaller the size of RVE pertaining to Darcy's law. Trias et al. [32] show that the minimum system size for typical carbon fibre polymer composites is  $\Omega = L/d = 25$  (where  $d$  and  $L$  are the actual diameter of fibres and system length, respectively).

To study the effect of system size, I use two statistical tools, namely the pair distribution function and the nearest neighbor distance, both measure short range correlations. The so-called "structure factor" for long range correlations is not addressed here.

### 3.B.1 Pair distribution function $g(r)$

In Fig. 3.B1 the pair distribution function ( $g(r)$ ) is plotted for different numbers of fibres at the two cases of (a) low porosity (dense system)  $\varepsilon=0.4$  and (b) dilute system  $\varepsilon=0.9$ . At higher porosities, we observe that by using only the center part-away from the walls/boundaries, there is no systematic size dependence concerning short range order and increasing  $N$  does not create any substantial differences in  $g(r)$ . However, for dense systems, the correlations reach to larger and larger distances and one needs a bigger system so that the order does not “reach” the walls. The exponential decrease in the local peaks of  $g(r)$  at higher densities might explain the exponential distribution of nearest neighbor distances in the next subsection. The same trend was observed for periodic boundaries as the center area was used to calculate  $g(r)$  (data are not shown here).

Note that by knowing the optimum number of fibres, one can easily calculate the optimum system size as  $\Omega = L/d = \sqrt{N\pi/(4(1-\varepsilon))}$  since  $(1-\varepsilon) \equiv V_p/V = N\pi d^2/(4L^2)$  with the volume of a single particle  $V_p$ .

The pair distribution function,  $g(r)$ , is useful in describing short- and medium- range averaged correlations among the fibres.

### 3.B.2 Nearest neighbor distance

Nearest-neighbor distances are an essential class of spatial descriptors useful in materials science and other disciplines [33, 34]. They are well established as a tool for qualitatively characterizing deviation from a “random” state. Given a set of points (fibre centers), the nearest neighbor distance distribution function for the  $n$ -th nearest neighbor is the probability density function  $\psi_n(r)$  such that  $\psi_n(r)dr$  is the probability of finding the  $n$ -th nearest neighbor ( $n=1,2,3,\dots$ , etc.) in the distance range  $r$  to  $(r+dr)$ .



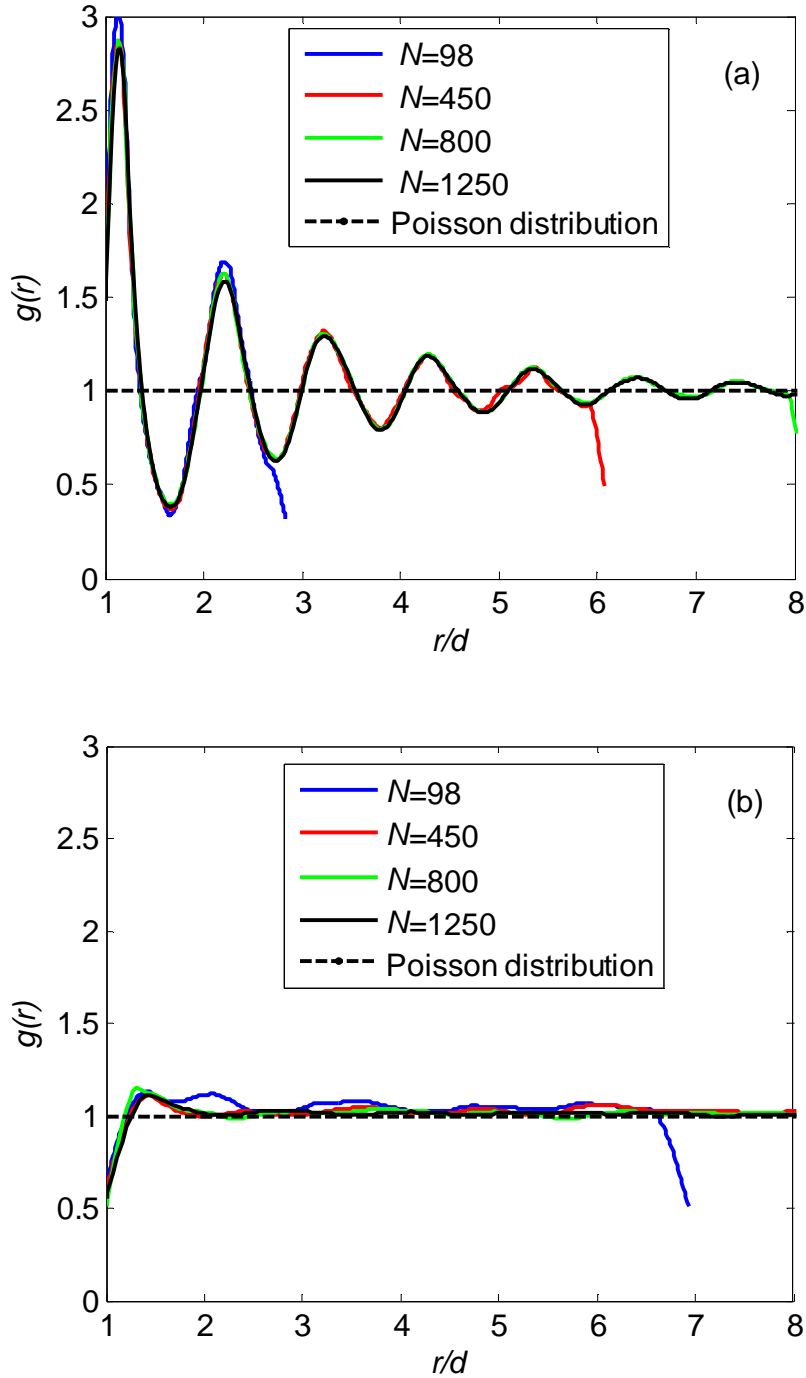


**Figure 3.B1:** Plot of  $g(r)$  for different number of fibres (system size) at (a) porosity  $\varepsilon = 0.4$  and (b)  $\varepsilon = 0.9$  from 10 realizations. The dashed line at  $g(r) = 1$  indicates a completely random point structure. The drop of the data comes from the finite size of the center area used for averaging (see Fig. 3.3).

The analytical prediction for the mean value of the  $n$ -th nearest neighbor distance  $\langle D_n^p \rangle$  is the first moment of the distribution function  $\psi_n(r)$ , and for the uniform random spatial distribution of points is:

$$\langle D_n^p \rangle = \frac{\Gamma(n+1/2)}{\sqrt{\pi}(n-1)!\lambda^{1/2}}. \quad (3.B.1)$$

where  $\lambda = (1-\varepsilon)/V_p$  is the intensity (number of points per unit area) and  $\Gamma(n+1/2)$  is the gamma function<sup>6</sup>. While formulae have been derived that place bounds on  $\langle D_n^p \rangle$  for equilibrium ensembles of monodisperse particles in two- and three-dimensions [29], exact analytical expressions are not available. Therefore, computer simulations are needed to calculate the mean value of the  $n$ -th nearest neighbor distances as a function of porosity (or volume fraction) for ensembles of mono(poly)disperse fibres, e.g. see Eq. (3.8). For more details see Section 3.4.1, where, among others, the mean normalized 1<sup>st</sup> and 2<sup>nd</sup> nearest neighbor distances are used to characterize the effective/narrow channels and predict the sample permeability.

The 1<sup>st</sup> nearest neighbor distance,  $D_1^p$ , is simply the minimum of all distances from one fibre to all others. Similar to the  $g(r)$  data, at low porosities one needs more fibres (bigger systems) to get reasonable statistics for the distribution of short-range distances ( $N > 800$ ). However at high porosities, increasing the number of fibres will not much affect the probability distribution function (PDF). The distributions of 1<sup>st</sup> nearest neighbor distances were found to follow the exponential distribution at low porosities and normal (Gaussian) distribution at high porosity. By increasing the porosity the PDF of nearest neighbor distances will change from exponential to Gaussian, i.e. a random point patterns. Furthermore, by decreasing the porosity (i.e. going from 0.9 to 0.6), the probability of finding a particle at exactly  $1.05d$  (i.e. minimum possible distance) becomes  $\sim 10$  times larger (data not shown).

### 3.B.3 Wall versus periodic boundaries

Another factor that not only affects the fibre distribution but also the macroscopic permeability of the medium is the confining walls. In Fig. 3.B2 the normalized permeability is plotted against number of fibres for different boundary conditions (periodic or walls at top and bottom of the cell) at (a)  $\varepsilon = 0.4$  and (b)  $\varepsilon = 0.9$ . It shows that at low porosity, using the periodic boundary conditions can reduce the minimum required number of fibres ( $N > 200$ ). However, at high porosities the permeability becomes independent of the number of fibres for  $N > 200$  in both periodic and wall boundary conditions. It turns out that for systems with more than 800 fibres/cylinders the effect of

---

<sup>6</sup> Note that the real unidirectional composite microstructures consist of distribution of aligned fibres of “finite” size that cannot be regarded as zero dimensional points.

finite size and type of boundary conditions (periodic/no-slip/symmetric) on the permeability of the given structure diminishes.

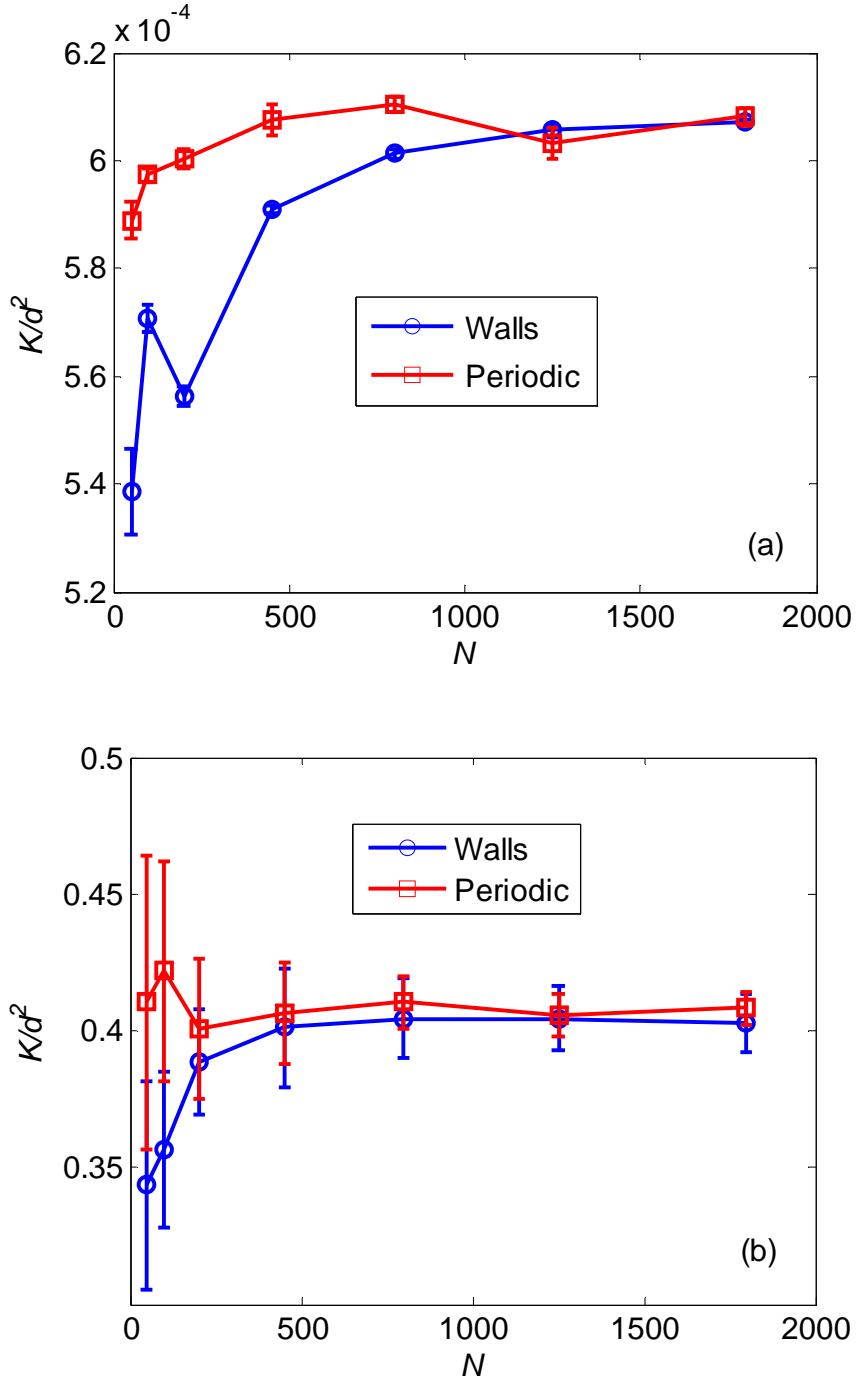


**Figure 3.B2:** Variation of normalized permeability plotted against number of fibres with different boundary conditions at (a) porosity  $\varepsilon = 0.4$  and (b)  $\varepsilon = 0.9$ . Fibre distributions generated by MC procedure with  $10^4$  perturbations and minimum inter fibre distance  $\Delta_{\min} = 0.05$ .

### Appendix 3.C Towards the dense regime

In order to have a better model for the very dense regime, i.e.  $\varepsilon^* < 0.3$ , we correct the original lubrication theory for perfectly hexagonal arrays, i.e. Eq. (3.9), in this appendix.

As mentioned in Section 3.4, the critical porosity obtained from computer simulations for the finite systems with walls is limited to  $\varepsilon_c^r \cong 0.16$  [26]. By correcting the lubrication theory of hexagonal arrays with  $\varepsilon_c^r = 0.16$ , one can predict the permeability at the random close packed limit more accurately as:

$$\frac{K - K^c}{d^2} = C^* \left( \sqrt{\frac{1 - \varepsilon_c^r}{1 - \varepsilon}} - 1 \right)^{2.5}. \quad (3.C.1)$$

where  $C^* \sim 0.035$  is obtained by fitting to the FEM results at low porosities. Fig. 3.C1 shows the variation of the normalized permeability as a function of porosity. Note that as I scale the data with  $K^c$ , the permeability values for different  $\Delta_{\min}$ , see the blue squares and the red triangles, collapse onto a single curve. As expected, Eq. (3.13), the proposed model based on shortest DT edges  $\gamma_1^T$  (or 2<sup>nd</sup> nearest neighbor distances,  $\gamma_2$ ) is valid at moderate and high porosities (i.e. the range of interest in composites manufacturing,  $\varepsilon^* \geq 0.3$ ), see the solid blue line. However, at very dense regime, i.e.  $\varepsilon^* < 0.3$ , Eq. (3.C.1) fits better to my FE results, see the solid red line. For comparison, the analytical prediction for ordered arrays (square and hexagonal configurations), i.e. Eq. (3.12) is also shown with dashed lines.

### Appendix 3.D Purely empirical, macroscopic permeability-porosity relation based on asymptotic solutions

In this appendix, based on analytical predictions of permeability for dilute and dense regimes, I present an empirical macroscopic relation for the permeability in terms of macroscopic porosity. Based on a unit cell approach, Drummond and Tahir [10] modeled analytically the flow around a fiber and obtained (applicable at high porosities):

$$\frac{K_D}{d^2} = \frac{1}{32(1-\varepsilon)} \left( -\ln(1-\varepsilon) - 1.497 + 2(1-\varepsilon) - \frac{(1-\varepsilon)^2}{2} - 0.739(1-\varepsilon)^4 + \frac{2.534(1-\varepsilon)^5}{1+1.2758(1-\varepsilon)} \right). \quad (3.D.1)$$

Similar to Ref. [8] and using the linear least square method, the linear correction,  $g(\varepsilon)$  to the Drummond relation, leads to a corrected permeability for  $\varepsilon > 0.7$  as:

$$K_{CD} = d_1 K_D (1 + d_2 \varepsilon), \quad \text{with} \quad d_1 = 0.97, \quad d_2 = 0.18, \quad (3.D.2)$$

with a maximum error of less than 5%. Similarly, the corrected lubrication theory of hexagonal arrays,  $K_G/d^2 = C^* \left( \sqrt{\frac{1-\varepsilon_c^r}{1-\varepsilon}} - 1 \right)^{2.5}$  in Eq. (3.C.1) is valid with maximum discrepancy of less than 5% at low porosities,  $\varepsilon < 0.5$ . To combine these two limit cases, I propose the following empirical merging function:

$$K = K_G + (K_{CD} - K_G) p(\varepsilon) \text{ with } p(\varepsilon) = \frac{1 + \tanh\left(\frac{(\varepsilon - \varepsilon_h)}{\varepsilon_t}\right)}{2}, \varepsilon_h \cong 0.67, \varepsilon_t \cong 0.1, \quad (3.D.3)$$

that is valid for the whole range of porosity, with maximum deviations of less than 5% that also includes the analytical relations for the limit cases, see the dashed blue line in Fig. 3.6. While the choice of  $p(\varepsilon)$  is arbitrary, the nonlinear least square fitting procedure is used to obtain the empirical coefficients  $\varepsilon_h$  and  $\varepsilon_t$ .

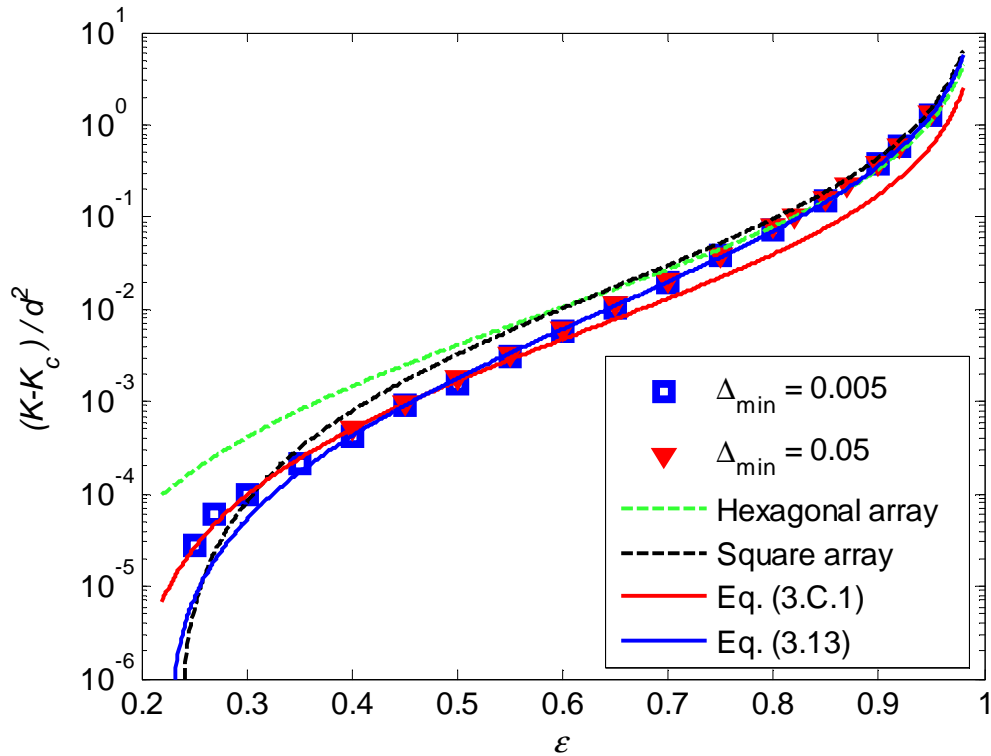


**Figure 3.C1:** Variation of scaled normalized permeability plotted against porosity.

## References

- [1] R.B. Bird, W.E. Stewart and E.N. Lightfoot, *Transport Phenomena*, 2nd edn., John Wiley & Sons, 2001.
- [2] K. Yazdchi, S. Srivastava, and S. Luding, Multi-Scale permeability of particulate and porous media, *Proceedings of World Congress Particle Technology 6*, Nürnberg Messe GmbH (Ed.), 2010, ISBN-978-3-00-030570-2.
- [3] X. Chen, T.D. Papathanasiou, The transverse permeability of disordered fiber arrays: A statistical correlation in terms of the mean nearest inter fiber spacing, *Transport in Porous Media*, 71 (2008) 233-251.
- [4] X. Chen, T.D. Papathanasiou, On the variability of the Kozeny constant for saturated flow across unidirectional disordered fibre arrays, *Composites: Part A*, 37 (2006) 836–846.
- [5] T.D. Papathanasiou, A structure-oriented micromechanical model for viscous flow through square arrays of fiber clusters, *Composites Science and Technology*, 56 (1996) 1055-1069.
- [6] Y.S. Song, K. Chung, T.J. Kang, J.R. Youn, Prediction of permeability tensor for three dimensional circular braided preform by applying a finite volume method to a unit cell, *Compos. Sci. Technol.*, 64 (2004) 1629–1636.
- [7] N. Takano, M. Zako, T. Okazaki and K. Terada, Microstructure-based evaluation of the influence of woven architecture on permeability by asymptotic homogenization theory, *Compos. Sci. Technol.*, 62 (2002) 1347-56.
- [8] K. Yazdchi, S. Srivastava and S. Luding, Microstructural effects on the permeability of periodic fibrous porous media, *Int. J. Multiphase Flow*, 37 (2011) 956-66.
- [9] D.L. Koch, J.F. Brady, The effective diffusivity of fibrous media, *AIChE J.*, 32 (1986) 575–591.
- [10] J.E. Drummond and M.I. Tahir, Laminar viscous flow through regular arrays of parallel solid cylinders, *Int. J. Multiphase Flow*, 10 (1984) 515-40.
- [11] B.R. Gebart, Permeability of Unidirectional Reinforcements for RTM, *Journal of Composite Materials*, 26 (1992) 1100–33.
- [12] P.C. Carman, Fluid flow through granular beds, *Transactions of the Institute of Chemical Engineering*, 15 (1937) 150–66.
- [13] T.G. Gutowski, T. Morigaki and Z. Cai, The Consolidation of Laminate Composites, *Journal of Composite Materials*, 21 (1987) 172-188.

- [14] M.V. Brusckhe and S.G. Advani, Flow of generalized Newtonian fluids across a periodic array of cylinders, *Journal of Rheology*, 37 (1993) 479-98.
- [15] B. Astroem, R. Pipes, S. Advani, On flow through aligned fiber beds and its application to composite processing, *J. Composite Materials*, 26 (1992) 1351–73.
- [16] A.J. Katz, A.H. Thompson, Quantitative prediction of permeability in porous rocks, *Phys. Rev. B*, 34 (1986) 8179–81.
- [17] K. Yazdchi, S. Luding, Towards unified drag laws for inertial flow through fibrous materials, *CEJ*, 207 (2012) 35-48.
- [18] R. Dickman, J.S. Wang and I. Jensen, Random sequential adsorption: Series and virial expansions, *J. Chem. Phys.*, 94 (1991) 8252-58.
- [19] E. L. Hinrichsen, J. Feder and T. Jøssang, Geometry of random sequential adsorption, *J. Stat. Phys.*, 44 (1986) 793-827.
- [20] X. Chen, T.D. Papathanasiou, Micro-scale modeling of axial flow through unidirectional disordered fiber arrays, *Compos. Sci. Technol.*, 67 (2007) 1286–93.
- [21] K.W. Desmond and E.R. Weeks, Random close packing of disks and spheres in confined geometries, *PRE*, 80 (2009) 051305.
- [22] S. Luding, Cohesive frictional powders: Contact models for tension, *Granular Matter*, 10 (2008) 235-246.
- [23] R. Pyrz, Quantitative description of the microstructure of composites. Part I: morphology of unidirectional composite systems, *Composites Science and Technology*, 50 (1994) 197-208.
- [24] I. Schenker, F.T. Filser, L.J. Gauckler, T. Aste, H.J. Herrmann, Quantification of the heterogeneity of particle packings, *PRE*, 80 (2009) 021302.
- [25] A. S. Sangani and C. Yao, Transport processes in random arrays of cylinders. II. Viscous flow, *Phys. Fluids*, 31 (1988) 2435-44.
- [26] James G. Berryman, Random close packing of hard spheres and disks, *Phys. Rev. A*, 27 (1983) 1053–1061.
- [27] A. Okabe, B. Boots and K. Sugihara, *Spatial Tessellations: Concepts and Applications of Voronoi Diagrams*, Wiley, Chichester, UK, 1992.
- [28] Ascânio D. Araújo, Wagner B. Bastos, José S. Andrade, Jr., and H.J. Herrmann, Distribution of local fluxes in diluted porous media, *PRE*, 74 (2006) 010401.

- [29] O. Duran, N.P. Kruyt and S. Luding, Analysis of three-dimensional micro-mechanical strain formulations for granular materials: evaluation of accuracy, *Int. J. of Solids and Structures*, 47 (2010) 251-260.
- [30] C. Grufman, F. Ellyin, Determining a representative volume element capturing the morphology of fibre reinforced polymer composites, *Composites Science and Technology*, 67 (2007) 766–775.
- [31] X. Du and M. Ostoja-Starzewski, On the size of representative volume element for Darcy law in random media, *Proc. R. Soc. A*, 462 (2006) 2949–2963.
- [32] D. Trias , J. Costa, A. Turon, J.E. Hurtado, Determination of the critical size of a statistical representative volume element (SRVE) for carbon reinforced polymers, *Acta Materialia*, 54 (2006) 3471–3484.
- [33] A.R. Melro, P.P. Camanho, S.T. Pinho, Generation of random distribution of fibres in long-fibre reinforced composites, *Compos. Sci. Technol.*, 68 (2008) 2092–2102.
- [34] S. Torquato, *Random heterogeneous materials – microstructure and macroscopic properties*. Springer-Verlag, New York, 2002.



# 4

## Upscaling the transport equations: Microstructural analysis

*"Imagination is more important than knowledge"*  
*~ Albert Einstein ~*

## Abstract

Owing largely to multiscale heterogeneity in the underlying fibrous structure, the physics of fluid flow in fibrous media is incredibly complex. This is particularly important in the hydrologic sciences wherein all geologic formations are heterogeneous over a hierarchy of scales in space, and from a process perspective, in time as well.

The microstructure at various porosities has a strong effect on the transport properties, such as permeability, of fibrous materials. In this chapter, several order parameters, based on Voronoi and Delaunay tessellations, are introduced to characterize the microstructure of randomly distributed non-overlapping fibre arrays. In particular, by analyzing the mean and the distribution of the topological and metrical properties of Voronoi polygons, we observe a smooth transition from disorder to order, controlled by the effective packing fraction. Using fully resolved finite element (FE) simulations of Newtonian, incompressible fluid flow perpendicular to the fibers, the macroscopic permeability is calculated in creeping flow regimes. The effect of fibre arrangement and local crystalline regions on the macroscopic permeability is discussed in detail. A simple microstructural model based on the lubrication theory of narrow channels is presented and its validity and limitations are highlighted.

Finally, I verify the validity of macroscopic Darcy's law at various length scales, using both uniform and nonuniform Voronoi/Delaunay cells, in a wide range of porosities. In this hierarchical upscaling method, the system is divided into a recursive hierarchy of cells. At each cell size, the average value and probability distributions of macroscopic quantities, such as superficial fluid velocity and macroscopic permeability, are obtained and compared with the macroscopic permeability in Darcy's law.<sup>1</sup>

## Highlights

- I relate the macroscopic flow properties to microscopic fibre arrangements.
- Several statistical properties of Voronoi polygons and Delaunay triangulation, constructed using the centers of the fibres, are used to characterize the microstructure.
- The same data structure is used for coarse graining the fluid velocity and pressure gradient.
- I verify the validity of Darcy's law at various length scales.

---

<sup>1</sup> K. Yazdchi and S. Luding, Fibrous materials: Microstructure and macroscopic properties, (2012) in preparation.

K. Yazdchi and S. Luding, Upscaling the transport equations in fibrous media, ECCOMAS (2012), 2 pages, Vienna, Austria.

## 4.1 Introduction

Fluid flow through fibrous materials has a wide range of applications including, composite materials, fuel cells, heat exchangers, (biological)filters and transport of ground water and pollutants [1]. Permeability, i.e. the ability of the fluid to flow, is perhaps the most important property in their manufacturing. Prediction of the macroscopic permeability is a longstanding but still challenging problem that dates back to the work of Happel [2] and Kuwabara [3] with more recent contributions by Sangani and Acrivos [4], Drummond and Tahir [5], Gebart [6] and Brusckhe and Advani [7]. Most of these models/predictions are complex with limited range of validity. For example, Gebart [6] presented an expression for the transverse permeability based on the lubrication approximation valid for ordered structures, which are different from the generally disordered fibrous materials. For a review of the theory, predictability and limitations of these models see [8] and references therein.

Darcy's law is the most widely used empirical relation for the calculation of the pressure drop across a homogeneous, isotropic and non-deformable porous medium. It states that, at the macroscopic level and the limit of creeping flow regimes, the pressure gradient  $\nabla p$ , and the flow rate have a linear relation given by

$$-\nabla p = \frac{\mu}{K} U, \quad (4.1)$$

where  $\mu$  and  $U$  are viscosity and horizontal *superficial* (discharge) velocity, respectively. The proportionality constant  $K$ , is called the permeability of the medium and it strongly depends on the microstructure (e.g. fibre/particle shape and arrangement, void connectivity and inhomogeneity of the medium) and porosity. Darcy's law was originally obtained from experiments [9] and later formalized using upscaling [10], homogenization [11] and volume averaging [12] techniques. It has been shown that Darcy's law actually represents the momentum equation for Stokes flow averaged over a representative volume element (RVE). In fact in this representation, all complicated interactions between fluid and solid (fibres) are lumped into the permeability (tensor),  $K$ .

The lack of a microscopic foundation has motivated the development of relationships between macroscopic parameters, like permeability, and microstructural parameters, like fibre arrangements, shape and orientation or tortuosity (flow path). Chen and Papathanasiou [13, 14] computationally investigated the flow across randomly distributed unidirectional arrays using the boundary element method (BEM) and found a direct correlation between permeability and the mean nearest inter-fibre spacing. Papathanasiou [15] performed a similar study for unidirectional square arrays of fibre clusters (tows) using the BEM. His employed unit cells are therefore characterized by two porosities: (i) inter-tow porosity, determined by the macroscopic spatial arrangement of the tows, and (ii) intra-tow porosity, determined by the fibre concentration inside each tow. He showed that the effective permeability of assemblies of fibre clusters depends strongly on the intra-tow porosity only at low inter-tow porosity. In a recent study (chapter 3), Yazdchi et al. [16] proposed a power law relation between the transverse permeability obtained from finite element (FE) simulations and the mean value of the shortest Delaunay triangulation

(DT) edges, constructed using the centers of the fibres. For sedimentary rocks, especially sandstones, Katz and Thompson [17] suggested, using percolation theory, a quadratic relation between permeability and microstructural descriptors for rocks, i.e. the critical pore diameter. Despite all these attempts, the effect of microscopic fibre arrangements/structures, controlled by the effective packing fraction, on macroscopic permeability is still unclear.

The objective of this chapter is to (i) computationally investigate transverse flow through random fibre arrays in a wide range of porosities, (ii) understand and characterize the microstructure, i.e. the ordered and disordered states, using several order parameters, (iii) establish a relationship between macroscopic permeability and the microstructure of the fibrous materials and (iv) verify the validity of the empirical Darcy's law at various length scales.

To this end, the algorithm used to build the initial fibre configurations and the numerical finite element (FE) procedure for solving flow/momentum equations are presented in Section 4.2. In Section 4.3, the geometrical (Voronoi tessellation) and bond orientational order parameters are introduced to quantify the microstructure. In particular, the transition from disordered to ordered regimes is discussed in detail. The connection between structural (dis)order and macroscopic permeability is explained using shortest Delaunay triangulation edges in Section 4.4. Finally, the validity of Darcy's law at different length scales is investigated by dividing the system into both smaller uniform cells and irregular Voronoi/Delaunay polygons/triangles in Section 4.5. The chapter is concluded in Section 4.6 with a summary and outlook for future.

## 4.2 Mathematical formulation and methodology

A Monte Carlo (MC) approach was used to generate  $N=3000$  randomly distributed, non-overlapping fibre/disc arrays in a square domain with length,  $L$ . Given an initial fibre configuration on a triangular lattice, the MC procedure perturbs fibre centre locations in randomly chosen directions and magnitudes [13, 14]. The perturbation was rejected if it leads to overlap with a neighboring disk (up to  $10^4$  perturbations were used in our simulations). With this procedure, we were able to generate various packings at different porosities,  $\varepsilon=1-N\pi d^2/(4L^2)$  with  $d$  the diameter of fibres, varying from dense/ordered ( $\varepsilon=0.3$ ) to very dilute/disordered ( $\varepsilon=0.95$ ) regimes. Fig. 4.1 shows a schematic of such a packing, the fibre long axis is normal to the flow direction, at porosity  $\varepsilon=0.6$ . Due to wall/edge effects, only the center part of the system will be analyzed. The effect of several microstructural parameters such as method of generation, system size, wall/periodic boundaries have been discussed elsewhere [16], see chapters 2 and 3.

The FE software ANSYS<sup>®</sup> was used to calculate the horizontal *superficial* (discharge) velocity,  $U$ , from the results of my computer simulations as

$$U = \frac{1}{A} \int_{A_f} u dA = \frac{1}{L^2} \sum_e u_e A_e, \quad (4.2)$$

where  $A$ ,  $A_f$  and  $u$  are the total area of the unit cell, the area of the fluid and the intrinsic fluid velocity, respectively. The subscript “ $e$ ” indicates the corresponding quantity for each triangular element. Using Eq. (4.1), the permeability of the fibrous media can then be calculated. On the flow domain, the steady state Navier–Stokes equations combined with the continuity equations were discretised into an unstructured, triangular mesh. They were then solved using a segregated, sequential solution algorithm. The developed matrices from assembly of linear triangular elements are then solved based on a Gaussian elimination algorithm. Some more technical details are given in Refs. [8, 16]. At the left and right pressure- and at the top and bottom and surface of the particles no-slip boundary conditions, i.e. zero velocity is applied. Similar to Chen and Papathanasiou [13, 14], a minimal distance,  $\Delta_{\min} = \delta_{\min}/d = 0.05$  is needed in 2D to avoid complete blockage. I assigned a virtual diameter  $d^* = d(1 + \Delta_{\min})$  to each fiber, leading to the virtual porosity  $\varepsilon^* = 1 - (1 - \varepsilon)(1 + \Delta_{\min})^2$ . While  $\varepsilon$  represents the porosity available for the fluid,  $\varepsilon^*$  (i.e. porosity with artificially enlarged particles) is actually used for packing generation. The effect of  $\Delta_{\min}$  on fibre arrangement and macroscopic permeability is investigated in [16] (chapter 3). The mesh size effect was examined by comparing the simulation results for different resolutions (data not shown here). The number of elements varied from  $5 \times 10^5$  to  $10^6$  depending on the porosity regime. The lower the porosity the more elements are needed in order to resolve the flow within the neighboring fibres. The horizontal velocity field of such a simulation at porosity  $\varepsilon = 0.6$  is shown in Fig. 4.1. We observed some dominant flow channels, especially at low porosities, which contribute over-proportionally to the fluid transport. More discussions on quantifying these channels and their relation to the macroscopic permeability are provided in Section 4.4.

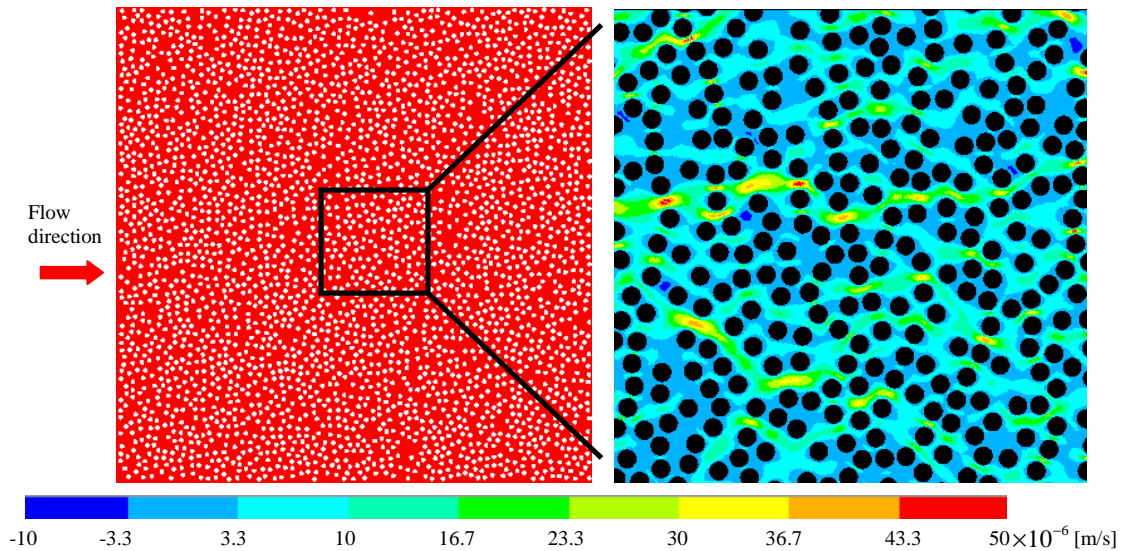


**Figure 4.1:** Illustration of  $N=3000$  randomly distributed fibres (particles) using a Monte Carlo procedure at porosity  $\varepsilon = 0.6$  with minimum inter fibre distance  $\Delta_{\min}=0.05$ . The zoom shows the corresponding horizontal velocity field.

### 4.3 Microstructure characterization

An important element in understanding of fibrous materials is the description of the local fibre arrangements and the possible correlations between their positions. The classical way for characterizing the structure, like disorder to order transition, is by inspection of its radial distribution function  $g(r)$ , which is defined as the probability of finding the centre of a fibre inside an annulus of internal radius  $r$  and thickness  $dr$  [13-14, 16, 18]. As the crystallization begins to occur at moderate porosities, peaks appear for values of  $r$  which correspond to the second (linear) neighbors in a hexagonal lattice in 2D or a FCC or HCP arrangements in 3D. The complete randomness of the fibre distribution on larger scale will assure that  $g(r)=1$ . However, as pointed out by Rintoul and Torquato [19], this method is unsatisfying for two reasons: on the one hand the absence of clear peaks does not necessarily mean the absence of crystallization, and on the other hand it is difficult to determine exactly when the peak appears. In this section, I propose another way to characterize more quantitatively the microstructure of my 2D, non-overlapping fibre packings, namely by analyzing (i) the statistical geometry of the Voronoi/Delaunay tessellation and (ii) the bond orientational order parameter, in a wide range of porosities.

#### 4.3.1 Voronoi diagram (VD)

The Voronoi tessellation can be used to study the local and/or global ordering of packings of discs/fibres in 2D. Motivation stems from their variety of applications in studying correlations in packings of spheres [20, 21], analysis for crystalline solids and super-cooled liquids [22, 23], the growth of cellular materials [24], and the geometrical analysis of colloidal aggregation [25] and plasma dust crystals [26]. For a review of the theory and applications of Voronoi tessellations, see the books by Okabe et al. [27] and Berg et al. [28], and the surveys by Aurenhammer [29] and Schliecker [30].

For equal discs as considered here, given a set of two or more but a finite number of distinct points (generators) in the Euclidean plane, we associate all locations in that space with the closest member(s) of the point set with respect to the Euclidean distance. The result is a tessellation, called Voronoi diagram, of the plane into a set of regions associated with members of the point set, see thick red lines in Fig. 4.2. This construction is unique and fills the whole space with convex polygons. In a hexagonally close packed (densest) configuration, i.e.  $\varepsilon_{hex}^* \cong 0.093$ , the Voronoi tessellation consists of regular hexagons. It allows us to define the notion of “neighbor” without ambiguity for any packing fraction: two spheres/discs are neighbor if their Voronoi polyhedra share one face/edge. It can be easily generalized to radical tessellation for polydisperse assemblies of spheres [31] or discs [32] by using the Laguerre distance between obstacles, which takes into account the size of each point species.

The Delaunay triangulation (DT) is the dual graph of the Voronoi diagram. This graph has a node for every Voronoi cell and has an edge between two nodes if the corresponding cells share an edge, see thin blue lines in Fig. 4.2. DT cells are always triangles in 2D, and are thus typically smaller than Voronoi cells.

Recently, various studies have focused on the geometrical properties of Voronoi tessellations resulting from random point processes, i.e.  $\varepsilon=1$ , to densely packed hard discs or spheres. In particular, Zhu et al. [33] and Kumar and Kumaran [34] observed that by decreasing the porosity the degree of randomness of the tessellation is decreased - the probability distribution functions (PDFs) of the statistical properties of the geometrical characteristics become more and more peaked and narrower - until the unique critical value of a regular tessellation, i.e. of hexagonal cells, is adapted.

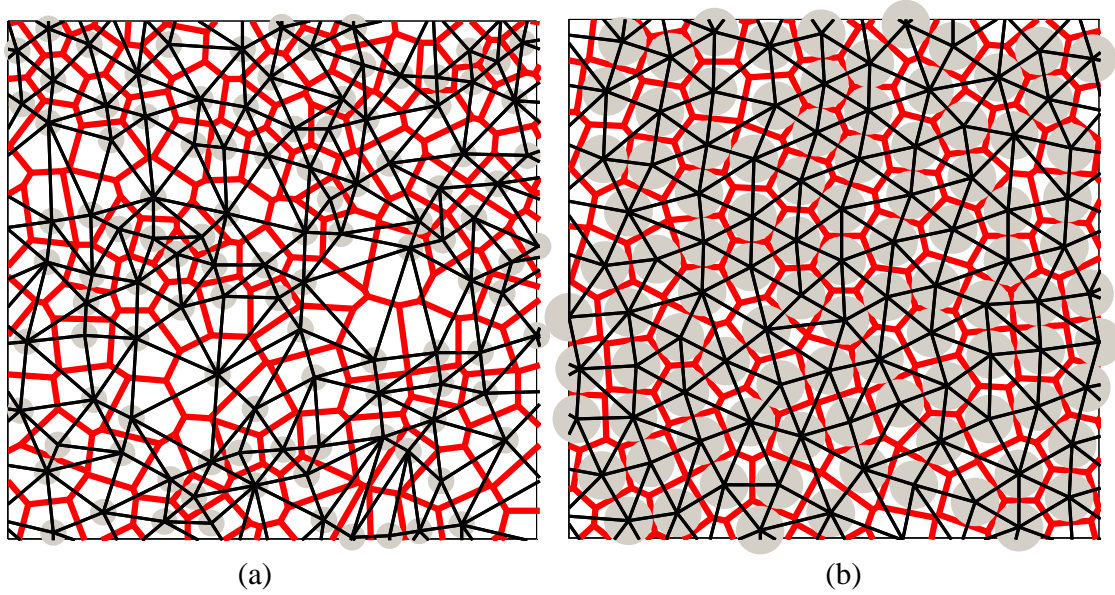


**Figure 4.2:** Illustration of the Voronoi (red line) and Delaunay (blue lines) tessellations for the center part of a system of identical discs at (a) dilute,  $\varepsilon = 0.8$  and (b) dense,  $\varepsilon = 0.4$  regimes for  $\Delta_{\min}=0.05$ .

In order to gain further insight into the relative arrangement of the Voronoi cells, their topological correlations and metric properties have been studied in the following. In particular, I focus on (i) the distribution and evolution of the number of faces,  $p(n)$  together with their 2<sup>nd</sup> and 3<sup>rd</sup> moments and (ii) the shape and regularity (or isotropy) of the Voronoi polygons at different porosities.

#### 4.3.1.1 Topological correlations for Voronoi tessellations

This section is dedicated to the study of the evolution of the probability distribution of  $n$ -sided polygons,  $p(n)$  when changing the porosity. Note that only the information obtained from the inner discs, which were at least 5 disc diameters away from the wall, was included in my analysis. This treatment should satisfactorily eliminate the wall/edge effects up to high densities. To get better statistics, the results were averaged over 10 realizations with  $10^4$  MC perturbations. The two straightforward conservation laws are

$$\sum_n p(n) = 1 \quad (\text{normalization}), \quad \text{and} \quad (4.3)$$

$$\sum_n np(n) = 6 \quad (\text{the average number of edges is } 6), \quad (4.4)$$

as the consequence of the Euler theorem [27, 35]. The distributions of the cell topologies,  $p(n)$  of Voronoi tessellations, generated at various porosities are observed to follow a discretised and truncated Gaussian shape (not shown here). The perfectly ordered structure is manifested by hexagonal cells, i.e.  $n=6$  and  $p(n)=1$ , and disorder/randomness shows up as the presence of cells with other than six sides (topological defects). The increase of disorder in the disc assemblies at high porosities leads to an increase of the topological defect concentration, i.e. a broadening of  $p(n)$ .

In the literature, both the topological defect concentration  $1-p(6)$ , and the variance (2<sup>nd</sup> central moment)  $\mu_2 = \langle n^2 \rangle - \langle n \rangle^2 \equiv \langle (n - \langle n \rangle)^2 \rangle \equiv \sum_n p(n)(n-6)^2$  of the cell topologies, are used as measures of the degree of disorder [36-40]. Lemaître et al. [40] were, to my knowledge, the first to suggest that the equation of state  $\mu_2 = f(p(6))$  could be universal in mosaics. In this sense, all information about topological disorder in these systems is contained in  $p(6)$ . Astonishingly, Lemaître's law holds very robustly for most of experimental, numerical, and analytical data [36-41].

Fig. 4.3(a) shows the correlation between  $p(6)$  and the topological variance  $\mu_2$  for different microstructures and at various porosities. In the ordered regime, i.e.  $p(6) > 0.65$ , mainly 5, 6 and 7 sided polygons with  $p(5) \cong p(7) \cong (1 - p(6))/2$  occur, and by applying the maximum entropy principle with the constraints in Eqs. (4.3) and (4.4) [39], one obtains  $\mu_2 = 1 - p(6)$ ; it has the trivial virial expansion that corresponds to an ideal gas. By increasing the porosity, i.e.  $\varepsilon > 0.45$  or  $\varepsilon^* > 0.39$ , one enters the disordered regime and  $\mu_2 \cong 1/(2\pi p^2(6))$ . Finally, in the limit of vanishing density ( $\varepsilon = 1$ ), the discs are randomly distributed and one has  $p(6) \cong 0.3$  and  $\mu_2 \cong 1.78$ . This limit is obtained by analyzing the Voronoi polygons generated from  $10^7$  randomly distributed points. The transition porosity  $\varepsilon_t^* \cong 0.39$  can be more clearly determined by plotting the third central moments of the  $n$ -sided polygon distributions,  $\mu_3 = \langle (n - \langle n \rangle)^3 \rangle$  against porosity, as shown in Fig. 4.3(b). Note that this value is still far above the random close packing limit  $\varepsilon_{rcp}^* \cong 0.16$  [42], as compared also to the minimum hexagonal lattice porosity  $\varepsilon_{hex}^* \cong 0.093$ , the freezing point  $\varepsilon_f^* \cong 0.309$  [43] or the melting point  $\varepsilon_m^* \cong 0.284$  [43].



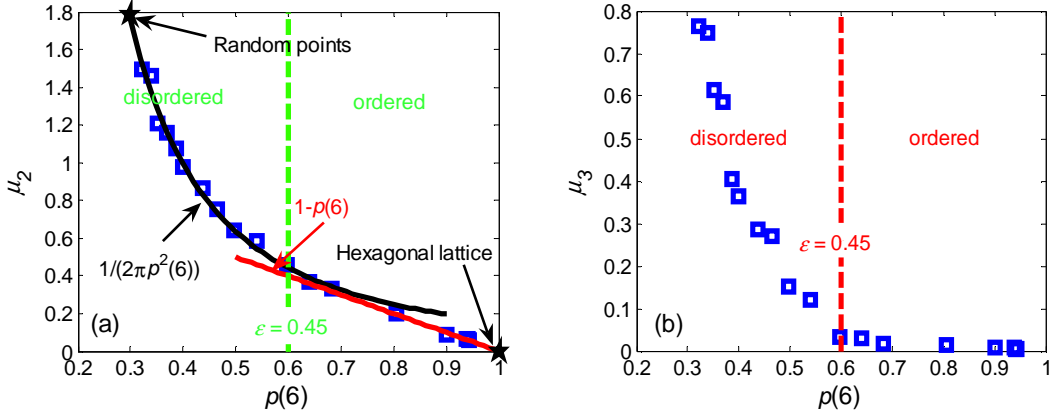


**Figure 4.3:** (a) The correlation between  $p(6)$  and the topological variance  $\mu_2$  for various structures and porosities. The analytical theories, represented by solid lines, are calculated by the Maxent method [39]. (b) Variation of the third moment of  $n$ -sided polygon distributions,  $\mu_3$  plotted against porosity. The transition from order to disorder occurs at  $\varepsilon_t \cong 0.45$  ( $\varepsilon_t^* \cong 0.39$ ).

#### 4.3.1.2 Metric properties

The metrical properties of two-dimensional froths are often studied in terms of the average  $n$ -sided cell areas,  $\langle A_n \rangle$  or the average cell perimeters,  $\langle L_n \rangle$ . Lewis's law [44] and Desch's law [45] are two empirical relations which state that the average cell areas and perimeters vary linearly with  $n$  for certain systems, while for others nonlinear analogs have been observed [37, 46, 47]. Only recently, using the local, correlation-free granocentric model approach with no free parameters, Miklius and Hilgenfeldt [36] construct accurate analytical descriptions for these empirical laws in 2D and Clusel et al. [48] in 3D.

Combining the cell area and its perimeters, I apply the concept of shape factor, to further quantify the shape/circularity of the Voronoi cells as

$$\zeta = \frac{L^2}{4\pi A}. \quad (4.5)$$

In this dimensionless representation, two Voronoi polygons can have the same number of sides,  $n$ , but different values of  $\zeta$  (due to the irregularity of the polygons), since one of the advantages is that the shape factor,  $\zeta$  is a continuous variable while  $n$  is discrete. This quantity was recently used to study crystallization of 2D systems, both in simulation [49] and experiment [18, 50, 51]. By construction,  $\zeta = 1$  for a perfect circle, and is larger for more rough or elongated shapes, like pentagons or heptagons. For a hexagonal lattice

(densest packing) one has  $\zeta_{hex} = 1.103$  and, in general, for a regular  $n$ -sided polygon  $\zeta = (n/\pi) \tan(n/\pi)$ .

The shape factor distributions,  $p(\zeta)$  and the way they change with porosity are displayed in Fig. 4.4(a). For dilute systems (disordered regime),  $p(\zeta)$  exhibits a broad and flat distribution with values above  $\zeta_{hex}$ , maximum at about  $\zeta \approx 1.25$  and an exponential tail. In this case, in fact, the particles are randomly distributed with no preferential type of polygons. At lower porosities, this peak progressively moves towards lower values, i.e. to more circular domains, and eventually bifurcates into two sharper peaks. Fig. 4.4(b) shows the average shape factor,  $\langle \zeta \rangle$  taken over all polygons at different porosities for various system sizes (number of particles,  $N$ ). The numerical results show that  $\langle \zeta \rangle$  is not noticeably affected by system size. Interestingly, one observes that it increases almost linearly with porosity (for  $0.3 < \varepsilon < 0.85$ ). A similar linear dependence was observed for packing configurations obtained from a different generation algorithms, namely an energy minimization approach [16] (data not shown here). Unlike the data presented in Fig. 4.3, the trend does not indicate a change at the transition porosity  $\varepsilon_t \approx 0.45$  ( $\varepsilon_t^* \approx 0.39$ ), and therefore this is not a good criterion for detecting the order to disorder transition. Finally, in the limit of random point distributions one has  $\langle \zeta \rangle \approx 1.4$ .

A drawback of the shape factor is that, with this definition, the regularity (or isotropy) of the Voronoi polygons can not be deduced. In other words, how far each vertex of a polygon deviates from the principal axis. This can be answered by the dimensionless parameter,  $\Phi$  defined as

$$\Phi = \left| \frac{I_1 - I_2}{I_1 + I_2} \right|, \quad (4.6)$$

where  $I_1$  and  $I_2$  are area moments about the principal axes of a polygon. For all Voronoi shapes,  $\Phi$  varies between zero and unity, although my numerical results show that it does not exceed a maximum value corresponding to a random cloud of points  $\Phi \approx 0.43$  (see Fig. 4.5). For the polygons which are ‘‘isotropic’’, like hexagons, one has  $I_1 \approx I_2$  and therefore  $\Phi \approx 0$ . Polygons which are stretched along one of their principal axes have larger values of  $\Phi$ , with  $\Phi = 1$  for as possible maximum.

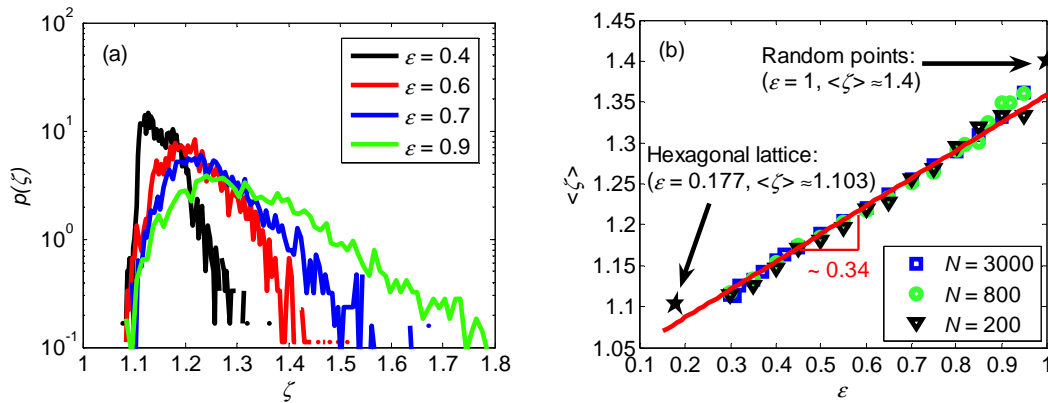


**Figure 4.4:** (a) The probability distribution of the shape factor,  $\zeta$  at different porosities. (b) Average shape factor plotted against porosity for different number of fibres/discs. The solid red line shows the best linear least square fit. All data are averaged over 10 realizations with  $10^4$  MC perturbations.

Fig. 4.5 shows the average  $\langle \Phi \rangle$  taken over all polygons against porosity. As the porosity increases, the  $\langle \Phi \rangle$  also increases, indicating a more anisotropic shape, until it reaches its maximum value for random points, i.e.  $\Phi \cong 0.43$ . Interestingly, two linear functions with different slopes can be fitted to the disordered and ordered regimes. Just as was observed in Fig. 4.3(b), the transition (crossing of the two lines) occurs at  $\varepsilon_t \cong 0.45$  ( $\varepsilon_t^* \cong 0.39$ ).

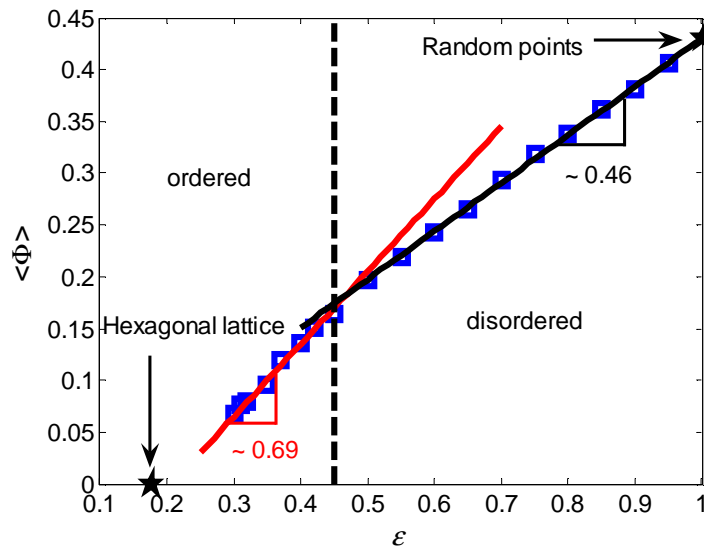


**Figure 4.5:** Variation of average  $\langle \Phi \rangle$  plotted against porosity. The solid lines show the best linear least square fits. Similar to the  $\mu_2 = f(p(6))$  relation, the transition from order to disorder occurs at  $\varepsilon_t \cong 0.45$  ( $\varepsilon_t^* \cong 0.39$ ).

#### 4.3.2 Bond orientational order parameter

The bond orientation angle,  $\psi_6$ , which is defined in terms of the nearest-neighbor bond angles, measures the hexagonal registry of nearest neighbors. This quantity has been used to detect local/global crystalline regions both in 2D and 3D, see for example [52-56] and references therein. The sixfold global bond-orientational order parameter of the 2D hard disk system is defined as

$$\psi_6^g = \frac{1}{N} \left| \sum_{i=1}^N \frac{1}{n_i} \sum_{j=1}^{n_i} e^{6i\theta_{ij}} \right|, \quad (4.7)$$

where  $\theta_{ij}$  is the angle between particle  $i$  and its neighbors  $j$  with respect to an arbitrary but fixed reference axis, and  $n_i$  denotes the number of nearest neighbors of particle  $i$ .  $\psi_6^g$  is sensitive to (partial) crystallization and increases significantly from  $\psi_6^g \sim 0$  for a dilute system to  $\psi_6^g = 1$  for a perfect hexagonal lattice.

A more local measure of orientational order can be obtained by evaluating the bond-orientational order of each particle individually, and then averaging over all particles to give

$$\psi_6^l = \frac{1}{N} \sum_{i=1}^N \frac{1}{n_i} \left| \sum_{j=1}^{n_i} e^{6i\theta_{ij}} \right|. \quad (4.8)$$

such a local measure of order is more sensitive to small local crystalline regions within a packing compared to its global counterpart  $\psi_6^g$ , and thus avoids the possibility of “destructive” interference between differently oriented crystalline regions [56]. Since  $\psi_6^g$  and  $\psi_6^l$  differ in the averaging procedure, they yield different numerical values.

The first step in evaluating  $\psi_6$ , which was not precisely addressed before, is to detect the nearest neighbors of a reference particle  $i$ . Fig. 4.6(a) shows the sensitivity of the local  $\psi_6^l$  to the number of nearest neighbors obtained from (i) a cutoff distance taken from the first minimum in the radial distribution function,  $g(r)$  (ii) Voronoi/ Delaunay neighbors or (iii) using up to and including the 6 nearest neighbors. Although the average of Voronoi neighbors is 6 (Eq. (4.4)), the local  $\psi_6^l$  calculated on the Voronoi neighbors have lower values than the ones calculated from the 6 nearest neighbors. Voronoi neighbors and the

neighbors based on the cutoff distance result in almost the same numerical values. For decreasing porosity, the local  $\psi_6^l$  rises sharply at  $\varepsilon \cong 0.45$ , indicating highly correlated local order. However, the transition is not sharp, since the order parameter increases slightly for  $\varepsilon \leq 0.7$ . In very dilute regimes, the local order parameter  $(\psi_6^l)_{ran} \cong 0.21$  is larger than zero, leading to the interesting question of whether there is a minimum, nonzero value of this parameter for a random system. A possible answer is that in random hard disk structures, there are still some local crystalline regions, due to the lack of geometric frustration, which are not correlated. In Fig. 4.6(b) the numerical values of the global,  $\psi_6^g$  and local,  $\psi_6^l$  are compared and plotted against porosity, using the Voronoi neighbors. Unlike the local definition, the global  $\psi_6^g$  is almost zero in the disordered regime, due to phase cancellations, and increases sharply at  $\varepsilon \cong 0.37$ , i.e. the freezing point [43], with the onset of hexagonal order.

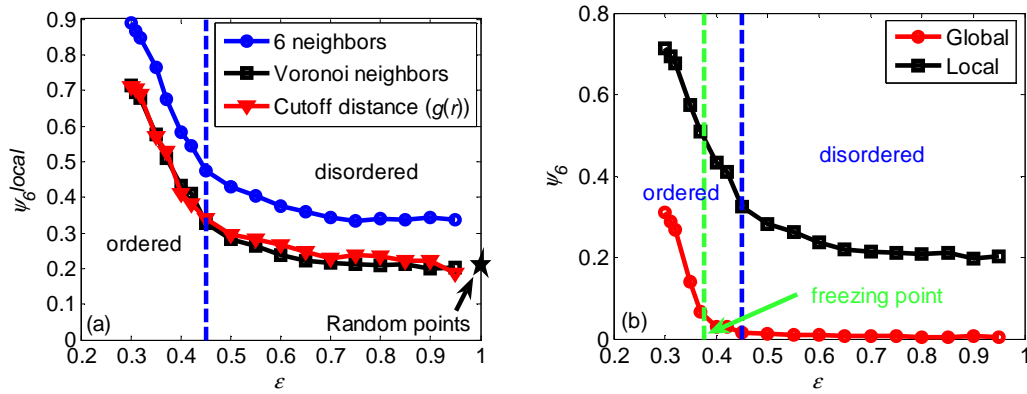


**Figure 4.6:** (a) Illustration of the sensitivity of the local  $\psi_6^l$  to the nearest neighbor selection method. (b) Variation of the global,  $\psi_6^g$  and the local,  $\psi_6^l$  bond orientational order parameter plotted against porosity, using the Voronoi neighbors.

Beyond the classification of the microstructure, one would like to understand how (dis)order affects the transport properties, like permeability, of the fibrous material. This is the topic of the next section.

#### 4.4 Macroscopic properties

Recently, Yazdchi et al. [16] (chapter 3) showed that the mean values of the shortest Delaunay triangulation (DT) edges are nicely correlated with the macroscopic permeability at dilute and moderate porosities. In this section, I elaborate more on characterizing of these channels (edges).

#### 4.4.1 Effective channels based on Delaunay triangulations

Similar to previous chapter, I define  $\gamma$  as the mean channel width (gap), i.e. surface-to-surface distance based on the shortest Delaunay edges  $\langle e_i \rangle$ , (averaged over Delaunay triangles) normalized by the fibre diameter,  $\gamma = (\langle e_i \rangle - d)/d$ . Fig. 4.7 shows these shortest edges with channel width indicated by line thickness. These edges form a percolated edge-network channels through which the flow must go and, therefore correlate nicely with the permeability (see next section). Fig. 4.8 shows the PDF of widths and the histogram of the orientations of these channels. The distribution of the width of the channels,  $p(\gamma)$  undergoes a transition from a very wide distribution to a narrower with increasing peak at lower  $\gamma$ , and eventually to a steep exponential distribution as the porosity decreases. For a perfect triangular lattice it reduces to exactly the inter fibre (surface-to-surface) distance, i.e.  $\gamma = \Delta_{\min} = 0.05$ . The orientation of the channels is not much affected by the porosity and remains isotropic (no preferential direction) even for partially ordered structures at  $\varepsilon = 0.4$ .

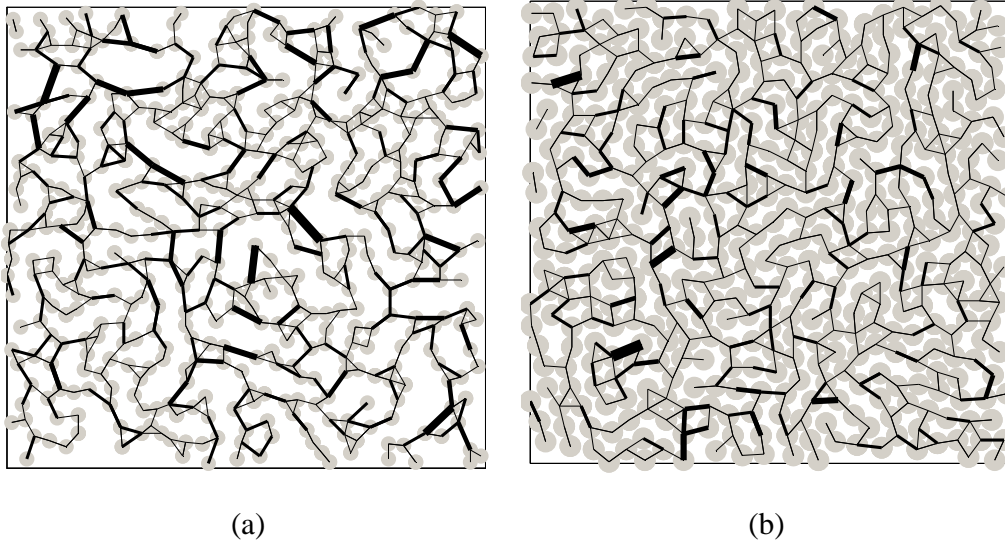


**Figure 4.7:** The minimum Delaunay edges plotted for each Delaunay triangle for (a) dilute,  $\varepsilon = 0.8$  and (b) dense,  $\varepsilon = 0.4$  systems. The link between two particles is thicker when the channel is wider. Only the center part of the system is shown.

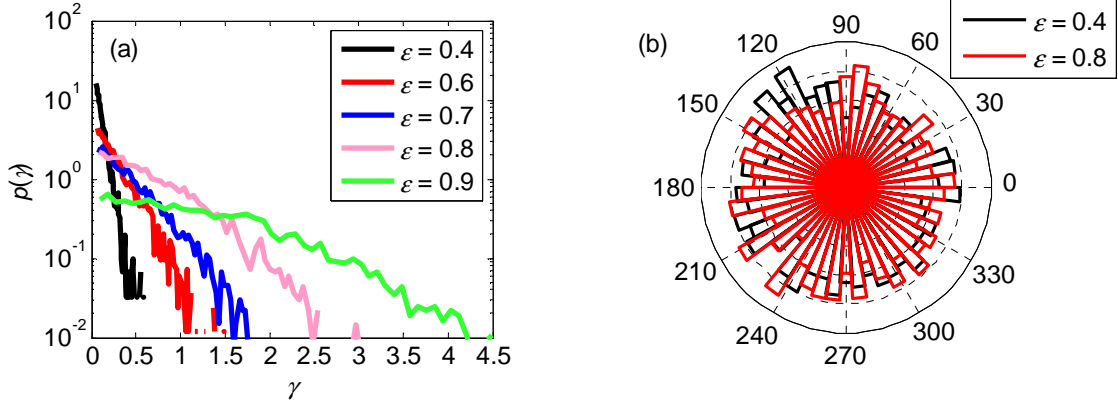


**Figure 4.8:** (a) The probability distribution function of shortest Delaunay edges,  $\gamma$  at different porosities. (b) Polar histogram of the orientation of shortest Delaunay edges. All data are averaged over 10 realizations with  $10^4$  MC perturbations.

#### 4.4.2 Permeability calculation

Based on the Navier-Stokes equation, Gebart [6] derived the permeability of an idealized unidirectional reinforcement consisting of regularly ordered, parallel fibres both for flow along and for flow perpendicular to the fibres. The solution for flow along fibres has the same form as the Carman-Kozeny (CK) equation [8, 57], while the solution for transverse flow has a different form

$$\frac{K}{d^2} = C \left( \sqrt{\frac{1-\varepsilon_o}{1-\varepsilon}} - 1 \right)^{2.5}, \quad (4.9)$$

where  $\varepsilon_o$  is the critical porosity below which there is no permeating flow and  $C$  is a geometric factor ( $C \cong 0.1, \varepsilon_o \cong 0.2146$  for square and  $C \cong 0.0578, \varepsilon_o \cong 0.0931$  for hexagonal arrays [6]). Eq. (4.9) can be rewritten in terms of  $\gamma$  as

$$\frac{K}{d^2} = C \gamma^{2.5}, \quad (4.10)$$

which is exact for regular/ordered arrays and was shown to be valid also for disordered arrays at high and moderate porosities [16], with  $C \cong 0.2$ . Relation (10) is remarkable, since it enables one to accurately determine the macroscopic permeability of a given packing just by averaging the narrowest Delaunay gaps,  $\gamma$  from Delaunay triangles. Fig. 4.9(a) shows the variation of the normalized permeability (in red) as a function of  $\gamma$  together with the local bond orientational order parameter,  $\psi_6^l$  (in blue). The structural transition from disorder to order, indicated by strong increase in  $\psi_6^l$ , directly affects the macroscopic permeability. In disordered regimes the permeability data nicely collapse on

the theoretical power law relation (Eq. (4.10)). However, by appearance the local crystalline regions at  $\varepsilon > 0.45$ , the data start to deviate from the power law. In fact the lubrication theory, i.e. Eqs. (4.9) or (4.10), are only valid for perfectly ordered (hexagonal/square) or disordered (random) configurations with different pre-factor,  $C$ . System that is partially ordered has lower permeability compared to the predicted value in Eq. (4.10), i.e.  $(K/d^2)_{ran}$ , due to stagnancy of the fluid between fibre aggregates or within crystalline regions of close-by fibres. With decreasing porosity the data deviate from the solid line showing the appearance of ordering in the structure. In chapter 3, I showed that this deviation can be represented by an exponential term, see Eq. (3.13). Fig. 4.9(b) shows that indeed for both permeability and local bond orientation order parameter, this deviation, i.e.  $\chi_p = |1 - K / K_{ran}|$  and  $\chi_{\psi'_6} = |1 - \psi'_6 / (\psi'_6)_{ran}|$  respectively, can be well represented by exponential term.

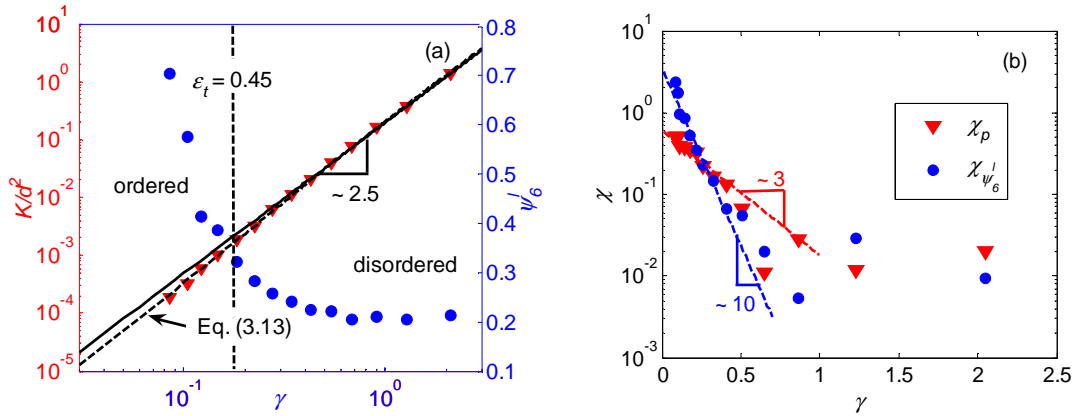


**Figure 4.9:** (a) Variation of normalized permeability (in red) and local bond orientational parameter (in blue) as function of mean shortest Delaunay gaps,  $\gamma$ . The solid line represents the power law, Eq. (4.10), obtained from lubrication theory. At the transition porosity  $\varepsilon_t \cong 0.45$ , the permeability data start to deviate strongly from the solid line. (b) Deviation of normalized permeability and local bond orientation order parameter from their random (disordered) values, i.e.  $\chi_p = |1 - K / K_{ran}|$  and  $\chi_{\psi'_6} = |1 - \psi'_6 / (\psi'_6)_{ran}|$  respectively, plotted against  $\gamma$ .

#### 4.5 Darcy's law – upscaling the transport equations

The empirical law of Darcy, Eq. (4.1), is the key constitutive equation required to model up-scaled (under)ground water flow at low velocities and to predict the permeability of porous media. Though the volume-averaged equations, like Darcy's law, are used extensively in the literature, the method relies on length- and time-scale constraints which remain poorly understood. The macroscopic transport properties, such as permeability,



are linked to more fundamental equations describing the microscale behavior of fluids in porous materials [1].

In this section, I verify the validity of the macroscopic phenomenological Darcy's law at various length scales in a wide range of porosities and recognize that the application of the pore-scale analysis requires characterization of the pore-scale geometry (and/or size) of the porous material. The Voronoi/Delaunay tessellation and their statistics are employed to obtain this essential geometrical (and/or length-scale) information.

#### 4.5.1 Uniform cells

In order to study the validity of Darcy's law at different length scales, I divide my system at porosity  $\varepsilon=0.6$  into smaller uniform cells as shown in Fig. 4.10(a). The corresponding fully resolved horizontal velocity field is shown in Fig. 4.10(b). Since we have sufficient number of elements between neighboring fibers, i.e. at least  $\sim 10$  elements, all the velocity fluctuations and flow patterns can be captured at this length-scale. By upscaling (smoothing out) the velocity field, the permeability of each square cell,  $K_c$  can be calculated from Darcy's law, as:

$$K_c = \frac{\mu U_c}{\nabla p_c}, \quad \text{with} \quad U_c = \frac{1}{A_c} \sum_{e_c} u_{e_c} A_{e_c}, \quad A_c = a_c^2, \quad (4.11)$$

where  $U_c$ ,  $a_c$ ,  $e_c$  and  $\nabla p_c = \left[ (p'_t + p'_b)/2 - (p'_r + p'_l)/2 \right] / a_c$  ( $t$ ,  $b$ ,  $r$  and  $l$  represent the pressure values at top, bottom, right and left sides of the cell, respectively) are average velocity, cell length, the elements within the cell and the pressure gradient for each individual cell, respectively. The variation of average cell velocity,  $U_c$  at porosity  $\varepsilon = 0.6$  for the different cell areas,  $A_c$  normalized by the particle area,  $A_p = \pi d^2 / 4$  is shown in Fig. 4.10(c) and (d) for  $A_c / A_p \cong 20$  and  $A_c / A_p \cong 160$ , respectively. At higher resolutions, i.e. smaller  $A_c / A_p$ , we see larger fluctuations (i.e. more flow heterogeneity/details) around the macroscopic average velocity,  $U = 4.07 \times 10^{-6}$  [m/s] obtained for the whole system, using the parameters specified in Section 4.2. This can be observed more clearly from the PDF of the cell average velocities,  $U_c$  at different resolutions as shown in Fig. 4.11(b). For small averaging cells, i.e.  $A_c / A_p \sim 1$ , the probability distribution of average cell velocities,  $p(U_c)$  can be described by the two-parameter Gamma distribution as

$$p(U_c) = \frac{\lambda^\theta}{\Gamma(\theta)} U_c^{\theta-1} \exp(-\theta U_c), \quad \text{for } \theta, \lambda > 0, \quad (4.12)$$

where  $\theta$  and  $\lambda$  are, by definition, shape and scale parameters and  $\Gamma(\theta)$  is the Gamma function.

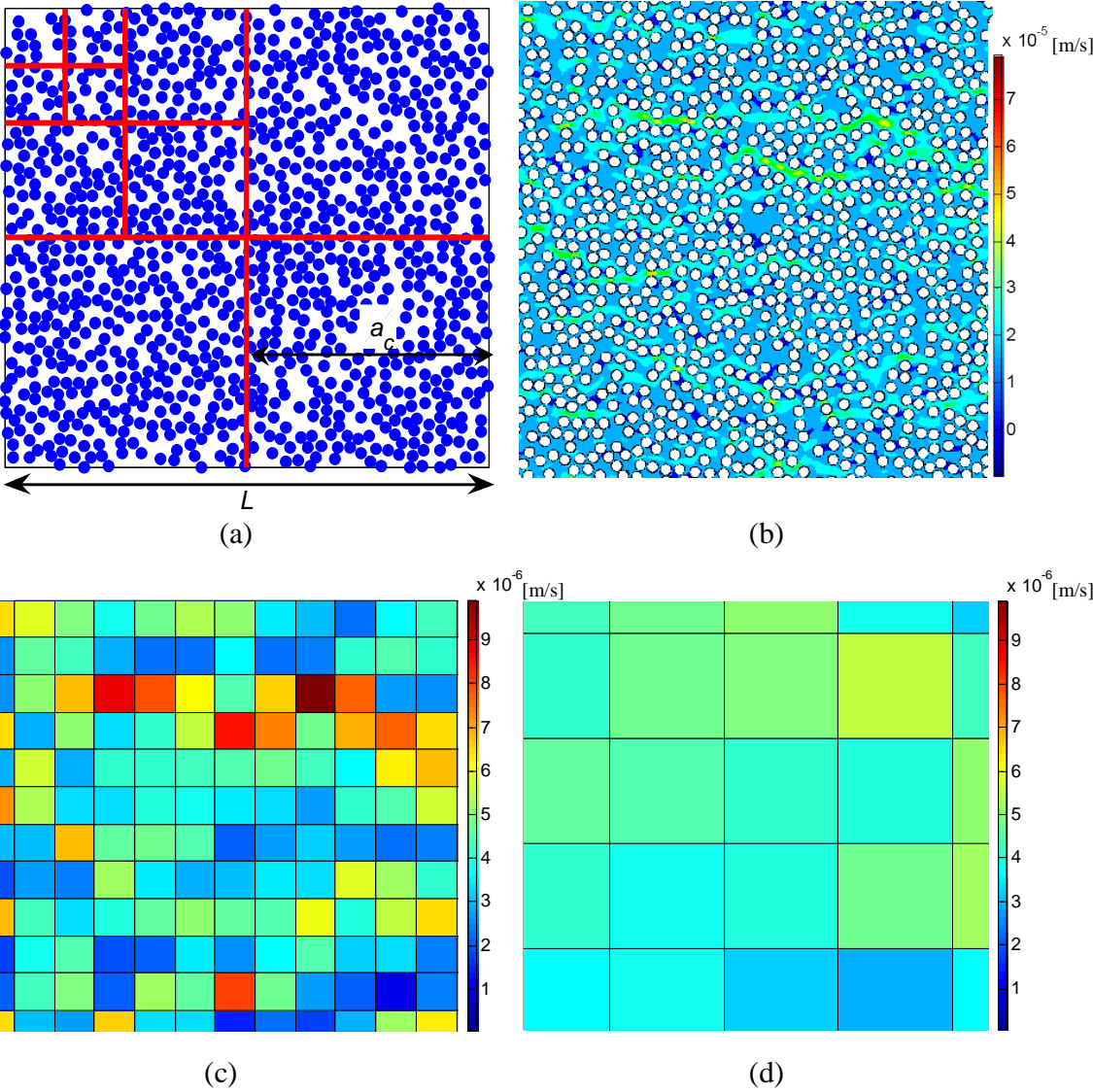


**Figure 4.10:** (a) Centre part of  $N=3000$  randomly distributed fibres (particles) at porosity  $\varepsilon=0.6$ . The red cells show the various averaging cell areas; (b) the corresponding horizontal velocity field. The variation of average velocity,  $U_c$  at porosity  $\varepsilon = 0.6$  for the cell sizes of (c)  $A_c / A_p \cong 20$ , and (d)  $A_c / A_p \cong 160$ .

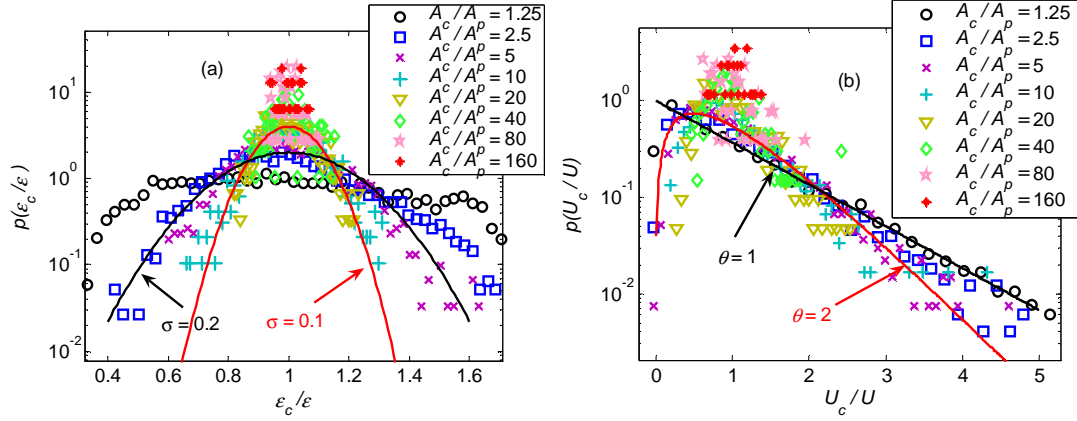


**Figure 4.11:** (a) The PDF of the cell porosity,  $\varepsilon_c$  normalized with the macroscopic porosity,  $\varepsilon = 0.6$  at different resolutions. The solid lines show the best fitted Gaussian distribution, see Eq. (4.14) for  $A_c/A_p = 5$  (black line) and  $A_c/A_p = 20$  (red line). (b) The PDF of the cell average velocities,  $U_c$  normalized with the macroscopic or mean value,  $U$  at different resolutions at porosity  $\varepsilon = 0.6$ . The solid lines show the best fitted gamma distribution, see Eq. (4.13) for  $A_c/A_p = 1.25$  (black line) and  $A_c/A_p = 5$  (red line).

The mean value of Gamma distributed average cell velocities is  $\langle U_c \rangle = U = \frac{\theta}{\lambda}$ . Written in terms of averaged velocity,  $p(U_c)$  has only one free parameter which is

$$p\left(\frac{U_c}{U}\right) = \frac{\theta^\theta}{\Gamma(\theta)} \left(\frac{U_c}{U}\right)^{\theta-1} \exp\left(-\theta\left(\frac{U_c}{U}\right)\right), \quad \text{for } \theta > 0. \quad (4.13)$$

The value of  $\theta$  starts from  $\theta = 1$ , i.e. exponential distribution, for small cell size,  $A_c/A_p \cong 1$  (see the black line in Fig. 4.11(b)) and increases to  $\sim 3$  for larger cell sizes,  $A_c/A_p \cong 10$ . For larger  $A_c/A_p > 20$ , the  $p(U_c/U)$  becomes more and more peaked and narrower. The PDF of cell porosities,  $p(\varepsilon_c/\varepsilon)$  at the macroscopic (average) porosity  $\varepsilon = 0.6$  is shown in Fig. 4.11(a). We observed that at small cell sizes, the  $p(\varepsilon_c/\varepsilon)$  follows a uniform distribution, i.e. horizontal line. However, at larger resolutions, the  $p(\varepsilon_c/\varepsilon)$  is fitted best by a Gaussian distribution as

$$p\left(\frac{\varepsilon_c}{\varepsilon}\right) = \frac{1}{\sigma\sqrt{2\pi}} \exp\left(-\frac{1}{2}\left(\frac{\varepsilon_c/\varepsilon - 1}{\sigma}\right)^2\right), \quad (4.14)$$

where  $\sigma$  is the standard deviation of the data. By increasing the cell size,  $\sigma$  decreases till it becomes only scattered points around the mean value, i.e.  $\varepsilon_c/\varepsilon \approx 1$ . Similar behavior and distributions were observed at different porosities (data not shown here). Note that at all cell lengths, the mean value of average cell velocity,  $\langle U_c \rangle$  or pressure gradients,  $\langle \nabla p_c \rangle$  are equal to their total average velocity,  $U$  or pressure gradient,  $\nabla p$  (with maximum discrepancy of 2% due to ignoring the boundary elements, not shown here).

Knowing the average velocity and pressure gradient for each cell, one can calculate, from Eq. (4.11), the permeabilities for each individual cell as shown in Fig. 4.12(a) as scattered data for different porosities and cell sizes. The solid line shows the macroscopic permeability obtained for the whole system.

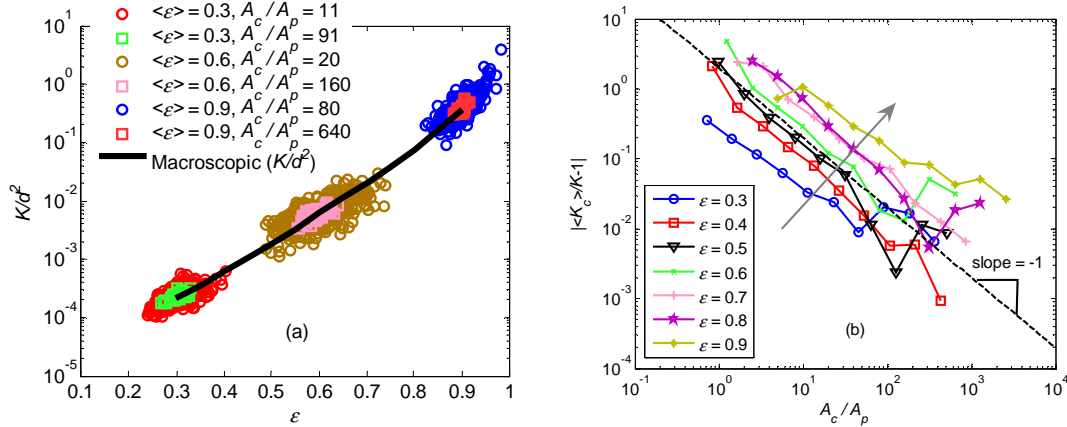


**Figure 4.12:** (a) variation of normalized permeability as a function of porosity for various averaging cell sizes. The circles and squares correspond to  $a_c/L \approx 0.05$  and  $a_c/L \approx 0.15$ , respectively. (b) Deviation of averaged permeability,  $\langle K_c \rangle$  from macroscopic permeability,  $K$  as a function of normalized cell area at different porosities.

As expected, smaller cell areas lead to more scattered (fluctuating) permeabilities around the macroscopic value (black line). For sufficiently large cell sizes, i.e.  $a_c \sim L$ , the average of cell permeabilities,  $\langle K_c \rangle$  approaches the macroscopic permeability,  $K$  obtained for the whole system. Fig. 4.12(b) shows the deviation of  $\langle K_c \rangle$  from the macroscopic permeability plotted against normalized cell area,  $A_c/A_p$  at different porosities. By increasing the normalized area, the deviation decreases linearly with slope  $\sim -1$ . Interestingly, this trend is almost the same at all porosities.

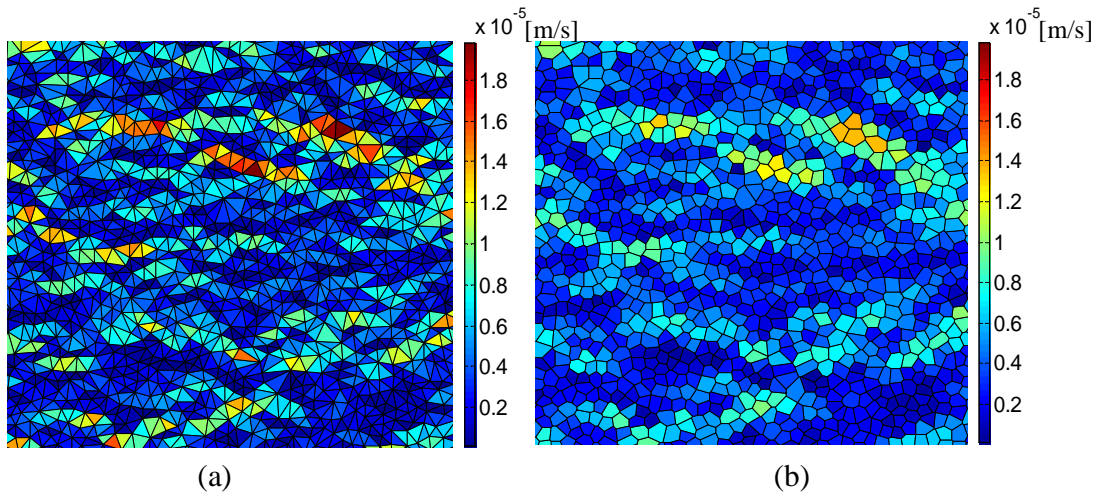
In summary, the permeability for each cell is very sensitive to the averaging area with slow statistical convergence to the macroscopic value. Small areas, i.e.  $A_c \sim A_p$ , lead to more fluctuations in permeability in which the average, unlike velocity and porosity, will

not approach the macroscopic value. Incorporating the observed distributions in a more accurate stochastic drag closure (or permeability) for advanced, coarse fluid-particle simulations can be conducted in future.

#### 4.5.2 Unstructured cells

To study the effect of shape of the averaging cell on the macroscopic permeability and averaging procedure, the Voronoi polygon and their dual graph, the Delaunay triangulations (DT) are employed as basic area in this section.

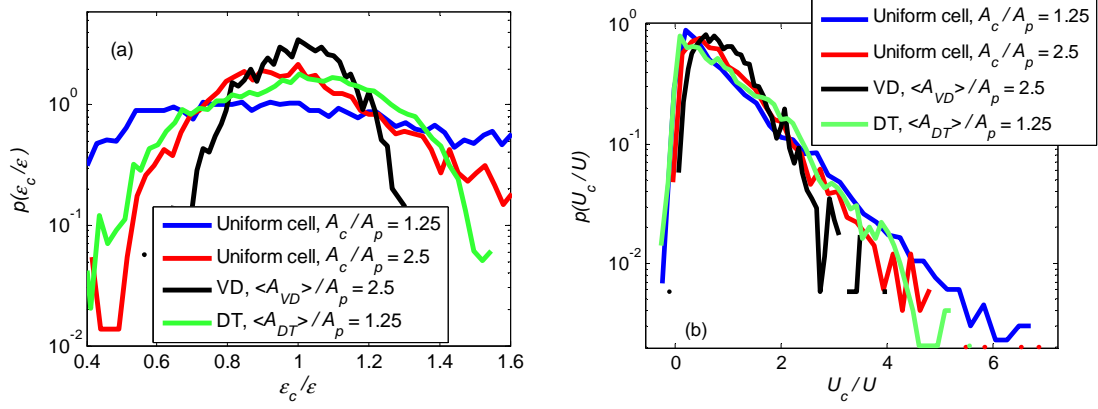
The variation of average velocity at porosity  $\varepsilon = 0.6$  is shown in Fig. 4.13 using (a) Delaunay triangulation and (b) Voronoi polygons as averaging area. The average Voronoi area  $\langle A_{VD} \rangle$  is always identical to the inverse of fibre density (number of fibres per unit area) equal to  $\langle A_{VD} \rangle = 0.5$ . Similarly, the average Delaunay triangle area is half of the Voronoi areas, i.e.  $\langle A_{DT} \rangle = \langle A_{VD} \rangle / 2 = 0.25$ .



**Figure 4.13:** Variation of average velocity at porosity  $\varepsilon = 0.6$  using (a) Delaunay triangulation and (b) Voronoi polygons as an averaging area.

As expected using DT, due to smaller average cell area or higher resolution, one can capture more fluid details and distinguish the dominant fluid channels.

The probability distribution function of cell porosities and average cell velocities at macroscopic porosity  $\varepsilon = 0.6$  is shown in Fig. 4.14. We observe that the PDF of the average cell porosity not only depends on the cell sizes but also on the shape of the cell area. Although the average cell area for both VD and DT are relatively small, however the PDF of cell porosities can be fitted by a Gaussian distribution, i.e. similar to larger uniform cell sizes. Surprisingly, the PDF of average cell velocities is not much affected by the cell shape and can be well approximated by a Gamma distribution for all VD, DT or uniform cells with  $\theta \sim 1$ , see Eq. (4.13).



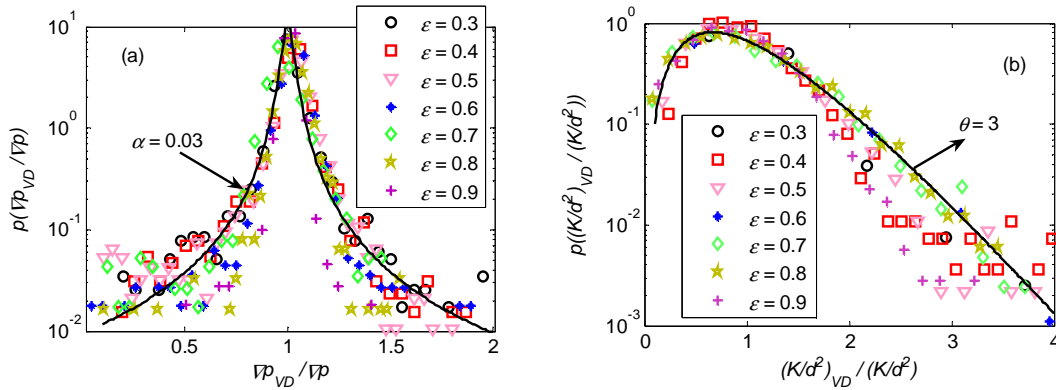
**Figure 4.14:** The probability distribution function of (a) cell porosities and (b) average cell velocities at macroscopic porosity  $\varepsilon = 0.6$ .

Fig. 4.15 shows the PDF of (a) pressure gradients and (b) normalized permeabilities using Voronoi cells at various porosities. We observed that PDF of pressure gradients in Voronoi polygons follows a Cauchy distribution as

$$p\left(\frac{\nabla p_{VD}}{\nabla p}\right) = \frac{1}{\pi} \left( \frac{\alpha}{(\nabla p_{VD} / \nabla p - 1)^2 + \alpha^2} \right), \quad (4.15)$$

where  $\alpha$  is the scale parameter and specifies the half-width at half-maximum (HWHM). For an infinitesimal scale parameter ( $\alpha \sim 0$ ), the Cauchy distribution reduces to Dirac delta function. However, the PDF of permeabilities within each Voronoi cell can be best fitted to a Gamma distribution. The both pressure gradient and permeability distributions seem to be weakly dependent on macroscopic porosity.

The physical interpretation and correlation between these probabilities is a challenge for future study. Another possible extension of the present study is to look at the distributions of pressure gradient or fluid velocity by going to coarser Delaunay or Voronoi cells, similar to the analysis we did for uniform cells, i.e. Fig. 4.11.



**Figure 4.15:** The probability distribution function of Voronoi cell (a) pressure gradients and (b) normalized permeabilities at various porosities. The solid lines show the best Cauchy distribution, Eq. (4.15), and Gamma distribution, Eq. (4.13), at porosity  $\varepsilon = 0.6$  in (a) and (b), respectively.

#### 4.6 Summary and conclusions

The transverse permeability for creeping flow through unidirectional (dis)ordered arrays of fibers/cylinders has been studied numerically using the finite element method (FEM). Several order parameters were introduced and employed to characterize the transition, controlled by the effective packing fraction, from disorder to order. In the present context, the Voronoi and Delaunay diagrams are of interest as they provide information about nearest neighbors and structural properties of fibrous materials. In an ongoing research, the Delaunay triangulations have been also used both as a contact detection tool and a FE mesh in dense particulate flows [58].

The disorder was characterized by the mean and distribution of local parameters, such as the number of faces, shape and regularity of Voronoi polygons, shortest Delaunay triangulation edges and bond orientational angle. The conclusions are:

- The 3<sup>rd</sup> moment of probability distribution of six-sided Voronoi polygons shows an increase at transition porosity  $\varepsilon_i^* \cong 0.39$ .
- The average shape of the Voronoi polygons,  $\langle \zeta \rangle$  increases almost linearly by increasing the porosity regardless of the system size and packing generator algorithm.
- The average area moment of the Voronoi polygons,  $\langle \Phi \rangle$  increases linearly by increasing the porosity with larger slope in ordered regime compared to the disordered one.

- Locally ordered regions, which cause a drop in the macroscopic permeability, can be detected by local definition of bond orientational order parameter.
- The shortest Delaunay triangulation edges (or effective flow channels), have a Gaussian and exponential distribution at high and low porosities, respectively. However, their orientation is not much affected by porosity.

Recently, we observed that the structural transition also affects the flow behavior at inertial (high Reynolds number) regimes [59], see chapter 5 for detail.

Finally, the validity of the macroscopic Darcy's law at various length scales was studied using both uniform and Voronoi/Delaunay cells, in a wide range of porosities. The numerical results show that small averaging cell areas ( $A_c / A_p \sim 1$ ) lead to heterogeneity in flow patterns in which the distribution and average values of permeabilities would deviate from its macroscopic values obtained for the whole domain. Furthermore, I found universal but different distributions for pressure gradient and permeabilities using Voronoi polygons as an averaging area. The application of proposed model/distributions for other macroscopic properties, like heat conductivity, and extension to 3D moving particles is a challenge for future work.

### Acknowledgements:

The authors would like to thank S. Srivastava, A. J. C. Ladd, P. Richard, K.W. Desmond and N. Rivier for helpful discussion and acknowledge the financial support of STW through the STW-MuST program, Project Number 10120.

### References

- [1] R.B. Bird, W.E. Stewart, and E.N. Lightfoot, *Transport Phenomena*, 2nd edn., John Wiley & Sons, 2001.
- [2] J. Happel, *Viscous flow relative to arrays of cylinders*, *AIChE*, 5 (1959) 174–7.
- [3] S. Kuwabara, *The forces experienced by randomly distributed parallel circular cylinders or spheres in a viscous flow at small Reynolds numbers*, *Journal of the Physical Society of Japan*, 14 (1959) 527–32.
- [4] A.S. Sangani, A. Acrivos, *Slow flow past periodic arrays of cylinders with application to heat transfer*, *Int. J. Multiphase Flow*, 8 (1982) 193–206.
- [5] J.E. Drummond, and M.I. Tahir, *Laminar viscous flow through regular arrays of parallel solid cylinders*, *Int. J. Multiphase Flow*, 10 (1984) 515–40.



- [6] B.R. Gebart, Permeability of Unidirectional Reinforcements for RTM, *Journal of Composite Materials*, 26 (1992) 1100–33.
- [7] M.V. Brusckhe and S.G. Advani, Flow of generalized Newtonian fluids across a periodic array of cylinders, *Journal of Rheology*, 37 (1993) 479-98.
- [8] K. Yazdchi, S. Srivastava and S. Luding, Microstructural effects on the permeability of periodic fibrous porous media, *Int. J. Multiphase Flow*, 37 (2011) 956-66.
- [9] J.L. Lage and B.V. Antohe, Darcy's Experiments and the Deviation to Nonlinear Flow Regime, *J Fluids Eng.*, 122 (2000) 619-25.
- [10] S. Whitaker, Flow in porous media I: A theoretical derivation of Darcy's law, *Transp. Porous Media*, 1 (1986) 3-25.
- [11] C.C. Mei, J.-L. Auriault, The effect of weak inertia on flow through a porous medium, *JFM*, 222 (1991) 647–63.
- [12] F.J. Valdes-Parada, J.A. Ochoa-Tapia, J. Alvarez-Ramirez, Validity of the permeability Carman Kozeny equation: A volume averaging approach, *Physica A*, 388 (2009) 789-98.
- [13] X. Chen, T.D. Papathanasiou, The transverse permeability of disordered fiber arrays: A statistical correlation in terms of the mean nearest inter fiber spacing, *Transport in Porous Media*, 71 (2008) 233-51.
- [14] X. Chen, T.D. Papathanasiou, Micro-scale modeling of axial flow through unidirectional disordered fiber arrays, *Composites Science and Technology*, 67 (2007) 1286–93.
- [15] T.D. Papathanasiou, A structure-oriented micromechanical model for viscous flow through square arrays of fiber clusters, *Composites Science and Technology*, 56 (1996) 1055-69.
- [16] K. Yazdchi, S. Srivastava and S. Luding, Micro-macro relations for flow through random arrays of cylinders, *Composites Part A*, 43 (2012) 2007-2020.
- [17] A.J. Katz, A.H. Thompson, Quantitative prediction of permeability in porous rocks, *Phys. Rev. B*, 34 (1986) 8179–81.
- [18] P.M. Reis, R.A. Ingale and M.D. Shattuck, Crystallization of a Quasi-Two-Dimensional Granular Fluid, *Phys. Rev. Lett.*, 96 (2006) 258001.
- [19] M.D. Rintoul and S. Torquato, Computer Simulations of Dense Hard-Sphere Systems, *J. Chem. Phys.*, 105 (1996) 9258- 65.
- [20] L. Oger, A. Gervois, J.P. Trodec, and N. Rivier, Voronoi tessellation of packings of spheres: Topological correlation and statistics, *Philos. Mag. B*, 74 (1996) 177-97.

- [21] P. Richard, L. Oger, Jean-Pau Troadec, and A. Gervois, Geometrical characterization of hard-sphere systems, *Phys. Rev. E*, 60 (1999) 4551–58.
- [22] K. Tsumuraya, K. Ishibashi, K. Kusunoki, Statistics of Voronoi polyhedra in a model silicon glass, *Phys. Rev. B*, 47 (1993) 8552-57.
- [23] D.-Q. Yu, M. Chen, X.-J. Han, Structure analysis methods for crystalline solids and supercooled liquids, *Phys. Rev. E*, 72 (2005) 051202-7.
- [24] N Pittet, Dynamical percolation through the Voronoi tessellations, *J. Phys. A: Math. Gen.*, 32 (1999) 4611–21.
- [25] J.C. Earnshaw, M.B.J. Harrison and D.J. Robinson, Local order in two-dimensional colloidal aggregation, *Phys. Rev. E*, 53 (1996) 6155–63.
- [26] X.H. Zheng and J.C. Earnshaw, Plasma-Dust Crystals and Brownian Motion, *Phys. Rev. Lett.*, 75 (1995) 4214–17.
- [27] A. Okabe, B. Boots, and K. Sugihara, *Spatial Tessellations: Concepts and Applications of Voronoi Diagrams*, John Wiley & Sons, UK, 1992.
- [28] M. de Berg, O. Cheong, M. van Kreveld, M. Overmars, *Computational Geometry Algorithms and Applications*, Springer-Verlag, Berlin, 2008.
- [29] F. Aurenhammer, Voronoi diagrams: A survey of a fundamental geometric data structure, *ACM Comput. Surv.*, 23 (1991) 345-405.
- [30] G. Schliecker, Structure and dynamics of cellular systems, *Advances in Physics*, 51 (2002) 1319-78.
- [31] P. Richard, L. Oger, J.P. Troadec, A. Gervois, Tessellation of binary assemblies of spheres, *Physica A*, 259 (1998) 205-21.
- [32] A. Gervois, C. Annic, J. Lemaitre, M. Ammi, L. Oger, J.-P. Troadec, Arrangement of discs in 2d binary assemblies, *Physica A*, 218 (1995) 403-18.
- [33] Zhu, H.X., Thorpe, S.M., Windle, A.H.: The geometrical properties of irregular two-dimensional Voronoi tessellations. *Philos. Mag. A*, 81 (2001) 2765–83.
- [34] S. Kumar, V. Kumaran, Voronoi neighbor statistics of hard-disks and hard-spheres, *J. Chem. Phys.*, 123 (2005) 074502.
- [35] C.S. Smith, The shape of things, *Scientific American*, 190 (1954) 58-64.
- [36] M.P. Miklius and S. Hilgenfeldt, Analytical Results for Size-Topology Correlations in 2D Disk and Cellular Packings, *PRL*, 108 (2012) 015502.
- [37] G Le Caer and R Delannay, Correlations in topological models of 2D random cellular structures, *J. Phys. A: Math. Gen.*, 26 (1993) 3931-54.

- [38] J. Lemaitre, J.P. Troadec, A. Gervois and D. Bideau, Experimental Study of Densification of Disc Assemblies, *Europhys. Lett.*, 14 (1991) 77-83.
- [39] N. Rivier, Maximum Entropy for Random Cellular Structures, From statistical physics to statistical inference and back, *NATO Sci. Series*, 428 (1994) 77-93.
- [40] J. Lemaitre, A. Gervois, J.P. Troadec, N. Rivier, M. Ammi, L. Oger and D. Bideau, Arrangement of cells in Voronoi tessellations of monosize packing of discs, *Philosophical Magazine Part B*, 67 (1993) 347-62.
- [41] A. Gervois, J.P. Troadec and J. Lemaitre, Universal properties of Voronoi tessellations of hard discs, *J. Phys. A Math. Gen.*, 25 (1992) 6169-77.
- [42] James G. Berryman, Random close packing of hard spheres and disks, *Phys. Rev. A*, 27 (1983) 1053-61.
- [43] B.J. Alder and T.E. Wainwright, Phase Transition in Elastic Disks, *Phys. Rev.*, 127 (1962) 359-61.
- [44] F.T. Lewis, A comparison between the mosaic of polygons in a film of artificial emulsion and the pattern of simple epithelium in surface view (cucumber epidermis and human amnion), *Anat. Rec.*, 50 (1931) 235-65.
- [45] C.H. Desch, The solidification of metals from the liquid state, *J. Inst. Metals*, 22 (1919) 241.
- [46] C. Quilliet, S. Ataei Talebi, D. Rabaud, J. Kafer, S.J. Cox and F. Graner, Topological and geometrical disorders correlate robustly in two-dimensional foams, *Philosophical Magazine Letters*, 88 (2008) 651-60.
- [47] J.A. Glazier, S.P. Gross, and J. Stavans, Dynamics of two-dimensional soap froths, *Phys. Rev. A*, 36 (1987) 306-312.
- [48] M. Clusel, E. I. Corwin, A. O. N. Siemens, and J. Brujic, A 'granocentric' model for random packing of jammed emulsions, *Nature*, 460 (2009) 611-15.
- [49] F. Moucka and I. Nezbeda, Detection and Characterization of Structural Changes in the Hard-Disk Fluid under Freezing and Melting Conditions, *PRL*, 94 (2005) 040601.
- [50] A.R. Abate and D.J. Durian, Approach to jamming in an air-fluidized granular bed, *PRE*, 74 (2006) 031308.
- [51] Z. Wang, A.M. Alsayed, A.G. Yodh, and Y. Han, Two-dimensional freezing criteria for crystallizing colloidal monolayers, *J. Chem. Phys.*, 132 (2010) 154501.
- [52] V.S. Kumar and V. Kumaran, Bond-orientational analysis of hard-disk and hard-sphere structures, *J. Chem. Phys.*, 124 (2006) 204508.

- [53] B.I. Halperin and D.R. Nelson, Theory of Two-Dimensional Melting, *Phys. Rev. Lett.*, 41 (1978) 121-4.
- [54] A. Jaster, Computer simulations of the two-dimensional melting transition using hard disks, *PRE*, 59 (1999) 2594-2602.
- [55] T. Kawasaki and A. Onuki, Construction of a disorder variable from Steinhardt order parameters in binary mixtures at high densities in three dimensions, *J. Chem. Phys.*, 135 (2011) 174109.
- [56] A.R. Kansal, T.M. Truskett, S. Torquato, Nonequilibrium hard-disk packings with controlled orientational order, *J. Chem. Phys.*, 113 (2000) 4844-51.
- [57] P.C. Carman, Fluid flow through granular beds, *Transactions of the Institute of Chemical Engineering*, 15 (1937) 150–66.
- [58] S. Srivastava, K. Yazdchi, S. Luding, Meso-scale coupling of FEM/DEM for fluid-particle interactions, (2012) in preparation.
- [59] K. Yazdchi, S. Luding, Towards unified drag laws for inertial flow through fibrous materials, *CEJ*, 207 (2012) 35-48.

# 5

## Towards unified drag laws for inertial flow through fibrous materials

*"The scientist is not a person who gives the right answers; he's one who asks the right questions"*

*~Claude Levi-Strauss~*

## Abstract

I give a comprehensive survey of published experimental, numerical and theoretical work on the drag law correlations for fluidized beds and flow through porous media, together with an attempt of systematization. Ranges of validity as well as limitations of commonly used relations (i.e. the Ergun and Forchheimer relations for laminar and inertial flows) are studied for a wide range of porosities. The pressure gradient is linear in superficial velocity,  $U$  for low Reynolds numbers,  $Re$ , referred to as Darcy's law. Here, I focus on the non-linear contribution of inertia to the transport of momentum at the pore scale, and explain why there are different non-linear corrections in the literature.

From fully resolved finite element (FE) results, for both ordered and random fibre arrays, (i) the weak inertia correction to the linear Darcy relation is third power in  $U$ , up to small  $Re \sim 1-5$ . When attempting to fit the data with a particularly simple relation, (ii) a non-integer power law performs astonishingly well up to the moderate  $Re \sim 30$ . However, for randomly distributed arrays, (iii) a quadratic correction performs quite well as used in the Forchheimer (or Ergun) equation, from small to moderate  $Re$ .

Finally, as main result, the macroscopic properties of random, fibrous porous media are related to their microstructure (arrangement) and porosity. All results ( $Re < 30$ ) up to astonishingly large porosity,  $\varepsilon \sim 0.9$ , scale with  $Re_g$ , i.e. the gap Reynolds number, that is based on the average second nearest neighbor (surface to surface) distances. This universal result is given as analytical closure relation, which can readily be incorporated into existing multi-phase flow codes. In the transition regime, the universal curve actually can be fitted with a non-integer power law (better than  $\sim 1\%$  deviation), but also allows to define a critical  $Re_{gc} \sim 1$ , below which the third power correction holds and above which a correction with second power fits the data considerably better.<sup>1</sup>

## Highlights

- Extensive review of experimental, numerical and theoretical work on drag law correlations
- Finite element simulation of inertial flow through ordered and random fibre arrays
- The macroscopic properties of fibrous media are related to their microstructure and porosity
- Universal scaling of the friction factor with the “gap” Reynolds number up to  $Re_g < 10$

---

<sup>1</sup> K. Yazdchi and S. Luding, Towards unified drag laws for inertial flow through fibrous materials, Chemical Engineering Journal, 207 (2012) 35-48.

A. Narvaez, K. Yazdchi, S. Luding and J. Harting, From creeping to inertial flow in porous media: a lattice Boltzmann - Finite Element comparison, JSTAT, (2012) submitted.

K. Yazdchi, S. Srivastava and S. Luding, On the transition from creeping to inertial flow in arrays of cylinders, Proceedings of IMECE (2010), Vancouver, Canada.

## 5.1 Introduction

Transport phenomena in porous media have been the focus and interest of numerous studies for the past decades. This interest stems from a wide range of applications in such industries as chemical, mechanical, geological, environmental, petroleum, etc [1-5]. The flow conditions encountered are broad enough to cover a wide range of Reynolds numbers ( $Re$ ) and porosities. In practice, three distinct flow regimes are commonly defined in the literature in terms of Reynolds number: (i) stationary Darcy or creeping flow, (ii) steady, laminar inertial flow and (iii) unsteady chaotic/turbulent flow regimes. As an example, creeping flows (i.e.  $Re \ll 1$ ) may be encountered in ground water flows, composites manufacturing and filtering, whereas inertial flows are found in applications such as heat exchangers or packed bed chemical reactors. Highly turbulent flow is expected, e.g., in gas-fluidized beds. The flow regimes studied in this chapter are limited to regimes (i) and (ii). Several macroscopic parameters are often needed to complete coarse grained models that are employed to describe such applications. This has motivated the research in the development of relationships to describe macroscopic parameters, such as permeability and inertial coefficients, for different kinds of porous media at various porosities and flow regimes.

Most porous media are particulate, but some are composed of long particles/fibres and, therefore, may be considered as fibrous media. They are encountered in a variety of modern technology applications, predominantly in the manufacturing of fibre-reinforced composites, with extensive use in the aerospace and automobile industries.

With the recent progress in computational and numerical tools, one can now perform detailed calculations of heavily loaded, fluid-particle flows, based on two-fluid models (TFM) and/or the discrete particle method (DPM) [3, 4]. However, these methods require the knowledge of several constitutive laws (i.e. the interphase momentum-transfer coefficient of the gas/fluid phase acting on the particles/solid). Accurate drag laws are a basic requirement in simulations based on DPM or TFM to be successfully used in the design and optimization of industrial processes. Such correlations have a strong dependence on the pore structure and pore-level physics, which generally requires them to be estimated experimentally or through the use of existing empirical relations.

At the macroscopic level and in the limit of creeping flow regimes ( $Re \sim 0$ ), the pressure gradient  $\nabla p$ , and the flow rate have a linear relation, known as Darcy's law:

$$-\nabla p = \frac{\mu}{K} U \quad , \quad (5.1)$$

where  $\mu$  and  $U$  are viscosity and *superficial* (discharge) velocity, respectively. The proportionality constant  $K$ , is called the permeability of the medium, which strongly depends on porosity and microstructure (e.g., fibre/particle shape and arrangement, void connectivity and inhomogeneity of the medium). The effect of several microstructural parameters on macroscopic permeability was investigated for ordered (chapter 2) and disordered (chapter 3) fibrous media, see Refs. [5-7] and references therein.

Darcy's law was originally obtained from experiments [8] and later derived using upscaling [9], homogenization [10, 11] and volume averaging [12, 13] techniques. It has been shown that Darcy's law actually represents the momentum equation for Stokes flow averaged over a representative volume element (RVE), implying that it is valid only in the creeping flow regime [14].

The effect of fluid inertia, on the other hand, is a more complex problem, lending itself to numerical rather than analytical treatment. Active research has been dedicated to derive adequate corrections to the linear relationship in Eq. (5.1) from numerical, theoretical, and experimental points of view. Koch and Ladd [15] and Hill et al. [16] simulated moderate Reynolds number flows through periodic and random arrays of aligned cylinders and spheres using the Lattice Boltzmann Method (LBM). They showed that the inertial term made a transition from being linear to being quadratic in random arrays. The inertial effect became smaller at the volume fraction approaching close packing due to increased drag forces through the narrowing channels. The experimentation that proved this nonlinear relation was carried out by Forchheimer [17], who indicated that there exists a quadratic term of the flow rate when the Reynolds number is sufficiently high. While the LBM has been successfully applied for the simulation of porous media flow in the creeping regime [18-20], its applicability for high Reynolds numbers has been the subject of more speculation and debate due to selection of parameters, resolution and the necessity to reduce compressibility effects [21, 22]. Andrade et al. [23] demonstrated that, for a 2D disordered porous structure at high porosity, the incipient departure from the Darcy law could be observed already in the steady, laminar inertial flow before arriving at turbulent/chaotic regime.

To date, mainly empirical relations, such as by Ergun [24], and their components, the Carman-Kozeny (viscous term) and Burke-Plummer (inertial term) equations, have proved to be quite useful for predicting the pressure drop in packed beds [25, 26]. Liu et al [27] devised a semi-empirical formula for the pressure drop, which incorporates the tortuosity, the curvature ratio and the variation of the pore cross-sectional area. Jackson and James [28] conducted a comprehensive review of the literature on a variety of theoretical models and presented a large collection of experimental data for both natural and synthetic fibrous media. A recent discrete particle study by Bokkers et al. [29] showed that, with respect to bubble formation in fluidized beds, the drag relations derived from the lattice-Boltzmann simulations of Hill et al. [16] yielded better agreement with the experimental observations than the traditional Ergun and Wen & Yu [30] correlations. While the latter relation remains the most widely used in chemical engineering, an accurate description for the interphase momentum transfer has been a subject of debate. This has motivated the research in the development of more accurate relationships to describe the macroscopic momentum transfer in terms of microscopic pore-scale parameters.

Most of the previously obtained drag laws are only valid for 3D, spherical particles on a packed bed. Although the drag relation for 2D fibrous materials and 3D packed beds are quite different (for instance in 2D the drag diverges in the limit of close packing), my attempt is to check the validity of those relations for 2D systems. I establish the relationship between microscopic and macroscopic properties of fibrous media by



conducting a systematic study using numerical simulations based on the finite element method (FEM). In order to get a better understanding of the state-of-the-art on non-Darcy flow, literature concerning the theoretical basis of the Forchheimer equation and experimental work on the identification of flow regimes is reviewed in Section 5.2. After presenting the numerical method used to compute the permeability and inertial coefficients, results are discussed in Section 5.3. The steady state fluid flow across uni-directional arrays of cylinders are considered, for both ordered and disordered configurations. Accurate, high resolution computations were carried in order to investigate the existence of the different regimes and the corresponding scaling laws. The effects of several structural parameters, namely porosity, disorder and fibre-shape on the flow behavior at various regimes are discussed in detail. The chapter is concluded in Section 5.4 with a summary and outlook for future work.

## 5.2 Theoretical background

Flows in porous media can be studied at either microscopic or macroscopic scales. For the former scale the flow through individual pores is computed by solving the mass and momentum equations (i.e. the Navier–Stokes (NS) equation) numerically, whereas for the latter a continuum description is usually adopted based on volume averaging of the equations pertaining to microscopic scales. The linking of these two descriptions constitutes the well known scaling-up problem, which usually provides macroscopic properties in terms of the permeability, i.e. the ability of a porous material to transmit fluids. Although the permeability can, in principle, provide quantitative correlations between morphological features of pore geometry and its capacity to transmit liquid, its values depend on many factors such as porosity, typical length scale of pores, grain size distribution, shape, anisotropy and tortuosity of pore connections, see Refs. [5-7] and references therein (see chapters 2 and 3). Therefore, the permeability determined either analytically or empirically for porous media with complex structures involves considerable uncertainty – one can not determine microscopic properties only from the macroscopic permeability.

As mentioned already, Darcy’s law is the most widely used empirical correlation for the calculation of the pressure drop across a homogeneous, isotropic, unbounded and non-deformable porous medium. It is strictly valid for incompressible and isothermal Stokes flow ( $Re = 0$ ) of Newtonian fluids [9]. However, it is usually applicable in engineering applications for  $Re < 1$ , defined by  $Re = \rho Ul / \mu$  where  $l$  and  $\rho$  are the typical pore size of the structure and density of the fluid, respectively. Darcy’s law, since it lacks, among other reasons, the flow inhomogeneity/variability<sup>2</sup>, is not valid at the interface of a porous medium-solid or porous medium-free flow. Brinkman [31] added a diffusion-type term to Darcy’s law, leading to

$$-\nabla p = \frac{\mu}{K} U - \mu \nabla^2 U \quad . \quad (5.2)$$

---

<sup>2</sup> It can not account for the no-slip boundary condition at the solid boundary of the porous medium.

Brinkman's equation is, like Darcy's law, inertia-free and hence valid only for creeping flows. Recently, Auriault [32] discussed the validity and limitations of Brinkman's equation for "classical" porous media, swarms of low concentration particles and fibrous media at high porosities.

In the continuum approach one describes mass and momentum balance equations at macroscopic scale, using a specific averaging procedure. Therefore, it is difficult to adequately determine the averaging domain. Using a continuum approach, Hassanizadeh and Gray [33] developed a set of equations to describe the macroscopic behavior of fluid flow through porous media. Linearization of these equations yields a Darcy equation at low velocities.

Although the physical nature of the deviation from Darcy's law is still unclear and may have several causes (probably acting together), empirical relationships correlate the pressure drop and average fluid velocity in porous media. To account for the non-linear behavior of the flow in porous media, Forchheimer [17] added a quadratic velocity term to represent the microscopic inertial effect, and corrected Darcy's equation to get the Forchheimer equation

$$-\nabla p = \frac{\mu}{K}U + \beta\rho U^2, \quad (5.3)$$

where the constant,  $\beta$  is referred to as the non-Darcy coefficient which, like permeability, is an empirical value that depends on the micro-parameters of porous media. Just as is the case with Darcy's law, Forchheimer's law was originally postulated heuristically to fit experimental data. However, during the past decades there has been an effort to derive it from first principles. Some of the techniques used are matched asymptotic expansions [34], the capillary model [35], hybrid mixture theory [36] and volume averaging [12, 37, 38]. The physical justification of the quadratic nature of the correction was supported either by intuition or by dimensional analysis and the analogous turbulent kinetic energy loss in straight tubes [39]. Moutsopoulos et al. [40] investigated phenomenological relations for the Forchheimer equation experimentally and theoretically for both homogeneous and heterogeneous media. Using a homogenization approach, Chen et al. [41] claim that the nonlinear filtration law is quadratic. By generalizing the Forchheimer equation, Ergun obtained the following empirical relation for homogenous, packed beds of randomly distributed spheres:

$$-\nabla p = A \frac{(1-\varepsilon)^2}{\varepsilon^3} \frac{\mu U}{d^2} + B \frac{(1-\varepsilon)}{\varepsilon^3} \frac{\rho U^2}{d}, \quad (5.4)$$

where  $d$  is the average diameter of the particles in the domain and  $\varepsilon$  is the porosity<sup>3</sup>. After analysis of a large quantity of experimental data, Ergun concluded that their best representation could be obtained with  $A = 150$  and  $B = 1.75$ . However, in subsequent studies these values have been found to vary considerably with shape, porosity and Re

---

<sup>3</sup> Comparing Eqs. (5.3) and (5.4), one can relate the parameters  $A$ ,  $B$ , and  $\varepsilon$  to  $K$  and  $\beta$ .

number [42, 43]. In particular, after testing the Ergun equation using many more data than ever before, MacDonald et al. [42] found that  $A = 180$ , and  $B = 1.8$  (smooth particles) or 4.0 (rough particles) give the best fits to all of the data. Besides the Ergun equation, there are correlations that use the non-dimensional particle friction factor,  $f_p$ , through the following definition

$$f_p = \frac{-\nabla p d}{\rho U^2}. \quad (5.5)$$

By combining Eqs. (5.5) and (5.3), the Forchheimer equation can be written as:

$$f_p = \frac{1}{\text{Re} K'} + \beta', \quad (5.6)$$

where  $\text{Re} = \rho U d / \mu$ ,  $K' = K / d^2$  and  $\beta' = \beta d$  are the Reynolds number (based on diameter  $d$ ), the normalized permeability and the modified non-Darcy coefficient, respectively. The latter two parameters  $K'$  and  $\beta'$ , can be considered as the non-dimensional, macroscopic viscous and inertial coefficients with the advantage of an expected constant friction factor in the inertial regime. Looking at the literature, one found several definitions and relations between friction factor and  $\text{Re}$  (or sometimes pressure gradient and  $U$ ) which makes it difficult to establish a one-to-one comparison. Table 5.1 summarizes these definitions and their relations.

In Table 5.2, the available modifications of Ergun's equation and their range of validity are listed as functions of the particle  $\text{Re}$  number,  $\text{Re}_p = \text{Re} / (1 - \varepsilon)$ . Therefore, most equations have the typical porosity term,  $(1 - \varepsilon) / \varepsilon^3$ , for low  $\text{Re}$ , with various different constants and strongly varying further terms [42, 60, 62-64, 67-69] representing the effect of wall, shape, etc. A few of the equations also have non-linear corrections in the first term [54, 59, 66], and the last class are sums of several powers of  $\text{Re}$  used to fit into available experimental/numerical data [52, 53, 61]. A more complete list of correlations for the viscous term, i.e. at low  $\text{Re}$  numbers, of 2D fibrous materials can be found in Ref. [5]. Recently, Barree and Conway [44] conducted experiments suggesting that Forchheimer's equation is only valid over a limited range of velocities. Derivations using volume averaging were undertaken by Ruth and Ma [12], and Whitaker [38]. However, Ruth and Ma [12] explain that microscopic inertial effects are neglected in volume-averaging techniques and therefore cannot be used to derive a macroscopic law. They point out that the Forchheimer equation is not unique, and any number of polynomials could be used to describe nonlinear behavior due to inertia in non-laminar flow. This is confirmed in Bourgeat et al. [45], where the nonlinear filtration law is obtained as an infinite series in integer powers of the local Reynolds number. More recently, Balhoff et al. [46] used the method of homogenization to develop a general polynomial filtration law for low Reynolds numbers. In Marušić-Paloka and Mikelić [47], the existence, uniqueness and regularity of general non-local filtration law was rigorously established in the homogenization limit when the pore size tends to zero.

**Table 5.1:** Various definitions and relations between friction factors and Re (or pressure gradient and superficial velocity,  $U$ )

Friction factor – Re (or pressure gradient – $U$ ) relation	Comment
$-\nabla p \sim U$	Linear Darcy's law for creeping flow, Eq. (5.1)
$-\nabla p \sim U - \nabla^2 U$	Brinkman's equation for creeping flow at high porosities, Eq. (5.2)
$-\nabla p \sim U + U^2$	Forchheimer (Ergun) equation, quadratic correction to Darcy's law, Eq. (5.3)
$-\nabla p \sim U + U^3$	Cubic correction to Darcy's law valid at small Re, Eq. (5.7)
$f_p \sim -\nabla p / U^2 \sim \text{Re}^{-1} + \beta'$	Particle friction factor as function of Re. $\beta'$ is the inertial, porosity dependent parameter, see Table 5.2
$f' \equiv f_p \text{Re} \sim -\nabla p / U \sim \alpha' + \text{Re}^\lambda$	Non-integer, $\lambda$ , power law fit, used in this chapter, Eq. (5.8); $\alpha'$ is the viscous, porosity dependent term
$f^* \sim f' - \alpha' \sim \text{Re}_g^\lambda$	Isolated inertial term used for scaling the data in Appendix 5.D; $\text{Re}_g$ is "gap" Re number

One of the important observations from Wodié and Levy [48], Mei and Auriault [11], and Rasoloarijaona and Auriault [49] was that for an isotropic porous medium, the quadratic terms cancel and one has a cubic filtration law given by

$$-\nabla p = \frac{\mu}{K} U + \frac{\gamma^* \rho^2}{\mu} U^3 \quad \Rightarrow \quad f_p = \frac{1}{\text{Re} K} + \gamma^* \text{Re}, \quad (5.7)$$

where  $\gamma^*$  is a porosity dependent dimensionless parameter. This observation is confirmed analytically and numerically by Firdaouss et al. [50] and for periodic two-dimensional arrays of cylinders arranged in a regular pattern by Couland et al. [51]. In most cases, the cubic law is only valid at very low velocities ( $\text{Re} < 1$ , where Darcy's law is approximately valid anyway), and the quadratic Forchheimer equation appears applicable at higher, moderate velocities ( $1 < \text{Re} < 10$ ). Nonetheless, these findings are significant because they suggest that any power law with an integer power, such as in the Forchheimer equation, may not be universal and only valid for a limited range of velocities and porosities.

Despite extensive previous work, our understanding of the physical reasons for non-Darcy flow is incomplete. To better understand the microscopic origin of these correlations, I conduct a set of FE simulations on both ordered and disordered arrays of cylinders in a wide range of Reynolds numbers in the next section.

**Table 5.2:** Available modifications of the Ergun equation in terms of the particle friction factor,  $f_p$  and the particle Reynolds number  $Re_p = Re/(1-\varepsilon) = \frac{\rho U d}{(1-\varepsilon)\mu}$ . Unless explicitly stated, the relations are valid for 3D, disordered systems.

Author	$f_p$	Range of validity
Ergun [24]	$\left(\frac{1-\varepsilon}{\varepsilon^3}\right)\left(\frac{150}{Re_p} + 1.75\right)$	$\varepsilon < 0.8$
MacDonald et al. [42]	$\left(\frac{1-\varepsilon}{\varepsilon^3}\right)\left(\frac{180}{Re_p} + B'\right)$	$B' = 1.8$ , smooth particles $B' = 4$ , rough particles
Rose [52]	$1000 Re_p^{-1} + 60 Re_p^{-0.5} + 12$	Mean value of $Re_p \cong 140$
Rose and Rizk [53]	$1000 Re_p^{-1} + 125 Re_p^{-0.5} + 14$	$1000 < Re_p < 6000$
Hicks [54]	$6.8 \frac{(1-\varepsilon)^{1.2}}{\varepsilon^3} Re_p^{-0.2}$	$500 < Re_p < 60000$
Tallmadge [55]	$\frac{150}{Re_p} \frac{(1-\varepsilon)^2}{\varepsilon^3} + \frac{4.2(1-\varepsilon)^{1.166}}{\varepsilon^3} Re_p^{-1/6}$	$0.1 < Re_p < 10^5$
Lee and Ogawa [56]	$\frac{1}{2} \left(\frac{12.5}{\varepsilon^3} (1-\varepsilon)^2\right) (29.32 Re_p^{-1} + 1.56 Re_p^{-n} + 0.1)$ $n = 0.352 + 0.1\varepsilon + 0.275\varepsilon^2$	$1 < Re_p < 10^5$
Kürten et al. [57]	$\left(\frac{25}{4\varepsilon^3} (1-\varepsilon)^2\right) (21 Re_p^{-1} + 6 Re_p^{-0.5} + 0.28)$	$0.1 < Re_p < 4000$
Montillet et al. [58]	$\alpha (1000 Re_p^{-1} + 60 Re_p^{-0.5} + 12)$ $\alpha = 0.061 \left(\frac{1-\varepsilon}{\varepsilon^3}\right) \left(\frac{D}{d}\right)^{0.2}$	$10 < Re_p < 2500$ , $D$ : bed diameter
Özdiñç et al. [59]	$69.785 \left(\frac{d}{L}\right) \left(Re_p \left(\frac{d}{L}\right) \varepsilon^7\right)^{-0.4733}$	$675 < Re_p < 7772$ $L$ : bed length
Ozahi et al. [60]	$\left(\frac{1-\varepsilon}{\varepsilon^3}\right) \left(\frac{D}{d}\right) (3 \times 10^{-5} Re_p - 66.487 Re_p^{-1} + 0.1539)$	$800 < Re_p < 8000$ , $D$ : bed diameter
Gibilaro et al. [61]	$(17.3 Re_p^{-1} + 0.336(1-\varepsilon)) \varepsilon^{-4.8}$	In fluidized suspensions

Benyahia et al. [62]	$\frac{180(1-\varepsilon)}{\text{Re}_p \varepsilon^3} + 9F_3(1-\varepsilon)$ $F_3 = 0.0673 + 0.212(1-\varepsilon) + 0.0232\varepsilon^{-5}$	$\varepsilon < 0.6, \text{Re}_p > \frac{2F_3}{F_1(1-\varepsilon)},$ $F_1 = 0.11 + 0.00051e^{11.6(1-\varepsilon)}$
Molerus [63]	$\left(\frac{1-\varepsilon}{\varepsilon^2}\right) \left( \left( \frac{18}{1-\varepsilon} + \frac{49.5}{\varepsilon} \right) \text{Re}_p^{-1} + \frac{0.69}{\varepsilon^2} \right)$	$\varepsilon < 0.7$
Kovács [64]	$\left(\frac{1-\varepsilon}{\varepsilon^3}\right) \left( \frac{144}{\text{Re}_p} + 2.4 \right)$	$10 < \text{Re}_p(1-\varepsilon) < 100$
Kadlec and Knight [65]	$\left(\frac{1-\varepsilon}{\varepsilon^3}\right) \left( \frac{255}{\varepsilon^{0.7}(1-\varepsilon)\text{Re}_p} + 2 \right)$	In fluidized suspensions
Foscolo et al. [66]	$\left(\frac{1-\varepsilon}{\varepsilon^{4.8}}\right) \left( \frac{17.3}{\text{Re}_p(1-\varepsilon)} + 0.336 \right)$	Laminar and turbulent regimes, $\varepsilon > 0.4$
Mehta and Hawley [67]	$\left(\frac{1-\varepsilon}{\varepsilon^3}\right) M \left( \frac{150}{\text{Re}_p} M + 1.75 \right)$	$M = 1 + \frac{2d}{3D(1-\varepsilon)},$ D: bed diameter
Du Plessis [68]	$\left(\frac{1-\varepsilon}{\varepsilon^3}\right) \left( \frac{A}{\text{Re}_p} + \varepsilon^2 / \left(1 - (1-\varepsilon)^{2/3}\right)^2 \right),$ $A = \frac{41\varepsilon^2}{(1-\varepsilon)^{2/3} \left(1 - (1-\varepsilon)^{1/3}\right) \left(1 - (1-\varepsilon)^{2/3}\right)}$	Packed bed of spherical particles
Reichert [69]	$\left(\frac{1-\varepsilon}{\varepsilon^3}\right) \left( \frac{K_1 A_w^2}{\text{Re}_p} + B_w \right),$ $A_w = 1 + \frac{2}{3(D/d)(1-\varepsilon)}, B_w = \frac{1}{\left(k_1(d/D)^2 + k_2\right)^2}$	Spheres: $K_1 = 154, k_1 = 1.5, k_2 = 0.88$ Cylinders: $K_1 = 190, k_1 = 2, k_2 = 0.77$ D: bed diameter

<p>Martin et al. [70]</p>	$b\varepsilon^{-n} \left( \text{Re}_p \frac{\sqrt{K}}{d} (1-\varepsilon) \right)^m \frac{d}{\sqrt{K}}$	<p>Square and triangular fibre arrays, with <math>0.8 &lt; \varepsilon &lt; 0.99</math> and <math>3 &lt; \text{Re}_p &lt; 160</math>. The <math>n</math>, <math>m</math> and <math>b</math> are fitting parameters.</p>
<p>Papathanassiou et al. [26]</p>	$\frac{d^2}{\text{Re}_p K (1-\varepsilon)} + 0.08 \frac{(1-\varepsilon)d}{\varepsilon \sqrt{K}}$	<p>Square and hexagonal fibre arrays, with <math>0.3 &lt; \varepsilon &lt; 0.6</math> and <math>0 &lt; \text{Re}_p &lt; 400</math></p>
<p>Tamayol et al. [71]</p>	$\frac{d^2}{\text{Re}_p K (1-\varepsilon)} + \frac{(a+b\varepsilon)^{-1/c} d}{\sqrt{K}}$	<p>1D, 2D and 3D ordered fibrous media in the range of <math>0.35 &lt; \varepsilon &lt; 0.95</math> and <math>0.01 &lt; \text{Re}_p &lt; 4000</math>. The <math>a</math>, <math>b</math> and <math>c</math> are fitting parameters.</p>
<p>Koch et al. [15]</p>	<p>(a) <math>\frac{k_1}{\text{Re}_p} + k_2 \text{Re}_p</math></p> <p>(b) <math>\frac{c_1}{\text{Re}_p} + c_2</math></p>	<p>(a) For both periodic and random fiber arrays at <math>\text{Re} &lt; 1</math>; <math>k_1</math> and <math>k_2</math> are porosity dependent parameters.                  (b) For random arrays at <math>\text{Re} &gt; 5</math> (similar to Ergun relation); <math>c_1</math> and <math>c_2</math> are porosity dependent parameters.</p>
<p>Tanino and Nepf [72]</p>	$\frac{\alpha_0}{\text{Re}_p} + \alpha_1$	<p>Randomly distributed, rigid, emergent circular cylinders in the range of <math>0.65 &lt; \varepsilon &lt; 0.9</math> and <math>70 &lt; \text{Re}_p &lt; 6850</math> (similar to Ergun relation). The <math>\alpha_0</math> and <math>\alpha_1</math> are porosity dependent fitting parameters.</p>

### 5.3 Numerical results

This section is dedicated to finite element (FE) based model simulations of both ordered and disordered fibre arrays at various porosities and flow regimes. Alternatives to the FE method like the lattice Boltzmann method (LBM) can also deal with complex pore geometries and boundary conditions in the inertial regime, but are discussed and compared elsewhere [22]. The results on the friction factor (both the viscous and inertial components) as function of porosity, structure, shape, etc., are presented and discussed.

#### 5.3.1 Ordered structure

I start the analysis with the case of a 2D regular periodic array of cylinders, perpendicular to the flow direction, as shown in Fig. 5.1. These models rely on the assumption that the porous media is periodic and thus can be divided into unit cells that are then also representative volume elements (RVE). The friction factor is then determined by modeling the flow through these, more or less, idealized cells.

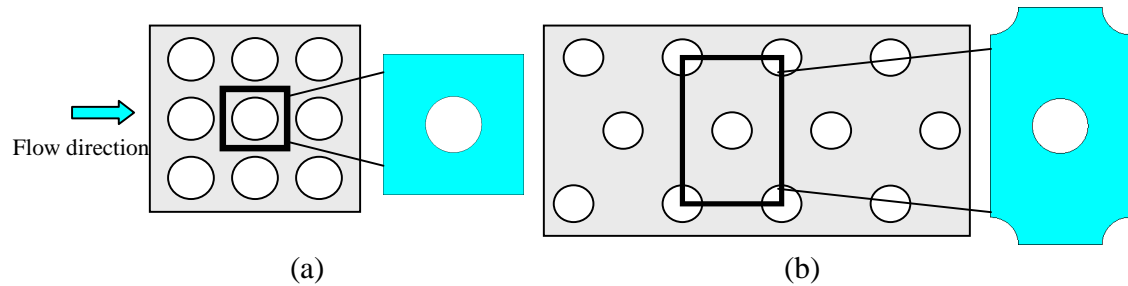


**Figure 5.1:** The geometry of the unit cells used for (a) square and (b) hexagonal configurations.

##### 5.3.1.1 Computational method and boundary conditions

The FE software ANSYS<sup>®</sup> is used to calculate the horizontal superficial velocity,  $U$ , from the results of the computer simulations as  $U = \frac{1}{A} \int_{A_f} u dA$ , where  $A$ ,  $A_f$  and  $u$  are the total

area of the unit cell, the area of the fluid and the intrinsic fluid velocity, respectively. In the flow domain, the steady state NS equations combined with the continuity equations were discretised into an unstructured, triangular element. They were then solved using segregated, sequential solution algorithm. The matrices developed from assembly of linear triangular elements are then solved based on a Gaussian elimination algorithm. Some more technical details are given in Refs. [5-7]. The mesh size effect is examined by



comparing the simulation results for different resolutions (data not shown here). At the left and right pressure- and at the top and bottom periodic-boundary conditions are applied. No-slip boundary conditions, i.e. zero velocity are applied on the surface of the particles/fibres. Computations were performed for Reynolds numbers  $10^{-5} < \text{Re} < 30$  and porosity  $0.3 < \varepsilon < 0.9$ , assuming that the stationary solution is still physically valid in the upper range of this Reynolds numbers.

### 5.3.1.2 Generalized Forchheimer equation

The validity of the Forchheimer equation for ordered structures (namely square and hexagonal configurations) is studied in this section. A generalized non-dimensional form of the Forchheimer Eq. (5.3) can be derived by postulating a power law and multiplying the friction factor by Re, so that:

$$-f' = \frac{1}{K'} + \gamma \left( \frac{U}{U^*} \right)^\lambda \equiv \frac{1}{K'} + \gamma \text{Re}^\lambda \quad (5.8)$$

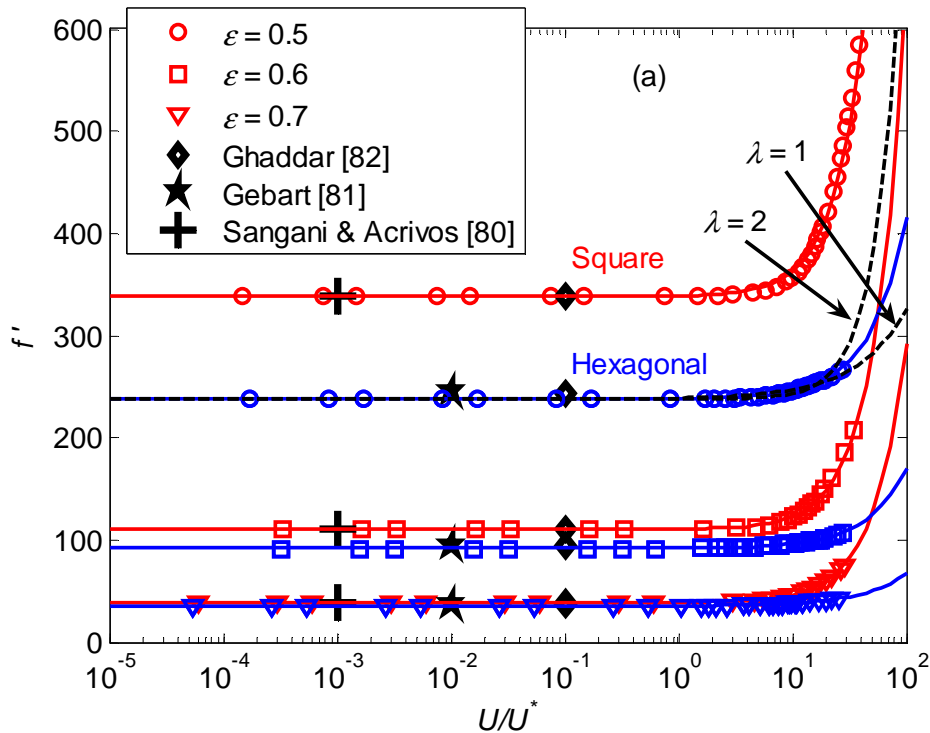
where  $f' = d^2 \nabla p / (\mu U) \equiv f_p \text{Re}$  and  $U^* = \mu / (\rho d)$  are, by definition, modified friction factor and scaled velocity, respectively. The normalized permeability  $K' = K / d^2$  and non-dimensional inertial coefficients  $\lambda$  and  $\gamma$ , in general, depend on the porosity and structure of the medium. The power  $\lambda$  represents the deviation from Darcy's regime ( $f' = \text{const.}$ ), so that the non-linear correction can be isolated by studying  $-f' - 1/K'$  (refer to Appendix 5.C). In case of  $\lambda = 1$ , Eq. (5.8) reduces to the Ergun equation (Eq. (5.4) or (5.6)) with  $K' = \varepsilon^3 / (150(1-\varepsilon)^2)$  and  $\gamma = 1.75(1-\varepsilon) / \varepsilon^3$ . Similarly, for  $\lambda = 2$ , Eq. (5.8) reduces to Eq. (5.7) with  $\gamma = \gamma^*$ . More discussion on the dependence of normalized permeability,  $K'$  on porosity and pore-structure for (dis)ordered fibrous medium is given in [5, 6] and references therein (chapters 2 and 3). In the following, I rather focus on the influence of micro-structural parameters on the inertial coefficients  $\lambda$  and  $\gamma$ , while  $1/K'$  is the low-Re permeability that only depends on porosity.

Fig. 5.2(a) shows the variation of the modified friction factor as function of normalized velocity,  $U/U^* \equiv \text{Re}$ , for square (red) and hexagonal (blue) configurations for three different porosities. The results are compared against lubrication theory of Gebart [81], FE results of Ghaddar [82] and numerical results of Sangani and Acrivos [80] for a creeping flow regime. The solid lines represent the best least square fit to the FE data using Eq. (5.8) with the power as the free parameter, while the upper black dashed line (only one is shown at  $\varepsilon = 0.6$ ) represents a fit to the cubic deviation ( $\lambda = 2$ ) from the Darcy regime, which is almost perfect (99.99% agreement) for  $\text{Re} < 3$ , but strongly overestimates the results for larger Re. As examples, the hexagonal structures at  $\varepsilon = 0.6, 0.7, 0.8$  correspond to  $1/K' = 91.5584, 35.3612, 12.3190$ , and  $\gamma_2 = 0.06993, 0.05330, 0.04297$ , respectively. Note that for all fits, first the constant, low Re regime was fitted and then the nonlinear correction was derived. While the cubic correction-term ( $\lambda = 2$ ) is

applicable, it does not give a good prediction for larger  $Re$ . Therefore, I will discuss fits with non-integer  $\lambda$  values since they are good approximations up to  $Re < 30$ .

As expected, by increasing the porosity, the normalized permeability,  $K'$ , increases, i.e. for higher pressure gradients the flow regime changes from Darcy (horizontal line) into inertial (nonlinear) regime. For square configurations the transition starts at lower velocities (i.e.  $Re \cong 10$ ) compared to the hexagonal configuration. Note that in Darcy's regime, the flow is symmetric about both horizontal and vertical axis (not shown here). However, in the inertial regime, due to the non-linear contribution of inertia to the transport of momentum, the symmetry about the vertical axes (normal to the flow direction) will break (see Section 5.3.1.4) while the flow is still stationary.

Fig. 5.2(b) shows the variations of inertial coefficients (i.e.  $\lambda$  and  $\gamma$ ) in Eq. (5.8) as function of porosity for both square and hexagonal configurations. We observe that the power  $\lambda$  is (i) larger than unity and varies between  $1 < \lambda < 2$  and (ii) depends on both porosity and structure/arrangements of the particles/fibres. By increasing the porosity (i.e. for more dilute systems) the power decreases and approaches the value of unity (i.e. the original quadratic Forchheimer correction, Eq. (5.3)). Square arrays have larger values of  $\lambda$  compared to hexagonal arrays implying that the transition to inertial regime starts earlier and sharper (see Fig. 5.2(a)). On the contrary, the pre-factor  $\gamma$  (in the inset) seems to be independent of structure and linearly decreases by increasing porosity as  $\gamma \cong 0.8(1 - \varepsilon)$ . In the appendix 5.A, the quality of the proposed power law fit (Eq. (5.8)) is compared with the quadratic ( $\lambda = 1$ ) and cubic ( $\lambda = 2$ ) fits at different porosity for both square and hexagonal configurations.



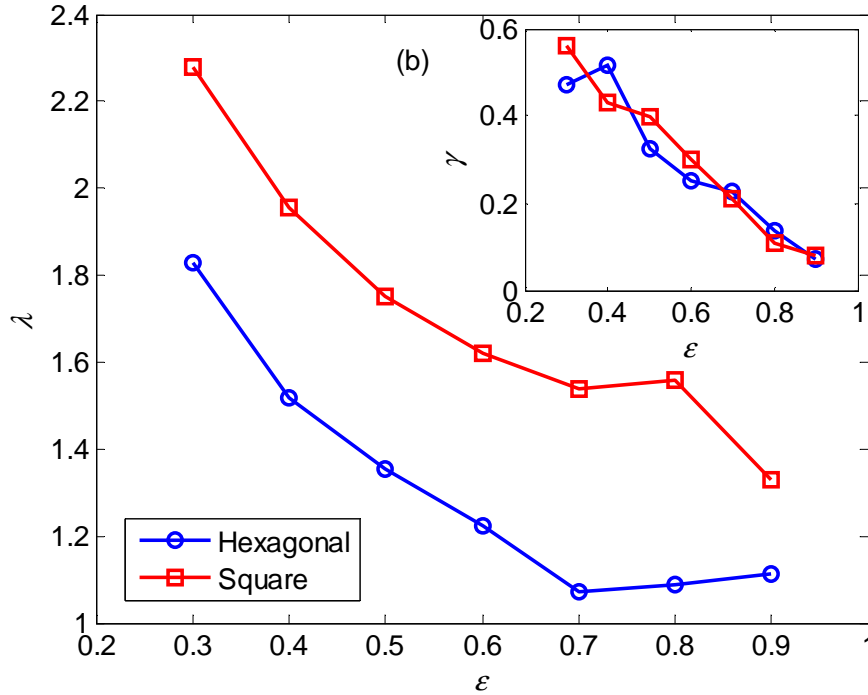


**Figure 5.2 (a):** Variation of the modified friction factor as function of the normalized velocity (or  $Re$ ) for square (red) and hexagonal (blue) configurations (solid lines show the best least square fit to Eq. (5.8) and the black dashed lines show the best quadratic ( $\lambda = 1$ ) and cubic ( $\lambda = 2$ ) fits in the range of  $10^{-5} < Re < 30$ ), symbols show the analytical/numerical data from literature; (b) Inertial coefficients  $\lambda$  and  $\gamma$  as in Eq. (5.8) plotted against porosity.

### 5.3.1.3 Effect of stagger cell angle

In this subsection, the effect of the stagger cell angle,  $\alpha$  on the inertial term is discussed. The stagger angle is defined as the angle between the diagonal of the unit-cell and flow-direction (horizontal), as shown in Fig. 5.3(a). In addition to the special cases  $\alpha = 45^\circ$  and  $\alpha = 60^\circ$ , i.e. square and hexagonal packings, respectively, several other angles are studied.

Fig. 5.3(b) shows the variation of the modified friction factor as function of normalized velocity for different stagger angles,  $\alpha$  at the constant porosity  $\varepsilon = 0.7$ . Similar to the normalized permeability, the inertial coefficient  $\gamma$  is weakly dependent on the stagger angle in the range of  $30^\circ < \alpha < 60^\circ$ . However,  $\lambda$  increases (almost) linearly from  $\lambda \cong 1$  at  $\alpha = 70^\circ$  to  $\lambda \cong 2$  at  $\alpha = 20^\circ$ . For  $\alpha = 70^\circ$  and higher (but lower than the maximum

achievable  $\alpha_{\max} = \tan^{-1}(\pi/(2(1-\varepsilon))) \cong 80^\circ$ , the flow generally follows a straight line with large superficial velocity and consequently large values of permeability and the transition starts at higher scaled velocities ( $Re$ ). On the other hand, at  $\alpha = 20^\circ$  and lower values of  $\alpha$  (but larger than the minimum allowable limit  $\alpha_{\min} = \tan^{-1}(2(1-\varepsilon)/\pi) \cong 11^\circ$ ), the flow is more tortuous and consequently it has lower permeability. At this range, the transition into non-Darcy regimes starts already at smaller superficial velocities.

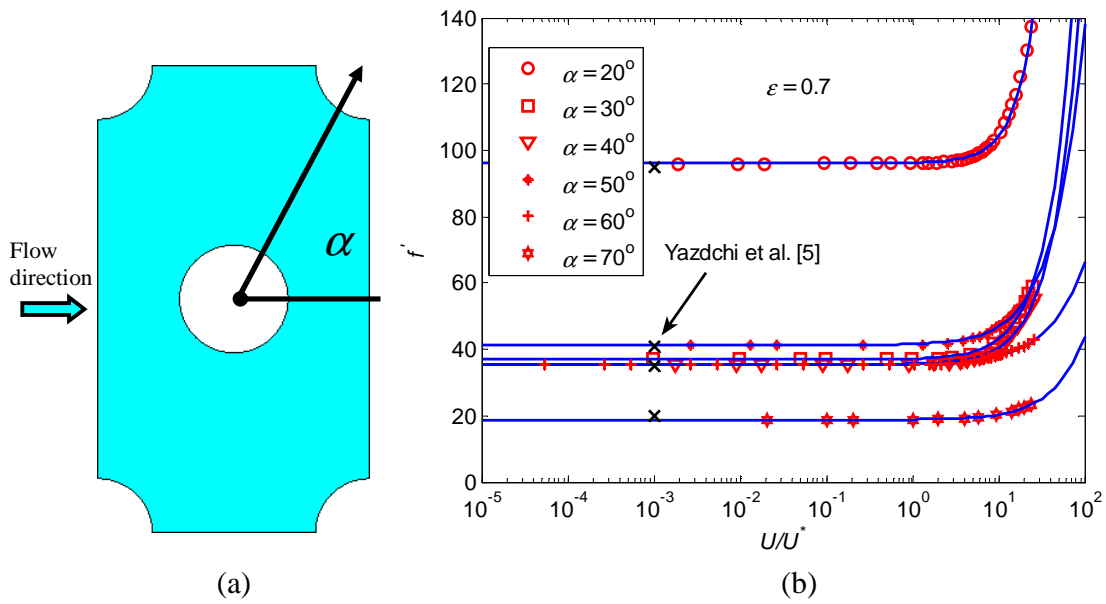


**Figure 5.3:** (a) stagger angle  $\alpha$  and (b) modified friction factor as function of normalized velocity for different  $\alpha$  at porosity  $\varepsilon = 0.7$ . The solid blue lines show the best least square fit in Eq. (5.8) in the range of  $10^{-5} < Re < 30$ .

#### 5.3.1.4 Effect of particle shape

In order to study the effect of particle/fibre shapes on the macroscopic permeability and inertial coefficients, the normalization is done with respect to the obstacle length,  $L_p$ , which is defined as

$L_p = 4 \text{ area} / \text{circumference}$ , with:

$$L_p = d \text{ (for circles), } L_p = c \text{ (for squares), and } L_p = 4\pi ab / A_L \text{ (for ellipses)} \quad (5.9)$$

where  $d$ ,  $c$ ,  $a$  and  $b=a/2$  are the diameter of the circle, the side-length of the square, the major (horizontal) and minor (vertical) lengths of the ellipse, respectively, and  $A_L$  is the circumference of the ellipse. By applying the same procedure as in the previous section, the normalized permeability and inertial coefficients are calculated for different shapes on a square configuration.

Fig. 5.4 shows the modified friction factor as function of the normalized velocity for different shapes. The circular shape has the lowest and horizontal ellipses the highest normalized permeability. The reason is that, at the same porosity, ellipses are more elongated in the flow direction and therefore the fluid can flow more easily on a straight line through the wider channels. However, at high porosities this effect diminishes (data not shown). Note that, due to the narrower channels, the local maximal velocity is higher for circular shapes, given the same porosity and pressure gradient. However, the superficial (discharge) velocities for ellipses are larger, leading to higher permeability, than other shapes. For the same reason, the transition to the inertial regime happens earlier for squares, whereas it occurs at higher velocities for ellipses. The values of the inertial coefficients  $\lambda$ ,  $\gamma$  and the viscous (normalized permeability,  $K'$ ) term, obtained by least square fitting to Eq. (5.8), are listed in Table 5.3. The power  $\lambda$  is not greatly affected by the shape (maximum variation less than  $\sim 10\%$ ), however, for squares, the  $\gamma$  value is  $\sim 5$  times larger than for ellipses at low porosities. The numerical results show that, similar to the normalized permeability, the effect of shape on the inertial parameters is less pronounced at high porosities ( $\varepsilon > 0.9$ ), not shown here. Establishing a common drag law based on the aspect ratio, sphericity or other shape parameters is still a challenge for future study.

To better understand and explain the flow characteristic in the inertial regime, the patterns of the streamlines for different shapes and the vortices generated behind the obstacle are shown in Fig. 5.5. The non-Darcy effect occurs because microscopic inertial effects alter the velocity and pressure fields. At the same porosity  $\varepsilon = 0.7$  and Reynolds number  $Re \cong 10$ , we observe that for the square shape one has stronger vortices (i.e. those that contribute more to the energy loss) compared to the ellipses in which the wake (or flow separation) zones behind the obstacle is flattened and stretched. These vortices increase in size as the velocity increases and eventually become unsteady and local turbulence occurs. At fixed porosity and pressure gradient, the flow for ellipses is – even though faster in average – less “turbulent” and smoother.

Note that the flow pattern is stationary and symmetric along the horizontal symmetry axis and non-symmetric relative to the vertical axes. The above example implies that the tortuosity (flow path) is one of the key factors in determining the viscous and non-Darcy coefficients (see Section 5.3.2.3 for more details).

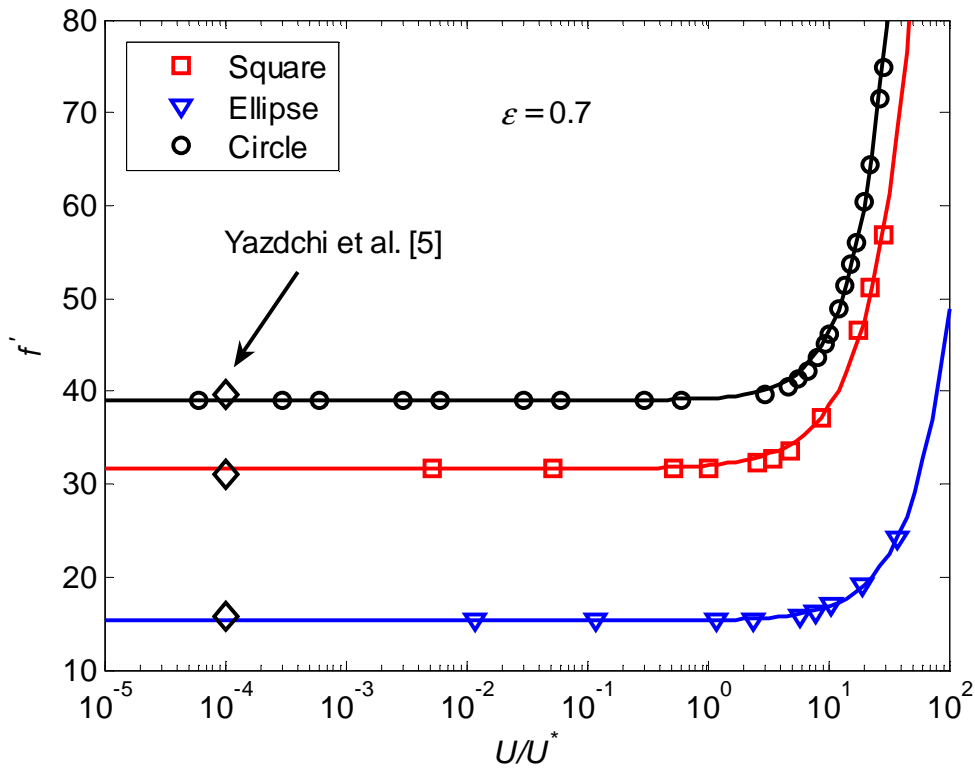


**Figure 5.4:** Modified friction factor plotted against normalized velocity for different shapes at porosity  $\varepsilon = 0.7$ . The solid lines show the best least square fit in Eq. (5.8) in the range of  $10^{-5} < Re < 30$ .

**Table 5.3:** The values of the inertial coefficients  $\lambda$ ,  $\gamma$  and viscous (normalized permeability,  $K'$  [5]) term, obtained by least square fitting of the FE results into the Eq. (5.8) in the range of  $10^{-5} < Re < 30$ , for different shapes and various porosities.

Shape	Circle			Ellipse			Square		
	Porosity, $\varepsilon$	0.7	0.8	0.9	0.7	0.8	0.9	0.7	0.8
$K' = K / L_p^2$ [5]	0.025	0.077	0.319	0.065	0.147	0.486	0.031	0.091	0.375
$\lambda$	1.544	1.561	1.338	1.343	1.436	1.111	1.281	1.342	1.129
$\gamma$	0.211	0.113	0.082	0.072	0.058	0.056	0.355	0.168	0.113

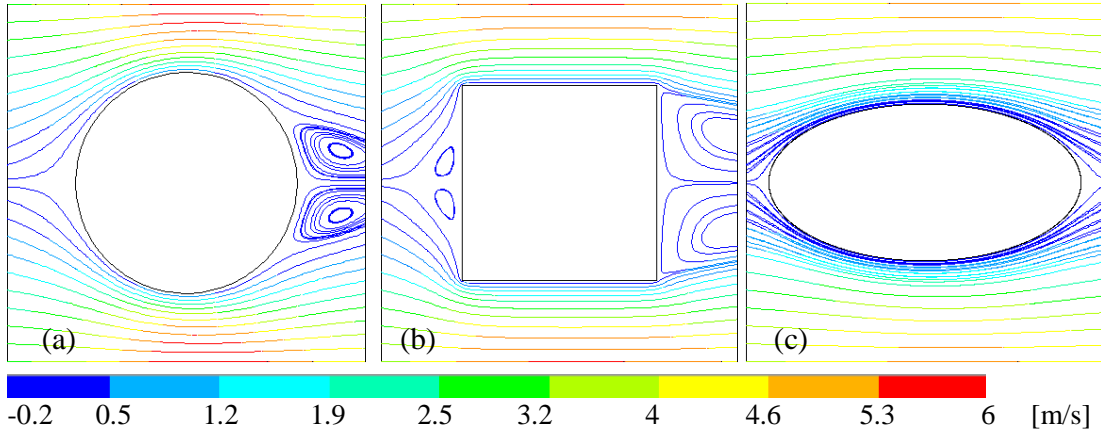


**Figure 5.5:** The streamline patterns around (a) circle, (b) square and (c) ellipse of the aspect ratio  $a/b=2$  at the constant porosity  $\varepsilon = 0.7$  and  $Re \cong 10$ . The color shows the magnitude of the horizontal velocity.

### 5.3.2 Structural disorder

Because of the complexity of pore-space geometry, classical numerical methods for solving flows through porous media are typically restricted to ordered and small or periodic domains. However, many realistic porous media are (i) confined with walls, (ii) are not truly two-dimensional, and (iii) possibly contain a degree of randomness (or disorder) at larger length scale that is not adequately represented in too small periodic boundary cells. In this section, I focus on (i), as compromise, and investigate the effect of disorder on both viscous and inertial coefficients in a moderately large system with  $N=800$  particles/fibres within a channel with walls.

#### 5.3.2.1 Computational domain and methodology

Fig. 5.6 shows a 2D representation of  $N=800$  randomly distributed fibres, generated by a Monte Carlo (MC) procedure [73], oriented normal to the flow direction at porosity  $\varepsilon=0.6$  with a minimum inter fibre distance  $\delta_{\min}=0.05d$  or in dimensionless form  $\Delta_{\min} = \delta_{\min} / d = 0.05$ . Similar to Chen and Papathanasiou [73], and Yazdchi et al. [5], a minimal distance is needed in 2D to avoid complete blockage. The microstructural parameters, namely the system size, method of generation, homogeneity and isotropy of the structure and their influence on macroscopic permeability have been discussed in [6]. At the left and right of the system the pressure boundary conditions are specified and at the top and bottom walls as well as at the surface of the particles/fibres no-slip boundary conditions are applied. The fibres are assumed to be very long so that a 2D solution can be applied. A typical fine, unstructured and triangular FE mesh is also shown in Fig. 5.6. The number of elements varied from about  $5 \times 10^5$  to about  $10^6$  depending on the porosity.

The lower the porosity the more elements are needed in order to resolve the flow along the many narrow channels between the neighboring fibres. The numerical results show that in all simulations one need at least  $\sim 10$  rows of elements between neighboring particles to correctly capture the fluid behavior and obtain a converging solution. Details of the comparison of different resolutions are provided in Appendix 5.B. To obtain good statistical accuracy, the permeability values and inertial coefficients were fitted to data averaged over 10 realizations of packings generated by the random MC procedure.

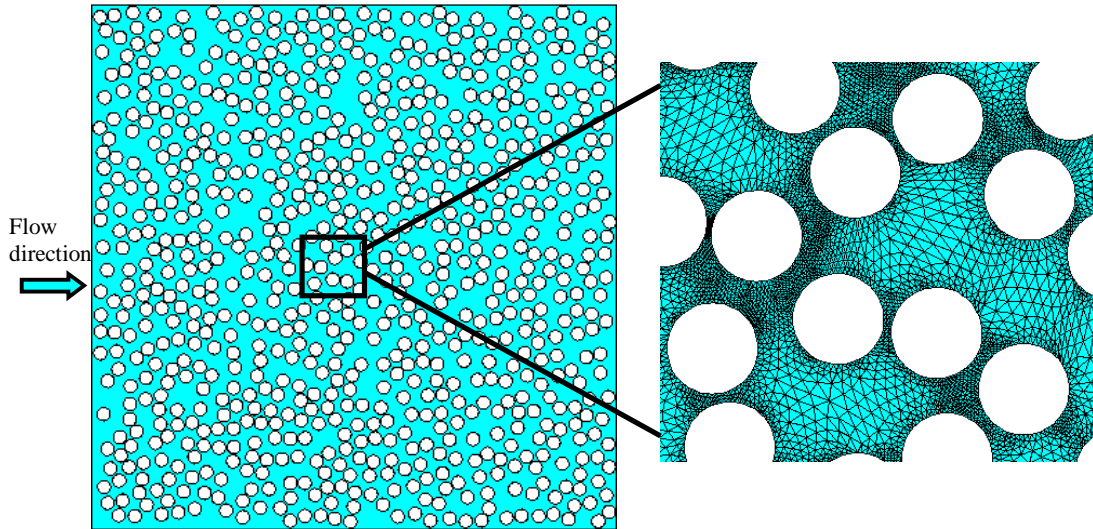


**Figure 5.6:** Fibre distributions generated by a Monte Carlo procedure, with  $N=800$  unidirectional cylinders, normal to the flow direction, with minimum inter fibre distance  $\delta_{\min}=0.05d$  at porosity  $\varepsilon=0.6$ . The zoom shows the fine, unstructured, triangular FE mesh.

Fig. 5.7(a) shows the variation of the modified friction factor as function of the normalized velocity,  $U/U^*$  for disordered configurations at various porosities. The results are compared with the FE results of Ghaddar [82], the numerical results of Sangani and Mo [83] and the LB results of Koch and Ladd [15]. As expected, increasing the porosity leads to an increased normalized permeability,  $K'$ . For  $Re < 3$ , like in the ordered hexagonal situations, the normalized friction factor is perfectly fitted by a cubic correction, e.g., for porosities 0.6, 0.7, 0.8, one has  $1/K' = 158.8418, 49.40725, 12.74905$ , and  $\gamma_2 = 0.6569, 0.5369, 0.2592$ , respectively. Thus the modified friction factor is considerably larger for low porosity in the random configurations, while the correction quadratic factor ( $\lambda=2$ )  $\gamma_2$  is about an order of magnitude larger, implying that the inertial effects already occur at much smaller Re numbers. The relative deviations at  $Re=1$  for the above porosities are 0.004, 0.01 and 0.02, respectively. Thus at  $Re \ll 1$  Darcy's law holds, yet for  $Re \sim 1$  stationary eddies (dead zones that do not participate in the overall mass-flux) exist mainly due to the geometry of the pores. The gradual deviation from



Darcy's law is due to the dynamic growth of pre-existing eddies within the micro-scale flow field and separation of flow in pores where flow diverged. Small deviation between my FE and LB results of Koch & Ladd [15] at creeping flow regime might be due to the difference in minimum inter-fibre distance, resolutions, number of fibers or boundary (periodic/wall) conditions.

Since the quadratic fit deteriorates for  $Re > 0.5-2$ , I again perform the nonlinear fits to my data up to about  $Re \sim 30$ , see Fig. 5.7(b), where the variations of the inertial coefficients ( $\lambda$  and  $\gamma$ ) in Eq. (5.8) are shown as function of porosity. We observe that for  $\varepsilon > 0.45$ , unlike the case of ordered arrays and similar to the Ergun equation, the power  $\lambda$  is approximately constant and close to unity, whereas the pre-factor  $\gamma$  decreases with increasing porosity. However, at very low porosities ( $\varepsilon < 0.45$ ),  $\lambda$  increases ( $\gamma$  decreases) with decreasing porosity and approaches the expected values ( $\lambda \cong 2$ ) for hexagonal arrays, corresponding to the appearance of ordered zones. Due to the (artificial) gap between fibres/discs, each disc has an effective diameter  $d^* = d(1 + \Delta_{\min})$  greater than its actual value,  $d$ . With this effective diameter, it is possible to define an effective porosity  $\varepsilon^* = 1 - (1 - \varepsilon)(1 + \Delta_{\min})^2$ . Inserting  $\Delta_{\min} = 0.05$  and  $\varepsilon = 0.45$ , the effective transition porosity from disorder to order arrangements is estimated as  $\varepsilon^* \cong 0.393$ . Note that this value is still far above the random close packing limit  $\varepsilon_{rcp}^* \cong 0.16$  [74], or the minimum hexagonal lattice  $\varepsilon_{hex}^* \cong 0.0931$ , and still above the freezing point  $\varepsilon_f^* \cong 0.309$  [75] or melting point  $\varepsilon_m^* \cong 0.284$  [75]. In fact it indicates that even small (partial) ordering in the system can drastically affect the transport properties, namely permeability [6] and inertial coefficients of porous media. The comparison of the quality of the proposed power law fit (Eq. (5.8)) with the quadratic ( $\lambda = 1$ ) and cubic ( $\lambda = 2$ ) fits at different porosities are given in the Appendix 5.A.

In Appendix 5.D, I present a universal scaling law, valid at all porosities, based on different definitions of  $Re$  and friction factor. It is shown that the inertial effect can be better explained as two distinct regimes: (i) cubic correction at  $Re < 1$  and (ii) quadratic fit at  $Re > 1$ , with almost the same accuracy as the proposed power law.

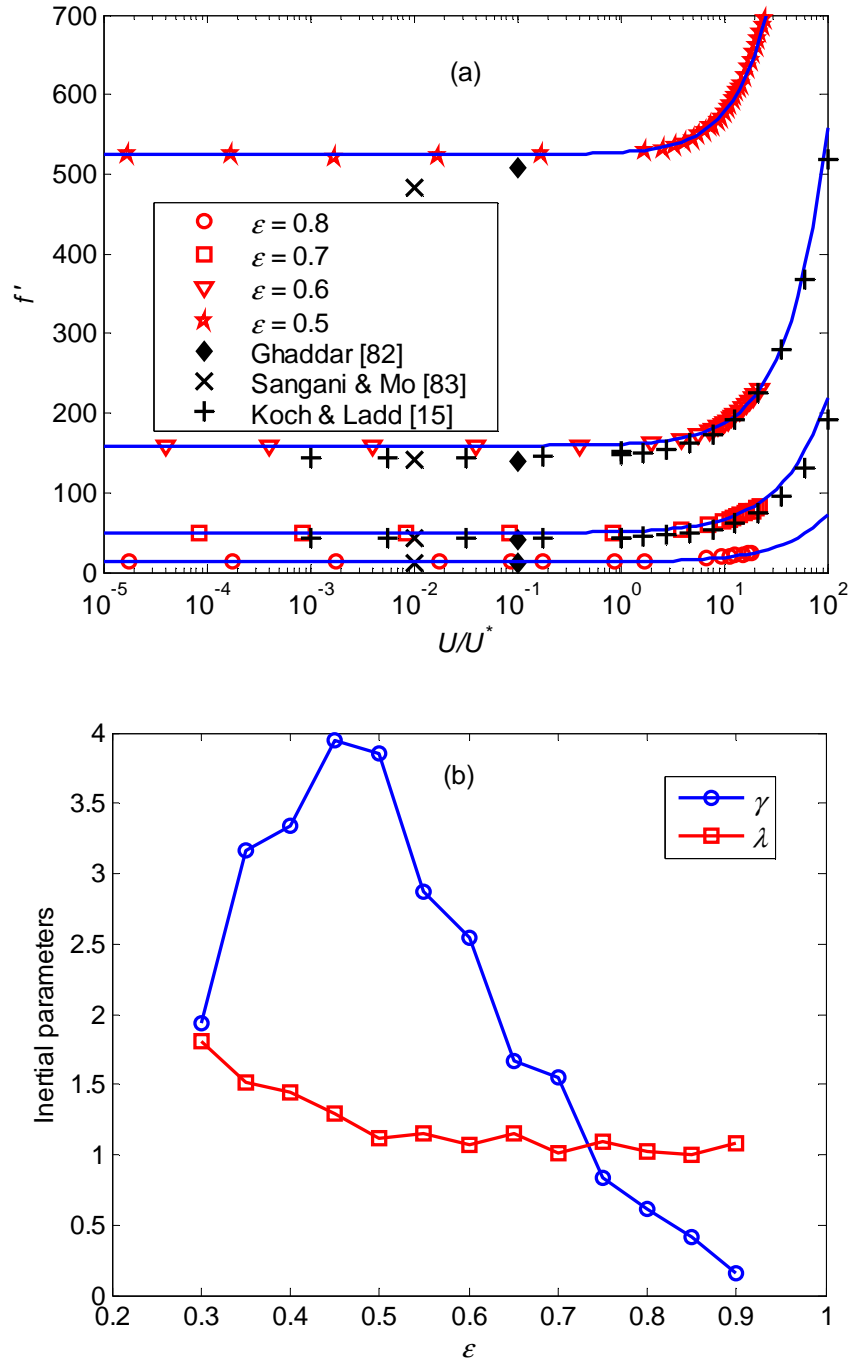


**Figure 5.7:** (a) Variation of modified friction factor as function of normalized velocity for disordered media at various porosities<sup>4</sup>. The solid lines show the best least square fit in Eq. (5.8) in the range of  $10^{-5} < Re < 30$  (b) Inertial parameters as function of porosity.

<sup>4</sup> Note that the numerical values in Koch & Ladd [15] were presented in the form of  $f_{KL} = F/(\mu U)$  ( $F$  is mean drag per unit length), as function of  $Re$ . At steady state, the

As mentioned before, most of the available correlations have a viscous porosity dependence that is similar to the Ergun equation with varying constants  $\psi_{CK}$ , while my data lead to a range of  $150 < \psi_{CK} < 300$  [76], see next section. Here we are curious to check the quantitative validity of the inertial component of the Ergun equation, i.e.  $\gamma = 1.75(1-\varepsilon)/\varepsilon^3$ . To this end, I fit my FE results into Eq. (5.8) assuming constant  $\lambda = 1$  (i.e. quadratic correction) for porosities  $\varepsilon > 0.45$ , i.e. random/disorder co-existence arrangements. Fig. 5.8 shows the comparison between the inertial coefficient  $\gamma$ , obtained from my FE simulations (blue squares) and those obtained from Ergun's equation (red line) at various porosities. The good agreement of these curves demonstrates the validity of the inertial component of the Ergun's equation, originally obtained for 3D spherical beds in nearly turbulent regime, also for 2D disordered fibrous media in laminar flows.

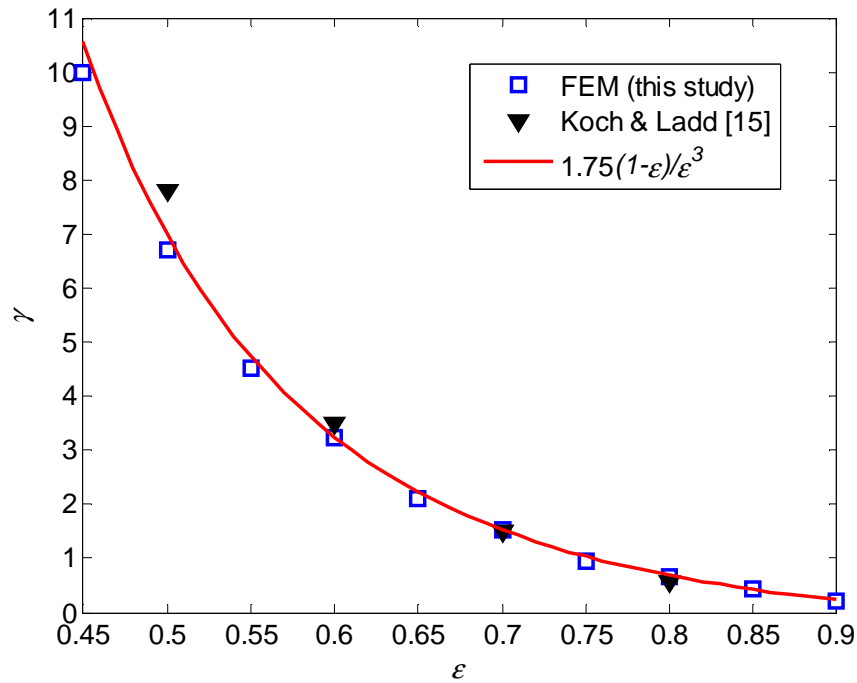


**Figure 5.8:** Variation of inertial coefficient  $\gamma$ , obtained from FE simulations (blue squares) and from Ergun equation (red line) at various porosities from disordered configurations.

---

average drag force multiplied by the cylinder number density,  $\xi$ , is equal to the applied pressure gradient, i.e.  $\nabla p = \xi F$ . Combining this relation with the definition of friction factor in this chapter, i.e. Eq. (5.8), leads to  $f' = (4(1-\varepsilon)/\pi) f_{KL}$ .

### 5.3.2.2 Different definitions of the Reynolds number

In analyzing flow through porous media, the superficial velocity and pressure drop are typically correlated through the particle friction factor,  $f_p$ , which appears as a function of Reynolds number,  $Re$ , see Eq. (5.6). Looking at the literature, several Reynolds numbers for porous media are defined, namely

$$\text{reference flow Reynolds number: } Re = \rho U d / \mu \quad (5.10)$$

$$\text{particle Reynolds number: } Re_p = \rho U d / ((1 - \varepsilon) \mu) \quad (5.11)$$

$$\text{modified Reynolds number: } Re_{\sqrt{k}} = \rho U \sqrt{K} / \mu \quad (5.12)$$

$$\text{interstitial Reynolds number: } Re_i = \rho U d / (\varepsilon \mu) \quad (5.13)$$

Recently, based on the lubrication effect of the narrow channels, I found a power law relationship between the permeability values obtained from fluid flow simulations and the mean value of 2<sup>nd</sup> nearest neighbor surface-to-surface fibre distances  $\Delta_{gap}$  normalized with the fibre diameters [6], see chapter 3. Therefore, another microstructural definition could be the “gap” Reynolds number, i.e.  $Re_g = \rho U \Delta_{gap} / \mu \equiv (\Delta_{gap} / d) Re$ , where  $(\Delta_{gap} / d)$  is a function of porosity [6]. In Appendix 5.D, I use this definition to get a universal friction factor- $Re_g$  relation valid at almost all porosities. By increasing the porosity and in the very dilute regime (i.e.  $\varepsilon \rightarrow 1$  or  $d \rightarrow 0$ ), by intuition, the Reynolds number should increase and approach its maximum value,  $Re_{max}$  for duct flow (i.e. flow between parallel plates). The definitions presented in Eq. (5.10) and (5.13) incorrectly approach zero values in this limit. On the other hand, the definition in Eq. (5.12) contains the macroscopic permeability which, in general, is an unknown quantity depending- a priori- on the microscopic level. This has motivated us to revisit the definition of the Reynolds number in terms of some measurable quantities of the (random) systems that a proper trend is recovered also in dilute regimes. A useful, measurable quantity that is frequently used in modeling of porous/fibrous structures is the hydraulic diameter,  $D_h$ . When one has obstacles like fibres (or particles) instead of straight pores, the hydraulic diameter can be defined as:

$$D_h = \frac{4\varepsilon V}{S_v} = \frac{4\varepsilon}{(1 - \varepsilon)a_v} = \frac{\varepsilon d}{(1 - \varepsilon)}, \quad \text{with } a_v = \frac{\text{particle surface}}{\text{particle volume}} = \frac{S_v}{(1 - \varepsilon)V} = \frac{4}{d}, \quad (5.14)$$

with the total volume of the unit cell,  $V$ , the total wetted surface,  $S_v$ , the specific surface area,  $a_v$ . Note that the hydraulic diameter, in this way, is expressed as a function of the measurable quantities porosity and specific surface area. The above value of  $a_v$  is for circles (cylinders) – for spheres one has  $a_v=6/d$ . Therefore the relation between normalized hydraulic diameter  $D_h/d$  and porosity for fibres will reduce to:

$$\frac{D_h}{d} = \frac{\varepsilon}{(1-\varepsilon)}. \quad (5.15)$$

Using the hydraulic diameter as the characteristic length, I define the pore Reynolds number to be

$$\text{Re}_{D_h} = \rho U D_h / \mu, \quad (5.16)$$

and combine it with Eq. (5.15) which leads to

$$\text{Re}_{D_h} = \rho U d \varepsilon / (\mu(1-\varepsilon)), \quad (5.17)$$

For the case of flow between parallel plates (slab flow), separated by a distance  $h_s$ , the hydraulic diameter is  $D_h = 2h_s$  and the superficial velocity,  $U$  is related to the pressure gradient as

$$U = -\frac{h_s^2}{12\mu} \nabla p. \quad (5.18)$$

Combing Eq. (5.18) and (5.16) leads to the maximum Reynolds number

$$\text{Re}_{\max} = \frac{-\rho h_s^3}{6\mu^2} \nabla p. \quad \text{Fig. 5.9 shows the variation of different definitions of Reynolds}$$

numbers as function of porosity at relatively low, constant pressure gradient  $\nabla p = 0.0005$  [Pa/m]. The non-Darcian behavior (i.e. high Re numbers) becomes important where there is a combination of high porosity and large pressure gradient. As it is seen, by increasing the porosity the Reynolds numbers (for all the definitions) increase and the flow approaches the inertial regimes even at a small applied pressure gradient. However,  $\text{Re}$  (reference Re number) and  $\text{Re}_i$  (interstitial Re number) will decrease at porosities  $\varepsilon > 0.95$  and asymptotically tend to zero. On the other hand, the particle Reynolds number ( $\text{Re}_p$ ) and the pore Reynolds number ( $\text{Re}_{D_h}$ ) increases and approaches the

maximum  $\text{Re}_{\max} = \frac{-\rho h_s^3}{6\mu^2} \nabla p \cong 66$  (though it is a sharp increase from  $\text{Re}_{D_h} \cong 0.032$  at

$\varepsilon = 0.99$  to  $\text{Re}_{D_h} \cong 66$  at  $\varepsilon = 1$ ). We observed that the  $\text{Re}_{D_h}$  gives a good fit to the exponential function with the power  $\sim 12.5$  for the wide range of porosities  $\varepsilon < 0.9$ . The numerical results show that this scaling remains valid also at larger applied pressure gradients (data not shown here). For the range of  $\varepsilon < 0.8$ , the variation of  $\text{Re}_{D_h}$  is similar to  $\text{Re}_g$  and  $\text{Re}_{D_h}/\text{Re}_g$  is almost constant equal to  $\sim 1/6$ . In Appendix 5.D, I use  $\text{Re}_{D_h}$  or  $\text{Re}_g$  to get a universal friction factor, valid for all porosities for random configurations.

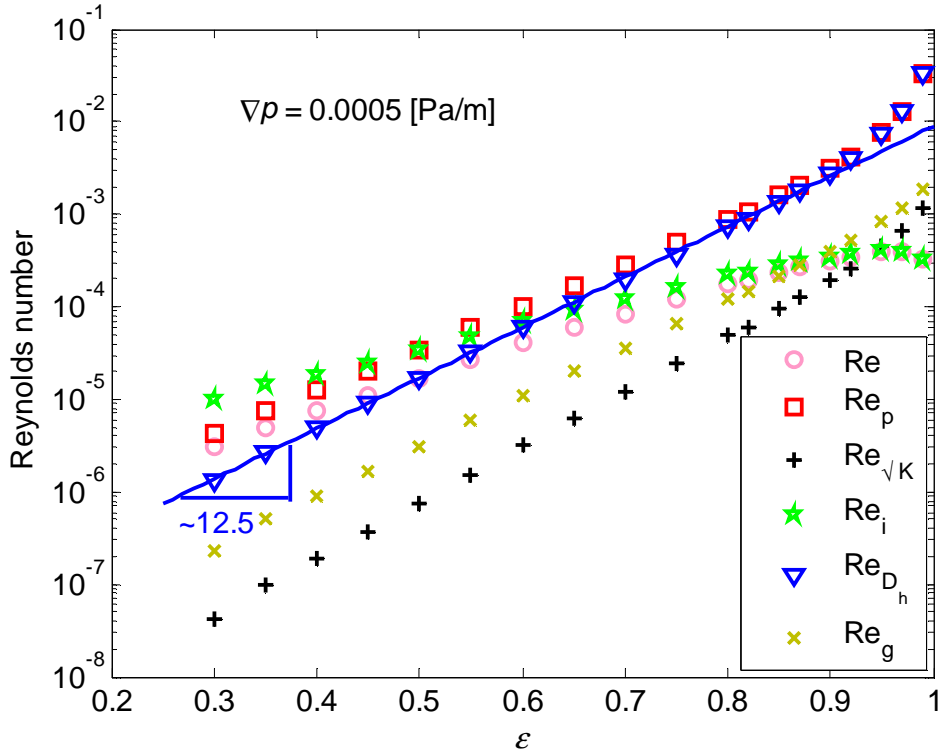


**Figure 5.9:** Variation of different definitions of Reynolds number as function of porosity at a constant pressure gradient  $\nabla p = 0.0005$  [Pa/m] for random configurations.

### 5.3.2.3 Effect of inertia on the viscous terms ( $K'$ ): Carman-Kozeny (CK) equation

The earliest and most widely applied approach in porous media literature for predicting the permeability in Stokes regimes, involves capillary models [77] such as the one that leads to the Carman-Kozeny (CK) equation. The approach is based on the analogy between Poiseuille flow through pipes and pore channels. By applying the Poiseuille equation in terms of the hydraulic diameter,  $D_h = \varepsilon d / (1 - \varepsilon)$  as  $U = -\frac{\varepsilon D_h^2}{32\mu} \nabla p$  and combining with Darcy's law, Eq. (5.1), the normalized permeability obtained is given by

$$K' = \frac{K}{d^2} = \frac{\varepsilon^3}{\psi_{CK} (1 - \varepsilon)^2} \quad (5.19)$$

where  $\psi_{CK}$  is the empirically measured CK factor which represents both the shape factor and the deviation of flow direction from that in a duct. It is approximated to be  $\psi_{CK}=180$  for random packed beds of spherical particles [77] or as in Ergun equation (Eq. (5.4))  $\psi_{CK}=150$ . Reported values of the CK factor for fibrous media vary between 80 and 320 [78, 79]. The same range of  $\psi_{CK}$  has been obtained from the theoretical results of Sangani

and Acrivos [80].

The principal limitation of the CK equation is the fact that all geometrical features of the medium are lumped into the CK factor. Even though attempts have been made to introduce microstructural features of the system into the CK equation by suitably modifying the mean hydraulic radius, it is fair to say that, at this stage, microstructural features can be included only semi-empirically through experimental determination of  $\psi_{CK}$ . An initial attempt was made by Carman [77] who considered the effect of flow path (tortuosity) on  $\psi_{CK}$ . Writing the CK factor in terms of its components, namely the pore shape factor  $\Phi$  and tortuosity  $L_e/L$

$$\psi_{CK} = \Phi \left( \frac{L_e}{L} \right)^2 \quad (5.20)$$

The tortuosity,  $L_e/L$  is the average effective streamline length,  $L_e$  scaled by the system length,  $L$ . In the original CK equation, for 3D random spherical beds, it was assumed that the tortuosity is constant ( $L_e/L = \sqrt{2}$ ) and  $\Phi=90$ , which gives us the CK factor as  $\psi_{CK} = 180$ . However, in a recent study [76] we showed that for fibrous media in the creeping (viscous) regime the tortuosity is not constant and depends on porosity. The effects of several microstructural parameters (namely particle shape, orientation, stagger angle etc) on tortuosity in creeping flow regimes have investigated elsewhere [5, 76]. From my numerical simulations, I extracted the average length of several streamlines (using 8 streamlines that divide the total mass in-flux into 9 zones, thus avoiding the center and the edges). By taking the average length of these lines, the tortuosity can be obtained, while by taking the standard deviation of the set of streamlines, the homogeneity of the flow can be judged. The tortuosity is plotted in Fig. 5.10 as function of normalized velocity at different porosities. Just as in the case of the modified friction factor, the tortuosity is a function of porosity at creeping flow regimes (horizontal line). However, by transitioning into inertial regimes, it decreases by increasing the flow rate implying that the fluid flows mainly on a straight line and become less tortuous.

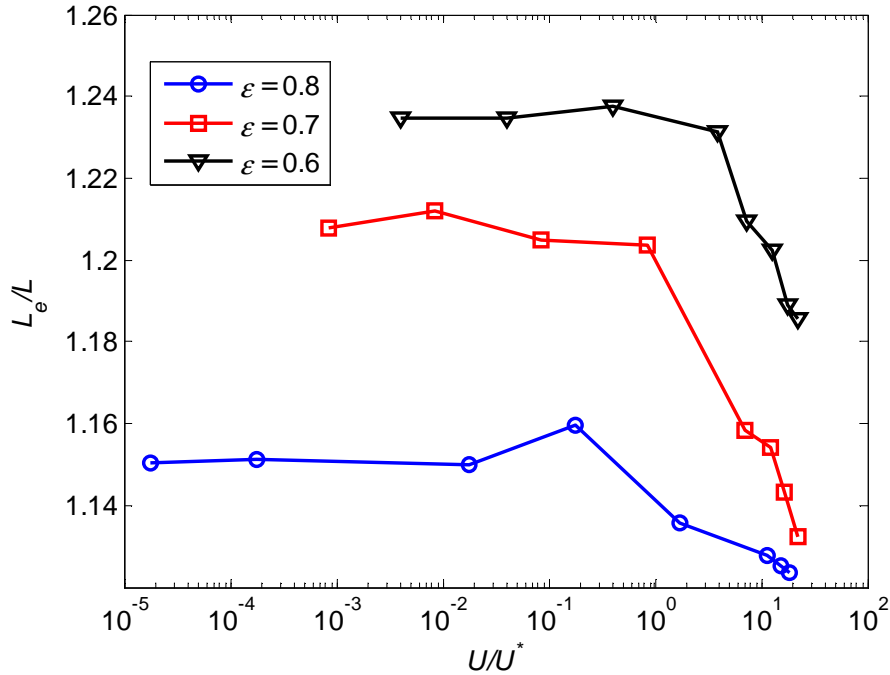


**Figure 5.10:** Tortuosity ( $L_e / L$ ) plotted as function of normalized velocity for different porosities on random configuration.

#### 5.4 Summary and conclusions

The chapter started with an extensive review of published experimental, numerical and theoretical work on the drag law correlations in fluidized beds and porous media with special attention to the intermediate-Re numbers (inertial) regime. Deviation from Darcy's law, for Newtonian, incompressible, stationary flow in homogeneous porous media, was then investigated numerically using FEM. We refer to Darcy's law as linear (in superficial velocity) while different nonlinear corrections for larger Re can be found on the market – from quadratic, intermediate to cubic. Computations were performed on model 2D systems with regularly and randomly distributed, rigid, uniform cylinders/fibres, oriented perpendicular to the flow direction. The effect of several microstructural parameters (namely the shape and structure/arrangement of the fibres) on the macroscopic permeability (viscous drag) and inertial coefficients was investigated first, before we turned to random configurations of cylinders. Major conclusions emerge from the numerical results and can be listed as follows.

For ordered and periodic structures:

- For small  $Re < 3$  (threshold varying with porosity, shape, etc.), a cubic correction in velocity ( $\lambda = 2$  is the power law for the dimensionless friction factor) works



well, with deviations stronger/earlier for larger porosities – given constant pressure drop.

- Based on the generalized, non-dimensional form of the Forchheimer equation, for larger  $Re < 30$ , the nonlinear correction to the Darcy drag law is a power law with powers  $1 < \lambda < 2$  depending on the porosity and the structure (i.e. square or hexagonal arrays), and with power decreasing from cubic at low porosity towards quadratic at high porosity.
- The viscous and inertial coefficients are not much affected (maximum variation 10%) by the stagger unit cell angle,  $\alpha$  in the range of  $30^\circ < \alpha < 60^\circ$ . However,  $\lambda$  increases (almost) linearly from  $\lambda \cong 1$  at  $\alpha = 70^\circ$  to  $\lambda \cong 2$  at  $\alpha = 20^\circ$ .
- The shape of the particles has a strong effect on both viscous and inertial drag coefficients, especially for porosities lower than approximately 0.9.

For disordered (random) structures:

- For moderate  $Re$ , the nonlinear correction to Darcy drag law is well approximated, to first order, by a quadratic term in velocity (i.e. with  $\lambda = 1$ ). The inertial pre-factor  $\gamma = 1.75(1 - \varepsilon) / \varepsilon^3$  turns out to be very similar to the one used in the Ergun equation, originally derived for 3D spherical packed beds in the range of  $\varepsilon > 0.45$  and  $Re < 30$ . A nonlinear function fits better including also the very small  $Re$  data, but best performs a cubic correction up to a critical Reynolds number,  $Re_c$ , and the same with a quadratic correction above  $Re_c$ .
- With decreasing porosity a structural transition from disordered to ordered packing occurs (for my preparation method) and the inertial coefficients approach values closer to those for the hexagonal lattice.
- The tortuosity (flow path) not only depends on the porosity and the pore structure but also on the fluid velocity (flow regime). At steady state and not fully turbulent flows, by increasing the porosity or flow rate, the flow becomes faster and less tortuous.
- A microstructural definition of the Reynolds number,  $Re_g$ , is based on the mean value of the averaged 2<sup>nd</sup> nearest neighbor surface-to-surface fibre distances  $\Delta_{gap}$ . The “gap” Reynolds number  $Re_g = \rho U \Delta_{gap} / \mu$ , is employed to get the universal friction factor as function of  $Re_g$  valid for all  $Re$  studied here and in an astonishingly wide range of porosities up to even  $\varepsilon \sim 0.9$ . After scaling/collapsing all data, both the non-linear fit with non-integer power ( $\lambda \cong 1.15$ ) and the two-regime approach fit the data for  $Re < 30$  very well.

Although disorder was investigated in two dimensions, these results provide insights and indicate that similar conclusions might be extended to 3D realistic random porous

structures. Further work can now be planned on anisotropic and/or heterogeneous media. The study of the fully turbulent regime, similar to the coupled DEM-LBM for inelastic soft spheres [84] or modeling the diffusion and relative dispersion of particles in homogeneous isotropic turbulence [85], can also be addressed in future.

### Acknowledgements:

The authors would like to thank S. Srivastava, M. van der Hoef, A. J. C. Ladd, K. Vafai, C. S. O'Hern, X. Chen, and A.R Thornton for helpful discussion and acknowledge the financial support of STW through the STW-MuST program, project number 10120.

### Appendix 5.A Comparison of the fit quality for ordered/disordered configurations

The quality of the proposed power law fit for the modified friction factor, Eq. (5.8), can be evaluated by the relative error,  $\chi$  defined as:

$$\chi = \left| 1 - \frac{f'_{\text{fit}}}{f'_{\text{FEM}}} \right| \quad (5.A.1)$$

The variation of  $\chi$  as function of  $U/U^* \equiv \text{Re}$  using quadratic (blue), cubic (red) and proposed power law fits (black), for (a) square and (b) hexagonal configurations is shown in Fig. 5.A1. The power law fits best to my FE results with maximum discrepancy less than 1%, when the fits are performed in the full range of available data up to  $\text{Re} < 30$ . (Note that the cubic fit performs even better, if not perfect, but only up to  $\text{Re} < 3$  (varying with porosity)).

The quality factor,  $\chi$  for a random configuration is shown in Fig. 5.A2. Contrary to the case of ordered arrays, the quadratic and power law fits have approximately the same accuracy (maximum discrepancy less than 2%). However, by decreasing the porosity the quadratic correction becomes less accurate.

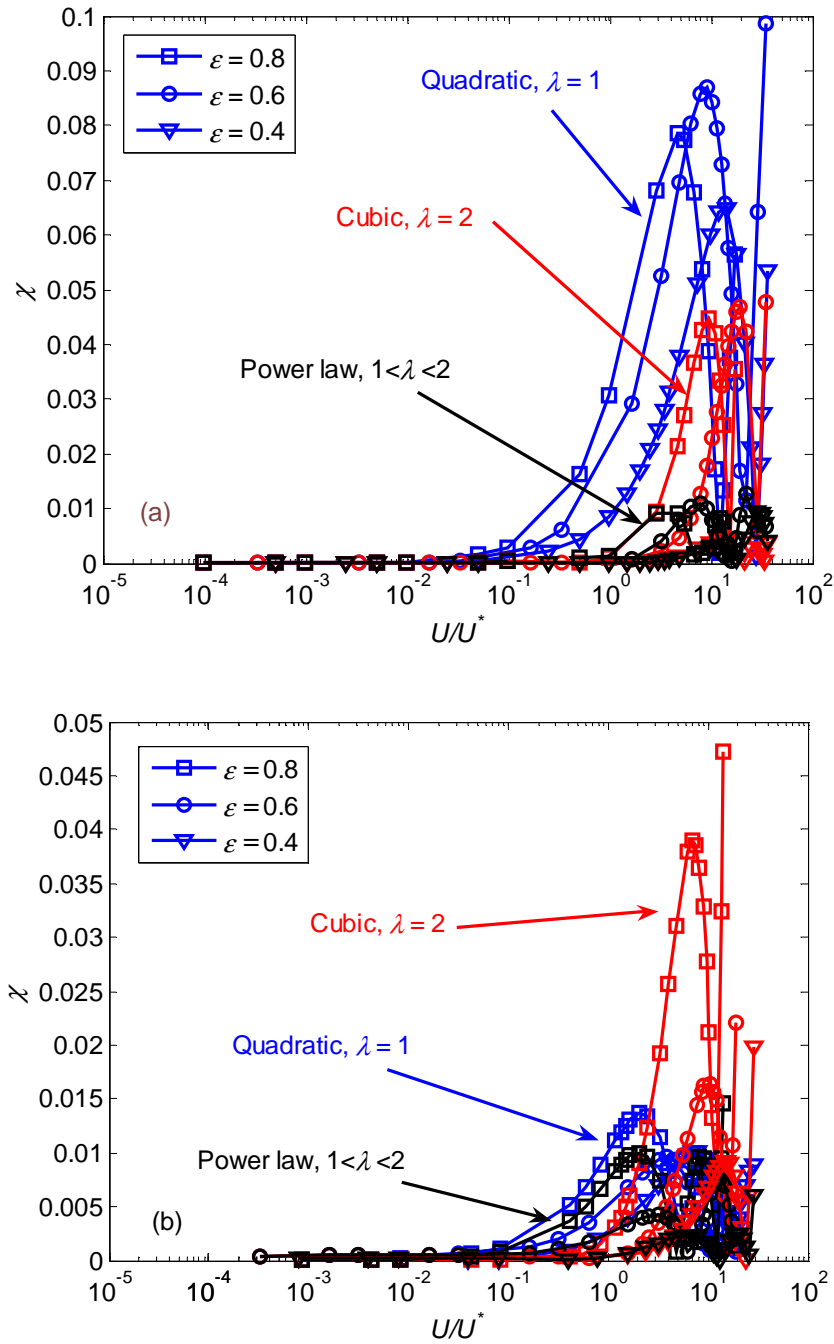


**Figure 5.A1:** The quality of the quadratic, cubic and proposed power law fit (Eq. (5.8)) in the range of  $10^{-5} < \text{Re} < 30$  for (a) square and (b) hexagonal configurations at different porosities.

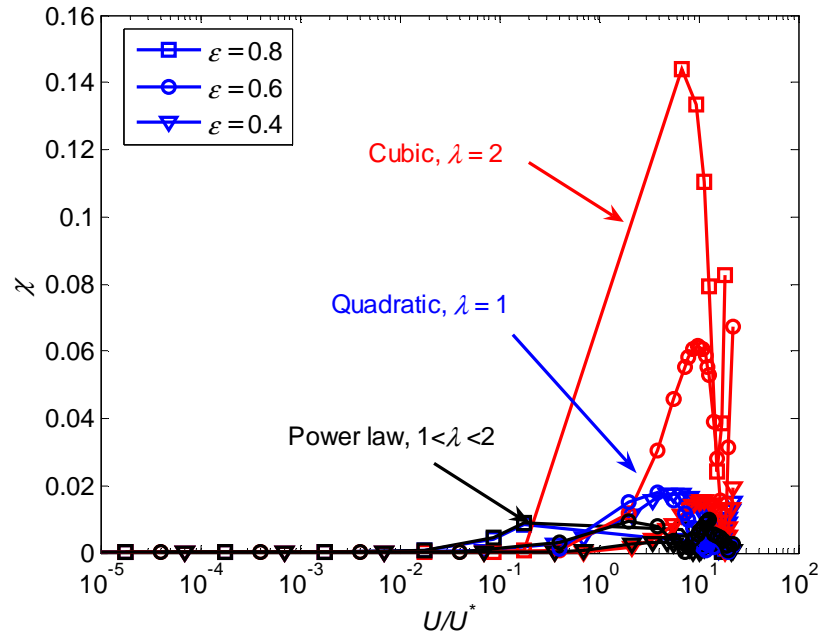


**Figure 5.A2:** The quality of the quadratic, cubic and proposed power law fit (Eq. (5.8)) in the range of  $10^{-5} < Re < 30$  for random arrangements at various porosities.

### Appendix 5.B Mesh sensitivity analysis for random arrangements

Due to the difference in scale between domain size and gap size between neighboring fibres, this typically requires local mesh refinement. For different porosities, flow through random fibre arrangements (Fig. 5.6) was simulated at different mesh resolutions (number of elements,  $N_e$ ). The dependence of the solution in terms of the calculated friction factor at (a) dense,  $\varepsilon = 0.4$ , and (b) dilute,  $\varepsilon = 0.8$ , systems is shown in Fig. 5.B1. The numerical results show that not only the inertial term (more elements are required to reach higher Re numbers), but also the viscous term (normalized permeability  $K'$ ) depends on the resolution,  $N_e$ . By increasing the porosity (dilute system) less elements would be sufficient to get a convergent solution.

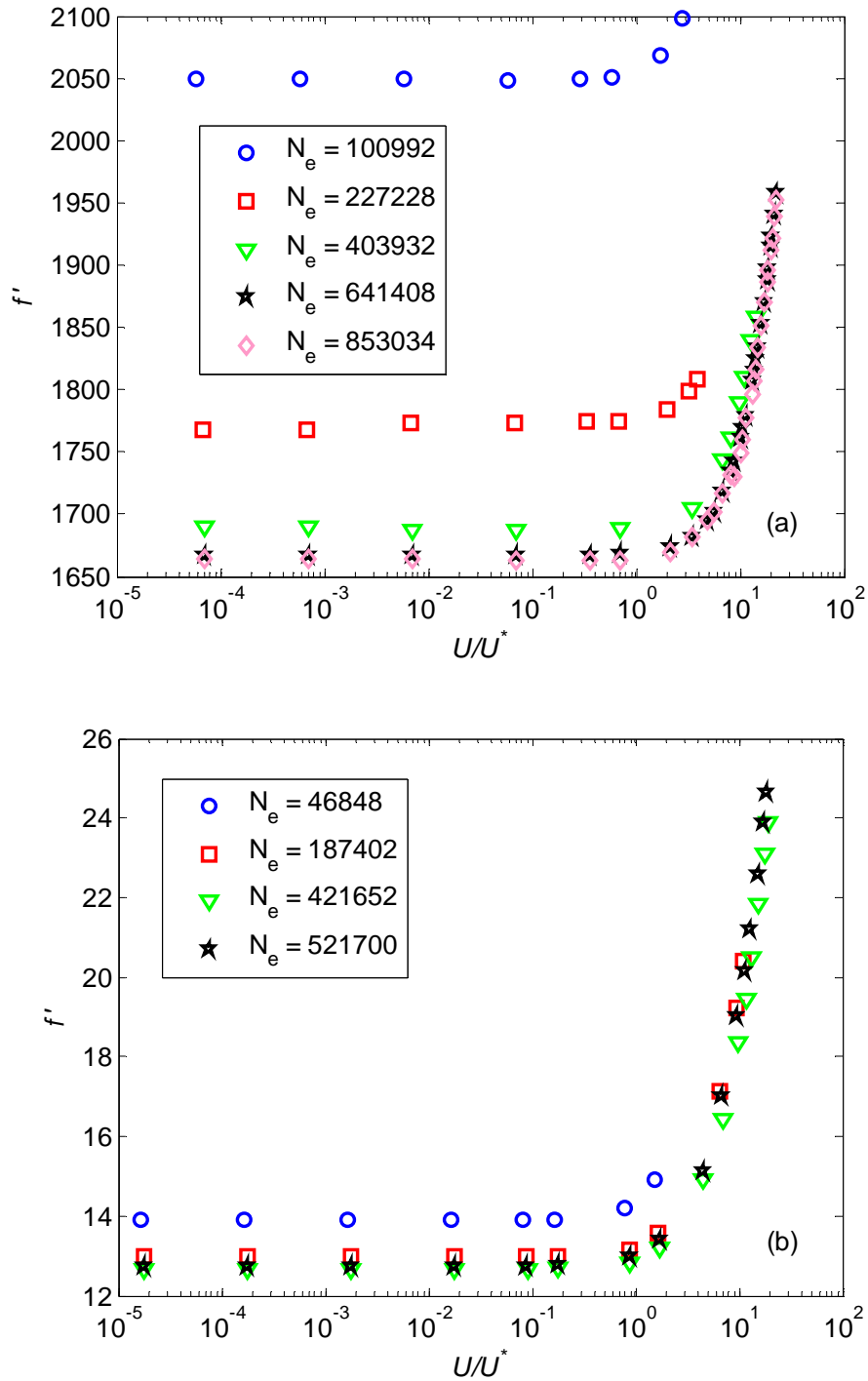


**Figure 5.B1:** The variation of friction factor as function of Reynolds number  $Re \equiv U/U^*$  at porosity (a)  $\varepsilon = 0.4$  and (b)  $\varepsilon = 0.8$  for different resolution (number of elements,  $N_e$ ).

### Appendix 5.C An alternative cubic ( $\lambda = 2$ ) correction fit for the friction factor

The following empirical fit is based on correction of the creep regime (constant  $f'$  for  $\text{Re} < \text{Re}_c$ ) with a cubic term ( $\lambda = 2$ ) and fitting the inertial deviation with another correction term,  $m(\text{Re})$  for  $\text{Re} > \text{Re}_c$ . The  $\text{Re}_c$  is the critical Re number in which the deviation starts. For the case of creeping regime one has the cubic correction for  $f'$  as

$$-f' = \frac{1}{K'}(1 + \gamma_2 K' \text{Re}^2), \quad (5.C.1)$$

and with the correction at  $\text{Re} > \text{Re}_c$  as

$$-f' = \frac{1}{K'}(1 + \gamma_2 K' \text{Re}^2)m(\text{Re}). \quad (5.C.2)$$

For the special case of random configuration at  $\varepsilon = 0.4$ , the numerical fitted values are

$$\begin{cases} K' = 5.9983 \times 10^{-4}, \gamma_2 = 1.1816, \text{Re}_c = 4.3, \\ m(\text{Re}) = 1 - a_1 (\text{Re} - \text{Re}_c)^2, a_1 = 4.3 \times 10^{-4} \end{cases} \quad (5.C.3)$$

Fig. 5.C1 shows the variation of friction factor as function of  $\text{Re} = U/U^*$  together with the proposed fits in Eqs. (5.C.1), (5.C.2) and non-integer power law in Eq. (5.8). The agreement is perfect (better than 99.9%) for  $\text{Re} < \text{Re}_c$  using the first correction (Eq. (5.C.1)) and extends with the same quality up to  $\text{Re} \sim 20$  with Eq. (5.C.2). This indicates that another type of correction is needed in order to improve the prediction for larger Re. Therefore, there is not a single integer power law correction. However, I stop this approach here as the non-integer power law (Eq. (5.8)) is already a good approximation (maximum discrepancy less than 1%) in wide range of  $\text{Re} < 30$ .

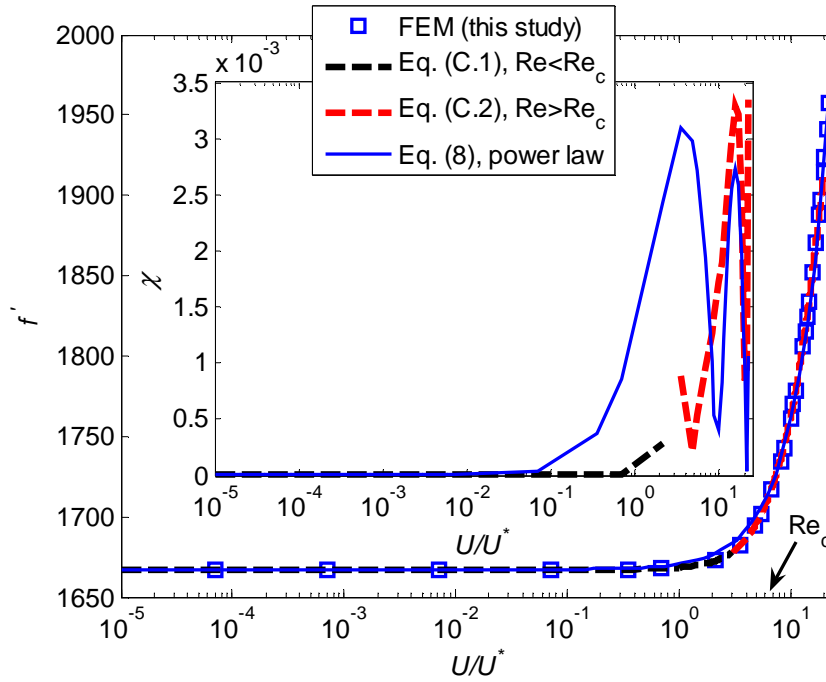


**Figure 5.C1:** The variation of friction factor as function of Reynolds number  $Re \equiv U/U^*$  for random configuration at porosity  $\varepsilon = 0.4$ . The dashed and solid lines represent the cubic correction ( $\lambda = 2$ ) fits in Eqs. (5.C.1), (5.C.2) and non-integer power law in Eq. (5.8), respectively. The inset shows the quality of the proposed fits.

## Appendix 5.D Towards unified friction factor using different definitions of Re numbers

In this Appendix, I present unified relations for the friction factor as function of  $Re_g$  or  $Re_{D_h}$ , valid at a wide range of porosities for random configurations. The non-linear correction in Eq. (5.8) can be isolated by studying  $f^* = -f'K' - 1$ , i.e. subtracting the viscous term, as

$$f^* = \gamma K' Re_{D_h}^\lambda \equiv \gamma K' \left( \frac{\varepsilon}{1-\varepsilon} \right)^\lambda Re^\lambda \quad \text{or} \quad f^* = \gamma K' Re_g^\lambda \equiv \gamma K' \left( \frac{\Delta_{gap}}{d} \right)^\lambda Re^\lambda. \quad (5.D.1)$$

Note that by replacing  $Re$  with  $Re_{D_h}$  or  $Re_g$ , the values of the fitting power  $\lambda$  would not change. Fig. 5.D1 shows the variation of  $f^*$  as function of (a)  $Re_{D_h}$  and (b)  $Re_g$  at various porosities for the case of random configurations. Using the alternative definitions of Reynolds numbers, i.e.  $Re_g$ , the values of  $f^*$  at different porosities collapse on a single curve up to astonishingly large porosity,  $\varepsilon \sim 0.9$ . The weak inertial regime seems to be cubic ( $\lambda = 2$ ), whereas the higher inertial regime fits better to quadratic ( $\lambda = 1$ )

correction. Note that the non-integer power law (Eq. (5.8)), with  $\lambda \cong 1.15$ , see the black line in Fig. 5.D1(b), is also fit to my data considering the whole range of  $Re$ . The numerical results show that one can not get such a scaling also for ordered (i.e. square or hexagonal) configurations (data not shown here).

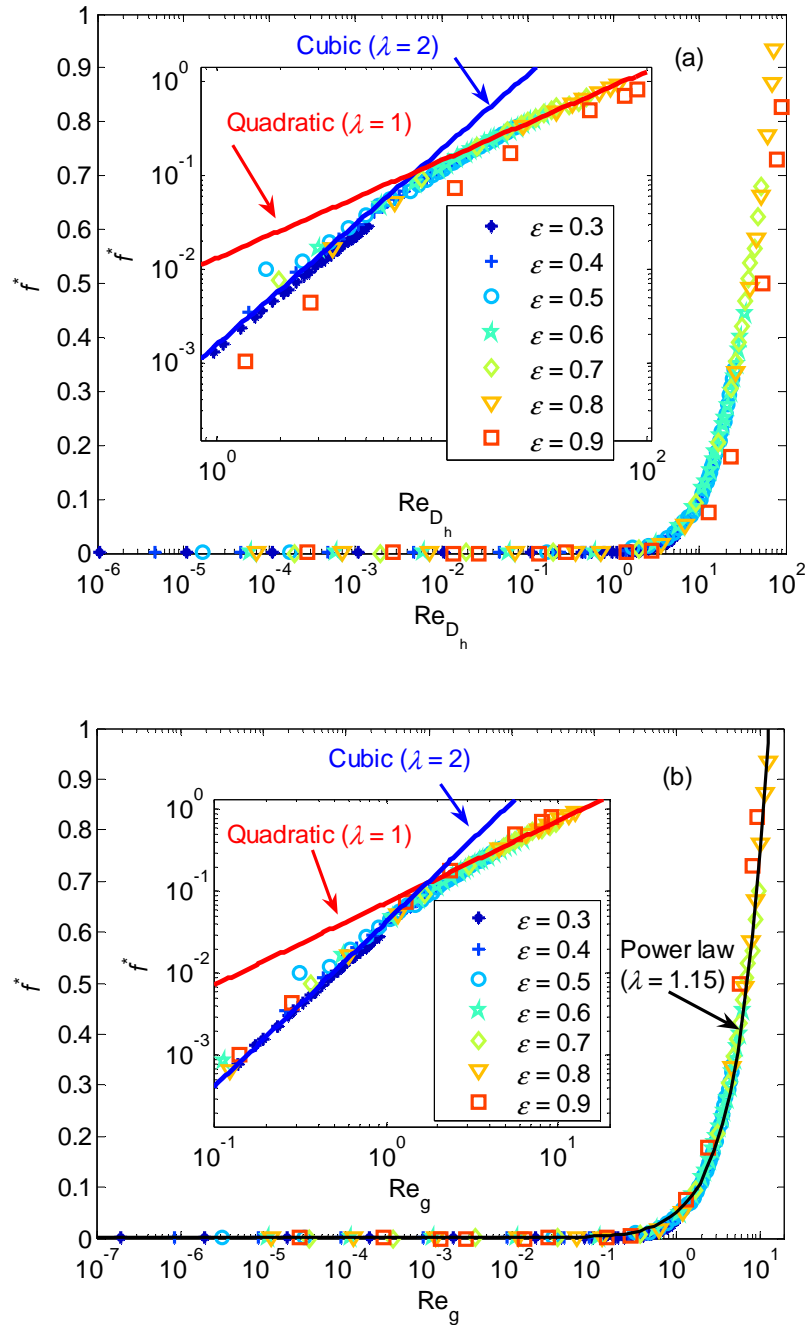


**Figure 5.D1:** The variation of friction factor as function of (a) hydraulic Reynolds number,  $Re_{D_h}$  and (b) gap Reynolds number,  $Re_g$  at various porosities for random



configurations. The inset shows the zoom. The solid lines show the best fitted cubic and quadratic corrections at weak and high inertial regimes, respectively.

## References

- [1] N.G. Deen, M. Van Sint Annaland, M.A. Van der Hoef, J.A.M. Kuipers, Review of discrete particle modeling of fluidized beds, *Chem. Eng. Sci.*, 62 (2007) 28-44.
- [2] Y. Tsuji, T. Kawaguchi, T. Tanaka, Discrete particle simulation of two dimensional fluidized bed, *Powder Technol.*, 77 (1993) 79-87.
- [3] H.P. Zhu, Z.Y. Zhou, R.Y. Yang, A.B. Yu, Discrete particle simulation of particulate systems: A review of major applications and findings, *Chem. Eng. Sci.*, 63 (2008) 5728–70.
- [4] H.P. Zhu, Z.Y. Zhou, R.Y. Yang, A.B. Yu, Discrete particle simulation of particulate systems: Theoretical developments, *Chem. Eng. Sci.*, 62 (2007) 3378–96.
- [5] K. Yazdchi, S. Srivastava and S. Luding, Microstructural effects on the permeability of periodic fibrous porous media, *Int. J. Multiphase Flow*, 37 (2011) 956-66.
- [6] K. Yazdchi, S. Srivastava and S. Luding, Micro-macro relations for flow through random arrays of cylinders, *Composites Part A*, 43 (2012) 2007-2020.
- [7] K. Yazdchi, S. Srivastava and S. Luding, On the transition from creeping to inertial flow in arrays of cylinders, *Proceedings of IMECE (2010)*, Vancouver, Canada.
- [8] J. L. Lage and B. V. Antohe, Darcy's Experiments and the Deviation to Nonlinear Flow Regime, *J Fluids Eng.*, 122 (2000) 619-25.
- [9] S. Whitaker, Flow in porous media I: A theoretical derivation of Darcy's law, *Transp. Porous Media*, 1 (1986) 3-25.
- [10] E. Sanchez-Palencia, *Non-Homogeneous Media and Vibration Theory*, Lecture Notes in Physics, 127 (1980).
- [11] C.C. Mei, J.-L. Auriault, The effect of weak inertia on flow through a porous medium. *J. Fluid Mech.*, 222 (1991) 647–63.
- [12] D.W. Ruth, H. Ma, On the derivation of the Forchheimer equation by means of the averaging theorem, *Transp. Porous Med.*, 7 (1992) 255–264.
- [13] F.J. Valdes-Parada, J.A. Ochoa-Tapia, J. Alvarez-Ramirez, Validity of the permeability Carman Kozeny equation: A volume averaging approach, *Physica A*, 388 (2009) 789-98.

- [14] J.L. Auriault, Nonsaturated deformable porous media: quasistatics, *Transport in Porous Media*, 2 (1987) 45-64.
- [15] D. Koch and A.J.C. Ladd, Moderate Reynolds number flows through periodic and random arrays of aligned cylinders, *J. Fluid Mech.*, 239 (1997) 31–66.
- [16] R.J. Hill, D.L. Koch and A.J.C. Ladd, Moderate-Reynolds-number flows in ordered and random arrays of spheres, *J. Fluid Mech.*, 448 (2001) 243–78.
- [17] P. Forchheimer, *Wasserbewegung durch Boden*, *Z. Ver. Deutsch. Ing.*, 45 (1901) 1782.
- [18] M. A. Van der Hoef, R. Beetstra and J. A. M. Kuipers, Lattice-Boltzmann simulations of low-Reynolds-number flow past mono- and bidisperse arrays of spheres: results for the permeability and drag force, *JFM*, 528 (2005) 233–254.
- [19] A. Narvaez, T. Zauner, F. Raischel, R. Hilfer and J. Harting, Quantitative analysis of numerical estimates for the permeability of porous media from lattice-Boltzmann simulations, *J. Stat. Mech.*, (2010) P11026.
- [20] Aydin Nabovati, Edward W. Llewellyn, Antonio C.M. Sousa, A general model for the permeability of fibrous porous media based on fluid flow simulations using the lattice Boltzmann method, *Composites: Part A*, 40 (2009) 860–869.
- [21] Z. Chai, B. Shi, , J. Lu, , Z. Guo, Non-Darcy flow in disordered porous media: A lattice Boltzmann study, *Computers & Fluids*, 39 (2010) 2069–77.
- [22] A. Narvaez, K. Yazdchi, S. Luding and J. Harting, From creeping to inertial flow in porous media: a lattice Boltzmann - Finite Element comparison, *JSTAT*, (2012), submitted.
- [23] J. A. Jr. Andrade, U.M.S. Costa, M.P. Almeida, H.A. Makse, and H.E. Stanley, Inertial effects on fluid flow through disordered porous media, *Phys. Rev. Lett.*, 82 (1998) 5249–52.
- [24] S. Ergun, *Fluid Flow through Packed Columns*, *Chem. Eng. Prog.*, 48 (1952) 89-94.
- [25] R.B. Bird, W.E. Stewart, E.N. Lightfoot, *Transport phenomena*, 2nd edn. Wiley, New York, 2002.
- [26] T.D. Papathanasiou, B. Markicevic, E.D. Dendy, A computational evaluation of the Ergun and Forchheimer equations for fibrous porous media, *Phys. Fluids*, 13 (2001) 2795–2804.
- [27] S. Liu, A. Afacan and J. Masliyah, Steady incompressible laminar flow in porous media, *Chem. Eng. Sci.*, 49 (1994) 3565-86.

- [28] G.W. Jackson, D.F. James, Permeability of fibrous porous media, *Can J Chem Eng.*, 64 (1986) 364–74.
- [29] G.A. Bokkers, M. van Sint Annaland, J.A.M. Kuipers, Mixing and segregation in a bidisperse gas–solid fluidized bed: a numerical and experimental study, *Powder Tech.*, 140 (2004) 176–86.
- [30] C.Y. Wen, and Y.H. Yu, Mechanics of fluidization, *AIChE J.*, 62 (1966) 100-11.
- [31] H.C. Brinkman, A calculation of the viscous force exerted by a flowing fluid on a dense swarm of particles, *Appl. Sci. Res. A*, 1 (1949) 27–34.
- [32] J.-L. Auriault, On the Domain of Validity of Brinkman’s Equation, *Transp. Porous Med.*, 79 (2009) 215–23.
- [33] M. Hassanizadeh, W.G. Gray, General conservation equations for multi-phase systems, *Adv. Water Res.*, 3 (1980) 25–40.
- [34] T. Giorgi, Derivation of the Forchheimer Law Via Matched Asymptotic Expansions, *Transport in Porous Media*, 29 (1997) 191–206.
- [35] M.I.S. Azzam and A.L. Dullien, Flow rate-pressure gradient measurements in periodically nonuniform capillary tubes, *AIChE J.*, 19 (1973) 222–29.
- [36] S.M. Hassanizadeh and W.G. Gray, High velocity flow in porous media, *Transport in Porous Media*, 2 (1987) 521–31.
- [37] N. Ahmed and D.K. Sunada, 1969, Nonlinear flow in porous media, *J. Hydr. Div. ASCE*, 95 (1969) 1847–57.
- [38] S. Whitaker, The Forchheimer equation: a theoretical development, *Transp. Porous Med.*, 25 (1996) 27–61.
- [39] D. Lasseux, A. A. Abbasian Arani, and A. Ahmadi, On the stationary macroscopic inertial effects for one phase flow in ordered and disordered porous media, *Physics of fluids*, 23 (2011) 073103.
- [40] K.N. Moutsopoulos, I.N.E. Papaspyros, V.A. Tsihrintzis, Experimental investigation of inertial flow processes in porous media, *J. of Hydrology*, 374 (2009) 242-54.
- [41] Z. Chen, S.L. Lyons, G. Qin, Derivation of the Forchheimer law via homogenization, *Transp. Porous Med.*, 44 (2001) 325–35.
- [42] I.F. MacDonald, M.S. El-Sayed, K. Mow, F.A.L. Dullien, Flow through Porous Media-the Ergun Equation Revisited, *Ind. Eng. Chem. Fundam.*, 18 (1979) 199-208.
- [43] T. Farkas, G. Zhong, G. Guiochon, Validity of Darcy's law at low flow-rates in liquid chromatography, *J. Chromatogr. A*, 849 (1999) 35-43.

- [44] R.D. Barree, M.W. Conway, Beyond beta factors: A complete model for Darcy, forchheimer, and trans-forchheimer flow in porous media, Proceedings - SPE Annual Technical Conference and Exhibition, (2004) 7-14.
- [45] A. Bourgeat, E. Marušić-Paloka, A. Mikelić, Weak non-linear corrections for Darcy's Law, Math. Models and Methods Appl. Sci., 6 (1996) 1143–55.
- [46] M. Balhoff, A. Mikelić, M.F. Wheeler, Polynomial Filtration Laws for Low Reynolds Number Flows Through Porous Media, Transp. Porous Med., 81 (2010) 35–60.
- [47] E. Marušić-Paloka, A. Mikelić, The derivation of a non-linear filtration law including the inertia effects via homogenization, Nonlinear Anal. Theory Methods Appl., 42 (2000) 97–137.
- [48] J.-C. Wodié, T. Levy, Correction non linéaire de la loi de Darcy. C.R. Acad. Sci. Paris t.312, Série II (1991) 157–161.
- [49] M. Rasoloarijaona, J.-L. Auriault, Non-linear seepage flow through a rigid porous medium, Eur. J. Mech. B Fluids, 13 (1994) 177–95.
- [50] M. Firdaouss, J.L. Guermond, P. Le Quéré, Nonlinear corrections to Darcy's law at low Reynolds numbers, J. Fluid Mech., 343 (1997) 331–50.
- [51] O. Couland, P. Morel, J.P. Caltagirone, Numerical modelling of nonlinear effects in laminar flow through a porous medium, J. Fluid Mech., 190 (1988) 393–407.
- [52] H.E. Rose, On the resistance coefficient–Reynolds number relationship for fluid flow through beds of granular materials, Proc. Inst. Mech. Eng., 153 (1945) 154–61.
- [53] H.E. Rose and A.M.A. Rizk, Further researches in fluid flow through beds of granular material, Proc. Inst. Mech. Eng., 160 (1949) 493–503.
- [54] R.E. Hicks, Pressure drop in packed beds of spheres, Ind. Eng. Chem. Fundam., 9 (1970) 500–502.
- [55] J.A. Tallmadge, Packed bed pressure drop - an extension to higher Reynolds numbers, AIChE J., 16 (1970) 1092–93.
- [56] J. Sug Lee and K. Ogawa, Pressure drop through packed beds, J. Chem. Eng., 27 (1974) 691–93.
- [57] H. Kürten, J. Raasch and H. Rumpf, Beschleunigung eines kugelförmigen Feststoffteilchens im Strömungsfall konstanter Geschwindigkeit, Chem. Ing. Tech., 38 (1966) 941–48.

- [58] A. Montillet, E. Akkari and J. Comiti, About a correlating equation for predicting pressure drops through packed beds of spheres in a large of Reynolds numbers, *Chem. Eng. Process.*, 46 (2007) 329–33.
- [59] M. Özdiñç Çarpinlioglu, E. Özahi, M.Y. Gündogdu, Determination of laminar and turbulent flow ranges through vertical packed beds in terms of particle friction factors, *Adv. Powder Tech.*, 20 (2009) 515–20.
- [60] E. Ozahi, M.Y. Gundogdu and Melda Ö. Carpinlioglu, A Modification on Ergun's Correlation for Use in Cylindrical Packed Beds With Non-spherical Particles, *Adv. Powder Tech.*, 19 (2008) 369-81.
- [61] L.G. Gibilaro, R. Di Felice, S.P. Waldram, P.U. Foscolo, Generalized friction factor and drag coefficient correlations for fluid-particle interactions, *Chem. Eng. Sci.*, 40 (1985) 1817-23.
- [62] S. Benyahia, M. Syamlal, and T.J. O'Brien, Extension of Hill–Koch–Ladd drag correlation over all ranges of Reynolds number and solids volume fraction, *Powder Tech.*, 162 (2006) 166-174.
- [63] O. Molerus, Druckverlustgleichung für die Durchströmung von Kugelschüttungen im laminaren und im Übergangsbereich, *Chem. Eng. Tech.*, 49 (1977) 675.
- [64] G. Kovács, Seepage Hydraulics, Development in Water Sciences, Elsevier, 1981.
- [65] H.R. Kadlec and L.R. Knight, Treatment Wetlands, Lewis Publishers, 1996.
- [66] P.U. Foscolo, L.G. Gibilaro and S.P. Waldram, A unified model for particulate expansion of fluidised beds and flow in fixed porous media, *Chem. Eng. Sci.*, 38 (1983) 1251-60.
- [67] D. Mehta, M.C. Hawley, Wall effect in packed columns. *Ind. Eng. Chem. Proc. Des. Dev.* 8 (1969) 280–82.
- [68] J.P. Du Plessis, Analytical Quantification of Coefficients in the Ergun Equation for Fluid Friction in a Packed Bed, *Transport in Porous Media*, 16 (1994) 189-207.
- [69] W. Reichelt, Zur Berechnung des Druckverlustes einphasig durchströmter Kugel- und Zylinderschüttungen, *Chemie-Ingenieur-Technik*, 44 (1972) 1068-71.
- [70] A.R. Martin, C. Saltiel, W. Shyy, Frictional losses and convective heat transfer in sparse, periodic cylinder arrays in cross flow, *Int. J. Heat Mass Transfer.*, 41 (1998) 2383–97.
- [71] A. Tamayol, K. W. Wong, and M. Bahrami, Effects of microstructure on flow properties of fibrous porous media at moderate Reynolds number, *Phys. Rev. E*, 85 (2012) 026318.

- [72] Y. Tanino and Heidi M. Nepf, Laboratory Investigation of Mean Drag in a Random Array of Rigid, Emergent Cylinders, *J. Hydraul. Eng.*, 134 (2008) 34-42.
- [73] X. Chen, T.D. Papathanasiou, The transverse permeability of disordered fiber arrays: A statistical correlation in terms of the mean nearest inter fiber spacing, *Transport in Porous Media*, 71 (2008) 233-51.
- [74] James G. Berryman, Random close packing of hard spheres and disks, *Phys. Rev. A*, 27 (1983) 1053-61.
- [75] B. J. Alder and T. E. Wainwright, Phase Transition in Elastic Disks, *Phys. Rev.*, 127 (1962) 359-61.
- [76] K. Yazdchi, S. Srivastava and S. Luding, On the validity of the Carman-Kozeny equation in random fibrous media, *Particle-Based Methods II - Fundamentals and Applications* (2011), 264-273, Barcelona, Spain.
- [77] P.C. Carman, Fluid flow through granular beds, *Transactions of the Institute of Chem. Eng.*, 15 (1937) 150-66.
- [78] B. Astroem, R. Pipes, S. Advani, On flow through aligned fiber beds and its application to composite processing, *J. of Composite Materials*, 26 (1992) 1351-73.
- [79] L. Skartsis, J.L. Kardos, B. Khomami, Resin flow through fiber beds during composite manufacturing processes. Part II. Numerical and experimental studies of Newtonian flow through ideal and actual fiber beds, *Polym. Eng. Sci.*, 32 (1992) 231-39.
- [80] A.S. Sangani, A. Acrivos, Slow flow past periodic arrays of cylinders with application to heat transfer, *Int. J. Multiphase Flow*, 3 (1982) 193-206.
- [81] B.R. Gebart, Permeability of Unidirectional Reinforcements for RTM, *Journal of Composite Materials*, 26 (1992) 1100-33.
- [82] Chahid K. Ghaddar, On the permeability of unidirectional fibrous media: A parallel computational approach, *Phys. Fluids*, 7 (1995) 2563-86.
- [83] A.S. Sangani and G. Mo, Inclusion of lubrication forces in dynamic simulations, *Phys. Fluids*, 6 (1994) 1653-62.
- [84] T. Burgener, D. Kadau, H.J. Herrmann, Clustering of inelastic soft spheres in homogeneous turbulence, *arXiv:1204.4985v2*.
- [85] T. Burgener, D. Kadau, H.J. Herrmann, Particle and particle pair dispersion in turbulence modeled with spatially and temporally correlated stochastic processes, *arXiv:1205.6297v2*.

# 6

## Mesoscale coupling of FEM/DEM for fluid-particle interactions

*"Intuition will tell the thinking mind where to look next"*

*~Jonas Salk~*

## Abstract

A new method for two-way fluid-particle coupling on an unstructured mesoscopically coarse mesh is presented. In this approach, we combine a higher order finite element method (FEM) on a moving mesh for the fluid with a soft sphere discrete element method (DEM) for the particles. The novel feature of the proposed scheme is that the FEM mesh is a dynamic Delaunay triangulation based on the positions of the moving particles. Thus, the mesh is multipurpose: it provides (i) a framework for the discretization of Navier-Stokes equations, (ii) a simple tool for detecting contacts between moving particles, and (iii) a basis for coarse graining and coupling of other physical fields (viz. temperature, electromagnetic, etc.). This approach is suitable for a wide range of dilute and dense flows, since the mesh resolution scales with particle density in a given region. Two-way momentum exchange is implemented using semi-empirical drag laws akin to other popular approaches, e.g. the discrete particle method, where a finite volume solver on a coarse and fixed grid is utilized. We validate the methodology with several test cases, including single- and double- particles settling and flow through ordered and random porous media, as compared against finely resolved FEM simulations.<sup>1</sup>

## Highlights

- A new mesoscopic approach is presented for two-way fluid-particle coupling on an unstructured moving mesh.
- The FEM mesh is a dynamic Delaunay triangulation based on the particle positions, which also provides a simple tool for detecting contacts between moving particles.
- Two-way momentum exchange is implemented using semi-empirical drag laws.
- The underlying data structure, i.e. the mesh, can be potentially used for coupling of other physical fields (viz. temperature, electromagnetic, etc.).

---

<sup>1</sup>S. Srivastava, K. Yazdchi, S. Luding, Meso-scale coupling of FEM/DEM for fluid-particle interactions, (2012) in preparation.

S. Srivastava, K. Yazdchi and S. Luding, Two way coupled fluid-particle interaction on a deforming unstructured mesh, ECCOMAS (2012), 2 pages, Vienna, Austria.

The FEM code was written by S. Srivastava, a former postdoc in our group.



## 6.1 Introduction

Fluid flow through particulate media is pivotal in many industrial processes, e.g. in fluidized beds, granular storage, industrial filtration and medical aerosols. Flow in these types of media is inherently complex and challenging to simulate, especially when the particulate phase is mobile. For the past two decades, particulate flows have been an active area of research and two widely used approaches are now considered state of the art. The first approach is based on an Eulerian continuum model of two phase flows, which only describes the averaged behavior of the multiphase media, see for example Kuipers et al. [1]. The second approach is based on an Eulerian-Lagrangian approach using finite volume/finite difference methods on a fixed grid as a fluid solver and either immersed boundary (IB) [2], fictitious domain (FD) [3], marker and cell (MAC) [4] or discrete element method (DEM) [5] for the particles. Both one-way and two-way couplings have been explored using these methods. While many fluid solvers are based on a stagger grid finite difference method, others e.g. Ladd [6, 7], Han et al. [8] and Feng et al. [2] have successfully utilized lattice Boltzmann method (LBM) as a fluid solver for particle-fluid suspensions. The LBM is an attractive alternative due to its ease of implementation and parallelization; however, it currently lacks the fidelity required for more complex flows.

A detailed description of flow through particulate media and accurate particle tracking can be obtained using discrete particle modeling (DPM) as proposed by Tsuji et al. [9], Kuipers et al. [10], Xu et al. [5] and Wu et al. [11]. In DPM, individual particles are tracked using Newton's laws of motion and particle-particle/wall interactions are also taken into account. These models invariably couple a continuum solver for fluid with DEM, as originally proposed by Cundall & Strack [12], for particles. The coupling between fluid and particles is explicit and is achieved using semi-empirical drag laws or closure relations of fluid-particle interactions, e.g. Ergun et al. [13], Gidaspow [14], Drummond et al. [15], Gebart et al. [16]. In a recent study, Yazdchi et al. [17, 18] proposed modified closure relations applicable to a wider range of porosities for both ordered (see chapter 2) and random (see chapter 3) porous media, valid for creeping flows. The DPM with hard sphere particle-particle interactions have been successfully applied to fluidized beds and slug formation in bubbly flows [19].

On one hand, for dense particulate flows, efficient contact detection in a DPM approach requires additional data structures and specialized algorithms adding to its computational overhead. On the other hand, the grid size for flow resolution is often very coarse, i.e. they are orders of magnitude bigger than the particle diameters. Thus, most DPM models ignore the sub-grid scale flow characteristics and this affects the small scale particle dynamics. Xu et al. [20] have recently proposed including sub-grid scale features to better capture the particle dynamics. Note that all the preceding methods [1-5] are based on explicit coupling between fluid- and particle solvers through empirical drag relations.

In contrast, in a finely resolved approach an implicit coupling is present. For example the distributed Lagrange multiplier (DLM) method of Glowinski et al. [21] has been successfully applied to simulate fluid-particle interaction in porous media and fluidized

beds. Due to additional set of Lagrange multipliers, DLM is more computationally expensive than DPM. However, similar to DPM, the particles are not modeled geometrically in this approach, but the flow in their vicinity of particles is better resolved. Using DLM, Pan et al. [22] simulated the behavior of fluidized bed; however, they ignored particle-particle interactions to keep the computational costs low. More recently, Kanarska et al. [23] have coupled the DLM with DEM for particle-particle interactions. Fully resolved simulations of particle laden flows using FD by Avci et al. [3] is in spirit similar to DLM, except that coupling forces are computed by integrating stress field at the surface of the particles. In essence, the two methods are exact as no drag correlations are required to couple the two phases.

Interest in using a deforming mesh for fluid-structure/particle interactions has persisted for sometime now. Tezduyar et al. [24] developed the so-called Deforming Spatial Domain/Deforming Space Time (DSD/DST)-FEM for flow problems with deforming interfaces using the so called arbitrary Lagrangian-Eulerian (ALE) methods and space-time finite element method. In this approach, particles are geometrically modeled in the mesh and the flow is fully resolved around each particle and hence is computationally expensive for dense flows [2].

In this chapter, we introduce a new method for fluid-particle interaction based on a two-way coupling between a higher order FEM and a soft sphere DEM approach on a deforming unstructured mesh. The main feature of our approach is a deforming Delaunay triangulation, which is utilized as an efficient contact detection tool for the moving particles as well as a finite element mesh for discretizing the Navier-Stokes equation. It is known that the nearest neighbor property of the Delaunay edges renders it an attractive algorithm for contact detection, see Ferrez et al. [25] and references therein. To better resolve the flow around the particles, we apply the interaction forces as point forces at the particle locations (see Section 6.3.1). To our knowledge, this study is the first attempt to apply a moving Delaunay triangulation (particle based) for both contact detection and finite element fluid solver. Coupling with FEM as fluid solver has several advantages namely, it may provide the leverage of higher order interpolations for simulating flow to the desired accuracy and scales, even when the mesh is coarse. Another motivation to use FEM is that for packed beds and dense particulate flows, the mesh can also be used as a coarse graining tool for stress and strain fields, which is often a quantity of interest.

Despite the advantages of using FEM for higher accuracies, Wu et al. [11] have pointed out several issues associated with implementing fluid-particle coupling on unstructured mesh. The most restrictive one pertains to computing the particle volume fraction in a given cell. This happens since particles may be shared between neighboring cells and thereby adding to the computational complexity. We circumvent this issue in present methodology by resorting to a moving mesh and an ALE formulation. In this way, the particles have finite radius and always lie at the element vertices and consequently, a coarse mesh generally remains robust with respect to element degeneration; in other cases, re-meshing is deployed whenever necessary. Furthermore, the particle-particle/wall interactions are modeled using a linear spring contact model with dissipation and friction.

The rest of this chapter is organized as follows. We start with an introduction to the mathematical model applicable to viscous, incompressible flow through an isotropic porous media in Section 6.2. The drag force model used for coupling FEM and DEM and the contact force model used in DEM are discussed in details. In Section 6.3, we detail the underlying finite element formulation and discuss the methodology for approximating of the porosity field and its impact on numerical computations. This is followed by numerical examples in Section 6.4, demonstrating flow in static and moving particulate media. Finally, Section 6.5 presents conclusions drawn in this chapter and an outlook for future studies.

## 6.2 Mathematical model

The governing equation for the multiphase flow is a set of porosity scaled Navier-Stokes equations, which define the flow of fluid in a particulate porous media (see Anderson et al. [26], Deen et al. [27], Xu et al. [5]). Considering an incompressible fluid (i.e. the density,  $\rho$  is constant) in an Eulerian flow domain,  $\Omega$ , we can write the equations of both fluid and solid phase as

Fluid phase:

$$\left. \begin{aligned} \rho \frac{\partial(\varepsilon \bar{u})}{\partial t} + \rho \nabla \cdot (\varepsilon \bar{u} \bar{u}) &= -\varepsilon \nabla p + \nabla \cdot (\varepsilon \boldsymbol{\tau}) + \varepsilon \rho \bar{g} - \sum_i \bar{f}_i^D \\ \boldsymbol{\tau} &= \mu \left( \nabla \bar{u} + (\nabla \bar{u})^T \right) - \frac{2}{3} \mu (\nabla \cdot \bar{u}) \mathbf{I} \\ \frac{\partial \varepsilon}{\partial t} + \nabla \cdot (\varepsilon \bar{u}) &= 0 \end{aligned} \right\} \text{in } \Omega \quad (6.1)$$

Solid phase:

$$\left. \begin{aligned} m_i \frac{d\bar{u}_i}{dt} &= \bar{F}_i^D + \sum_j \bar{F}_{ij}^C - V_i \nabla p + m_i \bar{g} \\ I_i \frac{d\bar{\omega}_i}{dt} &= \mathbf{T}_i^D + \sum_j r_i \hat{n}_{ij} \times \bar{F}_{ij}^C \end{aligned} \right\}, \quad (6.2)$$

where  $\varepsilon$ ,  $\mu$ ,  $\bar{u}$ ,  $p$ ,  $\boldsymbol{\tau}$  and  $\bar{g}$  are the porosity, viscosity, fluid velocity vector, pressure, shear stress and the acceleration due to gravity, respectively. For the particles  $m$ ,  $I$ ,  $r$ ,  $V$ ,  $\bar{u}$  and  $\bar{\omega}$  represent particle mass, moment of inertia, radius, volume, translational and angular velocity, respectively. The  $\bar{F}_{ij}^C$  represents the inter-particle/wall contact force and  $\hat{n}_{ij}$  is the unit vector point from the center of the particle to the contact point (with particle  $j$ ). Finally,  $\bar{f}_i^D$  and  $\bar{F}_i^D$  representing the drag force per unit volume

on the fluid due to interaction with the  $i^{\text{th}}$  particle and the total drag force acting on the  $i^{\text{th}}$  particle, defined in the following section. In the angular momentum equation,  $T_i^D$  represents the torque experienced by the  $i^{\text{th}}$  particle due to fluid drag when flow around the particle becomes asymmetric, as shown in Section 6.4.2. The pressure gradient term in Eq. (6.2) accounts for the net buoyancy force on each particle passing through its center. Since Eq. (6.2) is a system of ordinary differential equations in time, it can be integrated using a suitable numerical integrator. For accuracy and conservation properties, we use the velocity-Verlet time integrator, which is second order accurate in time<sup>2</sup>. Note that the indices  $i$  and  $j$  do not represent the tensorial components of respective fields in the above equation, instead  $i$  represents particle number and  $j$  is the index for the contacts of the  $i^{\text{th}}$  particle. In the rest of this section, we introduce the model for the drag force density, used to explicitly couple the fluid and particle dynamics.

### 6.2.1 Drag force model

The drag force accounts for the resistance to the flow through a porous media, and is inversely related to its permeability,  $K$ . The permeability is the proportionality constant in Darcy's equation

$$\vec{U} = \frac{-K\nabla p}{\mu}, \quad (6.3)$$

where  $U$  is the horizontal *superficial* (discharge) fluid velocity and defined to be

$$\vec{U} = \frac{1}{V} \int_{V_f} \vec{u} dV = \varepsilon \langle \vec{u} \rangle, \quad (6.4)$$

where  $V$  and  $V_f$  are total available volume and the volume of fluid. On the other hand, the *intrinsic* average flow velocity  $\langle \vec{u} \rangle = \frac{1}{V_f} \int_{V_f} \vec{u} dV$  defined over the fluid volume only.

Following Yazdchi et al. [17], the permeability,  $K$  is related to the drag coefficient,  $\beta$  as

$$\beta = \frac{\mu \varepsilon^2}{d^2 \lambda}, \quad (6.5)$$

where  $\lambda = K/d^2$  represents the non-dimensional permeability and is often used instead of  $K$  in literature. Several existing correlations for  $\lambda$  are listed in Table 6.1. Henceforth, the drag force density in the fluid,  $\vec{f}_i^D$  is defined at a point  $x_e$ , (see next section for details). The force density is modeled as

---

<sup>2</sup> Since the forces between particles can be dissipative the choice of an integrator does not have a major impact on either solution quality or the performance, thus will not be discussed in detail in this chapter.

$$\vec{f}_i^D = \beta(\langle \vec{u} \rangle - \vec{u}_i) \psi(x - x_e), \quad (6.6)$$

where  $\vec{u}_i$  is the instantaneous velocity of the  $i^{\text{th}}$  particle and  $\psi$  is a function describing the influence of the force density in its neighborhood. While for  $\psi$  several possibilities exist, e.g. a Gaussian function, in this chapter we restrict ourselves to  $\psi(x - x_e) = \delta(x - x_e)$ , i.e. the Dirac delta function, for reasons that are discussed in the next section. Eq. (6.6) is a model of the drag force density in the fluid in the neighborhood of the particle. The drag from fluid to particle is proportional to the relative velocity between particle and the fluid. In other words, a particle moving in the direction of the flow in its neighborhood with the average velocity does not experience any drag.

**Table 6.1:** Different non-dimensional permeabilities for monodisperse systems as a function of porosity ( $\varepsilon$ ) and particle diameter ( $d$ ) in the creeping flow ( $\text{Re} \ll 1$ ) regime.

Author	Porosity range	$\lambda$
<b>Ordered arrays (square configuration)</b>		
Drummond et al. [15]	$\varepsilon \geq 0.6$	$\lambda_D^s = \frac{1}{32\phi} \left( \ln\left(\frac{1}{\phi}\right) - 1.476 + \frac{2\phi - 0.796\phi^2}{1 + 0.489\phi - 1.605\phi^2} \right), \phi = 1 - \varepsilon$
Gebart [16]	$\varepsilon < 0.6$	$\lambda_G^s = C \left( \sqrt{\frac{1 - \varepsilon_c}{1 - \varepsilon}} - 1 \right)^{5/2}, \quad C = \frac{4}{9\pi\sqrt{2}}, \quad \varepsilon_c = 1 - \pi/4$
Yazdchi et al. [17]	$0.16 \leq \varepsilon \leq 0.95$	$\lambda_Y^s = \lambda_{G2}^s + \frac{(\lambda_D^s - \lambda_{G2}^s)}{2} \left( 1 + \tanh\left(\frac{\varepsilon - 0.75}{0.037}\right) \right), \quad \lambda_{G2}^s = \frac{\lambda_G^s}{1 + 0.336(\varepsilon - 0.21)}$
<b>Random arrays</b>		
Ergun [13]	$0.4 \leq \varepsilon \leq 0.8$	$\lambda_E^r = \frac{\varepsilon^3}{150(1 - \varepsilon)^2}$
Yazdchi et al. [18]	$0.16 \leq \varepsilon \leq 0.95$	$\lambda_Y^r = \lambda_G^r + \frac{(\lambda_{CD}^r - \lambda_G^r)}{2} \left( 1 + \tanh\left(\frac{\varepsilon - 0.67}{0.1}\right) \right), \quad \lambda_{CD}^r = 0.97\lambda_D^r(1 + 0.18\varepsilon),$ $\lambda_D^r = \frac{1}{32\phi} \left( -\ln(\phi) - 1.497 + 2\phi - \frac{\phi^2}{2} - 0.739\phi^4 + \frac{2.534\phi^5}{1 + 1.2758\phi} \right), \phi = 1 - \varepsilon,$ $\lambda_G^r = 0.035 \left( \sqrt{\frac{0.84}{1 - \varepsilon}} - 1 \right)^{5/2}$

Ergun's equation<sup>3</sup> is a commonly used drag law, which is a non-linear function of porosity, fluid velocity and particle size. It accurately predicts the total drag force for a limited range of porosities in 3D. Using this relation, one can derive the macroscopic permeability of the media and use Darcy's equation to determine the average flow

<sup>3</sup> Ergun equation is essentially a correction to the Carman-Kozeny [28] drag relation for creeping flows, which also takes into account the inertial drag at higher Reynolds numbers [29], see chapter 5.

velocity through the media. An aptly modified version of this equation applicable in 2D is deployed as suggested in [18], see chapters 2 and 5. Accordingly, a more general form of  $\beta$ , taken directly from Ergun et al. [13], applicable towards inertial regimes can be written as

$$\beta = \frac{\mu \varepsilon^2}{d^2 \lambda} + 1.75 \rho \frac{(1 - \varepsilon)(\langle \vec{u} \rangle - \vec{u}_i)}{d}, \quad (6.7)$$

which can be replaced by the results in chapter 5, see Eq. (5.8). In the following, we introduce a simple contact force model to account for inter-particle/wall forces.

### 6.2.2 Contact force model

We take into account the particle-particle/wall interactions and therefore, the contact forces are essential in order to integrate the particles equations of motion. As elsewhere [30], we use a linear spring-dashpot model for the contact force

$$\vec{F}_{ij}^C = \kappa \delta_{ij}^p \hat{n}_{ij} + \eta \vec{v}_{ij}, \quad (6.8)$$

where  $\kappa, \eta, \vec{v}_{ij}$  and  $\delta_{ij}^p$  are contact stiffness, viscous damping coefficient, relative velocity between particle  $i$  and  $j$  and the overlap, respectively. A similar model can also be implemented in the tangential direction along with a sliding spring based on tangential overlap, for cases where rotation and friction are relevant (but is not used in this chapter). The contact stiffness,  $\kappa$  and overlap,  $\delta_{ij}^p$  set a limit value for the DEM time step as

$$\Delta t_{\text{DEM}} \cong \frac{1}{50} \pi / \varpi \quad \text{and} \quad \varpi = \sqrt{2\kappa/m - (4\eta/m)^2} \quad \text{for numerical simulations.}$$

A particle may also have more than one contact at any given time, in this case the total contact force is found by summing over all the contacts. For further details and state of the art in DEM contact models, see the review paper by Luding [30] and references therein.

## 6.3 Finite element formulation

Let us assume we have suitably defined discrete finite element (polynomial) spaces  $V^h, S^h$  for trial and test solutions and let  $\vec{u}^h, p^h$  denote the trial solution of Eq. (6.1). Further, we divide our domain  $\Omega$  into non-overlapping triangles  $\Omega_k$  such that  $\bigcup_k \Omega_k = \Omega$ . The weak form is obtained by multiplying the Eq. (6.1) with appropriate test functions  $(\vec{v}^h, q^h)$  and performing integrating by parts on the diffusion term. This yields a mixed Galerkin formulation for  $(\vec{u}^h, p)$ , which reads as

$$\text{Find } (\vec{u}^h, p^h) \in V^h \times S^h \text{ such that } \forall (\vec{v}^h, q^h) \in V^h \times S^h,$$

$$\rho \left( \frac{\vec{u}^h \partial \varepsilon}{\partial t} + \frac{\varepsilon \partial \vec{u}^h}{\partial t}, \vec{v}^h \right) + \left( \varepsilon (\vec{u}^h - \vec{u}_M) \vec{u}^h, \nabla \vec{v}^h \right) + \left( \varepsilon \boldsymbol{\tau}^h, \nabla \vec{v}^h \right) = \left( \varepsilon p^h, \nabla \cdot \vec{v}^h \right) - \left( \vec{f}_i^D - \varepsilon \rho \vec{g}, \vec{v}^h \right) + \sum_{\Omega_k} \int_{\Omega_k} (\text{S.T.}), \quad (6.9)$$

$$\left( -\frac{\partial \varepsilon}{\partial t}, q^h \right) = \left( \varepsilon \nabla \cdot \vec{u}^h + \vec{u}^h \cdot \nabla \varepsilon, q^h \right)$$

where  $(x, y) = \int_{\Omega} xy d\Omega$  denotes the standard inner product on  $V^h$  and  $S^h$ . Notice that for

the moving mesh we replace the convection velocity  $\vec{u}^h$  by  $(\vec{u}^h - \vec{u}_M)$ , where  $\vec{u}_M$  is the mesh velocity in ALE formulation and essentially takes into account the convection of the fluid momentum due to mesh motion. To compute  $\vec{u}_M$  at quadrature points inside a triangle, we interpolate the velocities of the nodal particles of that triangle. Using nodal velocities ensures that the Geometric Conservation Law (GCL) for the ALE formulation is satisfied [31, 32], since a constant solution is reproduced trivially. The above formulation requires a priori knowledge of the porosity field at every point inside the domain, which can be computed using SPH interpolation, see Section 6.3.2.

For additional robustness and stability in our formulation, we add streamline-upwind/Petrov Galerkin (SUPG), pressure stabilized/Petrov Galerkin (PSPG) and other terms similar to least square incompressibility constraint (LSIC) as discussed in [33], to the above variational formulation. Forster et al. [34] have investigated that such stabilization is also effective when simulating on distorted meshes. Henceforth, following [24] we add residual based stabilization terms (S.T.) given by

$$\text{S.T.} = \left[ \boldsymbol{\tau}_{SUPG} \vec{u}^h \cdot \nabla \vec{v}^h + \frac{1}{\rho} \boldsymbol{\tau}_{PSPG} \nabla q^h \right] \cdot \vec{r}_u(\vec{u}^h, p^h) + \boldsymbol{\tau}_{LSIC} (\nabla \cdot \vec{v}^h) r_p(\vec{u}^h), \quad (6.10)$$

where  $\vec{r}(\vec{u}^h, p^h)$  denotes the residual of continuity equation, Eq. (6.1)

$$\vec{r}_u(\vec{u}^h, p^h) = \rho \left( \frac{\partial (\varepsilon \vec{u}^h)}{\partial t} + \nabla \cdot (\varepsilon \vec{u}^h \vec{u}^h) \right) + \varepsilon \nabla p - \nabla \cdot (\varepsilon \boldsymbol{\tau}^h) - \varepsilon \rho \vec{g}, \quad (6.11)$$

$$r_p(\vec{u}^h) = \frac{\partial \varepsilon}{\partial t} + \nabla \cdot (\varepsilon \vec{u}^h)$$

The stabilization parameters are fixed using the following expressions

$$\boldsymbol{\tau}_{SUPG} = \boldsymbol{\tau}_{PSPG} = \left[ \left( \frac{2}{\Delta t} \right)^2 + \left( 2 \frac{\|\vec{u}^h\|}{h_e} \right)^2 + \left( 4 \frac{\mu}{\rho h_e^2} \right)^2 \right]^{-1/2}, \quad (6.12)$$

$$\boldsymbol{\tau}_{LSIC} = \frac{h_e}{3} \|\vec{u}^h\|$$

where  $h_e$  is the length of the smallest edge of the element. Eq. (6.12) has shown to be a convenient choice in computations [33].

Stable discretization of Eq. (6.9) can be difficult to construct and solutions are well studied in literature, see [35] for a detailed theory. Classical methods forbid equal interpolation of both velocity and pressure variables in the above setting. Stable solutions can usually be obtained if  $P_p \subset P_u$  (polynomial spaces for  $p$  and  $u$ ) in numerical approximations. Furthermore, it is known that the incompressibility constraint is not strongly enforced when using a continuous approximation for the pressure field [36]. To circumvent this problem, we adopt a discontinuous polynomial space for pressure discretization. In this chapter, unless stated otherwise, we choose stabilized P1/P0 or P2/P1 elements with continuous velocities and discontinuous pressure polynomials. However, this formulation is not restricted at all in choosing higher order FE spaces.

### 6.3.1 The mesh and drag force computation

The FE mesh adapted in the above formulation is a Delaunay triangulation based on the particle locations. This implies that all interior vertex nodes of the mesh are occupied by particles at all times, while the boundary nodes are inserted only for the convenience of computation and application of boundary conditions, see Fig. 6.1.

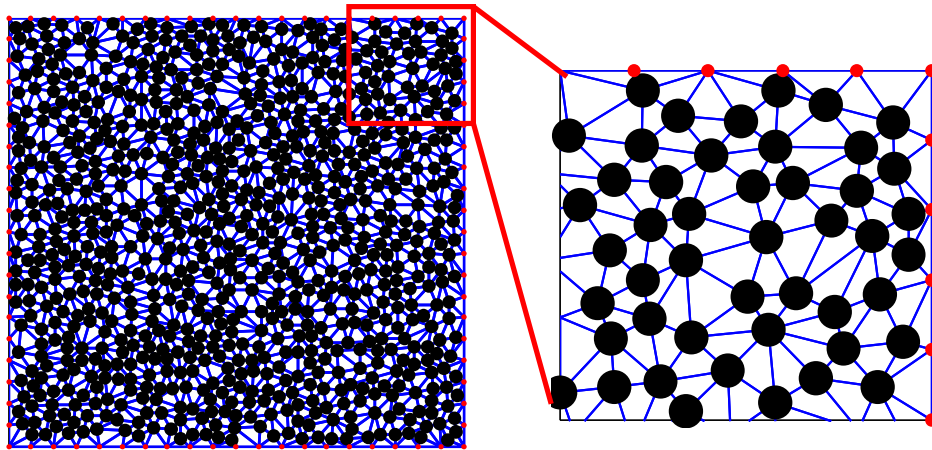


**Figure 6.1:** Finite element mesh based on 800 randomly distributed particles at porosity  $\varepsilon = 0.6$ . (right) Complete Mesh; (left) Zoomed in, upper right corner which shows the added boundary nodes (red points) to define the geometry. The boundary nodes are distributed at equal distances of approximately twice of the particle diameter (i.e.  $\sim 2d$ ).

For moving particles the mesh vertices move with the particles, thereby deforming the mesh. Currently, we re-mesh at fixed (short) time intervals in order to maintain the quality of triangles and use the triangulation for contact detection. This implies that a new



triangulation is created from the current particle positions and the solution from the old mesh is transferred to the new mesh using a simple projection scheme. To remain focused, we will not discuss the projection scheme in detail.

In Fig. 6.2(a) the particle overlaps with an element are shown for particles of different sizes. While we do not address polydisperse particles in a fluid flow in this paper, it is shown to highlight the generality of the proposed method. Fig. 6.2(b) shows the drag force contribution from each element. The total drag force and torque acting on the  $i^{\text{th}}$  particle is considered as a sum of contributions from all the overlap elements

$$\vec{f}_e^D = \frac{1}{A_e} \sum_{p=1}^3 \vec{F}_e^p \delta(x - x_e), \quad \vec{F}_p^D = \sum_{e=1}^{E_e} \vec{F}_e^p, \quad T_p^D = \sum_{e=1}^{E_e} r_p \hat{n} \times \vec{F}_e^p, \quad (6.13)$$

where  $e$  is the index counting the number of triangular overlaps,  $E_e$  of the  $i^{\text{th}}$  particle (for example  $E_e=5$  in Fig. 6.2(b)).

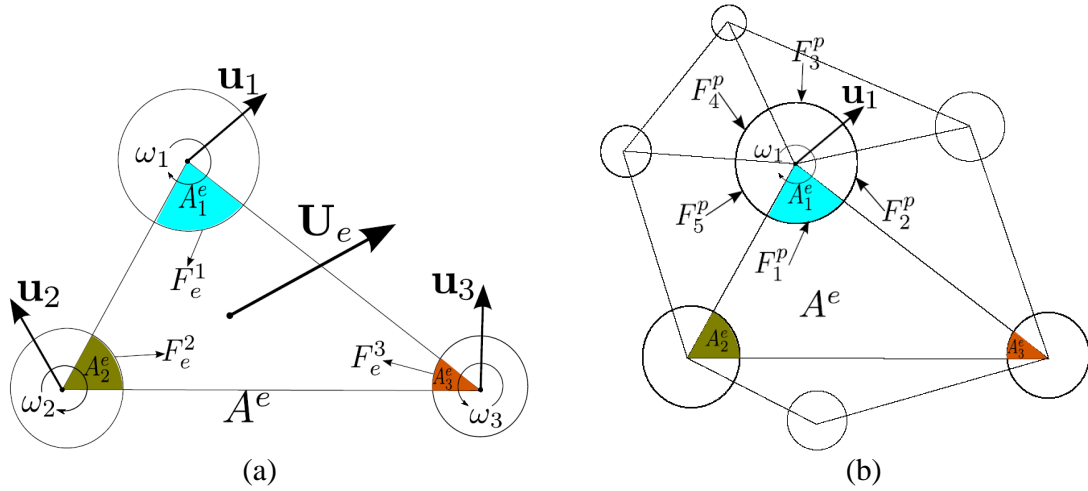


**Figure 6.2:** (a) An element from the mesh is shown with the 3 particles occupying its vertices. The particle translational and angular velocities are represented by  $u_1$ ,  $u_2$ ,  $u_3$ ,  $\omega_1$ ,  $\omega_2$ ,  $\omega_3$ , respectively.  $U_e$  represents the superficial velocity in the cell.  $A^e$  represents the area of the element  $e$  and  $A_i^e$  the area of the respective overlaps. (b) The drag force contributions to a particle from neighboring/touching fluid elements are shown.

An important modeling aspect from the numerical point of view is the location of the drag forces,  $x_e$  computed from Eq. (6.6). Here we list a few possibilities for application of the  $\vec{f}_i^D$  (as shown in Fig. 6.3):

- (a) At the mid point of the chord of the respective overlaps;
- (b) At the mid point of the arc in respective overlaps (as in Fig. 6.2);
- (c) At the intersection of particles circumference with element edges;

(d) At the nodal location of the respective particle.

Fig. 6.3 shows several possible sites for the application of the drag force. Unless specified otherwise, for simplicity, we choose the mid point of the chord (i.e. Fig. 6.3(a)), as it lies close to the fluid solid interface, where the momentum exchange occurs. We do not expect the above choices to have a major impact on the numerical results. However, it remains a task for future studies.

A force equal in magnitude but opposite in direction is applied to the fluid, i.e.  $\vec{F}_e^1 = -\vec{F}_1^p$ , at exactly the same point in the cell, thereby providing a consistent point force based coupling. The total force on the particle due to the fluid also consists of the buoyancy force, which is computed based on the pressure gradient at point  $x_e$ .

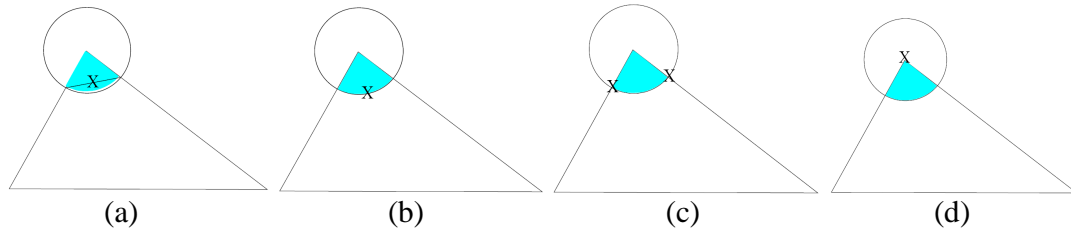


**Figure 6.3:** Point of application of the drag force; (a), (b), (c) and (d) show four distinct possibilities (marked with 'X') for  $x_e$ .

### 6.3.2 Local porosity calculation

At this point the general variational form, i.e. Eq. (6.9), can be solved using various assumptions for the porosity field. If the particles are fixed and are relatively homogeneously distributed, one can simplify Eq. (6.9) by making the assumption that the porosity is a constant for  $\forall \Omega_e$  and there is no temporal variation. Thus, for a locally averaged formulation, one could take a simpler approach and define a porosity for each triangle in the mesh, see Fig. 6.2, as

$$\varepsilon^e = 1 - \frac{\sum_{i=1}^3 A_i^e}{A^e} . \quad (6.14)$$

Although Eq. (6.14) is computationally efficient and simple to compute, this definition may lead to high fluctuations in the porosity field, thereby adding to the numerical instabilities especially for dynamic meshes. Therefore, in this chapter we utilize Eq. (6.14) only for static particles. To remedy this issue, we interpolate the particle number density using a smooth particle hydrodynamics (SPH) kernel function as given by

$$W(\vec{r}, h) = \frac{4}{\pi h^8} \begin{cases} (h^2 - r^2)^3 & 0 \leq r < h \\ 0 & r \geq h \end{cases}, \quad (6.15)$$

where  $h$  is the smoothing length. Following Xu et al. [20] one can evaluate the porosity and its gradient at an arbitrary point  $r$  as

$$\begin{aligned} \varepsilon(\vec{r}) &= 1 - \frac{\pi}{6} d^2 \sum_j W(|\vec{r} - \vec{r}_j|, h) \\ \nabla \varepsilon(\vec{r}) &= \frac{\pi}{6} d^2 \sum_j \nabla W(|\vec{r} - \vec{r}_j|, h) \end{aligned} \quad (6.16)$$

This definition yields a smoother porosity field; however, it incurs additional computation at each numerical quadrature point. Furthermore, special attention is required at the boundaries, e.g. Shepard correction, as to be studied elsewhere [37].

### 6.3.3 Time integration

After performing spatial integration, a second order finite difference scheme is utilized for time integration of the resulting system of equations. In a general form this can be written as

$$\vec{u} = \frac{\partial \vec{u}}{\partial t} = \frac{3\vec{u}^{n+1} - 4\vec{u}^n + \vec{u}^{n-1}}{2\Delta t}. \quad (6.17)$$

Using the necessary polynomial approximations of test and trial functions, the finite element matrices for each element in the mesh are assembled and the algebraic form of the equations is written as

$$\begin{aligned} [M]\{\vec{u}^h\} + [C(\vec{u}^h)]\{\vec{u}^h\} - [B]^T\{p^h\} + [A]\{\vec{u}^h\} &= \{\vec{f}\} \\ [B]\{\vec{u}^h\} + [\gamma_i]\{p^h\} &= \{\vec{f}_\varepsilon\} \end{aligned}, \quad (6.18)$$

where  $[M]$  represents the mass matrix,  $[C]$  is the matrix representing the convection term and  $[B]$  and  $[A]$  are the matrices due to pressure gradient and diffusion terms. The  $[\gamma_i]$  matrix is due to pressure penalty terms on interior boundaries. The terms in  $\{.\}$  denote the corresponding coefficients of the FE solution. We discretize in time using a second order scheme, i.e. Eq. (6.17), and the  $\theta$ -method (Crank-Nicolson method with  $\theta = 0.5$ ) for linearizing the convection term as

$$\begin{aligned}
& (3[M] + 2\Delta t\theta[C^n] + 2\Delta t[A])\{\bar{u}^h\}^{n+1} - 2\Delta t[B]^T\{p^h\}^{n+1} = \\
& 2\Delta t\{\bar{f}\} + (4[M] + 2\Delta t(1-\theta)[C^n])\{\bar{u}^h\}^n - [M]\{\bar{u}^h\}^{n-1}, \quad (6.19) \\
& [B]\{\bar{u}^h\} + [\gamma_i]\{p^h\} = \{\bar{f}_\varepsilon^n\}
\end{aligned}$$

where  $\{f\}$  represents the sum of the forces and explicit RHS terms. This implies that the drag forces are explicitly calculated. A suitable time-step size for the FEM is chosen according to Courant–Friedrichs–Lewy (CFL) condition and the DEM time-step is computed based on the natural frequency of particle contacts. In order to allow that at every fluid-time step  $n$  DEM time steps are performed, where the integer  $n = \Delta t_{FEM} / \Delta t_{DEM}$  is specified as input parameter together with  $\Delta t_{DEM}$ .

## 6.4 Numerical results

In this section the numerical results will be presented for both verification and validation of the code. The computational framework described in the previous section will be used to simulate several test cases for both static and moving particles. In the following subsection, we first present results for static particles before presenting the deforming mesh simulations.

### 6.4.1 Static particles

This subsection deals with flow through static porous media for both ordered and disordered cases. The first example is a simplified model of flow through a homogeneous porous media, which verifies the compatibility between the present model and Darcy's law. In the second example, we compare our mesoscale resolution simulation with the average velocities obtained from fully resolved ANSYS simulations of flow through both ordered and disordered arrays of static particles [17, 18]. The fully resolved simulations were performed using a fine mesh with  $\sim 10^5$  elements to accurately capture particle geometry and predict the flow around each particle. Our mesoscale approach, in contrast, contains elements of the same order of the number of particles (i.e. only a few hundreds). While the flow is not fully resolved, the comparison reassures that this scheme efficiently computes average velocities that are in the expected range and capture qualitatively the flow behavior at mesoscale.

#### 6.4.1.1 Case 0: Homogeneous porous media and Darcy flow

A well defined multiphase model should reproduce the behavior of single phase flow. When combined with a homogenized drag force (as opposed to point forces), the model must reproduce flow predictions from Darcy's law. As a preliminary verification and

validation case, we simulate flow through porous media using our formulation and a homogeneous body force (drag) in the test domain. We compare the average flow velocity from simulation with analytical results from Darcy's law. Recall that the permeability,  $K$  of the media describes the resistance to the flow and is intrinsically related to the drag coefficient,  $\beta$  via Eq. (6.5). Substituting Eq. (6.5) into (6.3) leads to

$$\varepsilon \langle \vec{u} \rangle = \vec{U} = -\frac{\varepsilon^2 \nabla p}{\beta}. \quad (6.20)$$

Setting  $\beta = 1 [\text{kg}/(\text{m}^3 \text{s})]$ ,  $\varepsilon = 0.5$  and  $\nabla p = -1 [\text{kg}/(\text{m}^2 \text{s}^2)]$ , one obtains  $\langle \vec{u} \rangle = 0.5 [\text{m/s}]$ . For this special case, Eq. (6.1) can be simplified to  $\frac{d\vec{u}}{dt} = -\frac{1}{\rho} \left( \nabla p + \frac{\beta}{\varepsilon} \vec{u} \right)$ , with  $\rho = 1 [\text{kg}/\text{m}^3]$ . Assuming that the fluid is at initially rest ( $\vec{u}(0) = 0$ ), the analytical, transient solution of the above equation is

$$\langle \vec{u}(t) \rangle = \frac{\varepsilon \nabla p}{\beta} \left( -1 + e^{\frac{-\beta}{\varepsilon} t} \right). \quad (6.21)$$

We also numerically solve Eqs. (6.1) and (6.2), where  $\vec{f}^D = \beta \langle \vec{u} \rangle$  acts as the distributed body force with stress-free boundary conditions. The problem setup is sketched in Fig. 6.4(a), and Fig. 6.4(b) shows that the flow quickly achieves a steady state value of  $\langle \vec{u} \rangle = 0.5 [\text{m/s}]$ , in perfect agreement with the analytical solution above.

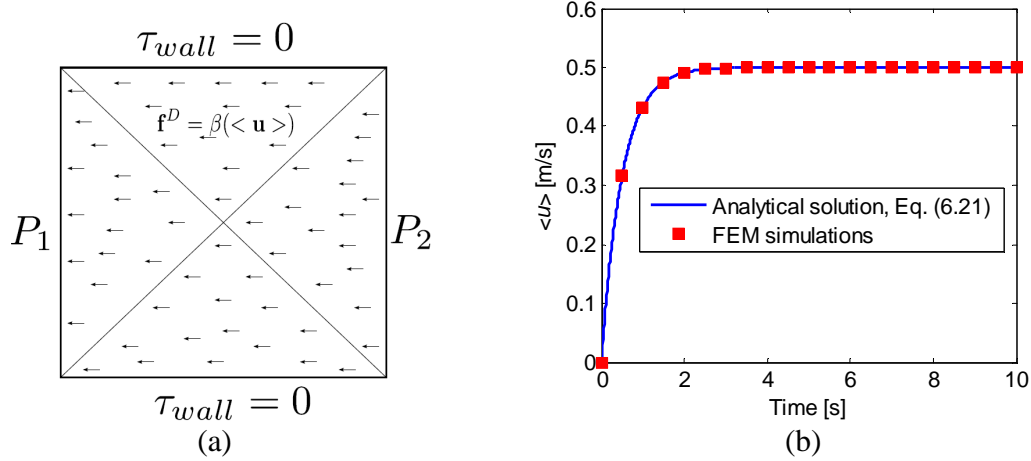


**Figure 6.4:** Darcy's homogenous flow calculation case: (a) Setup with a coarse mesh (4 triangular elements), where the flow is driven by a pressure gradient in  $x$  direction. The arrows depict the homogeneously smeared out resistive body force  $\vec{f}^D$ ; (b) For the given parameters, the simulation predicts the correct transient and steady state average velocity.

### 6.4.1.2 Case 1: Flow through ordered and random porous media

For this problem in a square domain, the top and the bottom boundaries have no-slip boundary conditions, while the left and right boundaries maintain a pressure gradient of  $5[\text{kg}/(\text{m}^2\text{s}^2)]$ . In Figs. 6.5 and 6.6, the color contours refer to the horizontal velocity in the ordered and random media, respectively. The blue regions indicate the slow flow region behind the each of  $5 \times 5$  particles in the array, while the predominant channel for the bulk flow lies between the two adjacent rows of particles. With decreasing porosity, the flow gradually confines itself between the walls and the top and bottom rows of particles as the interior becomes less and less permeable.

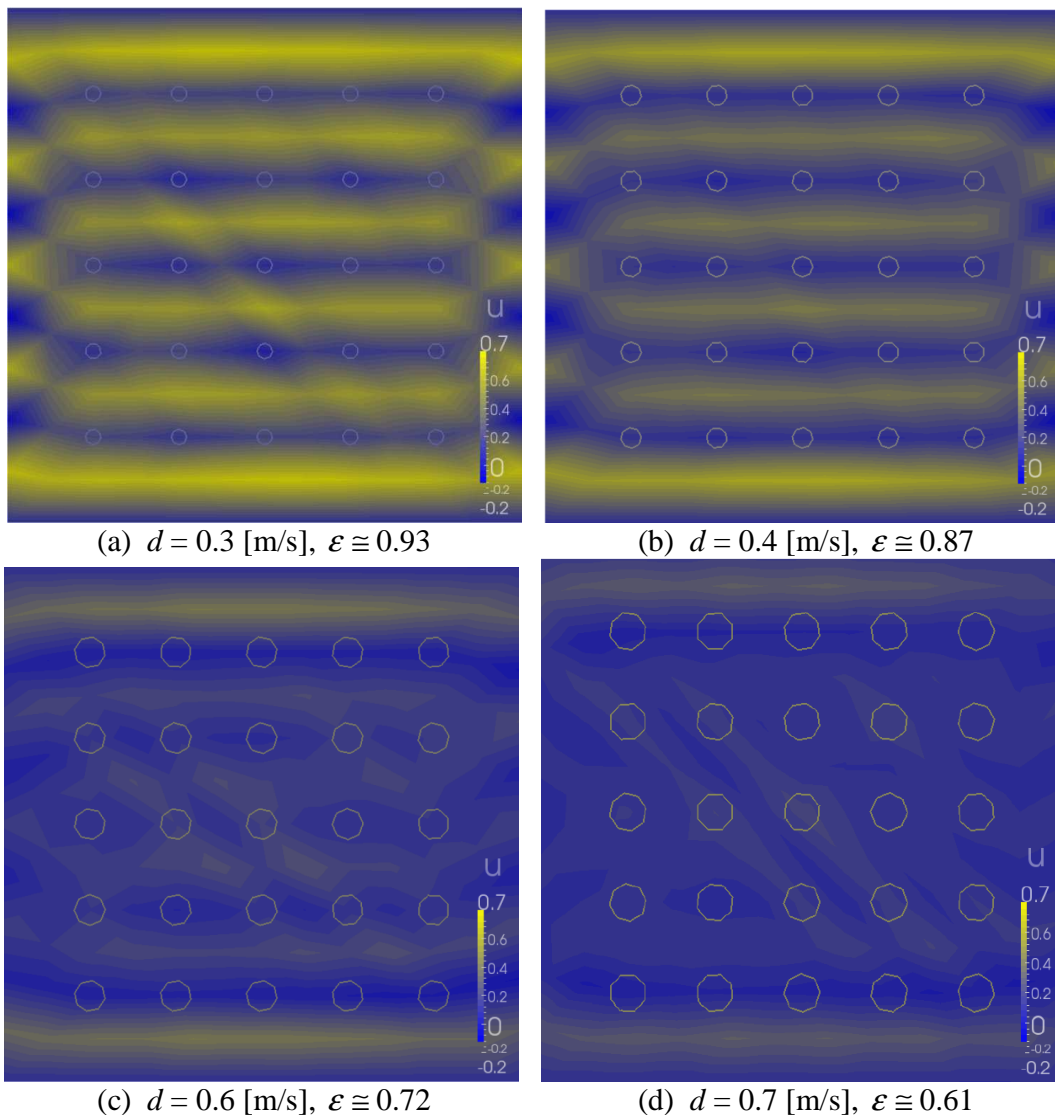


**Figure 6.5:** Horizontal velocity contours for ordered arrays (square configuration) of particles at different diameters,  $d$ , with  $\varepsilon$  given above.

For comparison purposes the average flow velocity is computed for the entire domain and compared with finely resolved FEM simulations. We utilized the drag law of Yazdchi et al. [17], from Table 6.1, in this simulation, which is valid for a wide range of porosities. The average flow predictions for both the ordered and random case agrees very well with data from finely resolved FEM simulations (see Fig. 6.7). The overall fit is remarkable as it closely follows the finely resolved curve. We must mention here that the fully resolved simulation is geometrically correct, i.e. particles are represented by holes with no-slip boundary conditions and contains more than  $10^5$  degrees of freedom (dof). Our simulation, in contrast, relies on a few hundred dofs only.

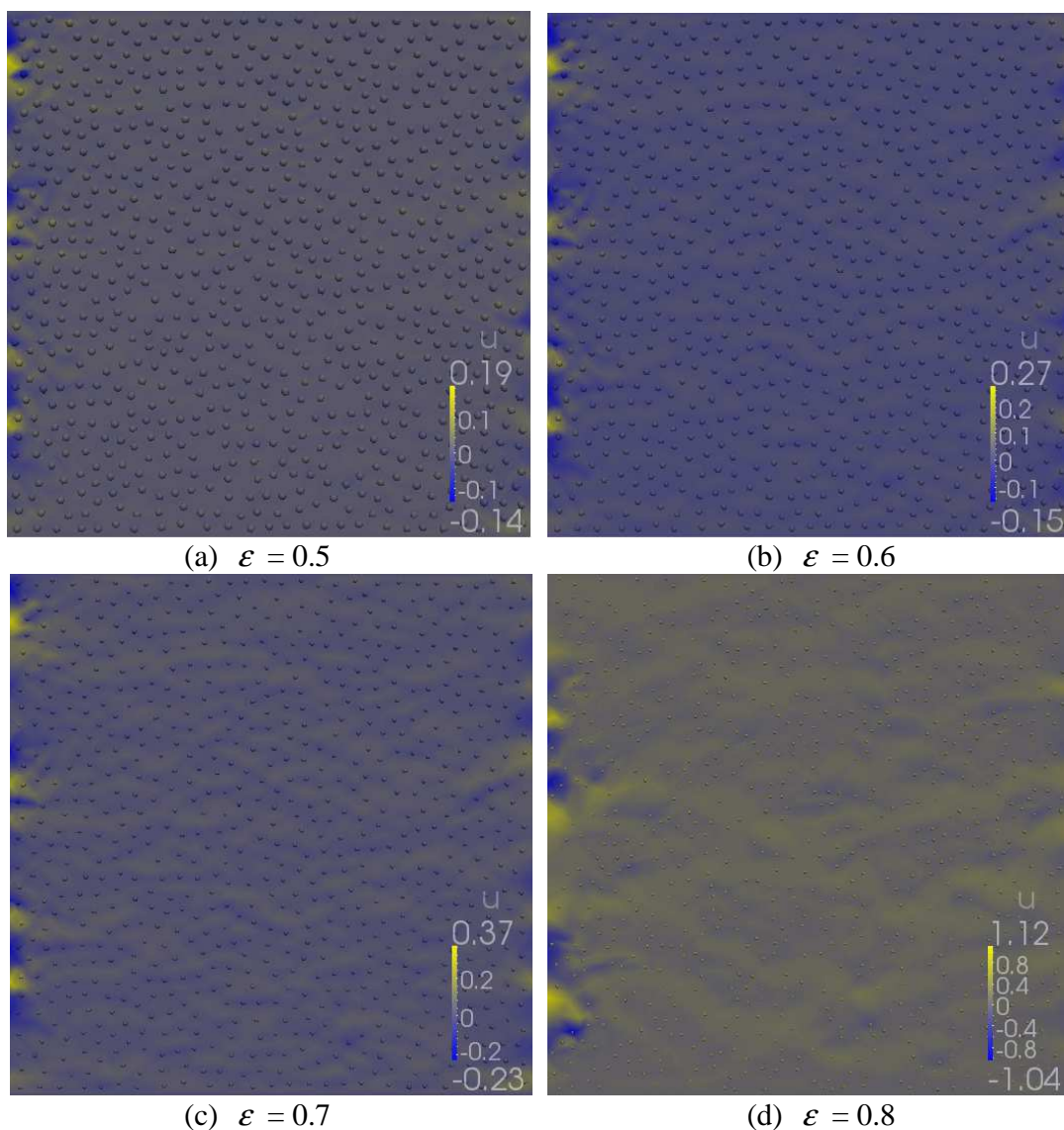


**Figure 6.6:** Horizontal velocity contours in homogeneous media with 800 randomly distributed particles at different porosities.

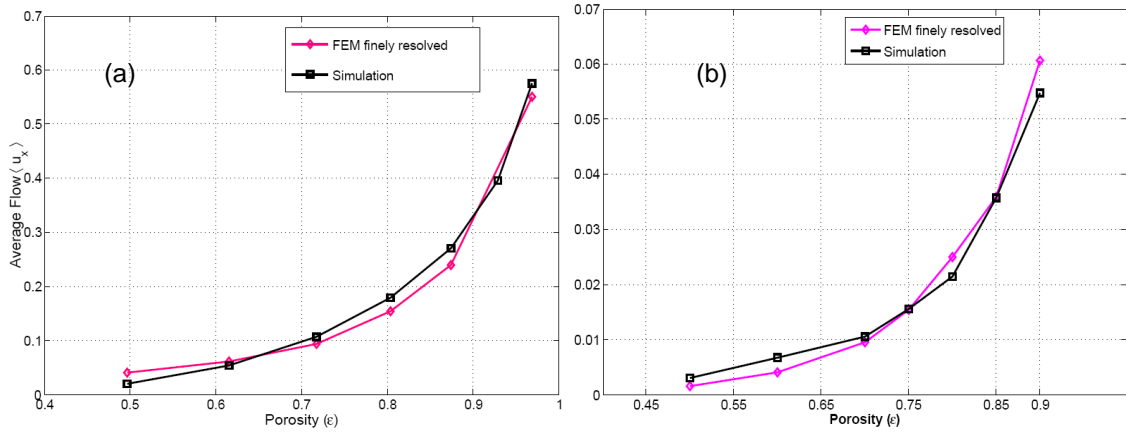


**Figure 6.7:** Average horizontal fluid velocity plotted against porosity through (a) ordered (square) and (b) random fibre arrays.

#### 6.4.2 Moving particles

For the case of moving particles, e.g. fluidized beds, the underlying grid deforms as the particles (and mesh-nodes they occupy) move. This is an important feature of our methodology, since the particle positions are known at all times, it reduces the computational overhead associated with finding particles inside the correct cell [11]. For verification, we present two test cases of one and two particle sedimentation. To circumvent the solution degeneracy due to the deforming mesh, we re-mesh at fixed intervals. Re-meshing is essential in this approach since we wish to preserve the nearest neighbor property characteristic of the Delaunay triangulation for contact detection at all times. However, this is not too restrictive as the particles do not move much per  $\Delta t_{FEM}$  time step and contact detection with walls is handled separately in our code. Therefore, we do not address the particles escaping the fluid flow region in the present work and it remains a limitation to address in future work.

##### 6.4.2.1 Case 1: Single particle settling

A particle under gravity in a viscous fluid, both initially at rest, will fall until it has reached the settling/terminal velocity,  $u_s$  calculated using the drag law prescribed in [38]. The parameters are  $\mu = 1.14$  [kg/(m.s)],  $\rho = 1.25 \times 10^3$  [kg/m<sup>3</sup>],  $\rho_p = 7.74 \times 10^3$  [kg/m<sup>3</sup>],  $d = 4.8 \times 10^{-3}$  [m] with drag force  $\vec{f}^D = 4\pi\mu\vec{u}_s / \ln(7.4/Re)$ , and  $Re = \rho\vec{u}_s d / \mu$ .

No slip boundary conditions are used at the top and bottom walls, while friction-less (no shear stress) boundary conditions are used along the left and right walls. The particle is released from  $Z_0 = 0.6H$  [m], where  $H = 2$  [m] is the height of the box. The mesh is based on the single particle location (corner points and two additional boundary points on each



wall) and consists of only 12 triangular elements, which is rather coarse. As mentioned before, we switch to 4<sup>th</sup> order polynomials for an increased flow resolution. The settling velocity can be computed when the frictional force,  $\vec{f}^D$ , combined with the buoyancy force exactly balance the gravitational force ( $m\vec{g}$ ) and is equal to  $\vec{u}_s \approx 0.17$  [m/s]. Fig. 6.8 shows the deforming mesh as the particle follows its trajectory. Near the particle surface a halo region with non-zero upwards fluid velocity appears due to the drag exerted by the falling particle. A trail of this halo is not evident since viscosity is large and our approach does not fully resolve the flow. Note that for this particular case no re-meshing was required as the mesh does not entangle throughout the simulation.

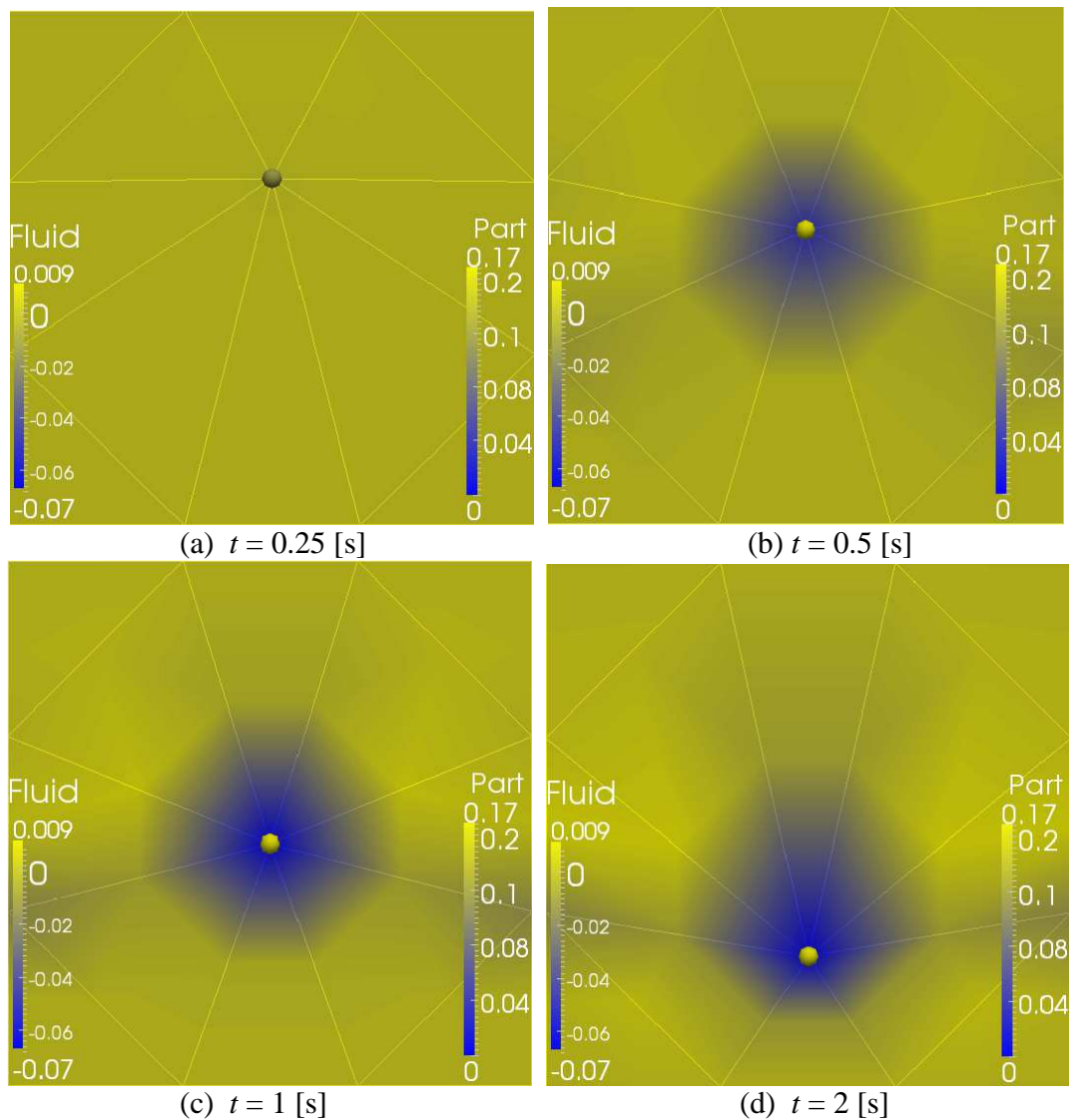


**Figure 6.8:** Deforming mesh with velocity contours for 1 particle settling using 4<sup>th</sup> order basis functions. The velocity of the falling particle quickly attains its settling velocity.

### 6.4.2.2 Case 2: The Drafting, Kissing, Tumbling (DKT) problem

We illustrate another benchmark case, where two particles are initially separated vertically and start falling under gravity. As in the previous case, both fluid and particles are initially at rest and particles are then released. The Stokes drag law, i.e.  $\vec{f}^D = 3\pi\mu d\vec{u}_s$ , with  $\mu = 10^{-3}$  [kg/(m.s)],  $\rho = 10^3$  [kg/m<sup>3</sup>],  $\rho_p = 1.01 \times 10^3$  [kg/m<sup>3</sup>] and  $d = 4 \times 10^{-3}$  [m] is used in the simulation.

Similar to the previous example, no slip boundary conditions are used at the top and bottom walls, while friction-less (no shear stress) boundary conditions are used on the left and right walls. Fig. 6.9 depicts several snapshots of the 2 particle settling behavior. While the bottom particle center is aligned with the centerline of the box, the top particle's center location is offset to the centerline by 1% to the right to trigger the instability. As the particles fall through the column of this fluid the top particle is observed to draft behind the first particle and catches up with the first particle (kissing) and then gets past it with a tumbling behavior. This behavior is very sensitive to flow resolution around particles as the draft of one particle affects the other. This behavior is well captured in using 3<sup>rd</sup> order polynomials for fluid resolution in this approach.

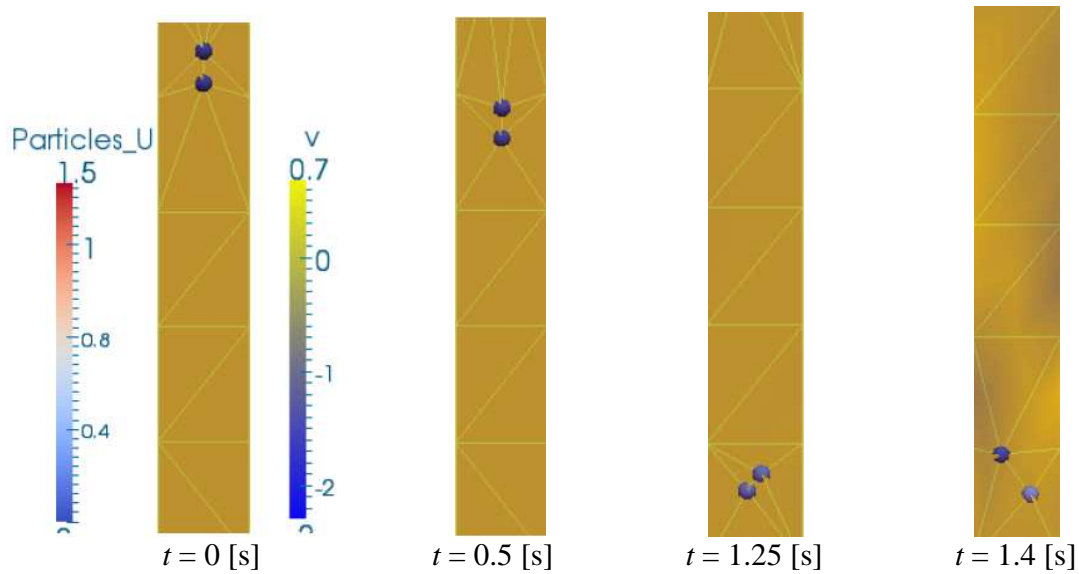


**Figure 6.9:** Snapshots of the Drafting, Kissing, Tumbling (DKT) problem. Triangles show the deforming mesh as the simulation progresses.

## 6.5 Summary and conclusions

A meso-scale, two-way, fluid-particle interaction framework based on coupling FEM and a soft particle DEM on an unstructured mesh has been proposed. The key component in our approach is a Delaunay triangulation, which serves both as a contact detection tool

and a FEM mesh. The triangulation deforms and changes with the particle motion. This design alleviates any computational overhead purported by existing methods for contact detections, particularly in dense particulate flows. Since particles always occupy nodal positions in our mesh, locating particles inside cells also becomes trivial.

A FEM based fluid solver allows for a higher order interpolation, therefore better resolution of the flow, whenever the underlying mesh is coarse. On the other hand, dense flows are resolved equally well since the mesh resolution is refining inversely proportional to the particle density. Different time scales in DEM and FEM are coupled through inner iterations of DEM steps. The approach provides the dynamics of the particles and the fluid using a deforming mesh, while reasonably resolving the fluid flow around the particles. The average velocities are accurately predicted when compared to fully resolved simulations. Furthermore, duplication of data for storing the mesh and particles as well as their contact detection, has been avoided by defining a triangulation based on particle locations. In future, we also aim to couple various other physical fields (e.g. temperature, electromagnetic, etc.), using the same data structure.

### Acknowledgements:

S.S. would like to thank S. Turek for the discussions related to the incompressible solver. KY also thanks S. Srivastava for providing me with the FEM-coupled code. This work is sponsored by STW through STW-MuST Project Number 10120.

### References

- [1] J.A.M. Kuipers and K.J. Van Duin and F.P.H. Van Beckum and W.P.M. Van Swaaij, A numerical model of gas-fluidized beds, *CES*, 47 (1992) 1913-24.
- [2] Z. Feng and E. E. Michaelides, The immersed boundary-lattice Boltzmann method for solving fluid-particles interaction problems, *JCP*, 195 (2004) 602-28.
- [3] B. Avci, P. Wriggers, A dem-fem coupling approach for the direct numerical simulation of 3d particulate flows, *J. Appl. Mech.*, 79 (2012) 10901.
- [4] S. Schwarzer, K. Höfler, B. Wachmann, H.J. Hermann, *Particle-level simulations of sedimentation and aggregation*, 1998, John Wiley, New York.
- [5] B.H. Xu and A.B. Yu, Numerical simulation of the gas-solid flow in a fluidized bed by combining discrete particle method with computational fluid dynamics, *Chemical Engineering Science*, 52 (1997) 2785 – 2809.
- [6] A.J.C. Ladd, Numerical simulations of particulate suspensions via a discretized Boltzmann equation. Part 1. Theoretical foundation, *JFIM*, 271 (1994) 285-309.
- [7] A.J.C. Ladd, Numerical simulations of particulate suspensions via a discretized Boltzmann equation. Part 2. Numerical results, *JFM*, 271 (1994) 311-339.

- [8] K. Han, Y.T. Feng, D.R.J. Owen, Coupled lattice Boltzmann and discrete element modelling of fluid-particle interaction problems, *Computers & Structures*, 85 (2007) 1080-88.
- [9] Y. Tsuji, T. Kawaguchi, T. Tanaka, Discrete particle simulation of two-dimensional fluidized bed, *Powder Technology*, 77 (1993) 79-87.
- [10] J.A.M. Kuipers, K.J.V. Duin, P.H.V. Beckum, W.P.M.V. Swaaij, Computer simulation of the hydrodynamics of a two-dimensional gas-fluidized bed, *Comput. Chem. Engrg.*, 17 (1993) 839-858.
- [11] C.L. Wu, A.S. Berrouk, K. Nandakumar, Three-dimensional discrete particle model for gas-solid fluidized beds on unstructured mesh, *Chem. Eng.*, 152 (2009) 514-529.
- [12] P.A. Cundall, O.D.L. Strack, A discrete numerical model for granular assemblies, *Geotechnique*, 29 (1979) 47-65.
- [13] S. Ergun, Fluid Flow through Packed Columns, *Chem. Eng. Prog.*, 48 (1952) 89-94.
- [14] D. Gidaspow, *Multiphase flow in fluidized beds*, (1994) Academic Press.
- [15] J.E. Drummond, and M.I. Tahir, Laminar viscous flow through regular arrays of parallel solid cylinders, *Int. J. Multiphase Flow*, 10 (1984) 515-40.
- [16] B.R. Gebart, Permeability of Unidirectional Reinforcements for RTM, *Journal of Composite Materials*, 26 (1992) 1100-33.
- [17] K. Yazdchi, S. Srivastava and S. Luding, Microstructural effects on the permeability of periodic fibrous porous media, *IJMF*, 37 (2011) 956-66.
- [18] K. Yazdchi, S. Srivastava and S. Luding, Micro-macro relations for flow through random arrays of cylinders, *Composites Part A*, 43 (2012) 2007-2020.
- [19] B.P.B. Hoomans, J.A.M. Kuipers, W.J. Briels, W.P.M. van Swaaij, Discrete particle simulation of bubble and slug formation in a two-dimensional gas-fluidized bed: A hard-sphere approach, *Chem. Eng. Sci.*, 51 (1996) 99-118.
- [20] M. Xu, W. Ge, J. Li, A discrete particle model for particle-fluid flow with considerations of sub-grid structures, *Chem. Eng. Sci.*, 62 (2007) 2302-08.
- [21] R. Glowinski, T.W. Pan, T.I. Hesla, D.D. Joseph, A distributed Lagrange multiplier/fictitious domain method for particulate flows, *Int. J. of Multiphase Flow*, 25 (1999) 755-794.
- [22] T.W. Pan, D.D. Joseph, R. Bai, R. Glowinski, V. Sarin, Fluidization of 1204 spheres: simulation and experiment, *JFM*, 451 (2002) 169-191.

- [23] Y. Kanarska, I. Lomov, T. Antoun, Mesoscale simulations of particulate flows with parallel distributed lagrange multiplier technique, *Comput. Fluids*, 48 (2011) 16-29.
- [24] T. Tezduyar, M. Behr, J. Liou, A new strategy for finite element computations involving moving boundaries and interfaces-the deformingspatial- domain/space-time procedure: I. the concept and the preliminary numerical tests, *Comput. Meth. Appl. Mech. Eng.*, 94 (1992) 339-351.
- [25] J.A. Ferrez, T. Liebling, D. Müller, Dynamic triangulations for granular media simulations, *Lecture Notes in Physics*, 554 (2000) 394-409.
- [26] T.B. Anderson, R. Jackson, A fluid mechanical description of fluidized beds, *I & EC fundamentals*, 6 (1967) 89-102.
- [27] N. Deen, M.V.S. Annaland, M.V. der Hoef, J.A.M. Kuipers, Review of discrete particle modeling of fluidized beds, *Chem. Engineering Science*, 62 (2007) 28-44.
- [28] P.C. Carman, Fluid flow through granular beds, *chemical engineering research and design. Transac. of the Inst. of Chem. Eng.*, 75 (1997) 32-48.
- [29] K. Yazdchi, S. Luding, Towards unified drag laws for inertial flow through fibrous materials, *CEJ*, 207 (2012) 35-48.
- [30] S. Luding, Cohesive frictional powders: Contact models for tension, *Granular Matter*, 10 (2008) 235-246.
- [31] D. Wan, S. Turek, Fictitious boundary and moving mesh methods for the numerical simulation of rigid particulate flows, *J. Comput. Phys.*, 222 (2007) 28-56.
- [32] C. Forster, W.A. Wall, E. Ramm, On the geometric conservation law in transient flow calculations on deforming domains, *IJNMF*, 50 (2006) 1369-79.
- [33] T. Tezduyar, S. Sathe, Stabilization parameters in SUPG and PSPG formulations, *J. Comput. Appl. Math*, 4 (2003) 71-88.
- [34] C. Forster, W.A. Wall, E. Ramm, Stabilized finite element formulation for incompressible flow on distorted meshes, *IJNMF*, 60 (2009) 1103-26.
- [35] F. Brezzi, M. Fortin, *Mixed and Hybrid Finite Element Method*, 1991, Springer Series in Computational Mechanics.
- [36] S. Turek, *Efficient Solvers for Incompressible Flow Problems: An Algorithmic and Computational Approach*, 1999, Springer.
- [37] M. Robinson, S. Luding and M. Ramaioli, Fluid-particle flow modelling and validation using two-way-coupled mesoscale SPH-DEM, *Int. Journal of Multiphase Flow*, (2012) submitted.

- [38] A.P. Peskin, G.R. Hardin, Moving particles through a finite element mesh, J. Research of National Inst. Standards and Technology, 103 (1998) 77-91.

# 7

## Summary and recommendations

*"In three words I can sum up everything I've learned about life: it goes on"*  
*~Robert Frost~*

## 7.1 Summary and general conclusions

The transport properties of fibrous porous media are essential for many processes in the chemical, petrochemical, metallurgical and food processing industries. The hydrodynamics of dispersed multiphase flows is very complex due to a wide range of time- and length-scales involved. Goal of a multiscale modeling approach is a continuum model to simulate engineering scale gas/fluid-solid flows. However, this approach requires closure equations for the unresolved sub-grid phenomena in the lower level (smaller scale) models. The interphase momentum transfer between gas/fluid and solid phases is one of the dominant forces in the gas/fluid- and solid-phase momentum balances. This momentum exchange is represented by a drag force. The drag force on a single sphere/cylinder in a fluid has been well studied for a wide range of Reynolds numbers,  $Re$ . However, when a single particle moves in a dispersed two-phase mixture, the drag is affected by the presence of other particles. Some of the drag closures can, in principle, be obtained from analytical theory, experiments and direct numerical simulations (DNS), each with their own strong and weak points.

Typically the macroscopic transport properties, like permeability or drag force, have a strong dependence on the physical properties, including porosity, pore size and structures, particle size distributions and physics of the transport processes. The need to understand these dependencies from a fundamental perspective dictates the need for modeling at the microscopic scale. Because it is experimentally difficult and expensive to study the flow characteristics at micro- or even nano- scale, deeper insights into microstructural effects have remained elusive until now.

This thesis focuses on the derivation of accurate drag (permeability) closures for 2D, unidirectional (dis)ordered arrays of cylinders/fibers, from fully resolved finite element (FE) simulations. In particular, I investigate the effect of several microstructural parameters, such as particle shape, orientation and arrangement, on the macroscopic permeability at both creeping and (moderate) inertial flow regimes. The results are given in the form of simple, universal closures valid at all porosities, which can readily be incorporated into existing multi-phase flow codes. Such relationships are of fundamental importance in many applications involving fluid flow through porous media.

In the following, the main conclusions related to each chapter will be briefly highlighted with further comments on the limitations and possible future work.

- **Chapter 2:** Based on the hydraulic diameter concept, the permeability is expressed in the general form of the Carman-Kozeny (CK) equation for *ordered* periodic structures. The numerical FE results show that the CK factor not only depends on the porosity but also on the microscopic pore structure, such as particle shape, orientation, etc. In the limits of high and low porosities, agreement with previous theoretical and numerical results is established and a unified relation is provided that is valid for all porosities.



- **Chapter 3:** A new, simple microstructural model for predicting the macroscopic permeability of *random* fibrous media is presented in terms of the statistics of the inter-fibre (surface to surface) distances. After detailed analysis of several microstructural distances (i.e. the 1<sup>st</sup>, 2<sup>nd</sup> and 3<sup>rd</sup> nearest neighbors, the hydraulic diameter, the Delaunay triangulation (DT) edges), only the 2<sup>nd</sup> nearest neighbor distance, or equivalently the shortest DT edges, lead to best correlation in a wide range of porosities. Astonishingly, a power law relation between macroscopic permeability and the average shortest DT edges, that resemble lubrication theory, is valid at high and moderate porosities for both ordered and random configurations. It is complemented by a closure relation, Eq. (3.8), which relates the effective microscopic channel length to the effective packing fraction or porosity. As an alternative, I propose a purely empirical merging function for calculating permeability in terms of porosity, which combines the analytical solutions of dilute and dense limit cases.
- **Chapter 4:** Several order parameters, based on Voronoi and Delaunay tessellations, are introduced to characterize the microstructure of randomly distributed non-overlapping fibre arrays. In particular, the mean and distributions of topological and metrical properties of Voronoi polygons have been employed to characterize the transition from disorder to order. Finally, the same quantities and data structures are used for coarse graining of the velocity and pressure gradient fields and for validation of Darcy's law at various length scales.
- **Chapter 5:** I extend my results into the *inertial flow* regime, aiming to establish a unified relationship between friction factor and Reynolds number. For ordered periodic structures: (i) the weak inertia correction to the linear Darcy relation is third power in superficial velocity, up to small Reynolds numbers,  $Re \sim 1-5$ ; (ii) a non-integer power law performs astonishingly well up to moderate  $Re \leq 30$ . For disordered (random) structures: (i) using the new definition of "gap" Reynolds number,  $Re_g$ , I obtained a universal friction factor- $Re_g$  relation, valid at almost all porosities; (ii) after scaling/collapsing all data, the two-regime approach, i.e. cubic correction at low and quadratic correction at higher  $Re$ , fit the data very well. I compare my data with the lattice Boltzmann (LB) simulations and demonstrate a good quantitative agreement for the full range of  $Re$  studied.
- **Chapter 6:** A new multiscale framework for modeling two-phase flows is presented by combining the discrete element method (DEM) for the particulate/solid phase with finite element (FE) simulations for the fluid/gas phase. The key component in this approach is a Delaunay triangulation, which serves both as a contact detection tool in DEM and as FE moving adaptive coarse mesh. Two-way momentum exchange is implemented using the previously obtained accurate and universal drag (permeability) laws for 2D fibrous systems. I illustrate and validate the methodology with several test cases, including flow through porous media, as compared against fully resolved FE simulations.

To summarize the key new findings of this thesis: (i) I present a universal relationship between macroscopic permeability/drag and porosity of fibrous media for ordered (in

chapter 2) and disordered (in chapter 3) fibre arrays at creeping flow regime. Using lubrication theory, I correlate the permeability of porous media with their microscopic properties (chapters 3 and 4); (ii) Using a new definition of gap Reynolds number, I present a unified drag laws for inertial flow regimes, valid at all porosities and Reynolds numbers up to  $Re \sim 30$  (chapter 5); (iii) I incorporate the previously obtained drag closures into the new multiscale framework for modeling two-phase flows (chapter 6). Due to the broad generality, applicability in many processes in the chemical, petrochemical and mechanical industries, my new findings deserve the wide readership and would have great impact on multiphase flow simulations and advanced models for particle-fluid interactions.

## 7.2 Outlook and recommendations

Although I addressed several aspects of microscopic and macroscopic flow relations through fibrous media, in the following, several remarks and recommendations are given that need to be improved or explored further. I highlight the issues per chapter, before discussing the higher priorities. The remaining open issues are

- **Chapter 2:** for *ordered* case: (i) validating the results against experimental measurements, such as resin transfer through unidirectional fibers; (ii) establishing a common permeability relation based on the aspect ratio, sphericity or other shape parameters; (iii) giving a physical interpretation for the cubic polynomial permeability relation (Eq. (2.11)), obtained for different stagger unit cell angles; (iv) expressing the tortuosity as function of the stagger unit cell angle (see Fig. 2.10) and further explanation for its variation; (v) extending the results for unsteady, non-Newtonian fluids.
- **Chapter 3:** for *random* case: (i) investigating the effects of polydispersity, anisotropy and heterogeneity, that occur in practical applications; (ii) founding a physical justification for the correlation between permeability and the average 2<sup>nd</sup> nearest neighbor fibre distances (see Fig. 3.10); (iii) by analogy, the permeability in 3D random packings should depend on the smallest faces of Delaunay tetrahedrons, possibly with the chance for similar unique scaling relations as in 2D, i.e. Eq. (3.13), a prediction that waits for numerical or experimental proof.
- **Chapter 4:** for *multiscale and statistical* model: (i) further understanding of the transition porosity  $\varepsilon_t^* \cong 0.393$ , i.e. why the transition from disorder to order happens at this value which is still far above the random close packing limit, the minimum hexagonal lattice, freezing point or melting point; (ii) evaluating the proposed metrical and topological properties of Voronoi cells and order parameters in 3D and compare them with the 2D case; (iii) the physical interpretation and correlation between the mean value of average velocities and permeabilities and their probability density functions at different scales; (iv)

validating of the proposed model for other macroscopic properties, like heat conductivity.

- **Chapter 5:** for *inertial flow*: (i) extending the universal friction factor relation, i.e. Eq. (5.8), to 3D realistic random porous structures; (ii) study of the anisotropic and heterogeneous media and (iii) the fully turbulent regime; (iv) testing my model for parallel flow through unidirectional fiber arrays.
- **Chapter 6:** for possible applications, extension and validation of the coarsely resolved *FEM/DEM code*: (i) include chemical reaction, heat and mass transfer or electromagnetic fields, using the same data structure, for more realistic, complex chemical reactors; (ii) simulating many other chemical processes such as particle coating, particle growth, gasification etc., which are performed in a fluidized bed, for better understanding; (iii) extension of the method to 3D is straightforward in theory, but may require a parallel version of the code.

The above list includes many possible topics, worth to pursue in the future as extensions of the present work and cannot be a complete list. Although this study presents a solid step towards the unified drag laws, ultimately, combined research at the macroscopic and microscopic scales in 3D, will improve our understanding and ability to predict the phenomena accruing at a wide variety of multiphase porous media problems. Therefore, the immediate and relatively easy step would be revisiting (or validating) the proposed permeability/drag relations of (dis)ordered porous media at creeping and inertial flows, for 3D spherical particles with realistic particle size distributions.

# Acknowledgements

During the past four years in the Multi Scale Mechanics (MSM) group, at the University of Twente, I have received great support from my colleagues, family and friends. Here I would like to express my sincere thanks to you all for your help, support, discussion and friendship. First of all, I am deeply grateful to my supervisor, Prof. Stefan Luding for coaching and hosting me in his group as a PhD student, as this greatly changes my career life. He motivated and encouraged me during the research and writing of this thesis. His patience, guidance and kind help and discussions in all aspects have made the past years an ever-good memory in my life. I have learned a lot from his extensive knowledge and experience in physics, mechanics and fluid flow and software use and many brilliant and creative ideas both in science and daily life! I also would like to express my sincere thanks to his wife, Gerlinde for generating the homely stay in Enschede through managing the social side of the group and organizing group dinners and graduation hats!

Then I like to thank all other members of the MSM group, where I had the privilege to work in an international environment. I would like to thank my former and current colleagues: Abhi, Anjenet, Anthony, Brian, Dinant, Fatih, Holger, Katia, Kay, Kuni, Martin, Mateusz, Nicolas, Nishant, Orencio, Orion, Remco, Saurabh, Sebastian, Thomas, Vanessa, Vitaliy and Wouter for bringing the friendly and creative atmosphere. Special thanks should go to Sylvia who arranges nice X'mas parties and memorable events and helping me with the administration and other paper-works with kind and patience!

Many professors, postdocs, and students have helped me or collaborated with me; thanks to J. Harting, A. Narvaez, N.P. Kruyt, M. van der Hoef, C. O'Sullivan, A.J.C. Ladd, C.S. O'Hern, X. Chen, K.W. Desmond, S. Turek and D. Rixen. Thanks also to colleagues around the world that have shared their advice or codes with me, and to the open-source community for making computing a shared resource. I extend my sincere thanks to my friends and their families in- and outside Twente (Morteza, Mahdiar, Mahmoud, Mina, Niloofar, Faraz, Majid, Sadaf, Mehrdad, Farzin, Hamid, Amir, Hadi, Taher, Milad, Damoon, Mojtaba) for their friendship and support.

Last but not least, I owe many thanks to my family. I am grateful to my parents for giving me their deep love, sacrifice, encouragement and support during my years of education. I want to thank my sister Katayoun and my brother Kayvan and their families, my uncle Jamshid and my cousins Arzhang and Payam for all the support, which made my stay in the Netherlands possible. This thesis is dedicated to them.

Finally, I would like to thank the user committee members in the project and the financial support of STW through the STW-MuST program, Project Number 10120.

Kazem Yazdchi  
October, 2012, Enschede

# Curriculum vitae

Kazem Yazdchi

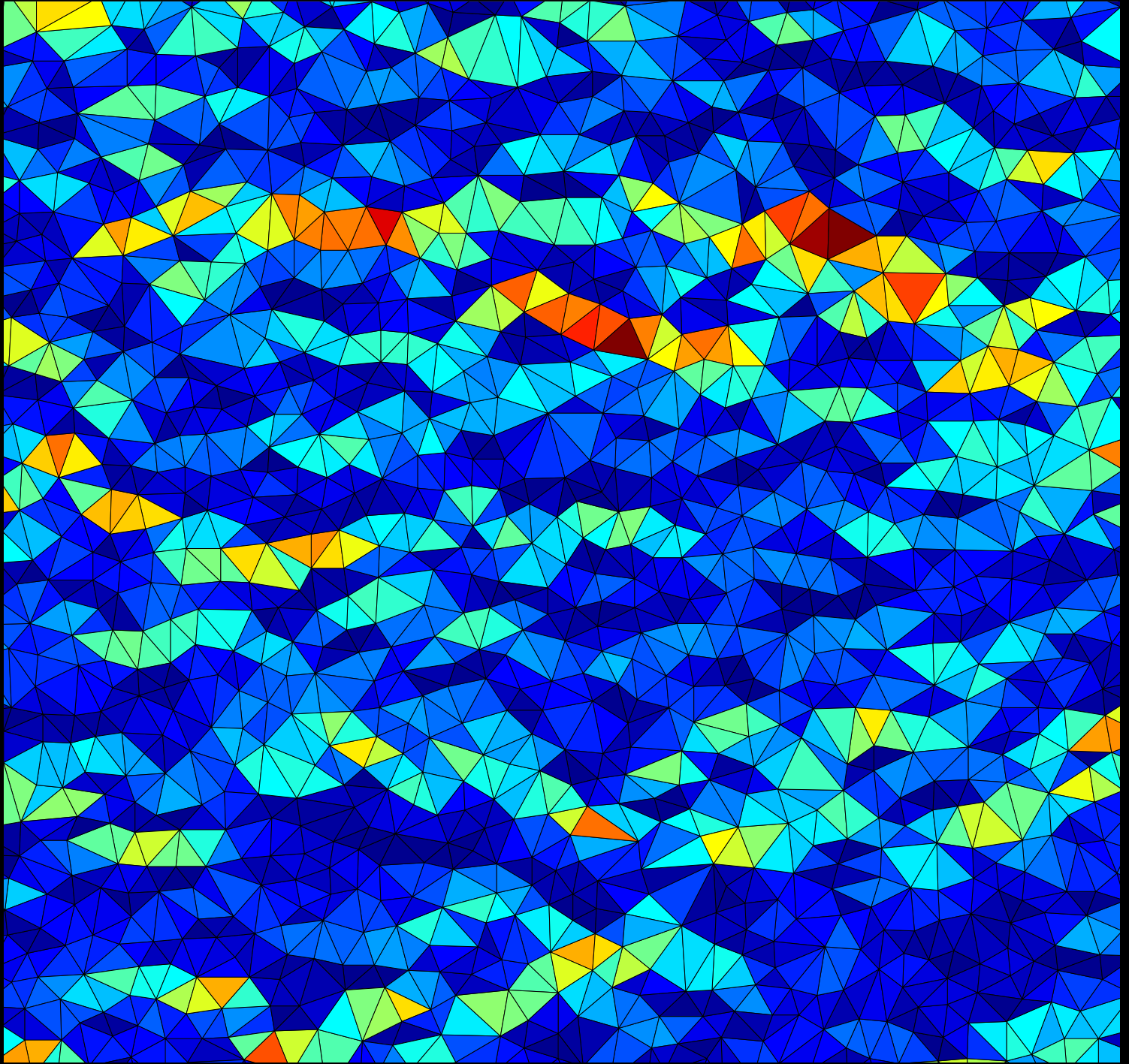
Born on September 21, 1984 in Esfahan, Iran

Ph.D.	University of Twente, Mechanical Engineering, Enschede, The Netherlands Thesis: Micro-Macro relations for flow through fibrous media Supervisor: Prof. S. Luding	2012
MSc (Hons)	Amirkabir University of Technology, Mechanical Engineering, Tehran, Iran Thesis: Constitutive modeling of viscoelastic behavior of carbon nanotube/polymer composites Supervisors: Prof. M. Salehi, Prof. M.M. Shokrieh GPA: 17.3/20	2008
BSc (Hons)	Iran University of Science and Technology, Mechanical Engineering, Tehran, Iran Thesis: Carrying capacity of edge cracked column under concentric vertical loads Supervisor: Prof. A.R. Gowhari Anaraki GPA: 16.5/20	2006
Diploma	Physics and Mathematics, Esfahan, Iran GPA: 19.3/20	2002

## Publications

- [1] K. Yazdchi, S. Srivastava, S. Luding, Microstructural effects on the permeability of periodic fibrous porous media, *Int. J. Multiphase Flow*, 37 (2011) 956-66.
- [2] K. Yazdchi, S. Luding, Towards unified drag laws for inertial flow through fibrous materials, *Chemical Engineering Journal*, 207 (2012) 35-48.

- [3] K. Yazdchi, S. Srivastava and S. Luding, Micro-macro relations for flow through random arrays of cylinders, *Composites Part A*, 43 (2012) 2007-2020.
- [4] K. Yazdchi, M. Salehi, The effects of CNT waviness on interfacial stress transfer characteristics of CNT/polymer composites, *Composites Part A*, 42 (2011) 1301-09.
- [5] K. Yazdchi, M. Salehi, M.M. Shokrieh, Analytical and numerical techniques for predicting interfacial stresses of wavy carbon nanotube/polymer composites, *Mechanics of Composite Materials*, 45 (2009) 207-212.
- [6] K. Yazdchi, A. R. Gowhari Anaraki, Carrying capacity of edge-cracked columns under concentric vertical loads, *Acta Mechanica*, 198 (2008) 1-19.
- [7] A. Narvaez, K. Yazdchi, S. Luding and J. Harting, From creeping to inertial flow in porous media: a lattice Boltzmann - Finite Element comparison, *JSTAT*, (2012), submitted.
- [8] S. Srivastava, K. Yazdchi, S. Luding, Meso-scale coupling of FEM/DEM for fluid-particle interactions, (2012) in preparation.
- [9] K. Yazdchi and S. Luding, Fibrous materials: Microstructure and macroscopic properties, (2012), in preparation.
- [10] K. Yazdchi, S. Srivastava and S. Luding, Multi-Scale permeability of particulate and porous media, *WCPT 6* (2010), Nuremberg, Germany.
- [11] K. Yazdchi, S. Srivastava and S. Luding, On the validity of the Carman-Kozeny equation in random fibrous media, *Particle-Based Methods II - Fundamentals and Applications* (2011), 264-273, Barcelona, Spain.
- [12] K. Yazdchi and S. Luding, Upscaling the transport equations in fibrous media, *ECCOMAS* (2012), Vienna, Austria.
- [13] K. Yazdchi, S. Srivastava and S. Luding, On the transition from creeping to inertial flow in arrays of cylinders, *Proceedings of IMECE* (2010), Vancouver, Canada.
- [14] S. Srivastava, K. Yazdchi and S. Luding, Two way coupled fluid-particle interaction on a deforming unstructured mesh, *ECCOMAS* (2012), Vienna, Austria.



UNIVERSITY OF TWENTE.

ISBN: 978-90-365-3414-7

